Weaving and Carrying: The Versatility of Tailored Transition-Metal Based Polypyridyl Complexes

Inauguraldissertation

zur

Erlangung der Würde eines Doktors der Philosophie

vorgelegt der

Philosophisch-Naturwissenschaftlichen Fakultät

der Universität Basel

von

Alfredo Di Silvestro

2022

Genehmigt von der Philosophisch-Naturwissenschaftlichen Fakultät

auf Anfrage von

Prof. Dr. Marcel Mayor

Prof. Dr. Oliver Wenger

Prof. Dr. Dieter A. Schlüter

Basel, den 16.11.2021

Prof. Dr. Marcel Mayor (Dekan)

Abstract

Alfredo Di Silvestro

Weaving and Carrying: The Versatility of Tailored Transition-Metal Based Polypyridyl Complexes
University of Basel, PhD thesis 2021.

The interdisciplinary scientific field of coordination chemistry describes the interaction of inorganic and/or organic ligands with transition metals and most metallic elements of the periodic table. Specific physical and chemical properties arise from the coordination between tailor-made ligands and an appropriate metal center, which can be used in several scientific fields, such as molecular electronics, life science or supramolecular chemistry. In particular, metal-based polypyridyl complexes are of fundamental interest for the preparation of functional materials due to their excellent coordinating, photophysical and biological properties. Furthermore, the synthetic procedures described for the modification of the mono-, bi- or tridentate polypyridyl ligands are very accessible and well established.

This PhD thesis is mainly focused on the design, the synthesis and the investigation of novel organometallic complexes that are strategical components for the self-assembly of a two-dimensional molecular textile, and the photodissociation of a charge-carrying photocleavable tag. The main connection between the two individual projects lies in the use of tailored polypyridyl ligands for coordination complexes, that incorporate a specific property.

The herein presented thesis is divided in 3 chapters. Within chapter 1 and 2, the synthesis and the properties of the novel functional materials prepared is discussed,

and chapter 3 provides the experimental procedures of all compounds presented. The two projects in chapter 1 and 2 are introduced individually within the chapters, as the results and the discussions are not interdependent.

Individual Projects

The first chapter deals with the ambitious goal of mimicking two-dimensional textiles on a molecular level. A novel strategy for the preparation of single- layered interwoven materials based on tailor-made amphiphilic heteroleptic terpyridine complexes will be presented. This study necessitated to synthesize kinetically stable heteroleptic complexes, determine the most suitable method for their polymerization, asses their amphiphilic behavior on an air/water interface and to deposit of the self-assembled woven materials onto substrates suitable for solid-state characterization. Additionally, preliminary imaging attempts via atomic force microscopy will be presented and discussed. This work represents a new approach for the interfacial bottom-up preparation of two-dimensional molecular textiles, reporting about our achievements in this ambitious topic.

The second chapter describes the molecular structure and the synthesis of a new class of photolabile Ru(II)-based polypyridyl complexes, which are designed to respond to a laser irradiation in high vacuum. The overall goal of this project was to prepare photocleavable tags that act as charge carriers for polypeptides or proteins and improve their potential detection in mass analyses. These would allow to specifically control the molecules charge state and their spatio-temporal location thanks to the photo-induced dissociation process. In collaboration with the research group of Professor Markus Arndt from the University of Vienna, preliminary cleavage experiments could already be performed in a modified mass spectrometer.

Acknowledgments

I want to thank my supervisor Prof. Dr. Marcel Mayor for the opportunity to work on these fascinating topics, your support throughout my studies and the freedom in my research. I enjoyed our conversations in your office with a good cup of coffee and I feel honored for having worked with you.

I also would like to thank Prof. Dr. Oliver Wenger for kindly accepting to be my second supervisor from the very beginning of my studies and for the helpful inputs during the annual presentations.

Another thank you goes to Prof. Dr. Dieter A. Schlüter for the co-examination of this thesis and to Prof. Dr. Christof Sparr for chairing the exam.

I want to thank Prof. Dr. Markus Arndt and his research team, for the fruitful collaboration and for the photo-dissociation experiments at the University of Wien..

A special thanks goes to Prof. Dr. Daniel Häussinger and his research team for helping with NMR problems and for keeping the NMR working the whole time. I also thank Dr. Heinz Nadig, Sylvie Mittelheisser and Dr. Michael Pfeffer for measuring HRMS.

I am also grateful to the Werkstatt-Team for helping me to solve upcoming technical issues. I am thankful to the administrative team of the Chemistry Department for their support and the funny discussions out of the laboratories.

My greatest appreciation shall be expressed to Dr. Hervé Dekkiche and Dr. Valentin Köhler for proofreading this thesis.

Acknowledgments

Especially my gratefulness goes to my present lab mates Hervé, Tim and Valentin for the scientific contribution during the day, the great company and enduring the ammonium hydroxide smell of my columns.

A big thanks goes to the adventure trio Raj, Thomas and Almu for their great company, the fruitful scientific discussions and for letting me sleep one night in an elevator at the airport of Nice.

Also, I would like to thank Dr. Loïc Le Pleux and all the current and former scientists of the Mayor group, including the formidable people from Karlsruhe for the exchange of knowledge, the great hospitality and for the nice team spirit. I feel honored for having worked with you and found some new friends during this awesome time.

Moreover I thank all my golden friends for distraction out of the scientific field and especially to my best friend Riccardo, for his support, the nice adventures and your friendship.

Un ringraziamento speciale va alla mia splendida famiglia: A Mamma e Papà per avermi permesso di coltivare gli studi e per aver creduto sempre nelle mie capacità. Ai miei Nonni per l'affetto e i valori trasmessi in tutti questi anni. A mio fratello Stefano per essere stato sempre un buon amico e soprattutto un aiuto. A tutti i miei zii, cugini, cognata, nipotina per far parte della mia vita.

Finally, I thank Stephi for her love and support during the frustrating parts of this thesis and her patience during all our years together.

alla mia famiglia

"It`s kind of fun to do the impossible."

Walt Disney

Table of Contents

Table of Contents

Table of Contents

Table of Contents

Chapter 1

2D Molecular Textile based on Mechanically Interlocked Amphiphilic Terpyridines
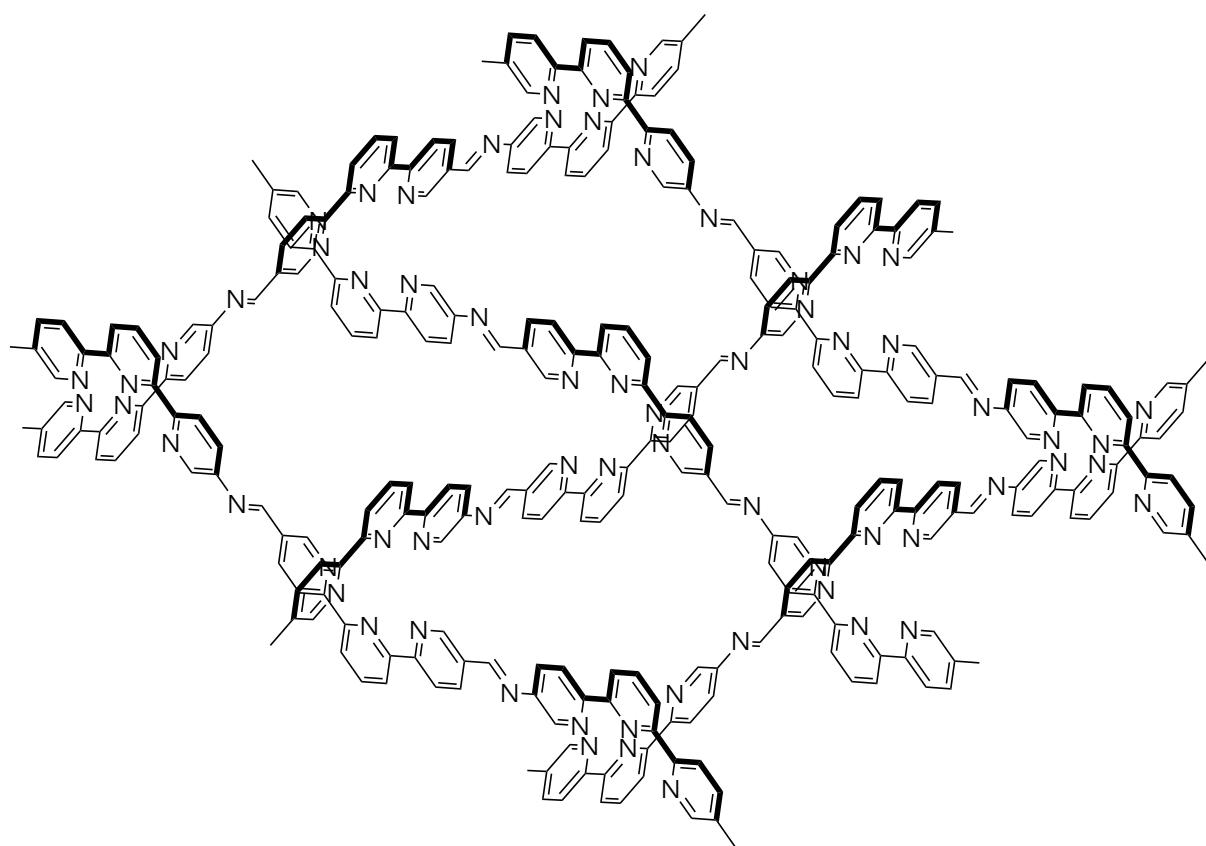
Introduction

Supramolecular Chemistry

Supramolecular chemistry is an interdisciplinary field of the modern science, that is investigating the molecular recognition and the formation of complex molecular structures, by non-covalent interactions of several chemical building blocks.[1] The main idea is to design and to synthesize fundamental building blocks, formed by strong covalent-bonds, that self-assemble to a higher order structure. The so-called supermolecule[2,3] is created through weak interactions such as π-π interactions, hydrogen bonds, van der Waals interactions or reversible covalent bonds.[4] In 1987 the Nobel Prize in Chemistry was awarded to J.–M. Lehn, C. J. Pederson and D. J. Cram "For their development and use of molecules with structure-specific interactions of high selectivity."[5]. [2,6,7]

The most obvious examples of supramolecular architectures are provided by nature, such as the deoxyribonucleic acid (DNA) double helix or the enzyme-substrate complex, which are showing working processes embedded in this interdisciplinary scientific field. In the last 60 years, scientists were able to synthesize ambitious molecular structures using template-controlled reactions and gave access to many functional materials such as molecular machines[8–11], molecular sensors[12–14] and nanoreactors[15–17]. As mentioned at the beginning of this subchapter, supramolecular chemistry is an interdisciplinary scientific field including many disciplines such as organic chemistry, physical chemistry, coordination chemistry, polymer chemistry, material science, biology and many other scientific branches.[18] Therefore, it was extensively reviewed over the last decades.[1,19–24]

Tpys and their Metal Complexes in Supramolecular Chemistry

The coordination driven self-assembly of tpys derivatives with a broad variety of transition and particular rare-earth metals, gave access to two-dimensional (2D) and three-dimensional (3D) metallosupramolecular architectures. The library of supramolecular structures based on the self-assembly of tpys, especially the 4'-substituted tpy building block, has been extensively reviewed over the last decades.[25–29] Therefore only selected examples can be highlighted hereafter.
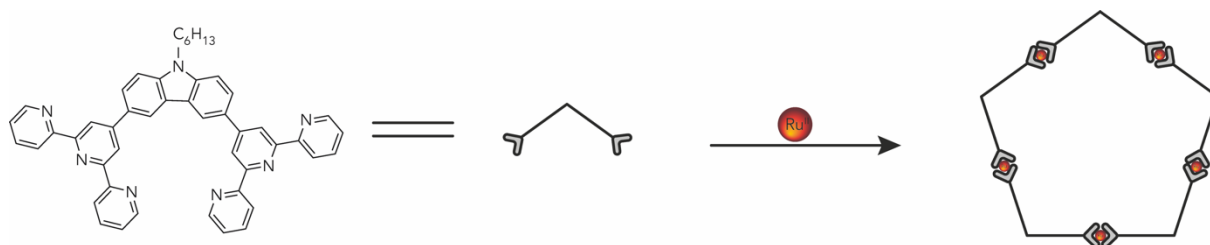
Figure 1: Molecular structure of 4,4''-bis(tpy)-carbazole monomer (left side) and the self-assembly reaction to a metallopentacyle as sketch.

As mentioned above, the 4'-substituted tpy derivative is a suitable linker for supramolecular structures, since the tridentate ligand can be utilized as 180° linker. For example 4,4''-bis(tpy)-carbazole (figure 1), has a fixed corner angle due to the rigid aromatic system and as reported by Newkome and collaborators,[30] a metallopentacylce can be obtained upon complexation with a transition metal ion such as Ru(II). Another astonishing example is the assembly of a molecular "Sierpinski hexagonal gasket" via Ru(II) and Fe(II) based bis(tpy) complexes, reported by Newkome and co-workers.[31] The supramolecular structure was obtained, by the coordination of bis(tpy) building blocks to 36 Ru(II) and 6 Fe(II) ions, leading to 6 nearly planar arrayed coordinated hexagons possessing an excellent inherent stability, as illustrated in figure 2.

a)

b)

84 (PF$_6^-$)

c)
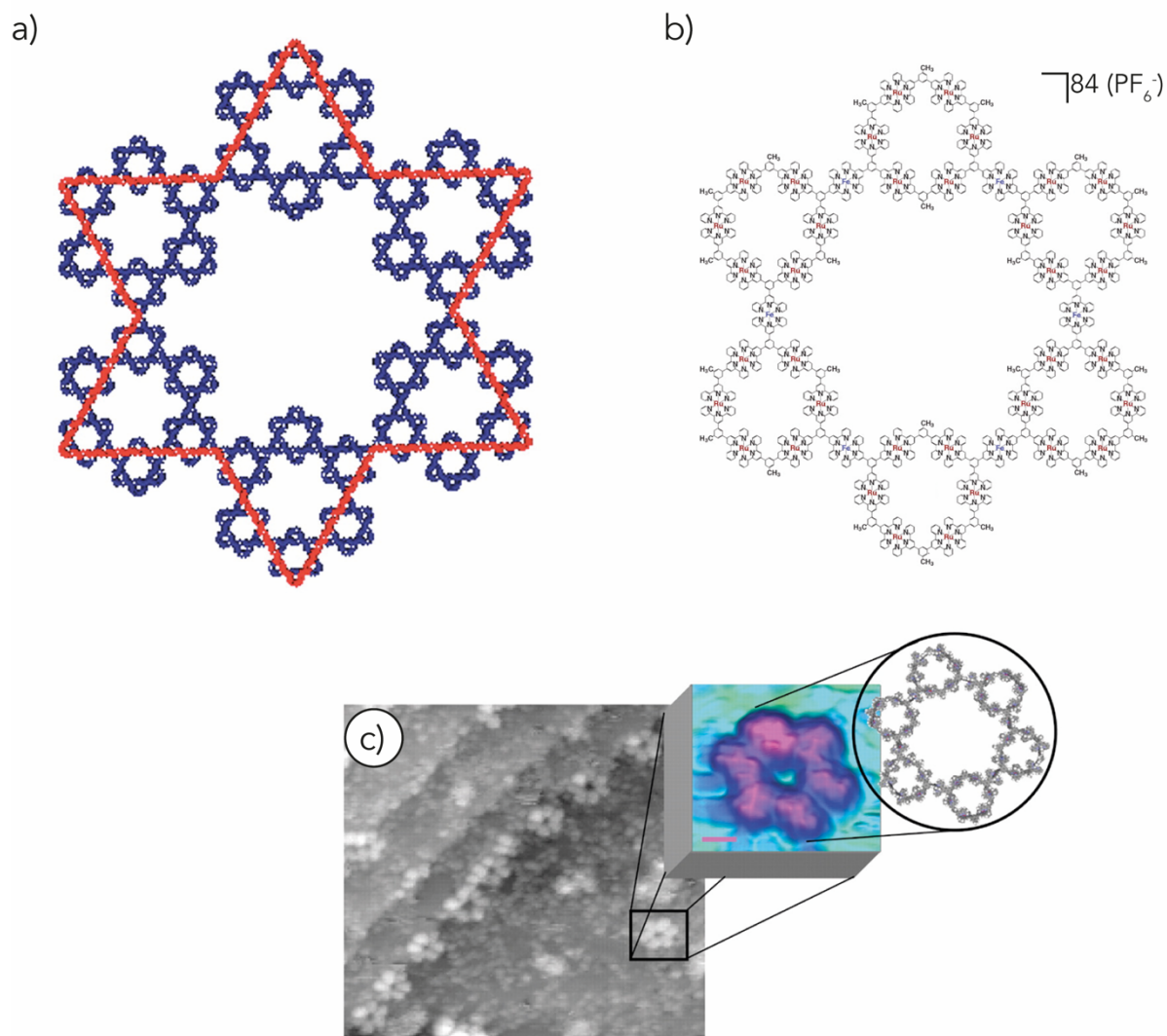
Figure 2: (a) Sketch of the Sierpinski hexagonal gasket, incorporating the David star highlighted in red.; (b) The molecular structure of the Sierpinski hexagonal gasket.; (c) UHV-STM images on an Au(111) surface at 6K, showing a line of hexagonal gaskets and a magnified image of a single molecule. Adapted from ref. [31] with permission from AAAS.

The study via high-resolution scanning tunnelling microscope (STM), could confirm the hexagonal gasket structure, as illustrated in figure 2c. In addition, several bis(tpy) building blocks were assembled with different metal ions and gave rise to supramolecular structures such as Sierpinski triangles[32–34], supramolecular stars[35], nanosnowflakes[36], hexagon wreaths[37] , 2D and 3D molecular spoked wheels[38,39] and a molecular trapezoid[40]. Moreover, tpy based derivatives were self-assembled into 3D architectures with large cavities, which can be utilized for host-guest chemistry such as the metallo-cuboctahedron reported by Newkome and co-workers.[41] The

cuboctahedron-shaped supramolecule was synthesized in a single-step using 12 tetradentate tetrakis(tpy) ligands with 24 Zn(II) ions, as illustrated in figure 3. The large cavity could show very promising results for drug transport and host-guest chemistry.
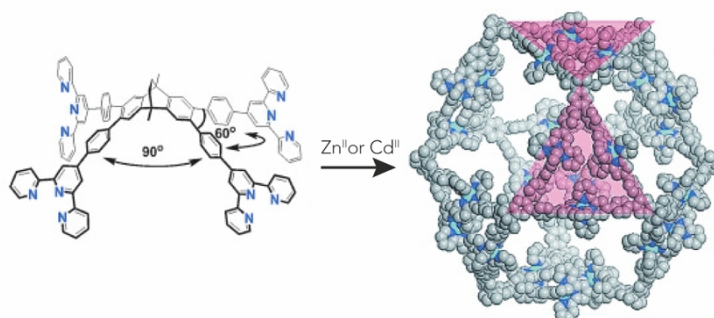
Figure 3: Molecular structure of tetrakis(tpy) monomer (left side) and the self-assembly process yielding the metallo cuboctahedron (right side), utilizing Zn(II) or Cd(II) as metal ions. Adapted from ref. [41] with permission from John Wiley and Sons.

Terpyridines

In 1932, the first publication concerning the synthesis of 2,2':6',2''-terpyridine (tpy) was published from Morgan and Brustall.[42] The oxidative condensation of pyridine, which was performed with anhydrous $FeCl_3$ in an autoclave (50 atm) at 340 °C for 36 h, yielded small amounts of the desired tpy, a myriad of different *N*-containing by-products and predominantly 2,2'-bipyridine (bpy). A few years later, the formation of an intensively coloured solution of tpy upon addition of Fe(II)-ions was discovered and the first indications for a metal complex were established.[43]
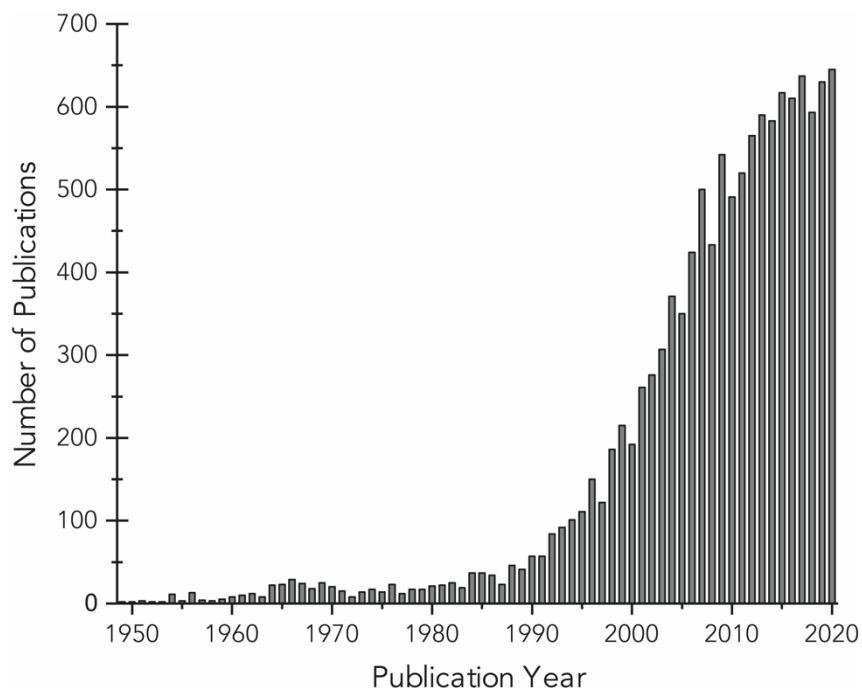
Figure 4: Histogram of the number of publications containing the term "terpyridine" using SciFinder™ (search performed on the 22nd July 2021).

As one can see in figure 4, the first reports about tpys appeared about 60 years ago. Though, its popularity drastically increased only in the 90's due to its huge potential as ligand for coordination and therefore supramolecular chemistry, which emerged at that very same time.
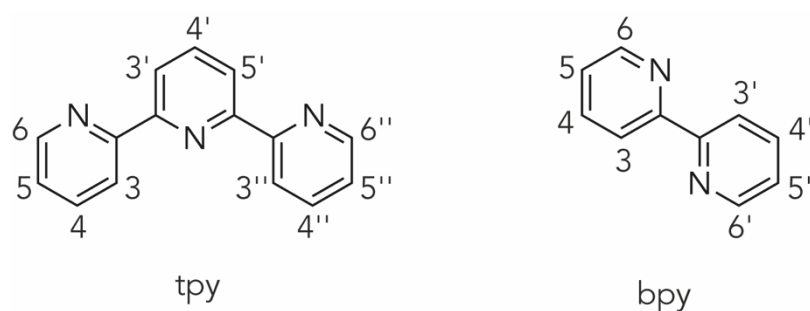
Figure 5: Chemical structure of 2,2':6',2''-terpyridine (tpy) and 2,2'-bipyridine (bpy).

The fact that tpy chemistry became popular with the advances in the preparation of supramolecular assemblies can be correlated with the coordination chemistry

between tpy ligand and metal, which is a fundamental tool of supramolecular chemistry. The three nitrogen atoms in the molecular structure of tpy, which can act as tridentate ligand, makes it very suitable for the complexation with a wide range of transition and rare earth metal ions.[44] Furthermore, the attractive photophysical and redox properties arising from the complexed species allows the substrate involved to be very interesting and relevant for different application areas.

Synthetic Approaches
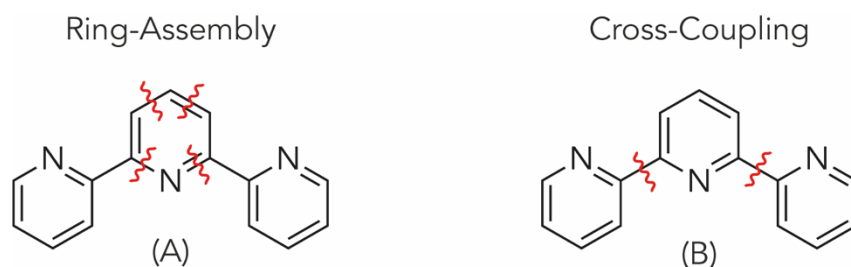
Figure 6: The two basic methods for the synthesis of tpys: (a) ring-assembly approach; (b) cross-coupling approach.

For the preparation of tpy-based molecular structures, there are two basic synthetic approaches: the ring-assembly and the transition metal-catalyzed cross-coupling strategies, as displayed in figure 6. One of the most documented ring-assembly strategies is the Kröhnke methodology, where the middle pyridine ring is assembled via condensation reaction to the desired tpy derivative. A competitive alternative to the ring closure procedures is the modern Pd^0-catalyzed cross-coupling method, where the peripheric pyridine rings are coupled to the middle pyridyl unit, leading to the target tpy-based structure. In this subchapter, the reader of this thesis will have an introduction of the two main approaches for the preparation of substituted tpys.

Ring-Assembly Approach

One of the most common and general strategies for the synthesis of tpys is the ring-assembly approach, which employs building blocks obtained by the classical Hantzsch-type[45] and Tschitschibabin-type[46] synthesis of pyridine derivatives. In this approach, the middle tpy ring is assembled via condensation reaction, yielding the tpy-based structure. Scheme 1 illustrates the most used strategies for the assembly of the tridentate ligand. One of the most common procedures for the synthesis of substituted tpys, like **III** (Scheme 1, route a) is the Kröhnke methodology, first reported from Fritz Kröhnke in 1976.[47]
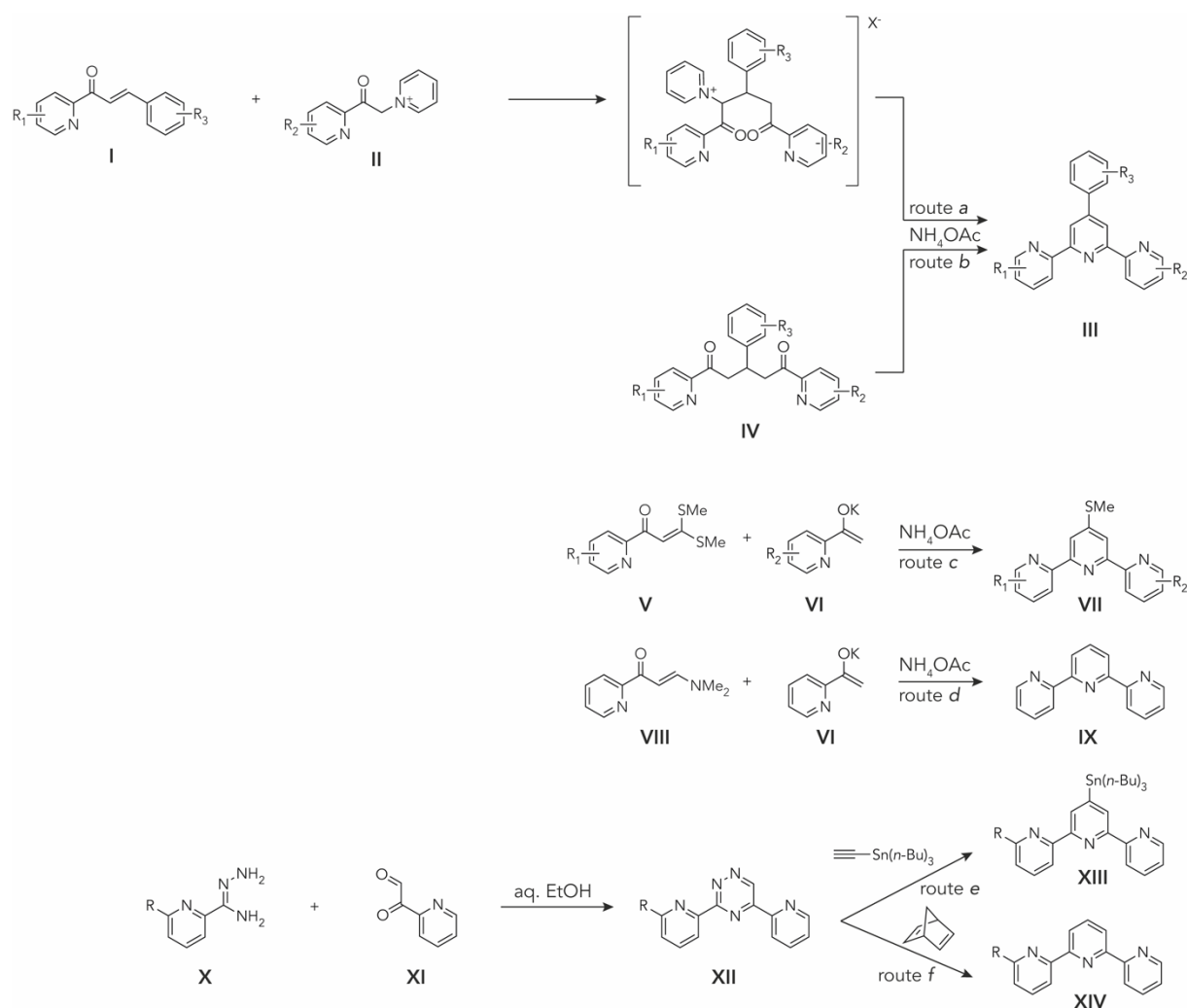
Scheme 1: An overview of the most common ring-assembly approaches: Kröhnke condensation (routes a and b), Potts' methodology (route c), Jameson's protocol (route d) and Sauer's inverse-type Diels-Alder methodology (routes e and f).

This strategy involves the condensation reaction of an enone **I** with pyridinium salts **II** (X = Br or I), which can be prepared via an Ortoleva-King reaction[48], yielding the so-called Kröhnke-type tpys (**III**). Enone **I** can be synthesized via aldol reaction, starting from 2-acetylpyridine and a (hetero)aromatic aldehyde. Route b is an alternative Kröhnke condensation, involving first the synthesis of 1,5-diketon (**IV**) via an aldol-Michael cascade reaction and subsequently the ring-closure with a suitable ammonia source, leading to Kröhnke-type tpys **III**.[49–51] It is important to mention that both routes are limited, since the harsh conditions needed are not suitable for sensitive functional groups and R_3 needs to be a (hetero)aromatic substituent.

Another relevant ring-assembly procedure is the Potts' methodology (route c), which uses an α-oxoketene dithioacetal (**V**), that can be synthesized from 2-acetylpyridine. In this methodology, α-oxoketene dithioacetals **V** reacts with a previously formed potassium enolate and the subsequent ring closure with ammonia acetate, yields the tpy derivative **VII**.[52,53] The Jameson's protocol (route d), can be seen as an improvement of Potts' methodology, as the tpy **IX** (analogous to **VII** without methylthiol group) is directly obtained using a similar synthetic path.[54] In this case tpy derivative **IX** is obtained by the condensation reaction of ß-(dimethyl-amino)vinyl 2-pyridyl ketone (**VIII**) with the potassium enolate of 2-acetylpyridine (**IV**) followed by the subsequent ring closure with ammonium acetate. An ultimate strategy to make tpy derivatives is the Sauer's methodology (route e and f), where an inverse-type Diels-Alder reaction of 3,5-di(pyridine-2-yl)[1,2,4]triazines (**XII**) with either ethynyltri(*n*-butyl)tin or norbornadiene is used for the preparation of tpy derivatives **XIII** (Scheme 1, route e) or **XIV** (Scheme 1, route f) in good yields.[55] **XII** can be synthesized from carboxamidrazones (**X**) and α-pyridylglyoxal (**XI**) via regioselective cyclocondensation in aqueous ethanol. In comparison with the Kröhnke condensation (route a and b), the Potts' (route c), Jameson's (route d) and Saure's (route e and f) methodologies provide compounds limited in structure and lack of diversity. To overcome this structural drawback, various methodologies were discovered for the multiple functionalization on the outer pyridyl rings, such as the high yielding four-

step synthesis of symmetric 5,5''-disubstituted tpys reported by Adrian and collaborators in 1998.[56] The broad application of the Kröhnke methodology inspired scientists to further improve this strategy, for example with the twofold Kröhnke-type procedure reported by Sasaki and co-workers in 1999, describing an effective method for the preparation of highly substituted symmetric tpys (Scheme 2a).[57] This procedure starts by the conversion of 2,6-diacetylpyridine (**XV**) to the corresponding bis(pyridinium) iodide salt (**XVI**) using the Ortoleva-King reaction. Afterwards, **XVI** is reacted with an appropriate α, ß-unsaturated aldehyde **XVII** in presence of ammonium acetate, to obtain the corresponding symmetric tpy derivative **XVIII**. In 1997, Fallahpour and collaborators were able to synthesize a 4-functionalized 2,6-diacetylpyridines **XXI** starting from chelidamic acid (**XIX**).[58] The acid **XIX** was first converted into a 4-substituted 2,6-bis(chlorocarbonyl)pyridine **XX**, followed by the treatment with Meldrum's acid and the subsequent hydrolysis with aqueous acetic acid.
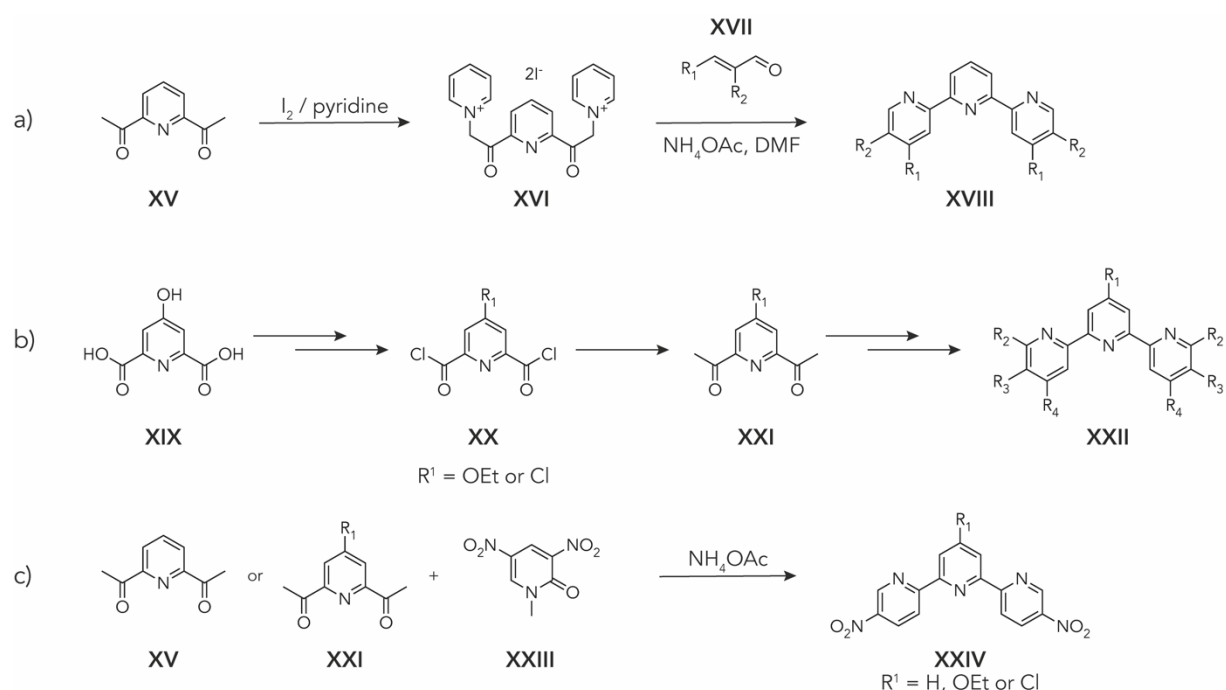
Scheme 2: Overview of different modified Kröhnke condensations according to Sasaki (a) and Fallahpour (b and c).

A 4-functionalized derivative **XXI**, where both sides of the pyridine ring are decarboxylated, is therefore obtained. With the key substrate for the Kröhnke

methodology in hands, Sasaki's procedure was adapted and extended for the preparation of 4'-subsituted tpys derivatives **XXII** (Scheme 2b).[59] Furthermore, as displayed in scheme 2c, 5,5''-dinitro-tpy (**XXIV**) can be obtained reacting **XV** or **XXI** with electron-deficient 1-methyl-3,5-dinitro-2-pyridone (**XXIII**) in presence of ammonium acetate, as reported by Tohda and co-workers.[60]

Cross-Coupling Approach

The second most common strategy for the assembly of tpys is the transition metal-catalyzed cross-coupling approach. This approach allows the direct coupling of the two peripherical pyridine rings to the central one by the formation of two new C-C bonds. In the last 30 years, the progress of Pd^0-catalyzed C-C cross-couplings allowed to employ milder reaction conditions, to give access to many functional groups and higher efficiency. The antiquated methodologies, such as the cross-coupling of organosulfur compounds[61] or the copper(II)-mediated coupling of lithiopyridines[62] suffered from harsh reaction conditions, low efficiency and a lack in directionality. Furthermore, the development of Pd^0-catalyzed cross-couplings gave the possibility to introduce tailor-made substitution patterns and a new library of accessible molecular structures. For these astonishing improvements and the pioneering research in modern Pd^0-catalyzed cross-coupling, the Nobel Prize in Chemistry was awarded to Heck, Negishi and Suzuki in 2010.[63–65] However, the preparation of tpy-based molecular structures via cross-coupling remains limited in literature compared with the ring-assembly approach, which was presented in the previous subchapter (Ring-Assembly Approach). The most common cross-coupling reactions such as the Heck-,[66–69] Hiyama-[70,71], Kumada-,[69,72,73] Negishi- ,[69,74,75] Sonogashira-,[69,76] Suzuki-Miyaura-[69,77–79] and Stille cross-coupling[69,80,81] are all based on a Pd^0 - or occasionally Ni^0 -catalytical circle. The Stille cross-coupling has become a suitable and common strategy for the synthesis of tpys, because of the broad selection of building blocks,

the multigram scale-up possibility and the high functionalization at almost every desired position of the pyridyl units.[82]
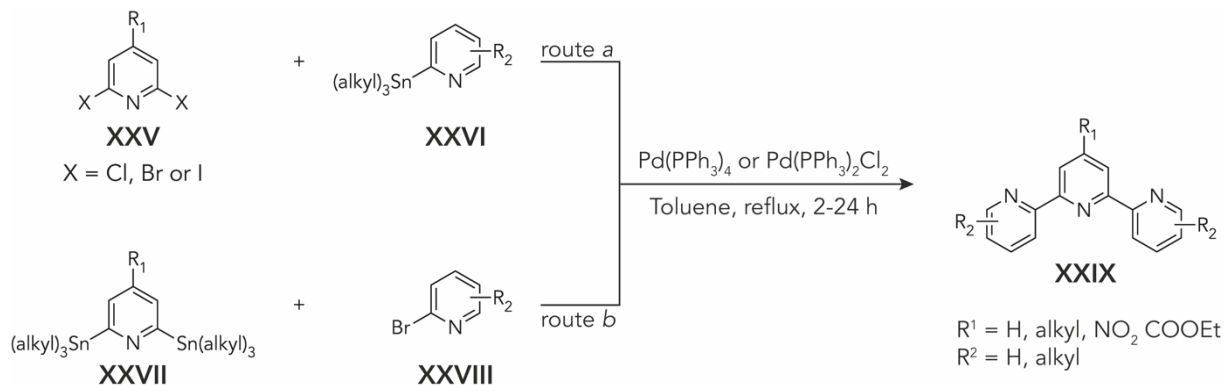
Scheme 3: Synthesis of substituted 2,2':6',2''-tpys via Stille cross-coupling using two different routes (route a and b).

Scheme 3 displays two general routes for the synthesis of tpys, bearing functional groups at the position 4' of the central pyridyl unit and/or the peripheric pyridine rings (**XXIX**) via Stille cross-coupling. The first strategy (scheme 3, route a) consists of the coupling between an appropriate 2,6-dihalopyridine **XXV** as central building block with 2-trialkylstannylpyridines **XXVI**.[83–90] The second route (scheme 3, route b) relies on the cross-coupling of 2,6-bis(trimethylstannyl)pyridines **XXVII**, with the corresponding 2-bromopyridines **XXVIII**.[91,92] It is important to mention, that in both approaches the same catalytic source and the same reaction conditions were used, but the reaction time is different. Though, the purification of the compounds formed is challenging and in addition, the handling of the highly toxic and volatile tin by-products formed during the transmetallation step, and the post-reaction workup are not pleasant. Louërat and collaborators reported about an alternative Pd-catalyzed cross-coupling procedure for the synthesis of 2,2':6',2''-dichloroterpyridine (**XXXIV**) using a copper-mediated Hiyama cross-coupling.[93] This approach was primarily developed for the synthesis of substituted 2,2'-bpys (**XXXII**), as illsutrated in scheme 4a. 4-Chloro-2-trimethylsilylpyridine (**XXX**) was reacted with differently

substituted halopyridines (**XXXI**) to yield a variety of 4-chloro-substituted bpys **XXXII**. Furthermore, reacting an excess of **XXX** with 2,6-dibromopyridine (**XXXIII**), affords the dichlorinated tpy **XXXIV** as illustrated in scheme 4b.
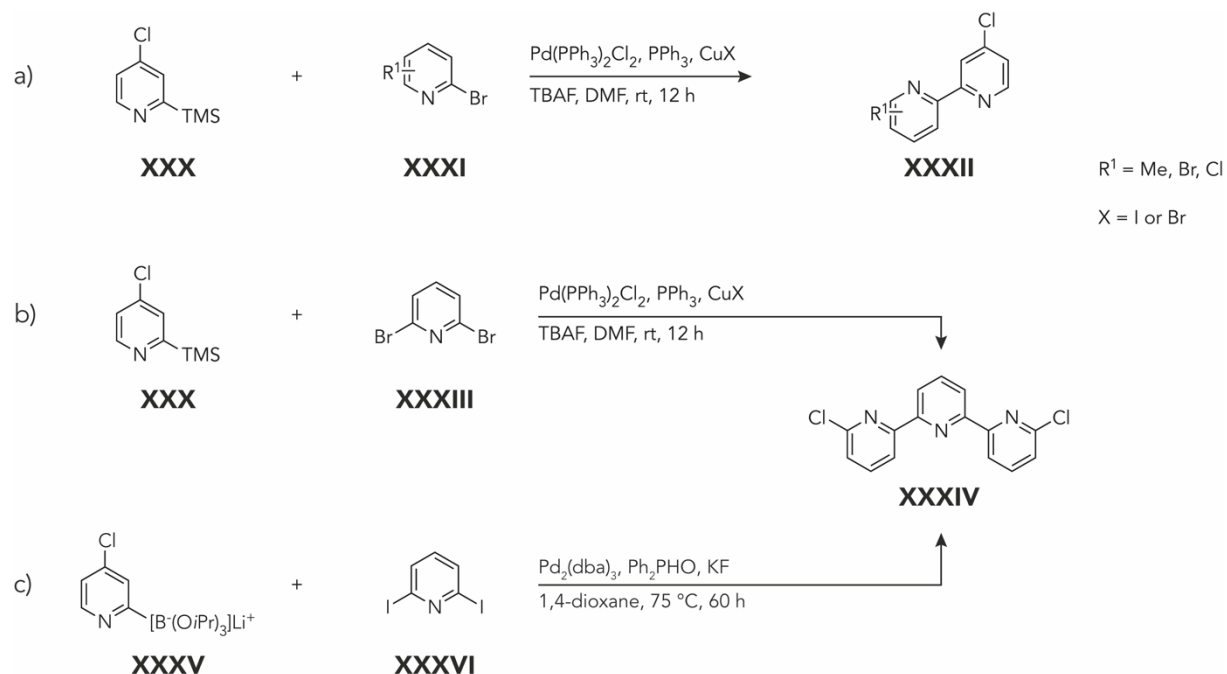
Scheme 4: Synthesis of substituted 2,2'-bpys (a) and 2,2':6',2''-dichloroterpyridine (**XXXIV**) (b) via Hiyama cross-coupling and (c) via adapted Suzuki-Miyaura cross-coupling.

Harzmann and co-workers reported about an efficient synthesis of **XXXIV**, using a Pd-catalyzed Suzuki-Miyaura cross coupling protocol.[94] Lithium triisopropyl 2-(4-chloro-pyridyl)borate (**XXXV**) was reacted with 2,6-diiodopyridine (**XXXVI**) using tris(dibenzylideneacetone)dipalladium (Pd$_2$(dba)$_3$) as catalyst, diphenylphosphane oxide (Ph$_2$PHO) as ligand and potassium fluoride (KF) as base to afford 66 % of the dichloro tpy species **XXXIV** (see scheme 4c). It is important to mention, that the lithium triisopropyl 2-pyridiylboronate **XXXV** seems to be stable against proton-deboronation during the coupling process. However, no other Pd-catalyzed cross-couplings approaches for the synthesis of tpys has been used to these days. Though, there are suitable procedures employing the Negishi cross-coupling for the synthesis of differently substituted bpys[95] or 2,6-di(pyridine-2-yl)benzenes[96], which are analogous

to tpys. Another potentially interesting procedure for the preparation of tpys involves the Suzuki-Miyaura cross-coupling using pyridine boronic acids or ester derivatives, since the precursors are accessible in a variety of substrates and it avoids the occurrence of toxic tin by-products such as in the Stille cross-coupling. Nevertheless, the lability of the 2-pyridyl boronic acid, better known as the 2-pyridily problem, which suffers from facile proton-deboronation during the coupling process, renders the formation of the target tpys almost impossible.[97] That is the reason why a successful tpy formation via the Suzuki-Miyaura method using pyridine boronic acids or esters derivatives have not been reported so far and that further investigation are needed.

Transition-Metal Complexes of Tpys

As mentioned at the beginning of this chapter (Terpyridines), Morgan and Burstall were the first scientists to report about the complexation of an Fe(II) transition metal ion with two tpy ligands.[43] This was the inauguration of an extensive library of tpy complexes, where tpy derivatives are coordinated to transition metal as well as lanthanide/actinide ions. Figure 7 illustrates the distribution of published reports or patents, dealing with the various metal tpy complexes. One can see that complexation of tpy derivatives with the early transition metals and actinide ions might be considered as rarities. An opposite trend is observed for late transition metals, and in particular with metal ions that can have a d^6- (e.g., Fe(II), Ru(II), Os(II) or Co(II)), a d^8-(e.g., Ni(II) or Pt(II)) or a d^{10}-configuration (e.g., Zn(II) or Cu(I)) and the lanthanide Eu(III), which were extensively studied in the last decades. The most common coordination geometry for tpy complexes, is the (distorted) octahedral geometry, where a metal ion is coordinating to two tpy ligands forming a bis(tpy) complex, or by one tpy ligand and additional ancillary ligands. The less common coordination geometries are the trigonal-bipyramidal (e.g. Cu(II) ions) or square-planar species (e.g. Pd(II), Pt(II) or Au(III) ions).[98]

H																	He
Li 16	Be 0											B	C	N	O	F	Ne
Na 85	Mg 17											Al 8	Si	P	S	Cl	Ar
K 38	Ca 11	Sc 4	Ti 14	V 47	Cr 65	Mn 299	Fe 903	Co 727	Ni 357	Cu 718	Zn 622	Ga 13	Ge 5	As	Se	Br	Kr
Rb 5	Sr 3	Y 27	Zr 4	Nb 2	Mo 29	Tc 10	Ru 3299	Rh 93	Pd 156	Ag 84	Cd 154	In 20	Sn 37	Sb 5	Te	I	Xe
Cs 7	Ba 6		Hf 0	Ta 1	W 9	Re 72	Os 322	Ir 163	Pt 746	Au 54	Hg 41	Tl 7	Pb 39	Bi 10	Po	At	Rn
Fr 0	Ra 0																

La 54	Ce 25	Pr 40	Nd 77	Pm 1	Sm 53	Eu 318	Gd 79	Tb 113	Dy 61	Ho 33	Er 74	Tm 23	Yb 66	Lu 31
Ac 0	Th 3	Pa 0	U 30	Np 4	Pu 1	Am 4	Cm 2	Bk 0	Cf 0	Es 0	Fm 0	Md 0	No 0	Lr 0

Figure 7: Periodic table of elements, illustrating the metals in black and the non-metals in grey. The number of under each symbol represents the amount of published scientific papers or patents, involving a tpy complexe with the corresponding element. The search was performed using SciFinder™ (search performed on the 28th July 2021).

Furthermore, rare-earth metals (e.g. Eu(III)) can have up to nine coordination sites, due to the participation of the f-orbitals and therefore bind three tridentate ligands.[99] However, the coordination geometry of the different complexes is absolutely dependent on the nature of the coordinated metal ions.[100]

As illustrated in figure 8, three different approaches are existing for the synthesis of bis(tpy) metal complexes. The One-step procedure can be applied in principle to all transition metal ions, complexing two identical tpy ligands forming a homoleptic bis(tpy) metal complex (figure 8a).
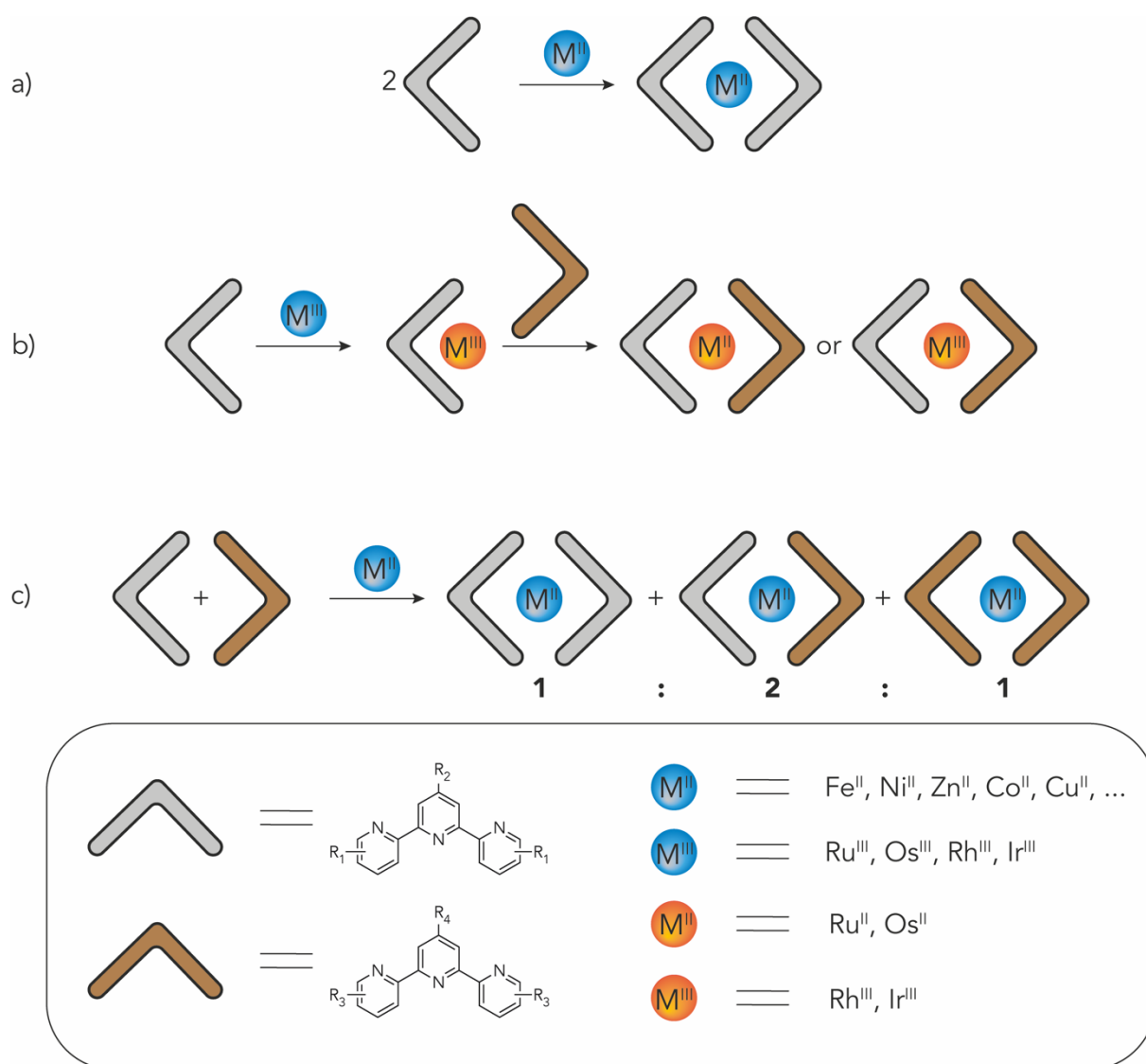
Figure 8: Overview of the different tpy metal complexation approaches: (a) One-step procedure for the preparation of homoleptic bis(tpy) metal complexes; (b) Directed two-step procedure for the synthesis of heteroleptic bis(tpy) metal complexes. (c) One-step procedure for the statistical preparation of homoleptic and heteroleptic bis(tpy) metal complexes.

The second method is a directed two-step procedure, where two different tpy ligands are yielding a kinetically stable heteroleptic bis(tpy) metal complex (Figure 8b). This strategy is only applicable for metal ions with a high binding constant (K) towards the tpy ligands such as Ni(II),[101] Os(II),[102] Ru(II),[102] Rh(III)[103,104] or Ir(III)[105,106] forming very stable thermodynamic products. The one-step procedure can be used also for the preparation of heteroleptic bis(tpy) metal complexes via statistical reaction, as illustrated in figure 8c. Within this method, two homoleptic and one heteroleptic

bis(tpy) complexes are synthesized with a relative ratio of 1:2:1. In this case the complexes are kinetically products, forming in most cases labile heteroleptic molecules.

2D Polymers

Our everyday life is surrounded by polymers in many different forms, such as naturally occurring biopolymers like DNA, which is carrying essential genetic information to build and maintain an organism or synthetic polymers such as polyethylene terephthalate (PET) which is used as suitable container for liquids and foods. All of them have one mutuality, they consist of repeating units, composed of just one monomer or a collection of related building blocks. In theory, the simplest polymeric structure is the one-dimensional polymer (1D), which is interlinking two neighbouring repeating units, forming a long linear chain. 2D polymers are topologically planar molecular sheets made of strong, preferable covalently interlinked repeating units extending exactly in 2D. On the opposite to 1D polymers, where the synthesis can be performed generally with an advanced level of control, the design and the production of 2D polymers presents far greater challenges. One of the most known and naturally occurring 2D material made exclusively by covalently connected carbon atoms is graphene. The periodical structure was intensively studied by Geim and Novoselov, which were awarded with the Nobel Prize in Physics in 2010.[107] In contrast to graphene and other 2D covalently bonded polymeric materials, 2D molecular textiles are mechanically interlocked 1D polymer chains, exhibiting a more flexible structure and shape adaptability. These mechanical properties of woven materials arise from the weak intramolecular interactions and the interlacing of the single fibres, which are distributing the forces equally in all the directions. The reader of this thesis will find a more detailed introduction in this fascinating scientific field of 2D interwoven materials in the next subsequent subchapter (Molecular Textiles).

Molecular Textiles

This subchapter provides an overview of the published concepts of molecular textiles, in form of a review entitled "From the Loom to the Laboratory: Molecular Textiles" published in the peer-reviewed scientific journal, CHIMIA. The reader of this thesis will have a deeper introduction about the strategy of molecular weaves, starting from superstructures like *Solomon* knots, which shows the interlaced concept of a cell unit, over DNA-based 2D striped lattices, 2D interwoven supramolecular structures based on coordination polymers and the weaving of small organic building blocks. Subsequently a recently developed concept will be presented as additional example for the preparation of molecular textiles based on small organic building blocks, not discussed in the review due to temporal mismatch.

From the Loom to the Laboratory: Molecular Textiles

Alfredo Di Silvestro[a] and Marcel Mayor*[abc]

Abstract: Weaving is an old technique producing fabric materials by interlocking yarns, which we appreciate every day by wearing textiles. The splendid mechanical features of these macroscopic interwoven structures such as stability, flexibility, and shape adaptability raised the question whether or not such properties might also be observed on a molecular level. In this article, molecular analogues to textiles are discussed and strategies to molecular weaves are presented. While there are impressive structural similarities between the macroscopic and the molecular world, molecular textiles consisting of interwoven linear polymers remain a challenge. The scope of the article ranges from discrete superstructures like *Solomon* knots, over deoxyribonucleic acid (DNA) based nanoscale patterns and interwoven 2D sheets of coordination polymers, to weaving strategies interlinking small organic precursors.

Keywords: 2D polymer · Interwoven network · Molecular textile · Molecular fabrics · Molecular weave

Alfredo Di Silvestro (right) was born in Basel (Switzerland) in 1991. He studied chemistry at the University of Basel and received his Master of Science in 2017 developing phthalocyanines with photocleavable tags. For his PhD he joined the group of Prof. Mayor at the University of Basel to study new concepts for molecular fabrics. ***Marcel Mayor*** (left) received his PhD in 1995 from the University of Bern under the supervision of Rolf Scheffold and Lorenz Walder. After working with Jean-Marie Lehn at the University Louis Pasteur in Strasbourg (France) and at the Collège de France in Paris (France), he founded his own research group in the Institute of Nanotechnology (INT) at the Karlsruhe Institute of Technology (KIT, Germany) in 1998. In 2004 he became Professor of Chemistry at the Department of Chemistry of the University of Basel (Switzerland), and in 2011 he became adjunct Professor of Chemistry of School of Chemistry of the Sun Yat-Sen University in Guangzhou (China). His current research interests are supramolecular chemistry, molecular electronics, nanoscale architectures, functional and hybrid materials.

1. Introduction

In our everyday lives, we are surrounded by two-dimensional materials with leaves, papers, carpets, and foils or even windows and tables as prominent examples. Particularly fascinating are fabric materials providing the flexibility required to adapt to curved shapes and thus play a key role in our society, *e.g.* as clothes keeping us warm by covering our bodies.[1,2] The flexibility arises from their structure consisting of interwoven yarns. While the yarns can be very strong with impressive tensile strength, the fabric material remains flexible due to the mechanical nature of the interyarn interaction.[2,3] The oldest and simplest fabrics are produced by two orthogonally interlaced yarns,[4] an arrangement obtained by so called biaxial weaving (Fig. 1a). The vertical or

lengthwise thread is called warp yarn and the horizontal is known as fill yarn or weft, pointing at their role in the production of the fabrics.[5] In a loom the warp yarns are mounted parallel and the mechanics of the device allows altering the relative heights of the even and uneven warp yarns. The weft is 'filled' between the even and uneven warp yarns and after each application of the weft yarn, the relative heights of the even and uneven warp yarns are inverted. Thereby the biaxial woven fabric is obtained and it is the spatial control over the yarns provided by the loom that allows its assembly.

The mechanical features of textiles combining stability, flexibility and shape adaptability makes them not only a very successful family of materials, it also provokes the question whether the design concept might not also be applied on a molecular level. This article provides an overview how the concepts of fabric materials inspired chemists in their search for new materials
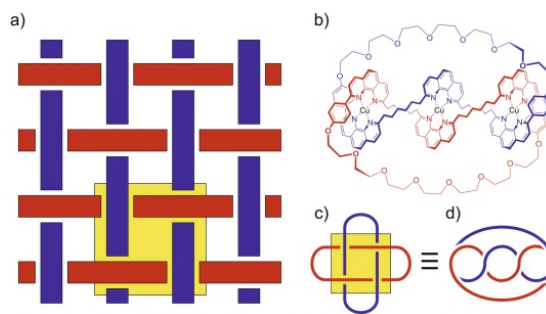
Fig. 1. a) Sketch of a biaxial woven fabric. b) Trinuclear Cu(II) complex resulting in a doubly interlocked [2]-catenane sketched in d) upon removal of the copper ions. c) Alternative representation of the doubly interlocked [2]-catenane as *Solomon* knot. The analogy of the *Solomon* knot with the unit cell of the fabric is highlighted by a yellow square.

Correspondence: Prof. M. Mayor[abc]

E-mail: marcel.mayor@unibas.ch, [a]Department of Chemistry, University of Basel, St. Johanns-Ring 19, CH-4056 Basel, Switzerland, [b]Institute for Nanotechnology (INT), Karlsruhe Institute of Technology (KIT), P. O. Box 3640, 76021 Karlsruhe, Germany, [c]Lehn Institute of Functional Materials (LIFM), School of Chemistry, Sun Yat-Sen University (SYSU), Guangzhou 510275, China

with unprecedented properties and novel behaviours. It is rather a collection of particular appealing examples representing the underlying concepts in a plausible manner than a comprehensive collection of reported achievements.

2. *Solomon* Knots: Mechanically Interlinked Model Compounds

With the rise of supramolecular chemistry in the past few decades, mechanically interlinked molecules gained increasing attention. And indeed, *Solomon* knots have been assembled consisting of two doubly interlinked macrocycles, which can be considered as the basic 'unit cell' of a fabric architecture (yellow square in Fig. 1a, and 1c). These mechanically interlinked superstructures are usually obtained by performing the macrocyclization(s) with suitably prearranged doubly wrapped precursors. In most cases, the required prearrangements of the reactants are based on supramolecular concepts like *e.g.* the engagement of the precursor in coordination compounds or the reliable design of multiple parallel hydrogen bonds in deoxyribonucleic acid (DNA) based model compounds. To the best of our knowledge, the first example of a *Solomon* knot was reported by Sauvage and coworkers profiting from the template effect of copper ions.[6] A macrocycle comprising three phenanotroline binding sites formed a trinuclear doubly intertwined helical complex with the open chain precursor. Upon formation of the second macrocycle (displayed in Fig. 1b) and removal of the copper ions, the two macrocycles were mechanically interlocked forming a doubly interlocked [2]-catenane as superstructure (Fig. 1d), which corresponds to a *Solomon* knot (Fig. 1c and 1d).

In a more recent example, *Solomon* knots were obtained as only one of several examples of mechanically interlinked macrocycles forming knots.[7] The reversible nature of the macrocyclization provided a dynamic combinatorial library of molecular knots in the solid state from which a particular species was favoured by the choice of coordinating ions and solvents. The *Solomon* knot of interest here crystallized only upon providing equal amounts of copper and zinc acetate. *Solomon* knots were also obtained from single-stranded DNA.[8] Careful design of both the DNA sequence and helical chirality of two DNA strands enabled the formation of a pair of twofold catenated precursors forming macrocycles upon ligation. Interestingly the motivation of these *Solomon* knots was exclusively to explore the suitability of the technique to provide fabric-type structures pointing at the promising prospects related with mechanically interwoven molecular structures. However, these *Solomon* knots are only models of the mechanical junction between the yarns of a fabric and thus can be considered as proof of concept for the mechanical joint. They are reduced in dimension representing exclusively a pair of crossing yarns and lack the lateral repetition of the motive making fabrics the promising 2D materials.

3. Fabric-type Interwoven Molecular Arrangements (in the crystalline state)

3.1 *Deoxyribonucleic acid (DNA)-based Fabrics*

As already displayed above with the controlled formation of a *Solomon* knot, DNA is an ideal material for the programmed assembly of complex nanoscale 2D patterns, structures and even 3D objects.[9,10] Customized DNA strands are accessible by automated synthesizers or by biotechnologies profiting from viral DNA syntheses. The predictable assembly due to *Watson-Crick* type base pairing combined with the geometrical stability and high persistence length of the obtained double helices enables the encoding of well-defined structures by molecular design.[8] Large numbers of identical spatially well-defined and shape-persistent nanoscale building blocks are self-assembled in solution and their periphery is decorated with single-stranded overhangs, so-called 'sticky-ends'. These 'sticky-ends' allow control over the

subsequent assembly of the building blocks in periodic patterns, as the arrangement of the building blocks in the resulting solid-state crystal is dictated by both, the position of the 'sticky-end' at the surface of the building block and the encoded DNA sequence complementarity. The helicity of the double helix results in twisted DNA strands and the interlinking of the prearranged single-strands by formation of phosphodiester bonds results in mechanically interlinked macrocycles. Thereby 3D objects, as demonstrated by the pioneering proof of concept DNA cube,[11] but also 2D periodic patterns can reliably be designed and subsequently assembled. Such laterally expanding 2D crystals are particular appealing as a proof of concept as their formation and dimensions are accessible by scanning probe techniques. The coating of a substrate with a periodic pattern of geometrically well-defined building blocks resembles the tiling of a floor and indeed, the pioneering 2D DNA striped lattice reported by Winfree and Seeman was inspired by the mathematical theory of *Wang* tiles, where tiles with similar coloured edges are placed next to each other.[12] In Fig. 2 the geometrically simplest 2D interwoven framework is displayed, which requires only two different DNA tiles and the inspiring *Wang* tile theory can still be recognized in their representation of the approach (Fig. 2a). It is labelled DAO as abbreviation for double crossover, antiparallel, odd spacing describing the nature of the connections defined by the DNA tiles. In Figs 2b and 2c each component oligonucleotide is displayed in a unique colour. While the crossover points are circled in Fig. 2b, the tiles defining the repeat units are highlighted by pale grey rectangle in Fig. 2c. The tile-type periodicity of the 2D object obtained by the approach can clearly be seen in the pictures obtained by atomic force microscopy (AFM) (Figs 2d and 2e). While these periodic lateral structures resemble in their shape a nanoscale fabric, the tiles are interlinked by base pairing of the sticky ends and thus, reversible supramolecular forces are holding the fabric together.
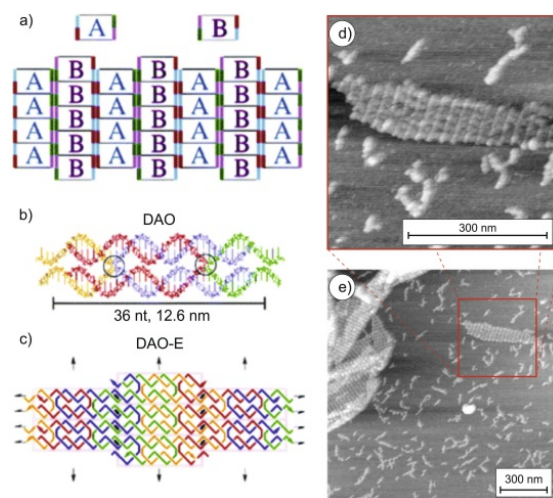
Fig. 2. 2D interwoven framework consisting of tailor-made DNA tiles inspired by the *Wang* tile theory. a) Sketch of the concept of tiling the surface with two different tiles exposing complementary attractive edges as indicated by the matching colours. The horizontal offset of tile B with respect to tile A results in the 2D network. b) Illustration of DAO model structure for type A unit consisting of 36 nucleotides. Each component oligonucleotide is displayed in a unique colour. The crossover points are highlighted by circles. c) Sketch of the woven lattice produced by the DAO units. Each repeating unit is indicated by a pale grey rectangle. d,e) The same AFM image of a DAO-E AB fabric in two different magnifications clearly showing the formation of the 2D lattice. Adapted from ref. [12] with permission from Springer Nature.

Two-dimensional DNA lattices became a mature technology enabling the spatial control of components on the nanoscale. Numerous fascinating aspects have been reported from various research groups and it would go beyond the scope of this article to provide a comprehensive overview. Also in analogy with most technologies, with increasing maturity the focus moves more and more towards their application potential away from fundamental structural aspects pointing at the interwoven fabric nature of their networks. This resembles very much our own appreciation of fabrics in the macroscopic world, where we are usually more interested in their properties (colours, cut, thickness, isolation features, *etc.*) than in the arrangement of the yarns resulting in the fabric. In the following only a very few examples of aspects related to fabrics will be discussed.

A particularly appealing example demonstrating the extent of lateral control over 2D DNA-based objects is the arrangement of long biological DNA strands by synthetic staple strands in well-defined shapes,[13] called Origami design. The concept is sketched in Fig. 3a with the biologically obtained single scaffold strand (coloured grey and black) laterally fixed by the coloured short oligonucleotides called staple strands. The potential and versatility of the approach is demonstrated with the AFM figures of the smiley faces (Fig. 3d and 3e) obtained by programming the lateral fixation of the scaffold strand by suitable staple strands (Fig. 3b and 3c).

With the lateral periodicity as the main feature, DNA networks tend to behave as a fishing net lacking the lateral flexibility of a fabric. Their design is also not restricted to the biaxial weaving with perpendicular yarns and alternative networks have been reported. A recent example even demonstrates the sensitivity of the lattice formation on the presence of additional species. Adding a recombinatorial bacterial protein as intrinsic component of the network varies the geometrical features of the networks formed by the same four nucleotides.[14] The bare four nucleotides form a so-called 'Holliday junction' exposing two complementary sets of sticky ends in a χ-stacked junction with an angle of about 120° (Fig. 4a) resulting in a *Kagome* lattice (Fig. 4b) with three interwoven DNA strands. Upon addition of the bacterial recombination protein (RuvA) the four nucleotides are arranged in a rectangular junction (Fig. 4d) resulting in a square planar lattice (Fig. 4e). The crystallized lattices have the dimensions and lateral periodicity to enable their observation by transmission electron microscopy (TEM) as displayed in Figs 4c and 4f.

Fig. 4. 2D DNA framework based on 'Holliday junctions'. a) Schematic representation of a χ-stacked junction composed of four nucleotides (red, blue, orange and green) with an angle of about 120°. The teeth at the end symbolize the complementary sticky ends. b) Sketch of the *Kagome* lattice formed by the assembly of χ-stacked junctions and c) the corresponding TEM micrograph. d) Representation of the square planar junction formed in the presence of the bacterial protein (RuvA). e) Sketch of the square lattice and f) the corresponding TEM micrograph. Adapted from ref. [14] with permission from John Wiley and Sons.

An increasing number of beautiful examples display the potential of net-type supramolecular DNA fabrics in controlling the spatial arrangement at the nanoscale,[9,10,15] and as a demonstrative example, the periodic arrangement of gold nanoparticles is shown in Fig. 5.[16] The network consists of a two tile-system (brown and blue in Fig. 5a and 5b), from which the blue tiles are exposing an additional 15 base-pair long single strand DNA (red in Fig. 5a and 5b). Upon addition of gold nanoparticles (5 nm in diameter) exposing the complementary single-stranded DNA, exclusively the blue tiles should be decorated with a gold nanoparticle. To the surprise of the authors, a periodic square lattice arrangement of the nanoparticles with a lateral spacing of 38 nm was observed, showing that only every second potential immobilization knot is involved in the immobilization of the particles. Both the net-type character of the DNA-tile architecture (Fig. 5c) and the spacing of the gold nanoparticles (Fig. 5d) are beautifully visualized by their AFM graphs.

In summary, the impressive level of control already encoded in the parent building blocks made DNA-based architectures a perfect tool to control the spatial arrangement at the nanoscale. The obtained fabrics are mainly used to laterally organize the objects of interest and have many features in common with our everyday macroscopic fabrics. However, with their mechanically interlinked subunits that self-assemble into periodic 2D patterns by supramolecular interactions, they rather resemble a fishing net with fixed knots at the junction of two yarns than an interwoven fabric with simply mechanically interwoven yarns.

3.2 Coordination Polymers Forming 2D Fabrics

Another class of supramolecular structures resembling interwoven fabrics are coordination polymers. The combination of interlinking ligands exposing two terminal binding sites with metal ions suitable to connect two ligands can yield in 1D chains

Fig. 3. The DNA origami approach for 2D interwoven networks with designed shapes. a) Sketch of the basic concept of controlling the lateral arrangement of the long scaffold strand (grey and black) by short staple strands (coloured). b) Design of the folding path for a smiley face. c) Model of the bend of helices at crossovers (where helices touch) and away from crossovers (where helices bend apart). The different colours represents the base-pair index along the folding path, where red is the first base and purple the 7000th. d,e) AFM image of the DNA origami in two different magnifications clearly showing the formation of the smiley structure programmed in the sequences of the DNA strands. Adapted from ref. [13] with permission from Springer Nature.

Fig. 5. a) Sketch of the DNA network obtained by a two tiles (brown and blue) from which only the blue tiles are exposing a 15-base pairs long single strand DNA (red). b) Immobilization of 5 nm large gold nanoparticles exposing complementary DNA strands. c) AFM picture of the DNA lattice before the addition of gold nanoparticles. d) AFM height picture of the gold nanoparticles assembled on the 2D DNA lattice. Reprinted with permission from ref. [16]. Copyright 2019 American Chemical Society.

Fig. 6. a) The coordination polymer chain formed by Au–Au bonds of $(AuI)_2(\mu\text{-dpph})$. The Au-atoms are displayed as orange 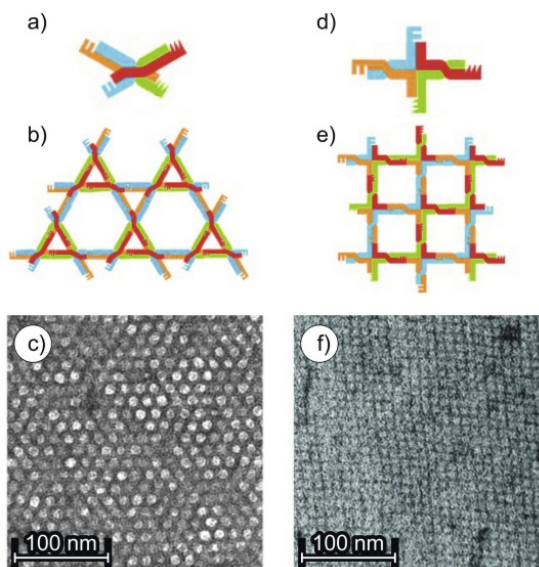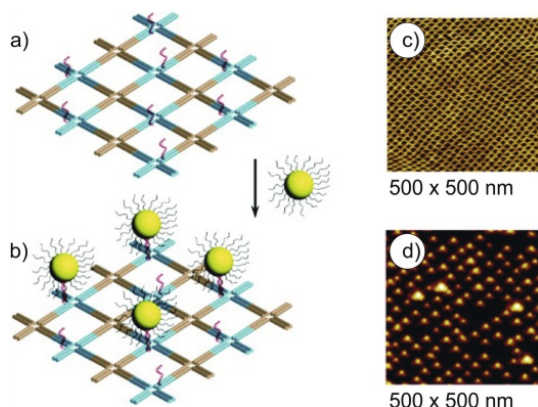circles. b) Sketch of the biaxial interwoven structure. The perpendicular strands are displayed in red and blue respectively. c) Side-view of the solid-state structure displaying the 2D sheets consisting of the interwoven coordination polymer. Adapted from ref. [18] with permission from the Royal Society of Chemistry.
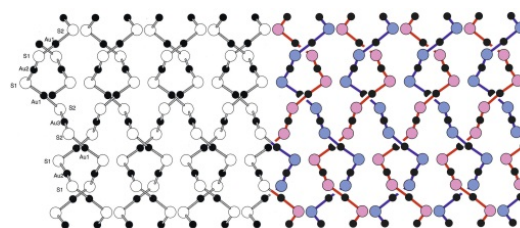
Fig. 7. 'Chicken-wire'-type interwoven network formed by $(AuS)_n^{n-}$ chains. The left side display the solid-state structure obtained by X-ray diffraction and the differently coloured 1D chains on the right side improve the visibility of the 'chicken-wire'-type interwoven network. Adapted with permission from ref. [21]. Copyright 2019 American Chemical Society.

of so-called coordination polymers.[17] While ligands and metal ions are dissolved, the macromolecular coordination polymers in many cases lack solubility and often conditions were chosen to allow their ordered arrangement by crystallization. The obtained single crystals are tightly packed and there are several reported cases where the 1D coordination polymer chains are interwoven in 2D sheets. In the following, the analogy of the observed arrangement with 2D fabrics is discussed with a few examples. However, due to the solid-state nature of the objects, there are hardly any particular features arising from the interwoven arrangement and the resemblance to 2D fabrics is restricted to the structural similarity.

An early illustrative example is the formation of an interwoven textile-type structure based on a gold–gold interactions.[18] The monomer consisting of two 1,6-bis(diphenylphosphino)hexane interlinked gold iodine centres $((AuI)_2(\mu\text{-dpph}))$ crystallizes from a dichloromethane-methanol mixture in long chains with gold-gold contacts (Fig. 6a). In the solid-state structure of the compound, these 1D-chains are arranged in 2D-sheets of interwoven chains. The biaxially woven textile type arrangement is sketched in Fig. 6b, while Fig. 6c displays a side-view of the X-ray structure displaying the arrangement in discrete 2D sheets.

Other examples of biaxial interwoven chains of coordination polymers are the solid-state structure obtained from 1-(isocyanidomethyl)-1*H*-benzotriazole and Ag(I) ions,[19] or the 'warp-and-woof' sheets consisting of 4,4'-bisazopyridine interlinked Cu ions exposing 2,2'-bipyridine corner units.[20]

In terms of atom diversity an even simpler compound is the solid-state structure obtained by the reaction of gold with sodium polysulfide liquids.[21] 1D infinite chains consisting of sulphur interlinked gold atoms $((AuS)_n^{n-})$ are formed, which arrange in parallel sheets separated by sodium cations. The $(AuS)_n^{n-}$ chains coil forming an interwoven layer structure resembling a 'chicken-wire'. The arrangement enables to establish interchain Au–Au contacts favouring the formation of these 'chicken-wire' fabrics. Fig. 7 displays the anionic 2D interwoven sheet with the X-ray structure at the left side and differently coloured 'chicken-wire'-type interwoven 1D strains at the right side.

Another fascinating example of mechanically interlocked 2D sheet has been observed in the solid-state structure of the coordination polymer $Ag_2(1,4\text{-bis(imidazol-1-ylmethyl})$

benzene)$_3(NO_3)_2$.[22] The compound crystallizes in infinite chains consisting of threefold-coordinated Ag(I) ions. As displayed in Fig. 8a), the threefold coordination sphere at the Ag ions is obtained by alternating single ligands with pairs of ligands forming macrocycles. The void opened by the macrocycles is filled by monomeric ligand sequences of perpendicular chains such that a 2D network of 'rotaxanated' (mechanically interlocked) chains is formed. In this fascinating arrangement (Fig. 8b) each chain of a sheet mechanically interacts with every perpendicular chain exactly once with alternating role as axes or macrocycle. To visualize the arrangement in the 2D sheet, the solid-state structure is displayed in Fig. 8b. As sketched in Fig. 8c and in analogy to biaxial woven fabrics, the sheets consist of mechanically fixed perpendicular chains but differ in the nature of the mechanical link.

Another type of interwoven 2D networks has been observed for the coordination polymer displayed in Fig. 9a).[23] The bifunctional and chiral ligand coordinates with metal ions (Zn(II) or Cd(II)) forming wavy grids with the coordinated ions as knot surrounded by four ligands (Fig. 9b). A pair of grids forms an interwoven 2D sheet, described by the authors as parallel double helices (Fig. 9c) interconnected by the metal centres. The interwoven sheet formation by interlinked double helices is conceptually visualized in Fig. 9d.

Interwoven grids were also observed for a coordination polymer consisting of Zn(II) ions as knots, which were interlinked by muconate ((*E,E*)-2,4-hexadienedioate) and 4,4'-bisazobipyridine ligands.[24] As displayed in Fig. 10a, the combination of both ligands formed grids consisting of parallel chains of muconate interlinked
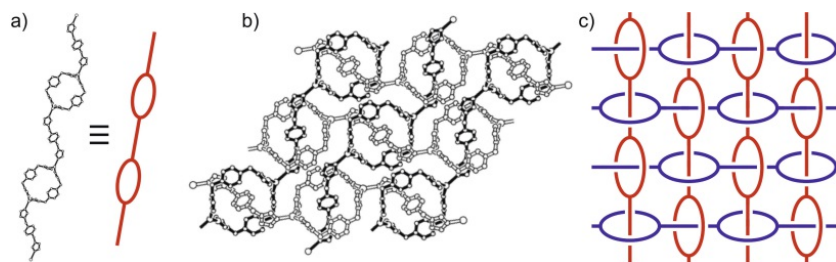
Fig. 8. Infinite 2D polyrotaxane network. a) X-ray structure and sketch of the 1D polymer chain. b) Solid-state structure of the polyrotaxane framework. c) Sketch of the mechanically interlocked 1D chains forming a 2D sheet. Adapted with permission from ref. [22]. Copyright 2019 American Chemical Society.
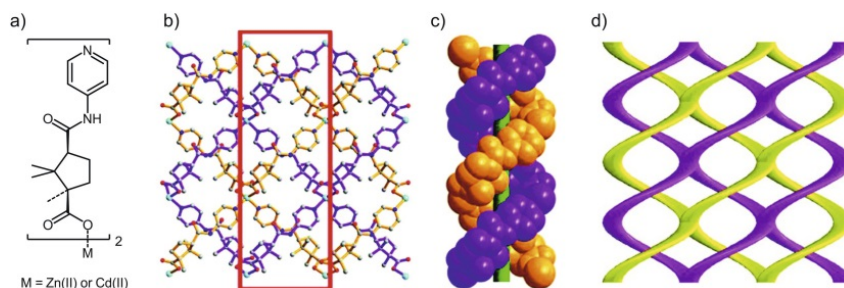
Fig. 9. Interwoven wavy grids formed by interconnected parallel double helices. a) Molecular structure of the coordination polymer chain. b) View from top of the 2D wavelike grid, highlighting the double helices with a red square. c) Space-filling structure to show the helix arrangement of the molecular grid. d) Schematic illustration of the parallel arrangement of the helices forming a mechanically interlocked woven textile. Adapted with permission from ref. [23]. Copyright 2019 American Chemical Society.

zinc centres, which were interconnected by 4,4'-bisazobipyridine ligands. To avoid empty space in the solid-state structure, two grids form a 2D sheet of interwoven grids (Fig. 10b).

Both last examples differ from fabrics as their 2D spread is provided by the grid-type coordination polymer and is not a result of the pairwise interwoven arrangement.

In summary, there are numerous coordination polymers with spatial arrangements in the solid-state resembling aspects of interwoven fabrics. However, the solid-state nature of the materials handicaps the exploitation of their mechanical, fabric-like features.

There are many more reported examples of interwoven networks[25,26] and the examples discussed here are more the representatives of a particular type of 2D fabric-type arrangement than a comprehensive collection. Also most examples report 3D networks, with 3D coordination polymers or metal organic frameworks (MOF) an emerging and fast growing research field of its own.[27–29] While there are numerous examples of interpenetrated 3D MOF structures[30] and their discussion is clearly beyond the scope of this article, MOFs are promising

Fig. 10. a) Solid-state structure of the 2D coordination polymer with Zn(II) muconate chains arranged horizontally and the interconnecting 4,4'-bisazobipyridines vertically. b) Closely-packed interwoven arrangement of two 2D grids (green and brown). Adapted from ref. [24] with permission from the Royal Society of Chemistry.

scaffolds with the potential to gain spatial control at the molecular level.

3.3 *Fabrics Based on Tailor-made Organic Structures*

Also the DNA-based lattices discussed in section 3.1 could be classified as being obtained from tailor-made organic structures. Here we would like to distinguish between the biomolecule-inspired strategies presented in section 3.1 profiting from the tuneable intermolecular attraction of DNA base pairing and concepts geared towards interlinking of purpose-designed and synthesized small molecules.

As presented in the article so far, there are numerous sophisticated strategies resulting in 2D interwoven frameworks. A major challenge for concepts aiming towards interwoven linear molecules is the high level of static and dynamic structural control required. A quickly growing number of 3D covalent organic frameworks (COF)[31–33] and 2D polymers[34,35] documents that the controlled growth is not limited to 1D polymer chains, strategies resulting in interwoven networks are still rare.

A first example profits from metal complexes to provide spatial control and predictable crossing geometries,[36] a strategy that was already applied successfully above for the assembly of *Solomon* knots.[6] The Cu(II) bis-phenantroline complex displayed in Fig. 11a exposes four aldehydes in a 'tetrahedral' geometry, which form a crystalline 3D COF network upon imine formation with 4,4'-diaminobiphenyl. The COF consists of linear polymers of imine interlinked alternating phenantroline and biphenyl subunits and due to the Cu(II) phenantroline complexes, crossing polymer chains are mechanically interlinked upon removal of the coordinating ions (Fig. 11b). The microcrystalline samples obtained were analyzed by powder X-ray diffraction (PXRD) techniques proving the periodic arrangement of the metal centers, but with limited sensitivity with respect to the perfection of the 3D interwoven organic network (Fig. 11b and 11c). The interwoven 3D network structure is likely to persist even with defects along the polymer chains. However, the mechanical properties of the minute samples obtained support their interwoven character as a tenfold increase in their elasticity was recorded compared to

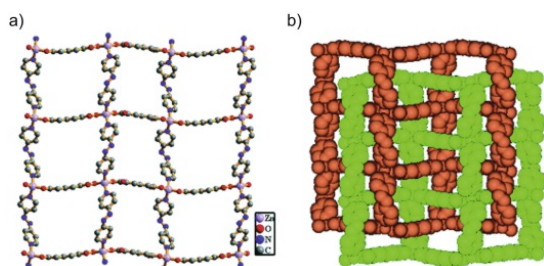the micro crystallites of the initial COF comprising the copper ions. Following the same strategy but using a larger counter ion for the Cu(II) phenantroline starting material, the ability of the resulting 3D interwoven network to accept larger guests was even improved.[37] Using cross-shaped tetraamine structures to interlink the copper phenantroline complexes resulted, after demetalation, in 3D frameworks consisting of mechanically interlinked 1D chains of macrocycles.[38]

These pioneering examples of mechanically interlinked polymer chains have the interwoven character in common with fabrics but differ in their expansion. While fabrics are two-dimensional arrangements, these COFs are bulk materials spreading out in three dimensions.

Molecular 2D fabrics require the arrangement of linear polymer chains in an interwoven fashion. In analogy to the loom that properly arranges the yarns resulting in a 2D textile, a tool organizing the linear polymer on a molecular level is required. As a potential technique that could provide the ordering power are the layer-by-layer grown metal organic frameworks, so called SURMOFs developed by Christof Wöll.[39,40] The layer-by-layer architecture enables the separation of particular layers and the fixation of the organic linker molecules as struts in the separated MOF plane can be used as preorganization for the fabric formation. As sketched in Fig. 12, a SURMOF was grown on a gold substrate consisting of layers of copper ion-interlinked 4,4''-*para*-terphenyl dicarbocylic acids forming squares.[41] The special MOF layers that shall form molecular fabrics were assembled with a tailor-made terphenyl dicarboxylic acid. This strut exposes on both sides perpendicular chains with a terminal acetylene (green in Fig. 12). After its fixation in the MOF plane, the MOF was exposed to reaction conditions enabling the crosslinking of the struts facing each other in the MOF squares by *Glaser*-type oxidative acetylene coupling forming linear polymers of interconnected MOF struts. The flexibility of the structures forming the polymer enabled the crosslinking of both pairs of struts to form a square of the MOF plane. The dimension of the polymer-forming structure was slightly too large for the MOF square, such that the connection was either formed above or below the MOF plane. As the polymer is mounted on the strut as rotation axis, a polymer connection in one square above the MOF plane forced the connection in the neighbouring square below the plane and vice versa. A connection of a vis-à-vis pair of

struts above the MOF plane further forced the second connection in the same MOF square below the plane. Considering these geometrical restrictions, a complete polymerization within the MOF plane should result in biaxial interwoven linear polymers. Upon disintegration of the MOF framework by demetalation, the molecular textile was released.

While the chemical transformation was spectroscopically observed in the crystalline SURMOF, flakes of molecular textiles down to three molecular layers thick were obtained and characterized by scanning electron microscopy (SEM) and AFM. The interwoven nature of these flakes was demonstrated by disassembling the 2D fabrics into individual polymer strands.

The major challenges to improve the dimension of the accessible fabrics are not only the quality of the single crystalline MOF plane, but also the control over the extent of linear polymer formation. To address the latter issue we are currently exploring the potential of reversible coupling chemistry.

Another elegant approach to interwoven organic fabrics is based on supramolecular interactions of a rigid oligoproline rod exposing two perylenemonoimides at a distance of about 18 Å to the same side (Fig. 13a).[42] The π-stacking between these perylenemonoimine subunits results in the formation of long linear threads with a regular periodicity of up and down oriented voids (Fig. 13b). To avoid empty voids the compound self-assembles into a triaxial interwoven network with the three crossing threads filling each other's voids (Fig. 13c). The resulting superstructure is a *Kagome* lattice of several micrometres in dimension, which can clearly be recognized by tunnelling electron microscopy (TEM, Fig. 13d). The system beautifully profits from the balanced interactions. While the threads formed by supramolecular forces probably have limited mechanical tensile strength, they enable the large scale self-assembly to regular interwoven 2D patterns.

4. Conclusion and Outlook

The collection of examples illustrate how interwoven fabrics and their properties inspired chemists in their search for new functions emerging from the molecular structure. While discrete (supra)molecular structures can be assembled to prove the validity of the concept, the fabrication of 2D molecular textiles of considerable dimensions remains challenging. In the case of the DNA-based self-assembled structures the framework itself becomes the tool enabling spatial control over nanoscale entities. However, the networks in most cases lack the lateral flexibility of textiles emerging from the sliding of the yarns at the intersection.
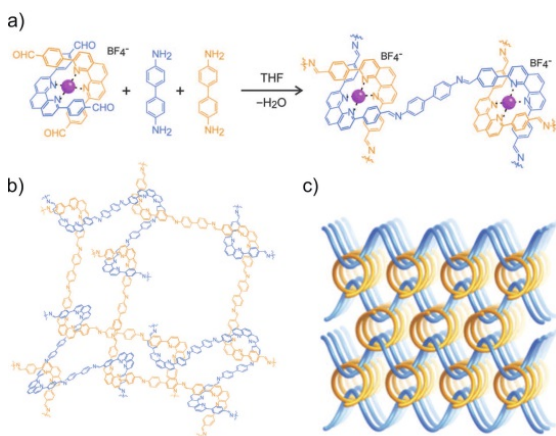
Fig. 11. 3D network consisting of interwoven linear polymers. a) Condensation reaction forming the COF consisting of interlinked copper phenantroline complexes. b) Molecular drawing of the interwoven polymer chains. c) Sketch of the 3D material consisting of interwoven 1D-polymer chains. Adapted from ref. [36] with permission from AAAS.
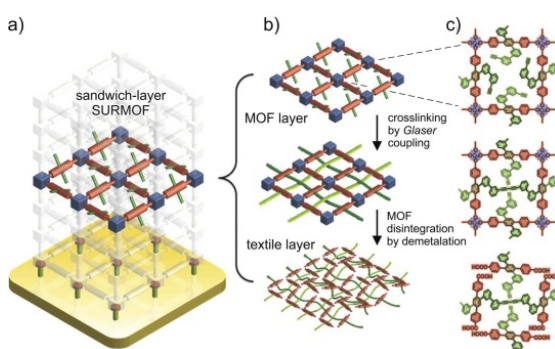
Fig. 12. Formation of a molecular textile in a layer of a SURMOF. a) Sandwich layer of the polymer precursor struts mounted in a SURMOF. b) Top: the sandwich layer fixed in the SURMOF. Middle: Linear polymers (green strands) formed upon crosslinking of the struts. Bottom: Release of the molecular textile upon disintegration of the SURMOF. c) Chemical transformations in a unit cell of the SURMOF plane. Adapted from ref. [41].
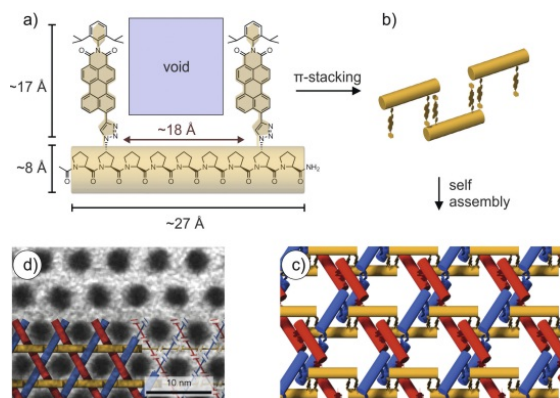
Fig. 13. The triaxial supramolecular *Kagome* lattice. a) Molecular design and dimensions of the oligoproline exposing two perylenemonoimides defining an empty void in between both chromophores. b) Formation of the threads by intermolecular π-stacking. c) Self-assembly into the triaxial weave forming the *Kagome*-lattice. d) TEM micrograph of the Kagome-lattice with the sketch of the molecular structure overlaid. Adapted from ref. [42] with permission from Springer Nature.

The examples of interwoven coordination polymers usually share exclusively the structural analogy to textiles and fabrics but barely profit from the interwoven spatial arrangement of the 1D-polymer chains due to the solid-state nature of the material. The rather recent approaches to assemble molecular weaves by suitably pre-organized small organic molecules are promising proofs of concept with considerable development potential.

In our own approach using a SURMOF to organize the polymer precursors, the dimensions of the obtained molecular textiles are limited. We are currently exploring the suitability of the air/water interface for the formation of molecular textiles with suitable supramolecular building blocks. While preliminary experiments are promising, the major challenge is the monomolecular nature of the sheet resulting in very moderate spectroscopic signals making its analysis and characterization demanding.

Strategies enabling the controlled interweaving of linear polymers remain an open challenge and a worthwhile aim, as the obtained molecular fabrics are likely to have interesting physical properties emerging form the mechanical nature of the cohesion of their subunits.

Acknowledgements

[1]   P. D. Dubrovski, 'Woven Fabric Engineering', IntechOpen, **2010**.
[2]   M. Akbari, A. Tamayol, S. Bagherifard, L. Serex, P. Mostafalu, N. Faramarzi, M. H. Mohammadi, A. Khademhosseini, *Adv. Healthc. Mater.* **2016**, *5*, 751.
[3]   V. B. C. Tan, X. S. Zeng, V. P. W. Shim, *Int. J. Impact Eng.* **2008**, *35*, 1303.
[4]   S. Adanur, 'Handbook of Weaving', CRC Press, n.d.
[5]   K. Gandhi, 'Woven Textiles: Principles, Technologies and Applications', Elsevier, **2012**.
[6]   J. F. Nierengarten, C. O. Dietrich-Buchecker, J. P. Sauvage, *J. Am. Chem. Soc.* **1994**, *116*, 375.
[7]   C. D. Pentecost, K. S. Chichak, A. J. Peters, G. W. V. Cave, S. J. Cantrill, J. F. Stoddart, *Angew. Chem. Int. Ed.* **2007**, *46*, 218.
[8]   T. Ciengshin, R. Sha, N. C. Seeman, *Angew. Chem.* **2011**, *123*, 4511.
[9]   M. R. Jones, N. C. Seeman, C. A. Mirkin, *Science* **2015**, *347*, 1260901.
[10] F. Hong, F. Zhang, Y. Liu, H. Yan, *Chem. Rev.* **2017**, *117*, 12584.
[11] J. Chen, N. C. Seeman, *Nature* **1991**, *350*, 631.
[12] E. Winfree, F. Liu, L. A. Wenzler, N. C. Seeman, *Nature* **1998**, *394*, 539.
[13] P. W. K. Rothemund, *Nature* **2006**, *440*, 297.
[14] J. Malo, J. C. Mitchell, C. Vénien-Bryan, J. R. Harris, H. Wille, D. J. Sherratt, A. J. Turberfield, *Angew. Chem. Int. Ed.* **2005**, *44*, 3057.
[15] C. Lin, Y. Liu, S. Rinker, H. Yan, *ChemPhysChem* **2006**, *7*, 1641.
[16] J. Zhang, Y. Liu, Y. Ke, H. Yan, *Nano Lett.* **2006**, *6*, 248.
[17] W. L. Leong, J. J. Vittal, *Chem. Rev.* **2011**, *111*, 688.
[18] P. M. Van Calcar, M. M. Olmstead, A. L. Balch, *J. Chem. Soc. Chem. Commun* **1995**, 1773.
[19] I. Ino, J. C. Zhong, M. Munakata, T. Kuroda-Sowa, M. Maekawa, Y. Suenaga, Y. Kitamori, *Inorg. Chem.* **2000**, *39*, 4273.
[20] L. Carlucci, G. Ciani, A. Gramaccioli, D. M. Proserpio, S. Rizzato, *CrystEngComm* **2000**, *2*, 154.
[21] E. A. Axtell, J.-H. Liao, M. G. Kanatzidis, *Inorg. Chem.* **1998**, *37*, 5583.
[22] B. F. Hoskins, R. Robson, D. A. Slizys, *J. Am. Chem. Soc.* **1997**, *119*, 2952.
[23] Q. Huang, J. Yu, J. Gao, X. Rao, X. Yang, Y. Cui, C. Wu, Z. Zhang, S. Xiang, B. Chen, G. Qian, *Cryst. Growth Des.* **2010**, *10*, 5291.
[24] C. M. Nagaraja, B. Ugale, A. Chanthapally, *CrystEngComm* **2014**, *16*, 4805.
[25] S. R. Batten, R. Robson, *Angew. Chem. Int. Ed.* **1998**, *37*, 1460.
[26] Y. Liu, M. O'Keeffe, M. M. J. Treacy, O. M. Yaghi, *Chem. Soc. Rev.* **2018**, *47*, 4642.
[27] H. Furukawa, K. E. Cordova, M. O'Keeffe, O. M. Yaghi, *Science* **2013**, *341*, 1230444.
[28] H.-C. Zhou, J. R. Long, O. M. Yaghi, *Chem. Rev.* **2012**, *112*, 673.
[29] S. Yuan, L. Feng, K. Wang, J. Pang, M. Bosch, C. Lollar, Y. Sun, J. Qin, X. Yang, P. Zhang, Q. Wang, L. Zou, Y. Zhang, L. Zhang, Y. Fang, J. Li, H. C. Zhou, *Adv. Mater.* **2018**, *30*, 1704303.
[30] Y.-N. Gong, D.-C. Zhong, T.-B. Lu, *CrystEngComm* **2016**, *18*, 2596.
[31] S.-Y. Ding, W. Wang, *Chem. Soc. Rev.* **2012**, *42*, 548.
[32] P. J. Waller, F. Gándara, O. M. Yaghi, *Acc. Chem. Res.* **2015**, *48*, 3053.
[33] M. S. Lohse, T. Bein, *Adv. Funct. Mater.* **2018**, *28*, 1705553.
[34] W. Wang, A. D. Schlüter, *Macromol. Rapid Commun.* **2019**, *40*, 1800719.
[35] J. Sakamoto, J. van Heijst, O. Lukin, A. D. Schlüter, *Angew. Chem. Int. Ed.* **2009**, *48*, 1030.
[36] Y. Liu, Y. Ma, Y. Zhao, X. Sun, F. Gandara, H. Furukawa, Z. Liu, H. Zhu, C. Zhu, K. Suenaga, P. Oleynikov, A. S. Alshammari, X. Zhang, O. Terasaki, O. M. Yaghi, *Science* **2016**, *351*, 365.
[37] Y. Liu, Y. Ma, J. Yang, C. S. Diercks, N. Tamura, F. Jin, O. M. Yaghi, *J. Am. Chem. Soc.* **2018**, *140*, 16015.
[38] Y. Liu, C. S. Diercks, Y. Ma, H. Lyu, C. Zhu, S. A. Alshmimri, S. Alshihri, O. M. Yaghi, *J. Am. Chem. Soc.* **2019**, *141*, 677.
[39] O. Shekhah, H. Wang, S. Kowarik, F. Schreiber, M. Paulus, M. Tolan, C. Sternemann, F. Evers, D. Zacher, R. A. Fischer, C. Wöll, *J. Am. Chem. Soc.* **2007**, *129*, 15118.
[40] J.-L. Zhuang, A. Terfort, C. Wöll, *Coord. Chem. Rev.* **2016**, *307*, 391.
[41] Z. Wang, A. Błaszczyk, O. Fuhr, S. Heissler, C. Wöll, M. Mayor, *Nat. Commun.* **2017**, *8*, 14442.
[42] U. Lewandowska, W. Zajaczkowski, S. Corra, J. Tanabe, R. Borrmann, E. M. Benetti, S. Stappert, K. Watanabe, N. A. K. Ochs, R. Schaeublin, C. Li, E. Yashmina, W. Pisula, K. Müllen, H. Wennemers, *Nat. Chem.* **2017**, *9*, 1068.

As discussed in the review about molecular textiles, one of the biggest challenge and dream in polymer chemistry is the direct bottom-up self-assembly of molecular building blocks into linear organic polymer chains woven in 2Ds. A breakthrough in this field, was the recently reported self-assembled 2D molecular woven fabric of Leigh and collaborators.[108] The concept of this work is illustrated in figure 9. The utilisation of a metal coordinated 3 x 3 interwoven grid with flexible hydrocarbon chains decorated with thiols as building block (figure 9aI) gave the opportunity to self-assemble a 2D molecular textile. In the first step, a 3 x 3 interwoven grid (monomer) is prepared by the self-assembling of six linear ligands strands coordinated with nine Fe(II) ions, as displayed in figure 9bI. The X-ray crystal structure presented in figure 9aI shows the interlaced nature of the six linear ligand strands running parallel or orthogonal to each other and stabilized by the template effect of the BF_4^- anions, which makes the monomer suitable for the preparation of a woven polymer. Furthermore, the 3 x 3 grid is adopting a layered structure in the solid state (Figure 9AIII) and therefore, the orientation of the single monomer is pre-arranged for the polymerisation in 2D, as illustrated in figure 9aII. It is important to mention, that this pre-arrangement in the 3 x 3 grid gives the possibility to perform a tessellation in 2Ds using both faces. In the second step, the interlaced monomers were linked together under aerobic conditions, and a woven metal-based polymer was afforded after formation of disulphide bridges and slow precipitation of the material out of solution (figure 9bII). In the last step, the Fe(II) ions are removed with potassium cyanide (KCN) and a mechanically interlocked molecular textile is obtained, as displayed in figure 9bIII. The polymer formed could be isolated as a flake-like solid (figure 9bIV), and the 2D structure was confirmed and characterized using different high-resolution microscopes and X-ray measurements. This method gives the opportunity to prepare 2D molecular textiles, using small interwoven building blocks that can be polymerized using both faces of the woven monomer. This is due to the planarity of the small building block employed and the obtention of a well separated layer-by-layer solid-state packing.
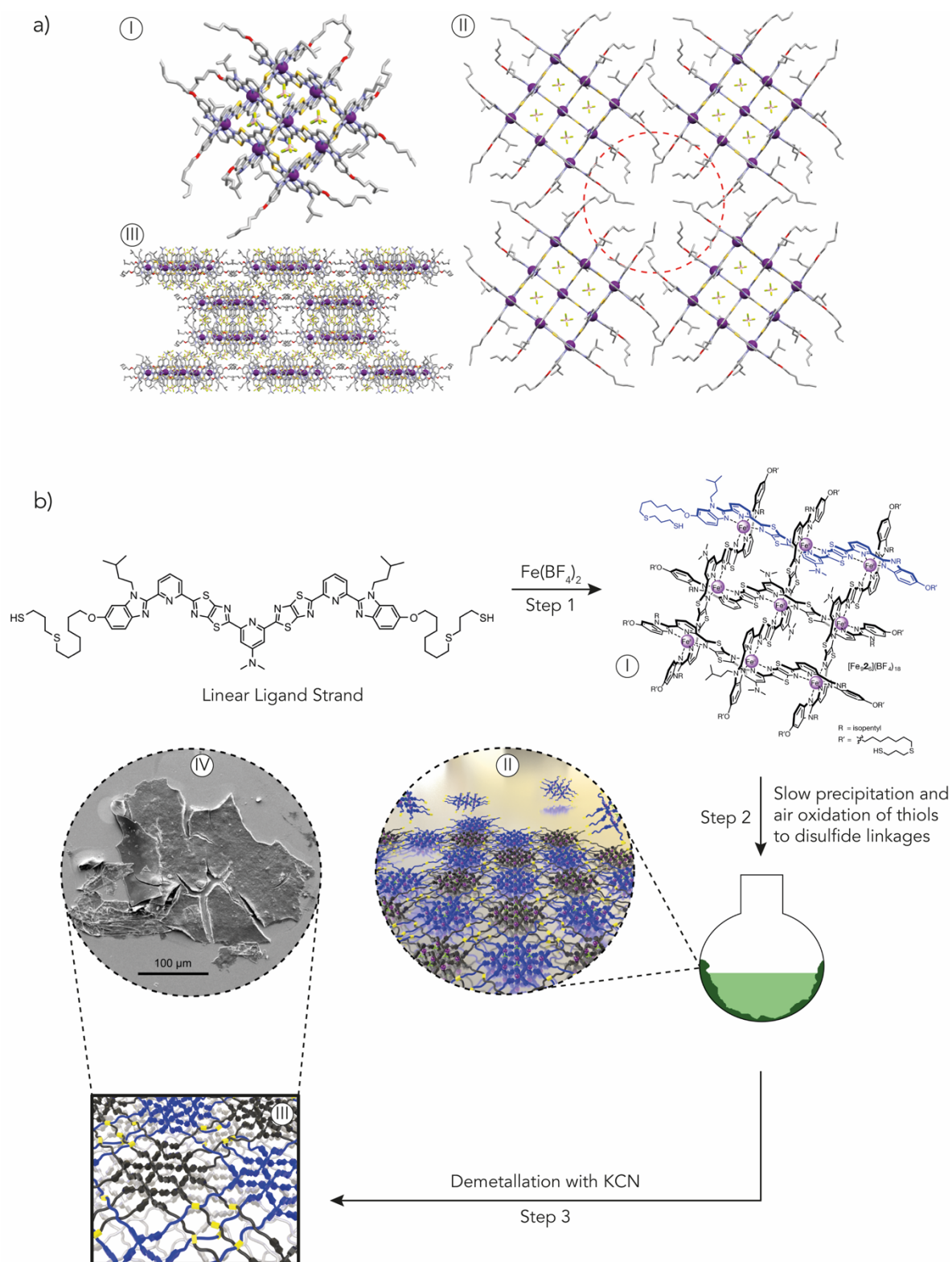
Figure 9: Self-assembly of 3 x 3 interwoven grid, polymerisation procedure to form 2D molecular textile and X-ray crystal structure of 3 x 3 grid; (aI-III) X-ray crystal structure of 3 x 3 grid; (bI) Molecular structure of 3 x 3 grid; (bII) Sketch of disulfide interlinked metal-based textile after slow precipitation under aerobic conditions.; (bIII) Sketch of demetallated mechanically interlocked 2D molecular textile.; (bIV) SEM image of the non-metalated mechanically interlocked woven polymer. Adapted from ref. [108] with permission from Springer Nature.

Aim of this Work

The aim of this project was to investigate a strategy for the preparation of a 2D mechanically interlocked interwoven molecular textile, while controlling the molecular expansion during the polymerisation at an air-water interface. The assembly of a mechanically interlocked woven structure, which mimics a traditional loom woven textile, i. e. that possess the same properties, such as stability, flexibility and shape adaptability arising from a 2 x 2 unit cell, is displayed in figure 10. The creation of such a molecular fibre is of crucial interest but to achieve its preparation several parameters must be taken into account and carefully investigated. This includes notably the choice of: the proper assembly strategy, the design of the building blocks, the right interlinking method for the polymerisation, the most suitable deposition approach and an eligible analytical method for the solid-state analysis of 1-2 nm thin interwoven monolayers.
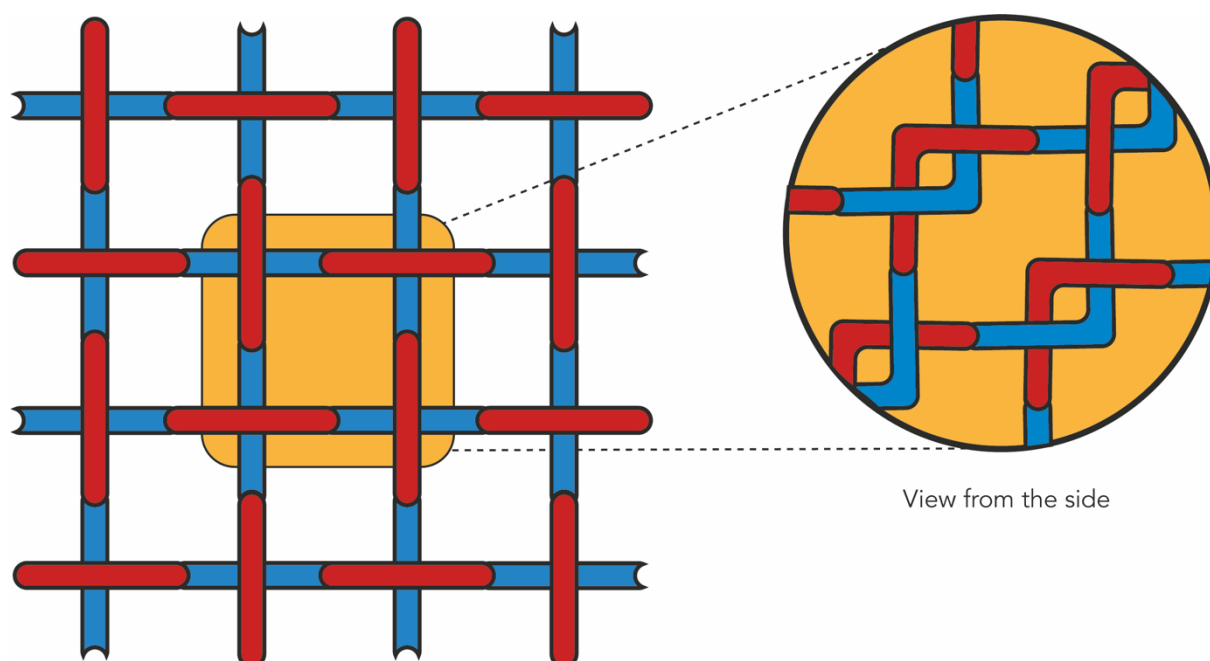
View from the side

Figure 10: Sketch of the 2D molecular textile from the bird`s eye perspective, highlighting the 2 x 2 unit cell by an orange square and the more detailed view from the side (right side).

Design of the Building Blocks and the Assembly Strategy

To imitate the yarns of a biaxial weaving with a 2 x 2 unit cell, we were looking for linear polymers, that can self-assemble to an interwoven structure. The best strategy that immediately came to our mind was the metal templated synthesis, which is a powerful tool for the preparation of challenging supramolecular architectures. Remarkable examples for its use would be the molecular *Solomon* knot reported by Sauvage[109] in 1994, where copper ions were involved, or the molecular woven textile published by the Leigh group in 2020[108] and discussed in the previous subchapter (Molecular Textiles). As outlined in the introduction, tpy ligands have a high affinity to metal ions and fulfil the requirements for the self-assembling process.
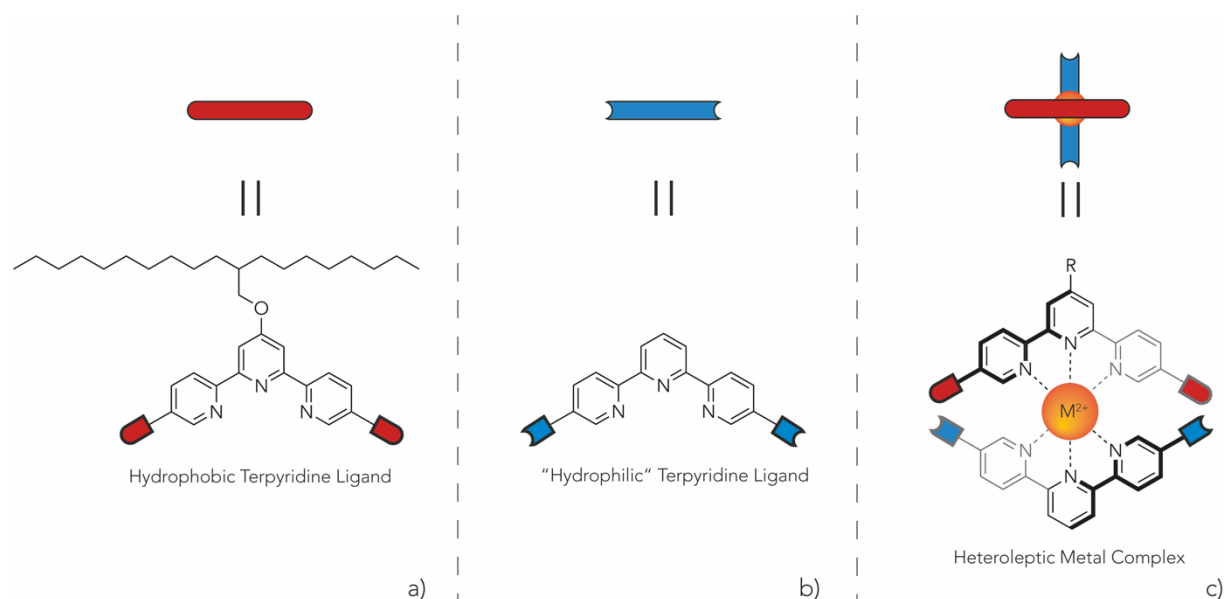
Figure 11: Sketch and molecular structure of the molecules. a) Red sketch showing the hydrophobic tpy ligand; b) Blue sketch showing the hydrophilic tpy ligand; c) Assembled sketch with a sphere in the middle showing the octahedral bis(tpy) heteroleptic metal complex derivative.

The use of heteroleptic tpy complexes gave us the opportunity to design two different ligands with different properties. Since we aim at controlling the orientation of the molecular fiber on a *Langmuir-Blodgett* (LB) trough, we decided to use an amphiphilic

species. Therefore, we designed a more water repellent tpy ligand (hydrophobic) and a more polar tpy (hydrophilic) ligand as illustrated in figure 11. The hydrophobic molecule sketched in red (figure 11a) has a flexible aliphatic hydrocarbon chain at substitution position 4', that ensures the insolubility of the building block in water and provides the desired control over the molecular orientation at the interface. The main advantage of this strategy lies on the prearrangement procedure at an air/water interface, which is assured by the molecular design of the heteroleptic tpy complex. Therefore, the functional groups attached at the position 5 and 5'' are pointing linearly in regard to the correct interlinking partner, since the complex is pre-arranged on the interface. As displayed in figure 11 the substitution pattern for the linkage between the neighbouring complexes is in both tpy ligands at position 5 and 5''. This position is very advantageous for the linearity of the molecules. For the interlinking strategy we decided to use the reversible *Schiff* base condensation where imine bonds are formed from a primary amine and an aldehyde. An alternative method would be the utilisation of a carboxylic acid and a primary amine to obtain an amide-based polymerisation.

The functionalities of the ligands are sketched in figure 11: (a) Shows the two primary amines in red and (b) represents the aldehydes or carboxylic acids in blue. It is important to mention, that the main contribution to the hydrophilicity is arising from the target heterolpetic bis(tpy) complex, which will be isolated as a salt and not deriving from the mentioned tpy ligands. Therefore, the name "hydrophilic" used within this thesis refers to the tpy ligands that does not possess an aliphatic chain (figure 11b) and should only be understood as conceptual. In this way, one can be more perspicuous on describing how the target building block will arrange at the interface. The suitability of the triangular shape of the tpy for the interwoven structure, is highlighted in figure 11c and becomes very clear. The metal complexed derivative presents a distorted octahedral molecular geometry, where the six nitrogen of the two tpy ligands are symmetrically arranged around the central metal atom and form an interwoven structure where one ligand interlace over the other one. The choice of the

metal ion is very important as it should be affine enough to permit the supramolecular self-assembly but labile enough for it to be removed afterwards using a concurrent ligand such as KCN [108] or electrochemically. Figure 12 illustrates the concept of this work and all the steps, for the self-assembling of a 2D mechanically interlocked molecular textile at an air/water interface. First, the amphiphilic heteroleptic bis(tpy) complexes are drop-casted at an air/water interface on a LB trough (figure 12a).
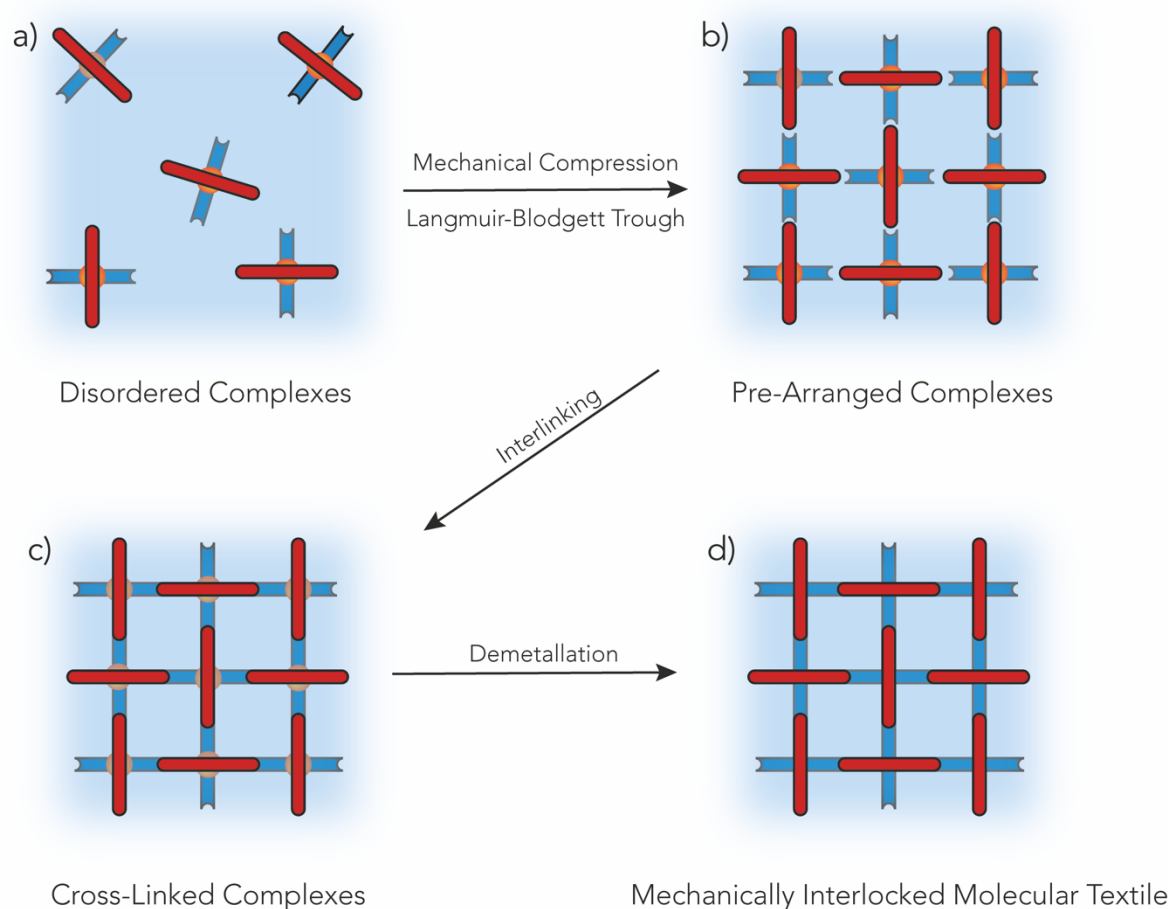
Figure 12: Sketch of the building strategy from the Bird`s-eye perspective at the interface.; (a) Drop-casted amphiphilic heteroleptic bis(tpy) complexes at the air/water interface.; (b) Pre-arrangement of heteroleptic bis(tpy) complexes at air/water interface by mechanical compression of the molecules on LB trough; (c) Polyimine interlinking of neighbouring complexes to a metal based interwoven monolayer at the interface.; (d) Metal free mechanically interlocked 2D molecular textile.

Upon mechanical compression of the dispersed complexes, the amphiphilic monomers are then forced to prearrange on the interface, as displayed in figure 12b. This step is crucial for properly organizing and orienting the complexes, as the neighbouring aliphatic chains can start to interact with each other and point towards the air, while the polar groups or the remaining part of the charged complex is pointing towards the water (subphase). The pre-arranged molecules are forming a compact layer at a particular surface-pressure and subsequently, an acid induced reversible *Schiff* base condensation is interlinking the neighbouring monomers and therefore forming a 2D metal-based molecular fibre (figure 12c). As illustrated in figure 12d, the last step is the demetallation process, which leads to the final mechanically interlocked molecular textile expanded in 2Ds. The concept presented herein is a breakthrough in the bottom-up preparation of 2D molecular textiles made of small organic building blocks and offers new opportunities and fundaments for the further research in this growing field.

Synthetic Strategy of the Tpy Ligands

As mentioned in the previous subchapter the hydrophilicity of the amphiphile is arising from the charged heteroleptic bis(tpy) complex and not from the proposed ligands. The assigned name of "hydrophilic ligands" for the tpy ligands without aliphatic chain is only chosen to emphasize how the monomer is self-orienting on the interface and should not be understood as a designed physical property.

Retrosynthesis of "Hydrophilic" Tpy Ligand 4
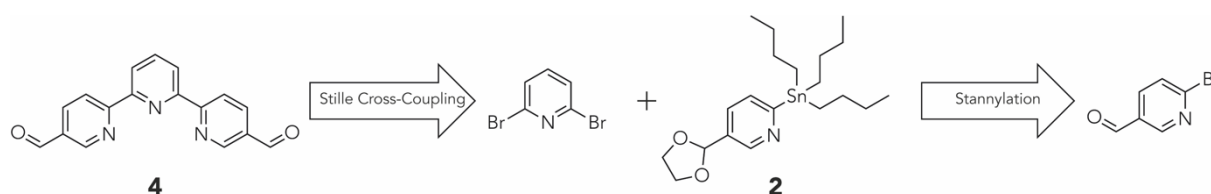
Scheme 5: Retrosynthetic analysis of the "hydrophilic" tpy ligand **4**.

The retrosynthetic route of target compound **4** starts from a twofold palladium catalyzed Stille crorss-coupling between the commercially available 2,6-dibromopyridine and the organostannylpyridine **2**. Compound **2** can be prepared by the stannylation of the acetal protected 5-bromopicolinaldehyde.[110]

Retrosynthesis of "Hydrophilic" Tpy Ligand 10

As seen with scheme 6, the target tpy ligand 4,4'-([2,2':6',2''-terpyridine]-5,5''-diyl)dibenzaldehyde (**10**) is accessible from a twofold Pd⁰-catalyzed Stille cross-coupling between organostannyl compound **8** and 5,5''-dibromo-tpy (**6**). Molecule **8** can be obtained by a stannylation reaction of the acetal protected 4-iodobenzaldehyde. Twofold brominated tpy **6** can be synthesized by the coupling of commercially available 2,6-dibromopyridine with organostannylpyridine **5**. Tin

reagent **5** can be prepared by the exclusively *ortho*-stannylation of the commercially available 2,5-dibromopyridine.[111]
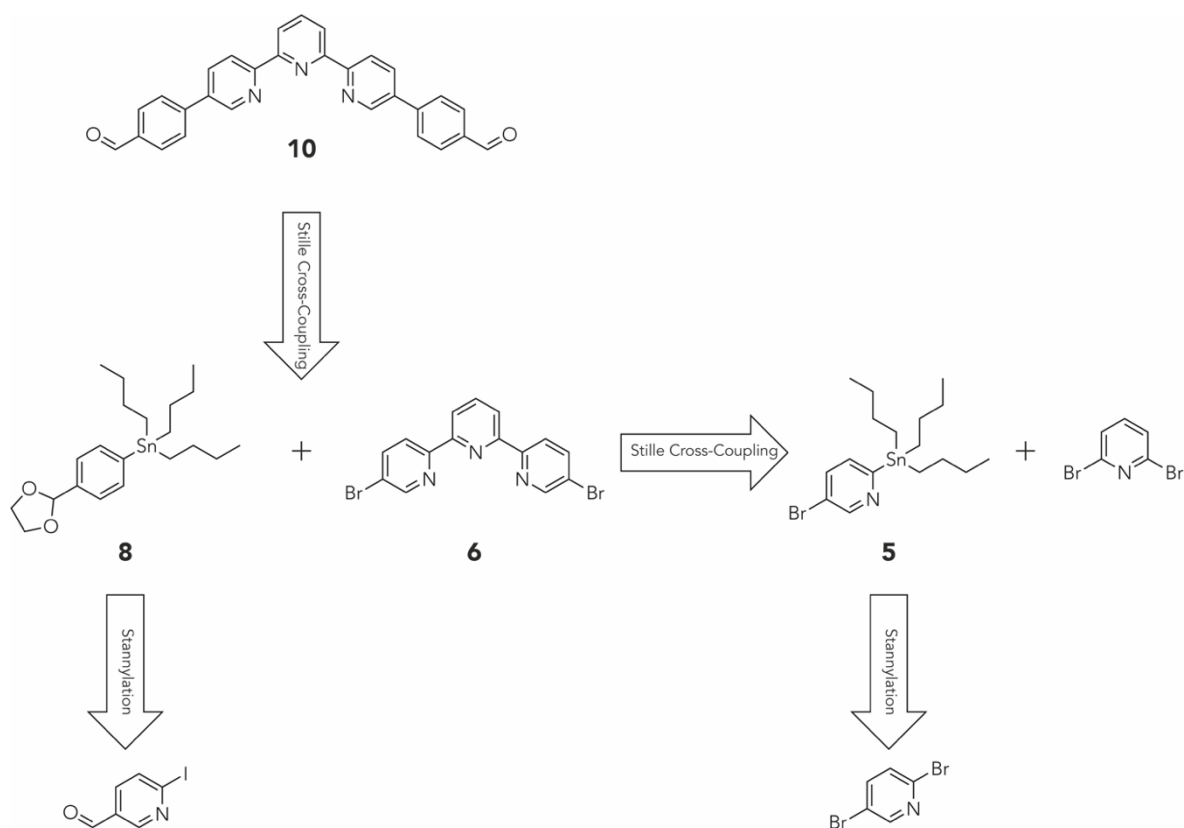
Scheme 6: Retrosynthetic analysis of the"hydrophilic" tpy ligand **10**.

Retrosynthesis of "Hydrophilic" Tpy Ligand 13
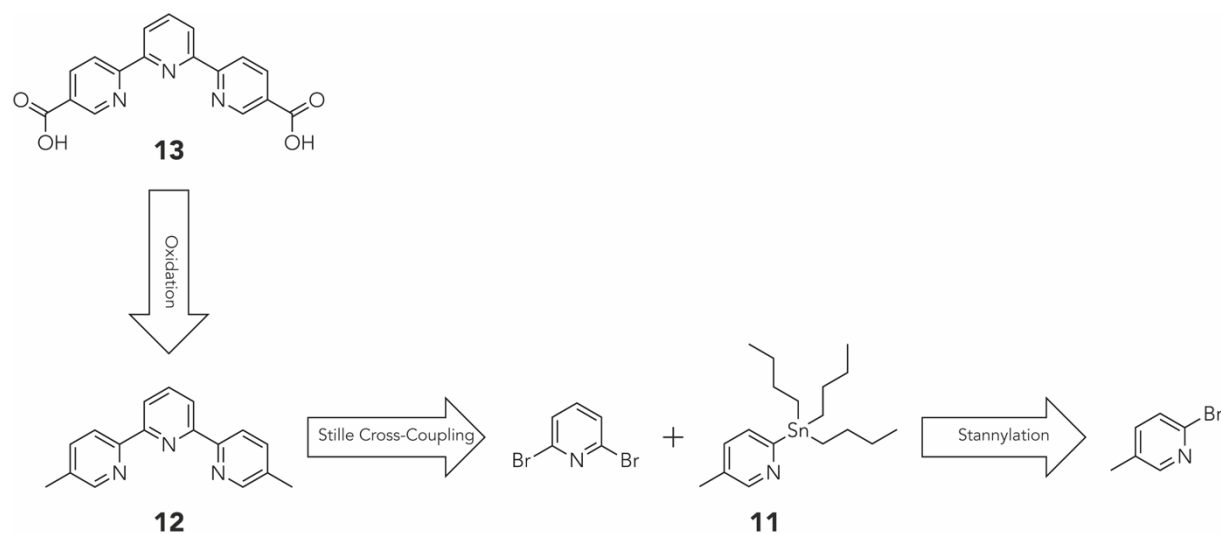
Scheme 7: Retrosynthetic analysis of the "hydrophilic" tpy ligand **13**.

The retrosynthetic route leading to the target compound [2,2':6',2''-terpyridine]-5,5''-dicarboxylic acid (**13**) is outlined in scheme 7. Target compound **13** can be obtained by an oxidation of 5,5''-Dimethyl-2,2':6',2''-terpyridine (**12**). The bis-methylated tpy **12** can be formed by a twofold Stille cross-coupling between commercially available 2,6-dibromopyridine and 5-methyl-2-(tributylstannyl)pyridine (**11**). Organostannyl compound **11** can be produced from the stannylation of 2-bromo-5-methylpyridine.

Retrosynthesis of Hydrophobic Tpy Ligand 22
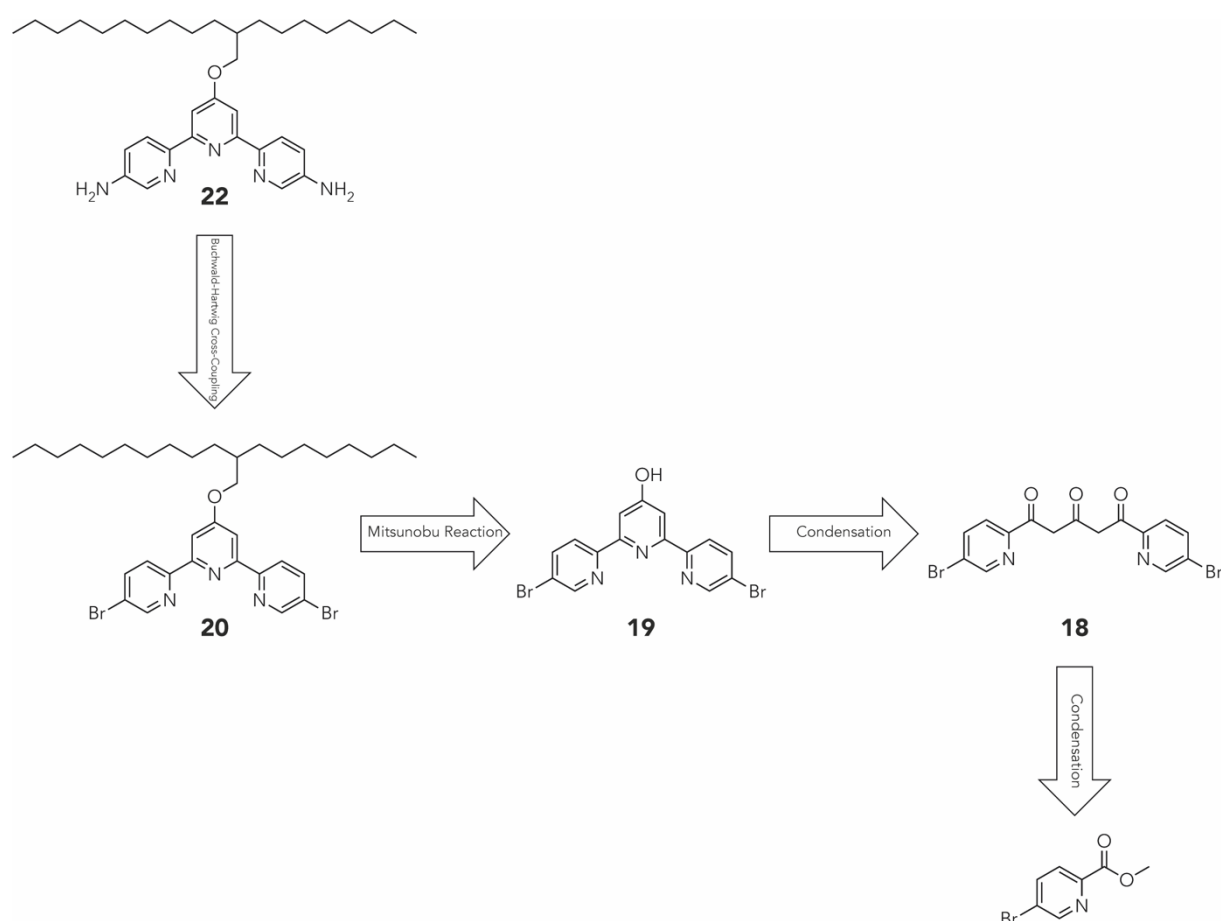
Scheme 8: Retrosynthetic analysis of the hydrophobic tpy ligand **22**.

Retrosynthetically, hydrophobic tpy ligand 4'-((2-octyldodecyl)oxy)-[2,2':6',2''-terpyridine]-5,5''-diamine (**22**) is accessible via a Buchwalt-Hartwig cross-coupling reaction starting from the brominated species **20** (scheme 8). Compound **20** can be

obtained thanks to a Mitsunobu reaction between the phenolic alcohol derivative 5,5''-dibromo-[2,2':6',2''-terpyridin]-4'(1'H)-one (**19**) and the corresponding aliphatic alcohol. The 4'-substituted tpy **19** can be derived from 1,5-bis(5-bromopyridin-2-yl)pentane-1,3,5-trione (**18**) by condensation of the central ring and in counterpart, **18** is produced from the commercially available methyl 5-bromopicolinate.

Results and Discussions

Synthesis of "Hydrophilic" Tpy Ligand **4**
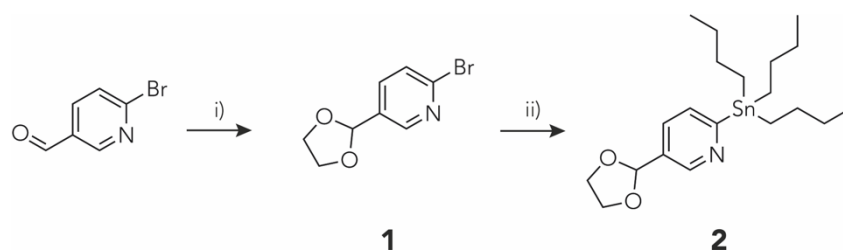
Scheme 9: Molecular structure and synthesis of 2-(1,3-dioxolan-2-yl)-5-(tributylstannyl)pyridine (**2**). i) ethylene glycol, *p*- TsOH, toluene, 130 °C, 12 h, quant.; ii) *n*-BuLi, SnBu$_3$Cl, Et$_2$O, -78 °C, 12 h, 98 %.

The multistep synthesis of compound **4** was already reported by the Balavoine group in 1998, by oxidizing 5,5''-dimethyl-2,2':6',2''-tpy (obtained in 2 steps) for 10 days with an overall yield about 20 %.[112] A few years later Baumgarten and collaborators prepared it by using the Pd^0-catalyzed Stille cross-coupling strategy, starting from the newly synthesized 6-bromo-2,2'-dipyridine-5'-carbaldehyde and 6 synthetic steps in total.[110]

Scheme 9 outlines the approach used for the synthesis of organostannylpyridine **2**. The carbaldehyde of 5-bromopicolinaldehyde was protected using an excess of ethylene glycol and catalytic amounts of *p*-toluenesulfonic acid monohydrate, forming the acetal protected compound **1**. The stannylation was performed by a bromine-lithium exchange with the halopyridine **1** in diethyl ether, followed by quenching with tributhyltinchloride (Bu$_3$SnCl) yielding the organostannylpyridine **2** in 98 % yield.
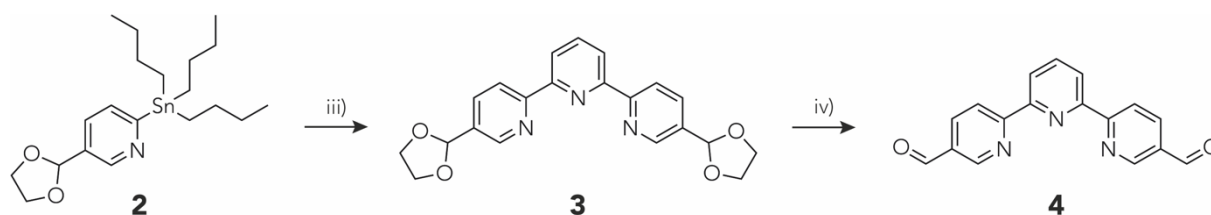
Scheme 10: Molecular structure and synthesis of 5,5''-diformyl-2,2':6',2''-tpy (**4**). iii) 2,6-dibromopyridine, Pd(PPh$_3$)$_4$, toluene, 130 °C, 12 h, 87 %; iv) HCl, H$_2$O, 100 °C, 1 h, 90 %.

The synthesized tin reagent **2** was reacted with 2,6-dibromopyridine by a twofold Stille cross-coupling using 0.1 equivalent of tetrakis(triphenylphosphine)palladium(0) (Pd(PPh$_3$)$_4$) as catalysator under argon, yielding 87 % of 5,5''-di(1,3-dioxolan-2-yl)-2,2':6',2''-tpy (**3**), as displayed in scheme 10. The deprotection of the dioxolane species **3** was performed under acidic conditions using aqueous hydrochloric acid (HCl), yielding 90 % of the target tpy **4**. In comparison to the route of Baumgarten[110], we saved 2 steps, minimized the dealing with the toxic tin reagents and obtained an overall yield of 76 %, by slightly changing the synthetic strategy and the experimental conditions used for the Stille cross-coupling.

Synthesis of "Hydrophilic" Tpy Ligand **10**
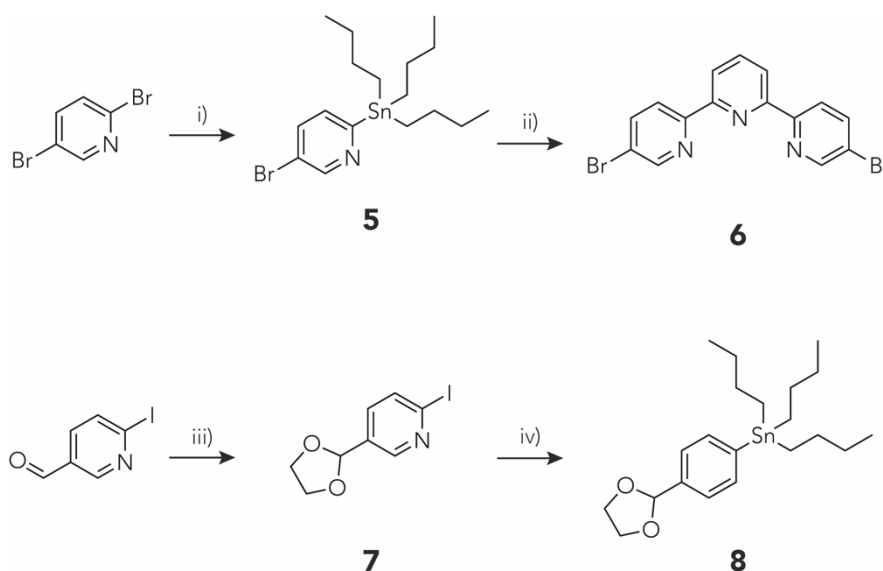
Scheme 11: Molecular structure and synthesis of tpy **6** and organnostannylpyridine **8**. i) *n*-BuLi, SnBu$_3$Cl, toluene, - 78 °C, 12 h, 91 %; ii) 2,6-dibromopyridine, Pd(PPh$_3$)$_4$, toluene, 130 °C, 12 h, 48 %; iii) ethylene glycol, *p* – TsOH, toluene, 130 °C, 12 h, 99 %; iv) *n*-BuLi, SnBu$_3$Cl, THF, -78 °C, 12 h, 77 %.

Only a few synthetic routes can be found in the literature for the synthesis of tpy **6**. In a strategy proposed by the Schlüter group, the Stille cross-coupling methodology between 2,5-dibromopyridine and 2,6-bis(trimethylstannyl)-pyridine was used, yielding the target compound with a decent yield of 26.5 % in the last step and an overall yield of 23.3 % over 2 steps.[113] Nevertheless, the high toxicity of the organnostannyl reagent employed makes it very unfavourable. A few years later Sauvage and co-workers improved the synthesis of **6** by introducing iodine in the middle pyridine unit and performing the stannylation on the two peripheric pyridine rings.[114] The toxic 2-trimethylstannyl-5-bromopyridine and 2,6-diiodopyridine were reacted in a classical twofold Stille cross-coupling with a yield of 90 % and allowed to obtain **6** with an overall yield of 69.8 % over 3 steps.
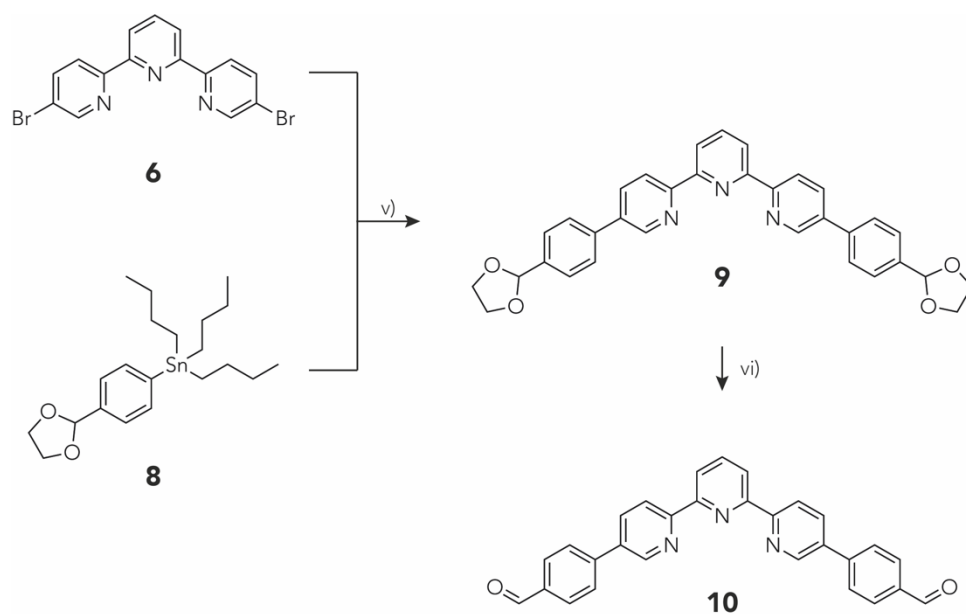
Scheme 12: Molecular structure and synthesis of tpy **10**. v) Pd(PPh₃)₄, toluene, 130 °C, 12 h, 12 %; vi) HCl, CHCl₃, 65 °C, 12 h, 96 %.

Scheme 11 outlines our approach used for the synthesis of **6**, mixing both mentioned strategies mentioned above. The trimethylated tin reagent was exchanged by the less volatile tributylstannyl species, in order to minimize its volatility and the cross-coupling was performed on 2,5-dibromopyridine. We could get a hold on compound **6** with only two synthetic steps starting from organnostannyl compound **5**, which could be

obtained by following the literature known selective stannylation of 2,5-dibromopyridine with 91 % yield.[111] The Pd^0-catalyzed Stille cross-coupling between **5** and 2,6-dibromopyridine lead to the dibromo-tpy **6** with a decent yield of 48 % and an overall yield of 43.6 % over 2 steps could be obtained. The acetal protection of 4-iodobenzaldehyde was performed according to the literature yielding 99 % of molecule **7**.[115] The stannylation was performed by a halogen-lithium exchange with the iodopyridine **7** in THF, followed by quenching with Bu_3SnCl yielding the stannylpyridine **8** in 77 % yield. The synthesized tin reagent **8** was then reacted with 2,6-dibromopyridine by a twofold Stille cross-coupling using 0.1 equivalent of $Pd(PPh_3)_4$ as catalyst under argon, yielding 12 % of 5,5''-bis(4-(1,3-dioxolan-2-yl)phenyl)- 2,2':6',2''-terpyridine (**9**). The deprotection of the dioxolane species **9** was performed under acidic conditions using aqueous HCl, yielding 96 % of target tpy ligand **10**.

Synthesis of "Hydrophilic" Tpy Ligand **13**
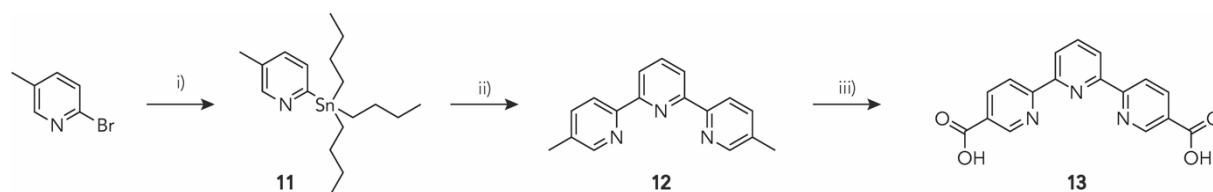
Scheme 13: Molecular structure and synthesis of tpy ligand **13**. i) *n*-BuLi, $SnBu_3Cl$, THF, -78 °C, 12 h, 98 %; ii) 2,6-dibromopyridine, $Pd(PPh_3)_4$, toluene, 130 °C, 24 h, 66 %; iii) $KMnO_4$, pyridine/H_2O, 120 °C, 18 h, 73 %.

Scheme 13 outlines the synthetic procedure used for the formation of target tpy **13**. The synthesis of tpy **12** was adapted from Seçkin and co-workers.[116] The stannylation reaction was achieved by performing a bromine-lithium exchange on 2-bromo-5-methylpyridine in THF, followed by quenching with Bu_3SnCl yielding the stannylpyridine **11** in 98 % yield. The pyridine ring were then merged via a classical Stille cross-coupling reaction, using 3 equivalents of the stannylpyridine **11**, 1 equivalent of 2,6-dibromopyridine and 0.1 equivalent of $Pd(PPh_3)_4$ as catalyst

yielding 66 % of target tpy **12**. The desired tpy **13** was obtained using the conditions of Cao and collaborators, which allows to convert 4-(5,5''-dimethyl-[2,2':6',2''-terpyridine-4'-yl)benzoic acid into the dicarboxylic acid derivative.[117] Molecule **12** was therefore oxidized in presence of an excess of potassium permanganate and the target dicarboxylic acid tpy **13** was obtained in 73 % yield.

Synthesis of Hydrophobic Tpy Ligand **22**
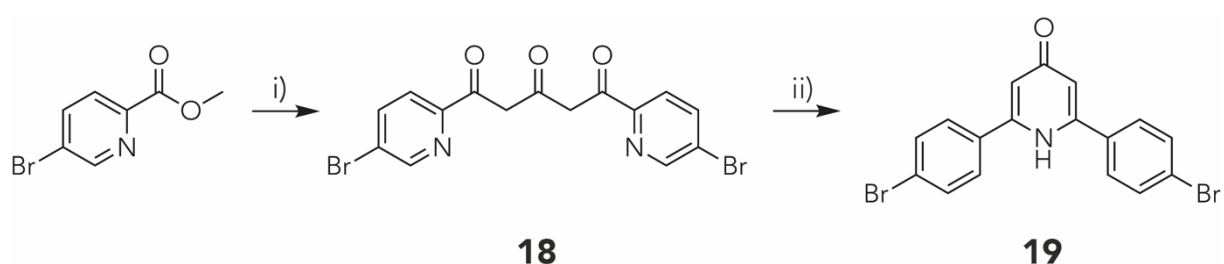
Scheme 14: Molecular structure and synthesis of compound **19**. i) NaH, acetone, DME, 90 °C, 4 h, 76 %; ii) NH₄OAc, EtOH, 85 °C, 12 h, 61 %.

4'-Pyridone derivative **19**, was prepared as shown in scheme 14, according to the two-step procedure established by Constable and Ward in 1990 for the preparation of terpyridine-4'-ones[118]. In the original procedure, 3 equivalents of the picolinate species, 5 equivalents of sodium hydride (NaH) and 1 equivalent of acetone were used for the first step, yielding 80 % of the triketone. Also, the generation of an exothermic reaction during the reflux period was reported. The group of Hearn investigated in 2014 the same Claisen-like condensation and synthesized other substituted triketones by using 2.5 equivalents of the picolinate species, 5 equivalents of NaH and 0.4 equivalents of acetone.[119] We combined and adapted those conditions and by reducing the amount of methyl 5-bromopicolinate to 2 equivalents, setting the amount of acetone to 0.8 equivalents and using 4 equivalents of NaH, we eventually managed to form the brominated ß-triketone **18** in 76 % yield. Due to the poor manoeuvrability of compound **18**, also reported by the research group of Hearn[119], it was directly used for the next step without further purification. The 1,3,5-triketone **18**

was then reacted with ammonium acetate in refluxing EtOH, allowing the ring-closure condensation of the central ring and leading to 4'-pyridone derivative **19** which was obtained in 61 % yield. In DMSO-d$_6$ the NH resonance is observed at 11.09 ppm, consistent with the signal reported by Constable and Ward for a similar species.[118]
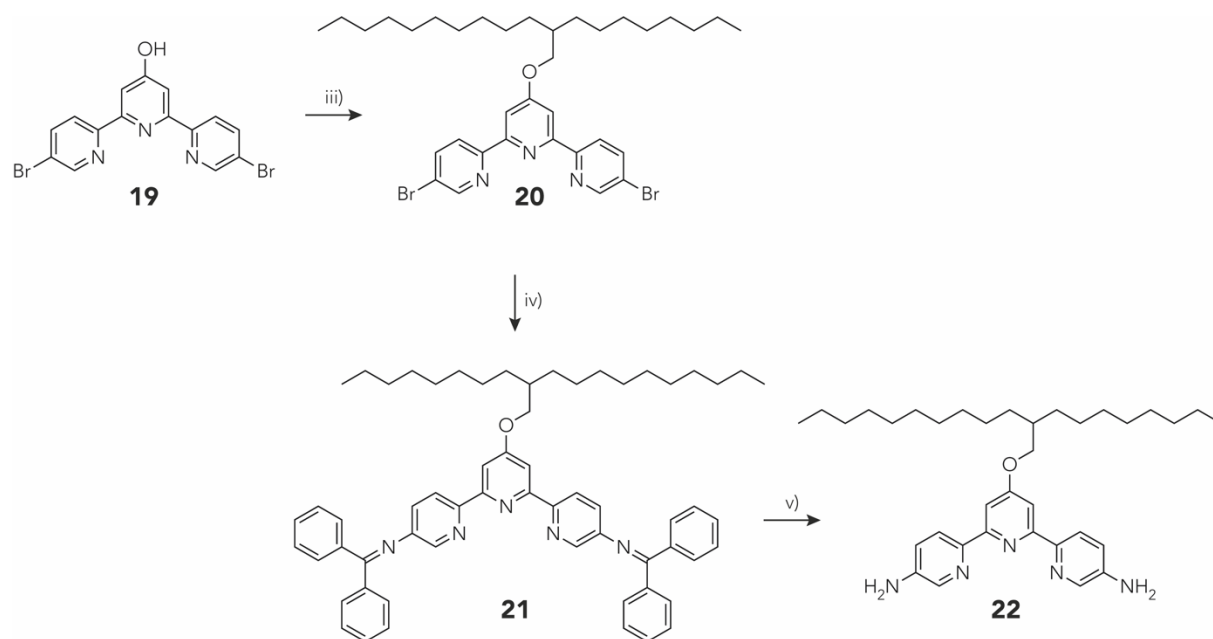
Scheme 15: Molecular structure and synthesis of tpy **22**. iii) 2-octyldodecan-1-ol, DIAD, PPh$_3$, THF, 0 °C - rt, 12 h, 82 %; iv) benzophenone imine, Pd$_2$(dba)$_3$, rac-BINAP, NaOt-Bu, toluene, 130 °C, 12 h, 77 %; v) HCl, THF, rt, 4 h, 91 %.

The preparation of 4'-tpy substituted ethers is very established in the literature. For example Newkome and He performed in 1997, a nucleophilic substitution of 4'-chloro-2,2':6',2''-terpyridine with different primary alcohols in the presence of an excess of potassium hydroxide (KOH) in DMSO at 60 °C.[120] Another method presented by the group of Constable, uses a S$_N$2 reaction between the nucleophilic 2,2':6',2''-terpyridin-4'(1'H)-one (HOtpy) and the electrophilic 1-3-iodopropyl-closo-1,2-carbaborane in the presence of potassium carbonate (K$_2$CO$_3$) at 60 °C for the preparation of ether-bridged tpy species.[121] The Mitsunobu reaction is also a strategy to consider, since the conditions proposed by Hovinen, where they converted HOtpy in different 4'-terpyridine substituted ethers, are milder and high yielding.[122] For the

introduction of the ether-bridged aliphatic chain, we chose to use the Mitsunobu reaction and applied a procedure adapted from the one described by Hovinen[122], as milder and more promising conditions compared to those mentioned above are employed. Molecule **19** was reacted with 1.1 equivalents of 2-octyldodecan-1-ol, 1.2 equivalents of triphenylphosphine (PPh₃) and 1.2 equivalents of diisopropyl azodicarboxylate (DIAD) in THF, yielding 82 % of tpy **20**. To introduce the carbon-nitrogen bond at the positions 5 and 5'', a slightly modified Pd⁰-catalyzed Buchwald-Hartwig amination procedure was chosen.[123] The reaction was performed using 1 equivalent of starting material **20**, 2.4 equivalents of benzophenone imine, 2.8 equivalents of sodium *tert*-butoxide (NaO*t*-Bu) as base, 0.65 equivalents of racemic 2,2'-bis(diphenylphosphino)-1,1'-binaphthyl (BINAP) as ligand and 0.5 equivalents of tris(dibenzylideneacetone)dipalladium(0) (Pd₂(dba)₃) as catalyst. After refluxing overnight and work-up, desired aminated species **21** was obtained in 77 % yield. The imine bonds formed were cleaved into the primary amine species using HCl in "wet" THF, yielding 91 % of the final compound **22**. The desired hydrophobic tpy ligand **22** was synthesized with an improved linear synthesis with an overall yield of 26 % over five steps.

Complexation of "Hydrophilic" and Hydrophobic Tpy Ligands

In this subchapter the preparation and the isolation of "hydrophilic" and hydrophobic tpy ligands complexes with different transition metals will be presented and discussed. The aim of this part was to find the most suitable transition metal for the assembly of the desired amphiphilic heteroleptic molecule. Mostly, it is about forming a kinetically stable complex, which has the ability to self-assemble at an air/water interface into a pre-ordered structure and that does not degrade into the two corresponding homoleptic species. As mentioned in the introduction of this thesis, three different approaches exists for the building of tpy-complexes, we will show how

we succeeded to synthesize and investigate the different Fe(II)-, Co(III) and Ru(II)-complexes using these strategies.

Heteroleptic [Fe^{2+}(**4**)(**22**)](PF$_6^-$)$_2$ – Complex **26**

The one-step approach was used for the preparation of heteroleptic complex **26**, as seen in scheme 16. To do so, 1 equivalent of iron(II)chloride (FeCl$_2$) was combined with an equimolar solution of tpy ligands **4** and **22** in MeOH/DCM and, whereupon the solution immediately turned purple. After evaporating most of the solvents, an anion metathesis was done by adding an excess of sat. aqueous NH$_4$PF$_6$ solution which resulted in the precipitation of the statistically formed Fe(II)-tpy-complexes.

Scheme 16: Molecular structure and synthesis of heteroleptic Fe(II)-tpy-complex **26**.

The dark purple coloured solid obtained was then filtered and washed several times with H_2O. As mentioned above, during the statistical reaction of compound **26**, three different species were obtained (one heteroleptic complex **26** and two homoleptic complexes **26a** and **26b**). The isolation of the heteroleptic target complex **26** from the statistical product mixtures was very challenging and despite numerous efforts, it was not possible to achieve any separation using normal or reversed phase flash column chromatography or size exclusion chromatography. The only efficient method found for the purification of this mixture of complexes was by reversed phase preparative high pressure liquid chromatography (HPLC). Figure 13 displays the HPLC chromatogram of the crude mixture containing the three Fe(II)-tpy-complexes using a specific gradient of H_2O/MeCN solvents mixture and small amounts of trifluoroacetic acid (TFA) as additive. Homoleptic compound **26a** is the most polar species and has a retention time of around 3 min.
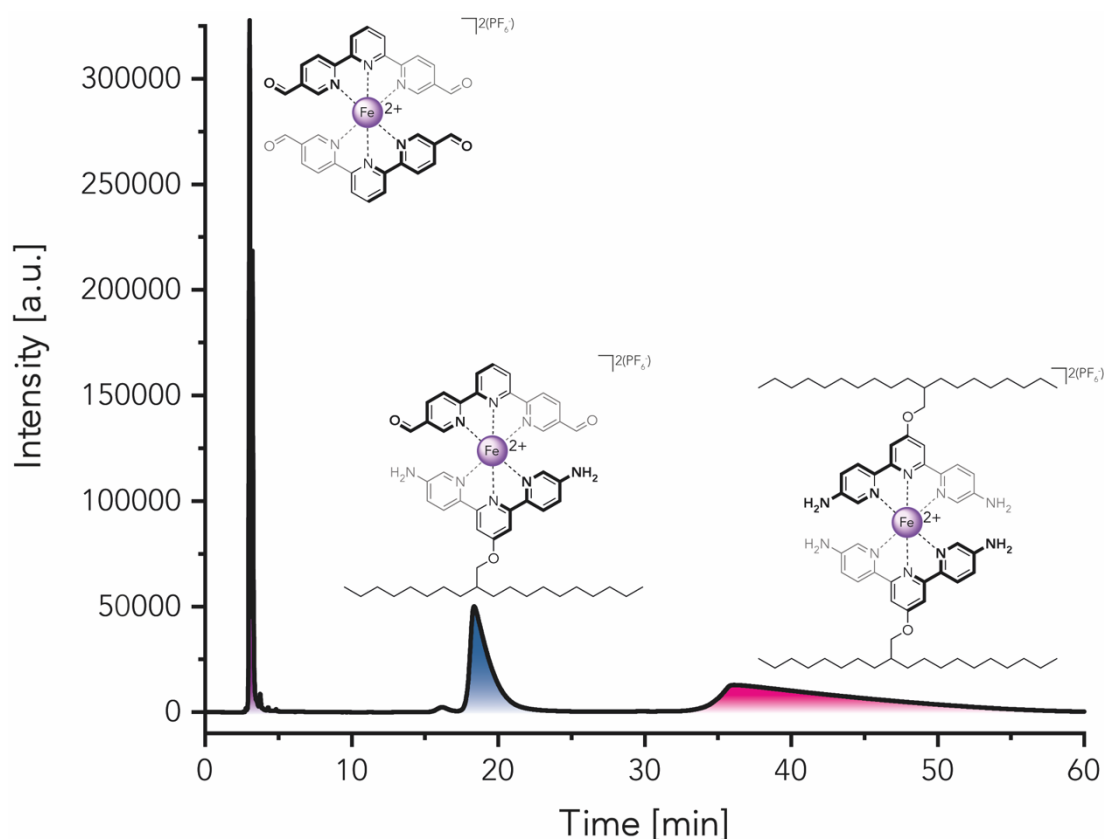
Figure 13: Molecular structures and reversed phase HPLC chromatogram of the crude mixture of homoleptic complex **26a** (highlighted in violet), heteroleptic complex **26** (highlighted in blue) and homoleptic complex **26b** (highlighted in magenta).

The target amphiphilic heteroleptic complex **26** has a retention time of approximately 17 min and the most apolar complex **26b** has a retention time siting around 35 min, showing a very broad and tailoring signal. The latter behaviour can be explained by the strong interaction of the pack material in the reversed phase column (Reprosil C18) with the aliphatic chains of the complex. Despite the wide peak area featured by the homoleptic complex **26b**, an expected statistical ratio of 1:2:1 was obtained for the **26a-26-26b** product distribution after comparison of three signal integrals. After preparative reversed phase HPLC, the target compound **26** was isolated as a purple solid in 44 % yield, molecule **26a** could be isolated in 26 % yield and compound **26b** could be isolated in 28 % yield. The yields obtained for this complexation reaction of heteroleptic complex **26** is not accurate, since it is rapidly degrading in three different complexes. However, the stability of the different heteroleptic complexes will be discussed in the corresponding chapter (Stability Investigation of Heteroleptic Tpy Complexes).

Heteroleptic [Co^{3+}(**4**)(**22**)](PF$_6^-$)$_3$ – Complex **27**

The kinetics of the formation and the dissociation of bis-tpy-complexes depends in part on the transition metals used for the complexes formation. This was reported in the 60's, by Wilkins and co-workers, who studied the rate constants of the formation and dissociation of tpy-complexes using different transition metals ions.[124,125] However, the Fe(II)-metal ion was not appropriate for the preparation of a kinetically stable heteroleptic complex, since complex **26** dissociated immediately after the isolation. Henderson and Hayward studied the substitution effect of amine and ether substituents at the position 4' of tpys on the kinetic stabilities of the bis-tpy-complexes of Fe(II) and Co(II). They observed that the presence of amines induces the fast oxidation by air, forming the kinetically inert Co(III) specie.[126] Our molecular design incorporates two primary amines at the substitution position 5 and 5'', and should therefore also induce a rapid oxidation by air to the kinetically inert Co(III) complex.
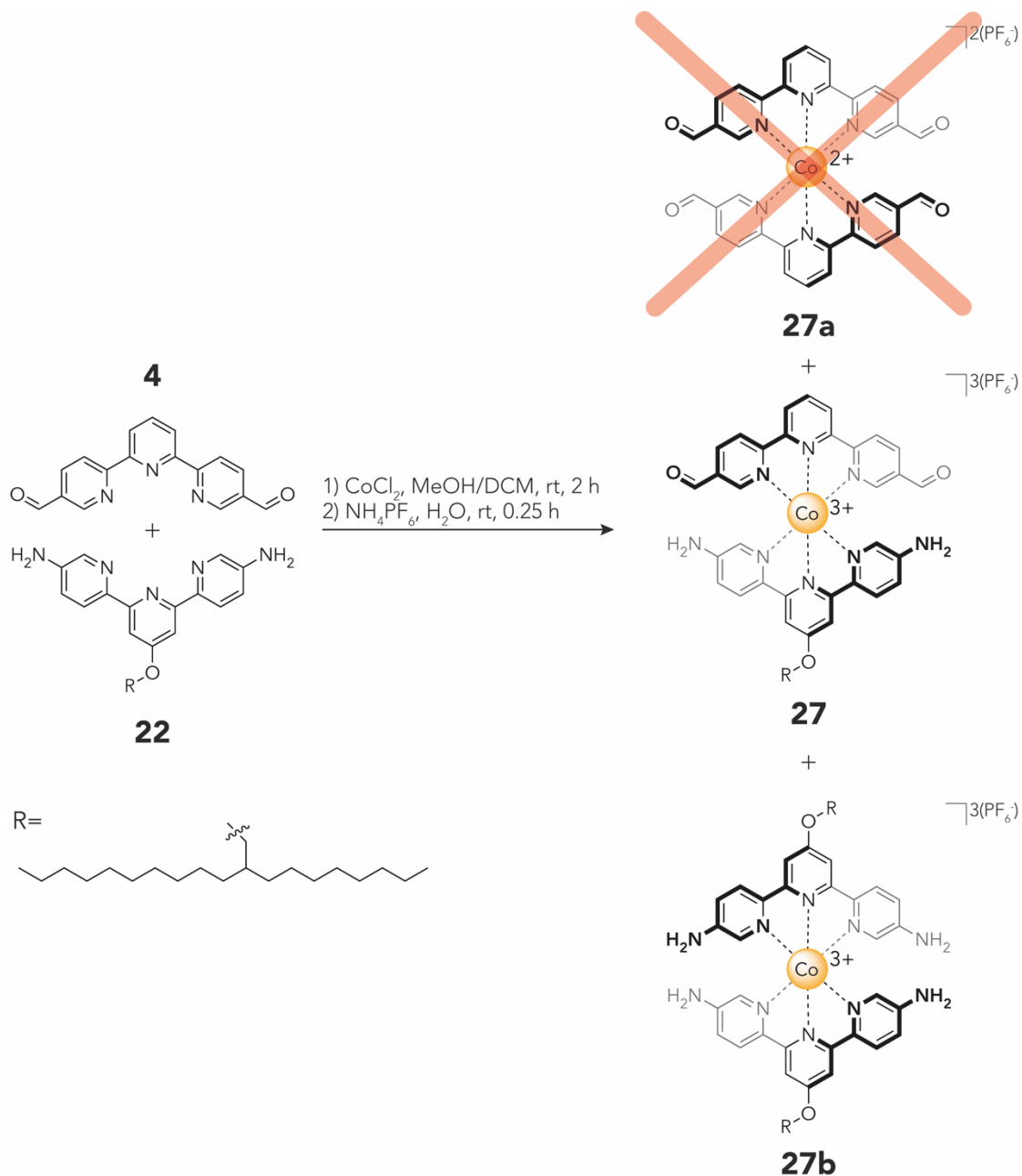
Scheme 17: Molecular structure and synthesis of heteroleptic Co(III)-tpy-complex **27**.

The one step synthetic approach used for the preparation of heteroleptic tpy-complex **27** is illustrated in scheme 17. Co(III)-complex **27** and **27b** were prepared in a similar fashion to the one presented for Fe(II)-complex **26a**, **26** and **26b**. The main difference lying between the two synthetic procedures is the use of cobalt(II)chloride (CoCl$_2$) instead of FeCl$_2$.
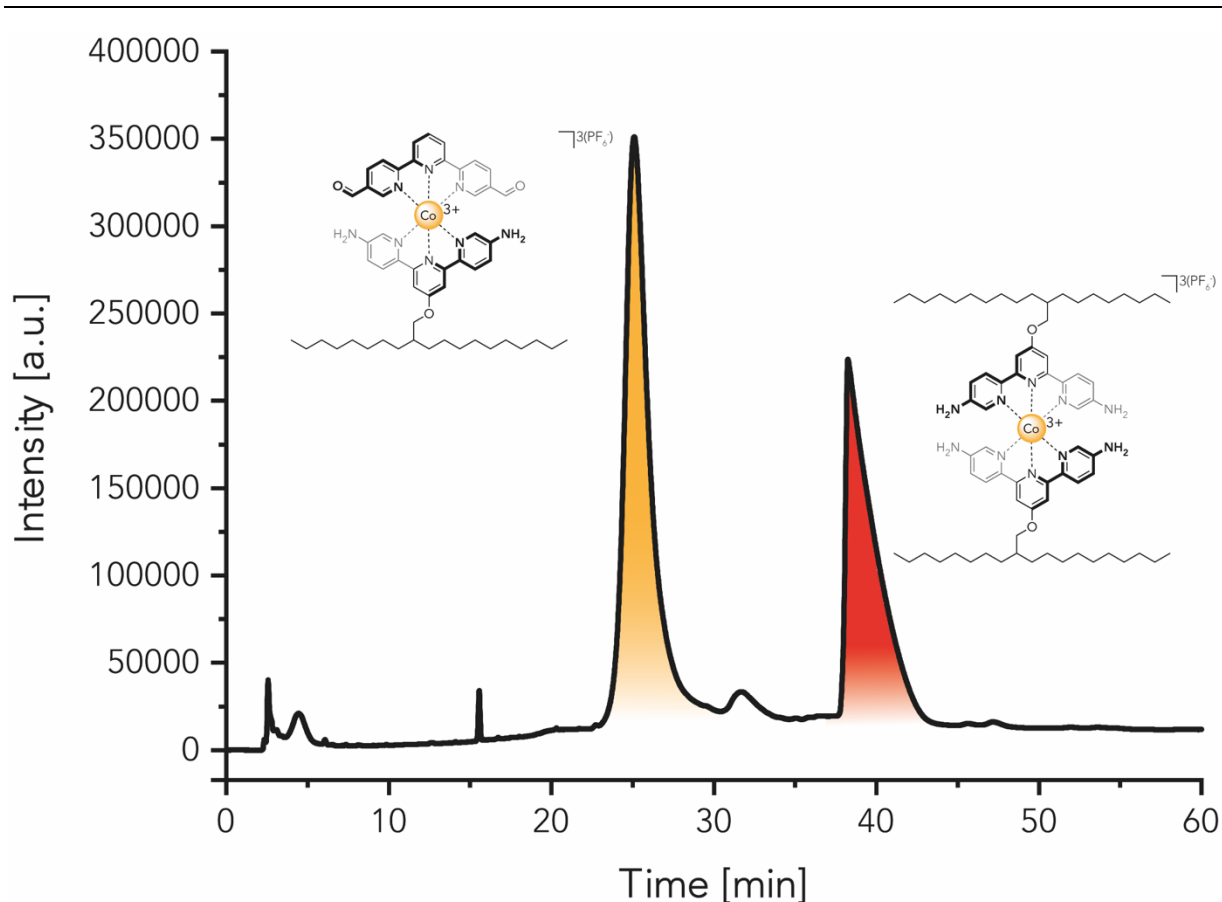
Figure 14: Molecular structures and reversed phase HPLC chromatogram of the crude mixture of heteroleptic complex **27** (highlighted in orange) and homoleptic complex **27b** (highlighted in red).

The different complexes were isolated by preparative reversed phase HPLC (Reprosil C18), using an appropriate gradient mixture made of H_2O/MeCN with small amounts of TFA as additive. Figure 14 is displaying the retention time of heteroleptic tpy-complex **27** at 23.0 min (highlighted in orange) and the retention time of homoleptic tpy-complex **27b** at 37.5 min (highlighted in red). It is important to mention, that homoleptic compound **27a** was not formed and different mass analysis methods and NMR experiments could not show any sign of its formation. This can be explained by the very weak stability of molecule **27a**, which is probably immediately dissociating to form the heteroleptic specie **27**. The statistical ratio of 1:2:1 expected for the preparation of such complexes seems to fit with the showed chromatogram, presented in figure 14. Indeed, if we integrate and compare the orange and the red areas of the HPLC chromatogram, we obtain a ratio of 66 % to 33 %, which is expected

for the statistical formation of only 2 complexes. However, after several runs on the preparative reversed phase HPLC, the target compound **27** was isolated as a brownish solid in 49 % yield and molecule **27b** could be isolated in 26 % yield. As mentioned at the beginning of this chapter, in presence of donating groups like amines, Co(II) can be oxidized by air to Co(III) and form a kinetically more inert bis-tpy-complex. A proof for the +3 oxidation state of the cobalt ions in complexes **27** and **27b** could be provided by ^{1}H - NMR experiments (figure 15). One can perfectly identify that the sample is a diamagnetic species, thus confirming the presence of Co(III) ions (which have a d^6 configuration) instead of Co(II) (d^7 configuration).
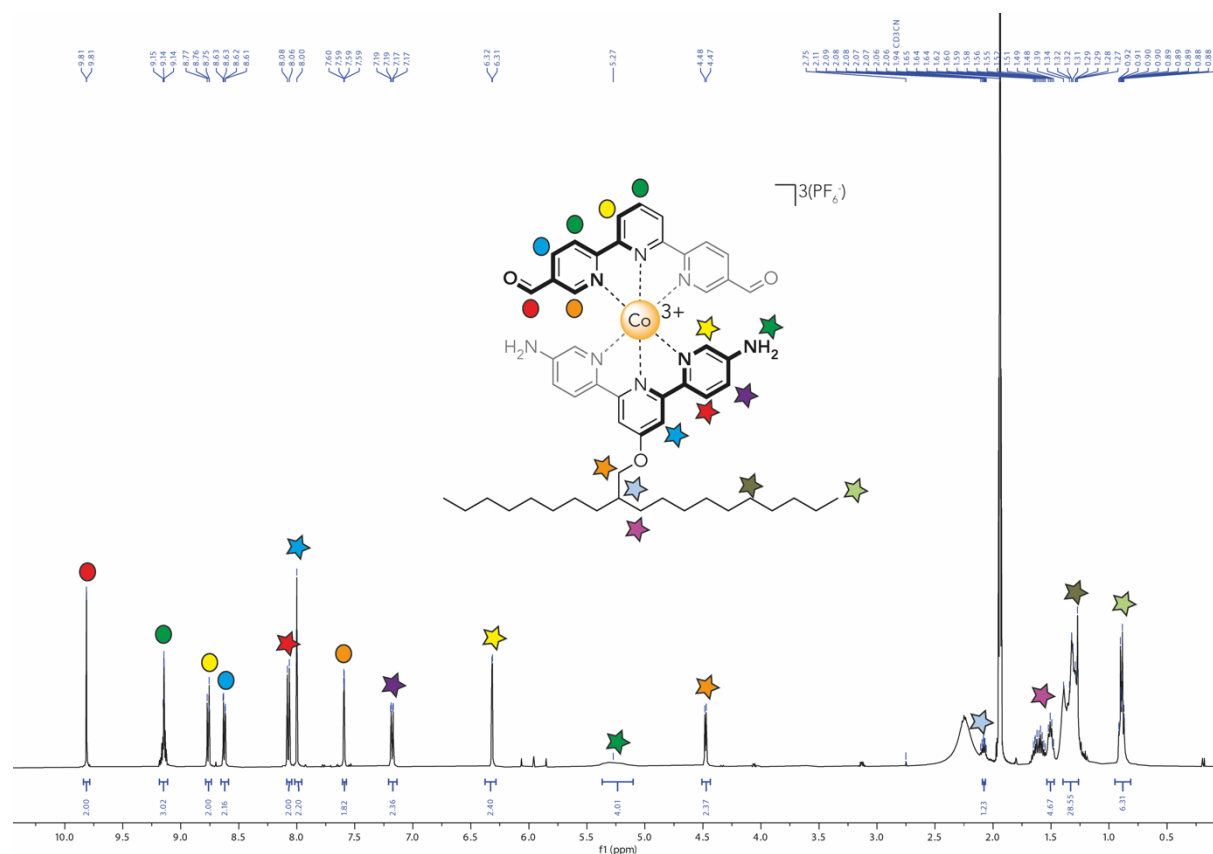
Figure 15: ^{1}H-NMR spectrum of compound **27**, assignment of protons by circles for "hydrophilic" ligand and stars for hydrophobic ligand.

Complementary a Diffusion Ordered SpectroscopY (DOSY) NMR experiment was performed to confirm that only one specie is present in the NMR tube (see Chapter 3, Appendix Molecule **27**).

Heteroleptic [Ru²⁺(**3**)(**22**)](PF₆⁻)₂ – Complex **30**

Heteroleptic bis(tpy) complex **30** was synthesised as reference compound within this project and is an analogue of complex **26** and **27**. The reason for the importance of molecule **30** lies in the fact that, due to Ru(II) large d-orbitals, the binding constant K with tpy ligands is stronger and renders the bis(tpy) complexes kinetically more inert.[127,128] The main idea was to use **30** as a test molecule in the investigation of the molecular design and to prove its amphiphilic behaviour on the LB trough. For the synthesis of a heteroleptic Ru(II)-bis(tpy) complex, a two-step sequence was chosen, involving first the formation of a Ru(III)-intermediate possessing one ligand followed by the introduction a different one under reductive conditions. The first attempt for the preparation of heteroleptic complex **51** is illustrated in Scheme 18.
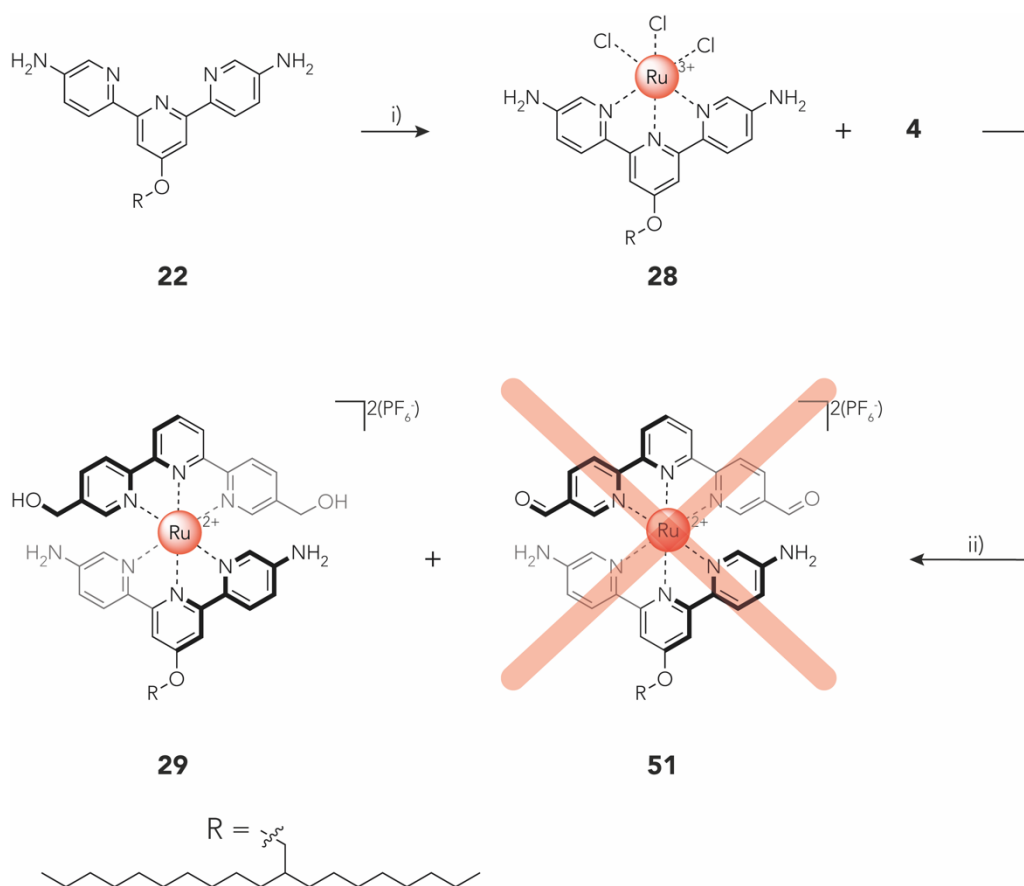
Scheme 18: Molecular structure and synthesis of heteroleptic Ru(II) bis(tpy) complex **29** instead of target **51**. i) RuCl₃ · 3H₂O, EtOH, 80 °C, 4 h, 70 %; ii) 1) Microwave, triethylamine, ethylene glycol, 170 °C, 20 min, 2) NH₄PF₆, H₂O, rt, 0.25 h, 61 %.

The reaction conditions for the preparation of Ru(III)-intermediate **28**, were adapted from the publication of Tatikonda and co-workers.[129] In the first step, 1 equivalent of hydrophobic tpy **22** and 1 equivalent of $RuCl_3 \cdot 3H_2O$ were dissolved in EtOH and refluxed for 4 h, to yielding 70 % of the Ru(III) mono-tpy complex **28** as crude product. It was unfortunately not possible to characterize this compound in solution due to its poor solubility, and NMR spectroscopy would not been suitable anyway due to its paramagnetic nature. Nevertheless, the crude product was used for the next step as such. The conditions used for the next step were adapted from Rupp and collaborators.[130] Intermediate **28** was suspended in ethylene glycol with ligand **4** along with small amounts of triethylamine which act as reductant. The mixture was heated in the microwave at 170 °C for 20 min. Upon addition of sat. aqueous NH_4PF_6 to the reaction mixture, heteroleptic complex **29** was isolated in 61 % yield instead of target compound **51**.
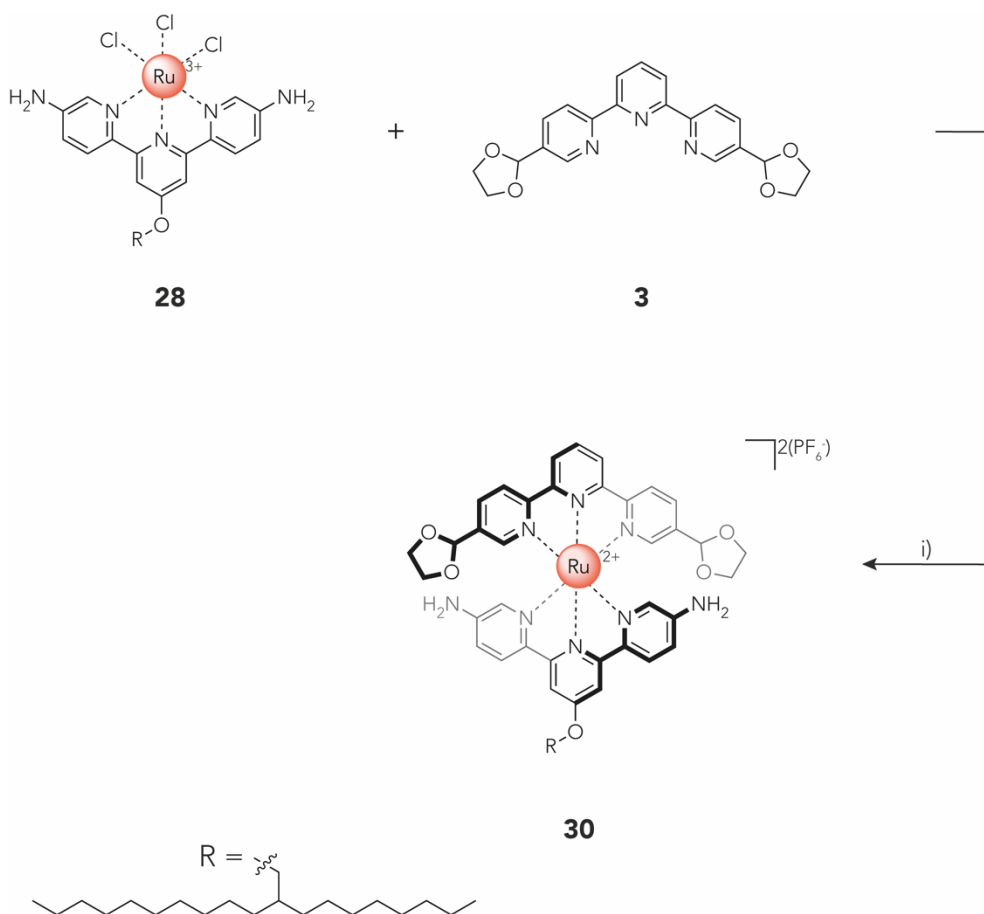
Scheme 19: Molecular structure and synthesis of heteroleptic Ru(II) bis(tpy) complex **30**. i) 1) Microwave, triethylamine, ethylene glycol, 170 °C, 20 min, 2) NH_4PF_6, H_2O, rt, 0.25 h, 49 %.

In this case, the reduction of the aldehyde moiety to a primary alcohol can be explained by the reductive conditions employed for the reaction or attributed to a reduction through a hydrogen transfer catalysed by Ru(II)[28–30]. To overcome the undesired aldehyde reduction process, we decided to form the asymmetric Ru(II)-based complex starting with the acetal protected aldehyde **3** as illustrated scheme 19. Heteroleptic compound **30** was prepared using the same conditions presented above and could be isolated as a deep red solid in 49 % yield.

Optical Investigation of bis(tpy) Metal Complexes

In this subchapter we will discuss the optical properties of the heteroleptic and homoleptic bis(tpy) complexes synthesized. The UV-Vis spectra of the prepared molecules throughout the present chapter were recorded at several concentrations, in MeCN and at room temperature. The averaged absorbances were converted into the corresponding extinction coefficients ε, following the *Beer-Lambert* law (Equation 1) and plotted against the respective wavelengths λ.

$$A = \varepsilon \cdot c \cdot d$$

Equation 1: *Beer-Lambert* law equation, where A is the absorbance, ε is the extinction coefficient, c is the concentration and d is the path length of the light in the UV-Vis cuvette.
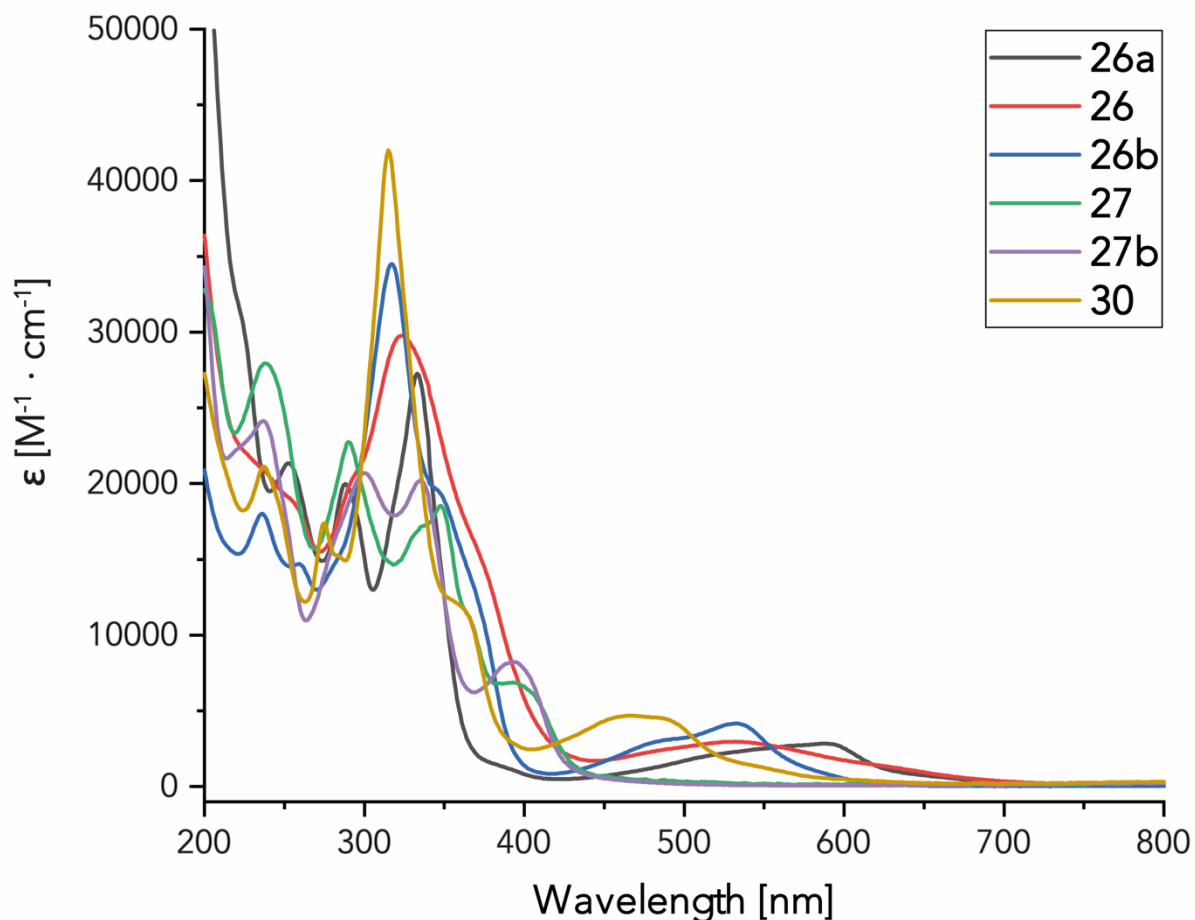
Figure 16: UV-Vis absorption spectra of bis(tpy) metal complexes. Fe(II)-complexes **26a**, **26** and **26b**; Co(III)- complexes **27** and **27b**; Ru(II)-complex **30**.

As displayed in figure 16, the Fe(II)- and Ru(II)-based bis(tpy) complexes **26a, 26, 26b** and **30** shows the characteristic metal-to-ligand charge-transfer (MLCT) bands, in the 460 - 590 nm region. The MLCT-transitions arises from the excitation of a primarily metal-localized electron from the respective $3d\pi$-orbital into the lowest unoccupied molecular orbital (LUMO) π^*-orbital of the tpy-ligand.[134] The characteristic intense colours of such complexes, for example purple for Fe(II)-based complexes and red for Ru(II)-based complexes, can be explained by the MLCT absorption lying in the visible region.[135]

Table 1 compares the λ_{max} and ε values of the ligand-cenetred (LC), metal-centered (MC) and the MLCT-bands of the synthesized metal complexes and reference compounds [Fe(tpy)$_2$](PF$_6$)$_2$[136,137], [Co(tpy)$_2$](PF$_6$)$_2$[138,139] and [Ru(tpy)$_2$](PF$_6$)$_2$[140].

Complex	λ_{max} (LC/MC) [nm]	ε [M$^{-1} \cdot$ cm^{-1}]	λ_{max} (MLCT) [nm]	ε [M$^{-1} \cdot$ cm^{-1}]
Fe(tpy)$_2$	266	45000	552	11900
	321	51000		
	365	416		
26a	253	21334	590	2849
	288	19989		
	333	27250		
26	260	18020	542	2904
	298	21021		
	315	42005		
26b	236	18019	532	4168
	259	14696		
	317	34502		
Co(tpy)$_2$	270	21562		
	282	22187		
	317	23750		
27	238	27962		
	290	22750		
	348	18530		
	397	6770		
27b	237	24136		
	300	20697		
	335	20207		
	394	8228		
Ru(tpy)$_2$	270	48000	475	17000
	307	78000		
30	237	21133	465	4686
	275	17384		
	315	42005		
	368	10461		

Table 1: Characteristic bands in the UV-Vis absorption spectra of complexes **26a** - **30** and reference compounds [Fe(tpy)$_2$](PF$_6$)$_2$[136,137], [Co(tpy)$_2$](PF$_6$)$_2$ and [Ru(tpy)$_2$](PF$_6$)$_2$[140].

The MLCT absorption band of Fe(II)-complex **26a** at 590 nm (ε = 2849 M$^{-1} \cdot$cm^{-1}) exhibits a bathochromic shift of 38 nm compared to the parent Fe(tpy)$_2$ complex. This can be explained by the electron-withdrawing nature of the aldehydes present in compound **26a**, leading to an energetic stabilization of the ligand-based LUMO π^*- orbital. On the other hand, the more electron-donating amine substituent in compound **26b** give rise to a hypsochromic shift of 20 nm (λ_{max} = 532 nm, ε = 4168 M$^{-1} \cdot$cm^{-1}). This can be rationalized by an increase in the HOMO-LUMO gap

induced by a stronger destabilization of the LC LUMO in comparison to the MC HOMO. Heteroleptic complex **26** exhibit a broad absorption band in the MLCT region without a sharp λ_{max}, since the molecule is kinetically labile and immediately dissociates in the two homoleptic species (**26a** and **26b**) and the desired heteroleptic molecule **26**. However, with λ_{max} of 542 nm (ε = 2904 $M^{-1} \cdot cm^{-1}$), a small hypsochromic shift compared with [Fe(tpy)$_2$] can still be observed, confirming the more dominant energetic stabilization of the MC HOMO by the electron-donating substituent and the destabilisation of the LC LUMO by the electron-withdrawing group (table 1).

Similar results were reported by Constable and collaborators, by studying the effect of electron-accepting and -donating substituents on different homoleptic and heteroleptic Ru(II)-bis(tpy) complexes.[141] Ru(II)-based compound **30**, with a λ_{max} of 465 nm (ε = 4686 $M^{-1} \cdot cm^{-1}$), exhibit a hypsochromic shift of 10 nm compared to the literature known [Ru(tpy)$_2$][140]. As for the Fe(II) complex, the result obtained for compound **30** can be explained by a destabilization of the LC LUMO π^*-orbital. Furthermore, several absorption maxima in the higher energetic spectral region between 236 – 397 nm are summarized in table 1. The less intense bands arising in the energetically lower region (397 – 368 nm) can be attributed most likely to MC electronic transitions, whereas the more intense bands in the energetically higher region (237 – 348 nm) may arise from the (either n-π^* or π-π) LC transitions.[135]

Stability Investigation of Heteroleptic bis(tpy) Complexes

In this subchapter we will discuss the stability of the different heteroleptic bis(tpy) complexes synthesized **26**, **27** and **30** by investigating the decomposition of the target compounds to their respective homoleptic species.

One of the major structural characteristics of heteroleptic bis-tpy-metal-complexes in form of [M(tpy)$_2$]X$_2$ (X$^-$ = counterion) is the strength of the metal-to-ligand coordinative bond with many transition metals in a low oxidation state.
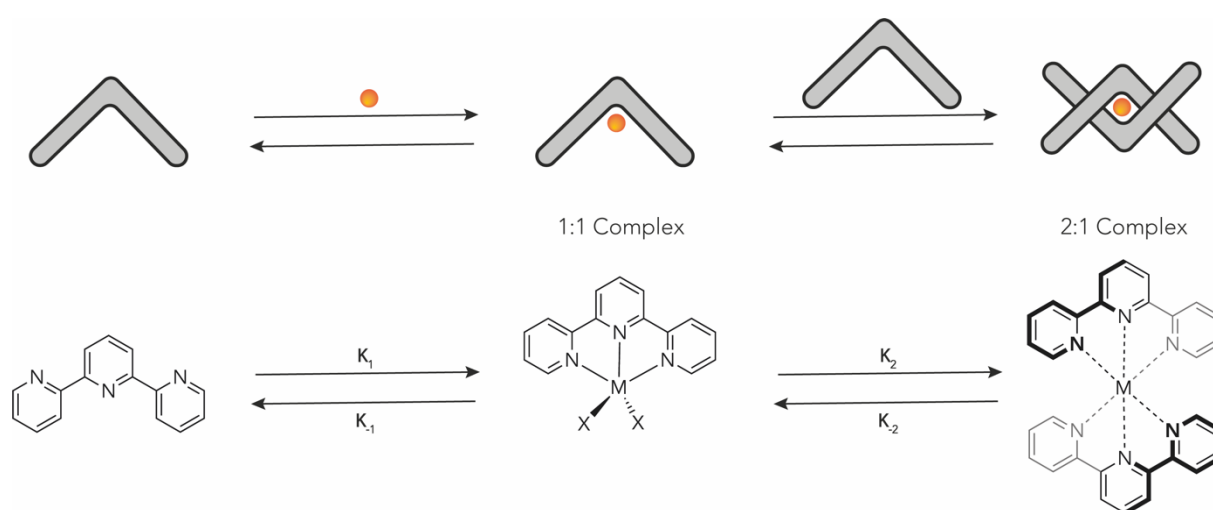
Figure 17: Sketch and molecular structures of complexation and decomposition of tpy (left), 1:1 complex (middle) and 2:1 complex (right).

This unique interaction between metal and ligand can be explained by a strong metal-ligand (d-π^*) back-donation and the dynamic chelate effect. The investigation of different tpy complexes with specific metal ions was reported in the work of Wilkins and collaborators in the 60's.[124,125] They were able to experimentally determine the stability constant (*K* values) of different complexes using the same ligand by means of a stopped-flow method. As illustrated in figure 17, $K_{1,-1}$ represents the complexation and the decomposition of the mono-complex (1:1) and $K_{2,-2}$ the bis-complex (2:1). The stability constants (*K*) determined experimentally by Wilkinson and co-workers[125] and the binding enthalpies (Δ*H*) obtained by Würthner and collaborators[142] of the different tpy-complexes were compared in table 2.

Metal Ion	Log K_1[a]	Log K_2[a]	ΔH^0_1[b][kJ/mol]	ΔH^0_2[b][kJ/mol]
Mn^{2+}	4.4	N.a.	N.a.	N.a.
Fe^{2+}	7.1	13.8	-79.9	-79.9
Co^{2+}	8.4	9.9	-61.5	-66.9
Ni^{2+}	10.7	11.1	-66.9	-54.4
Zn^{2+}	6.0	5.2	-60.7	-60.7

Table 2: Stability constants [104] and binding enthalpies [21] of different [M(tpy)$_2$] complexes. [a]Stability constants (*K*) were determined by a stopped-flow procedure in H$_2$O. [b]Binding enthalpies (Δ*H^0*) were determined by isothermal titration calorimetry (ITC) in MeCN. The table was adapted from Newkome and collaborators.[135]

According to table 2, [Zn(tpy)$_2$] complex is the kinetically most labile complex compared to complexes with other metal ions as it has the weakest K_2 and the lowest ΔH^0_2 values.

Stability of Heteroleptic Fe(II)-Based Complex 26

Different analytical methods were used to monitor the decomposition rate of the asymmetric species **26** into its corresponding homoleptic compounds, after its isolation via reversed phase HPLC (Reprosil C18) (see Figure 13). Mayor and collaborators reported about two different Fe(II)-based heteroleptic tpy-complexes containing a push-pull ligand system with a half-life time of about $t_{1/2} = 24$ h[143] and $t_{1/2} = 316$ h[144]. In the case of compound **26**, a fresh solution of the isolated species was immediately forming both homoleptic complexes (**26a** and **26b**) in MeCN at room temperature (figure 18).
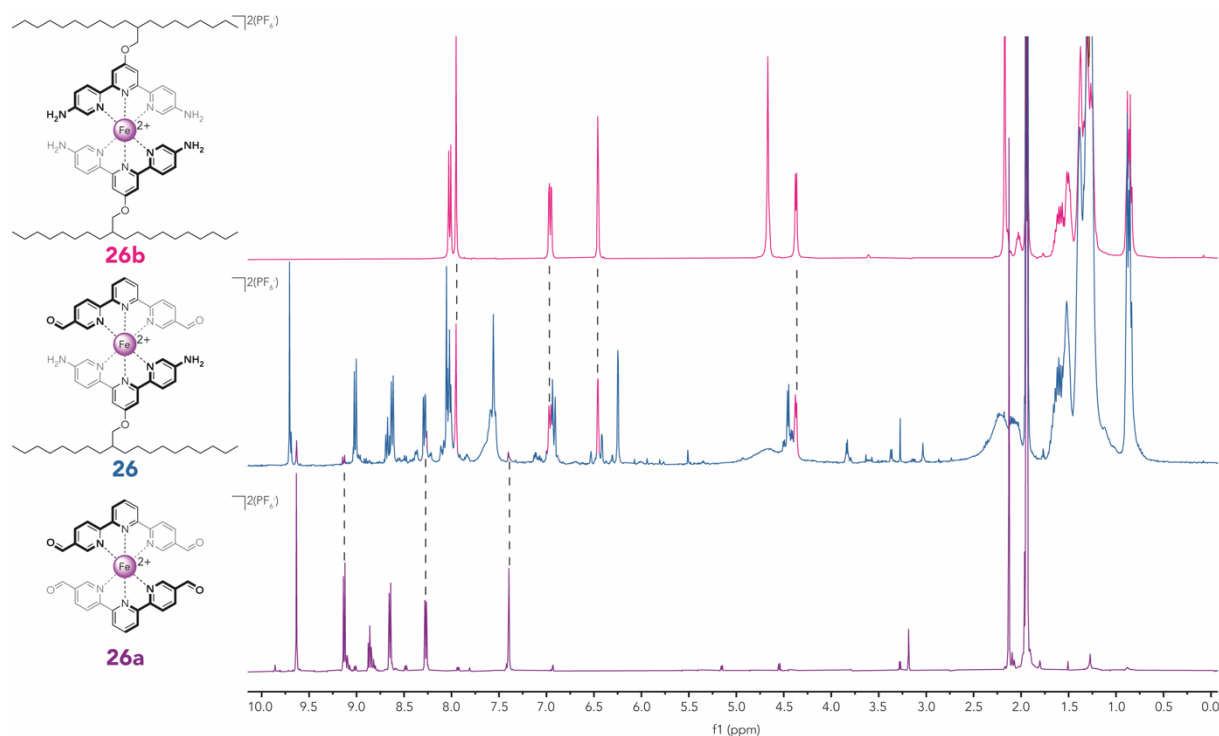
Figure 18: ^{1}H-NMR spectrum of a freshly prepared solution of **26** (middle), compared with the ^{1}H-NMR spectrum of both homoleptic tpy-complexes **26b** (on top) and **26a** (at the bottom). The same species were highlighted by the same colour and connected by dotted lines.

The ^{1}H-NMR spectrum of a freshly isolated **26** sample contains three different complexes as seen in figure 18. Different signals from the homoleptic species (**26a** and **26b**) are present in the spectrum, highlighted by the same colour and connected by dotted lines.
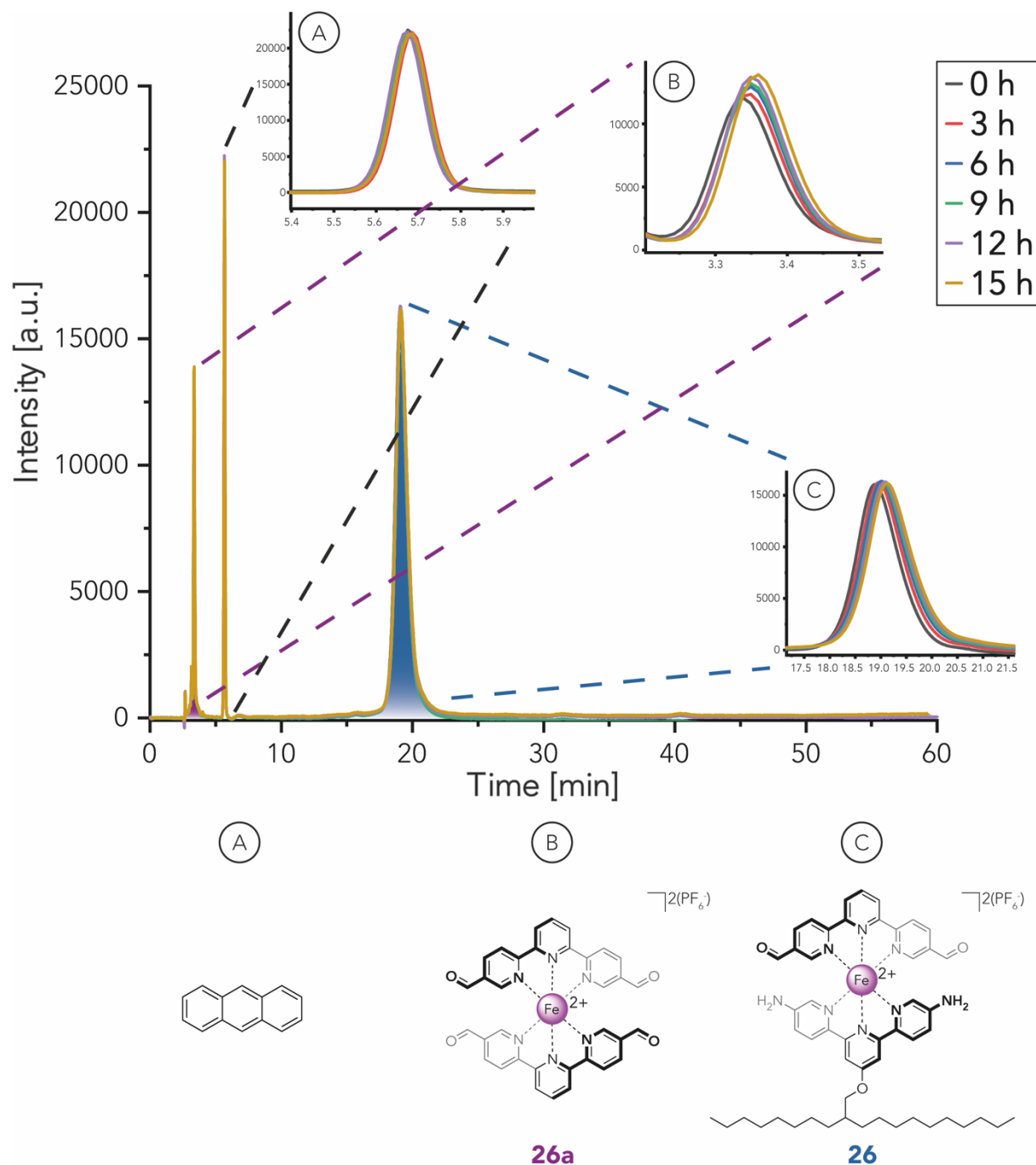
Figure 19: Molecular structures of heteroleptic complex **26** (highlighted in blue), homoleptic complex **26a** (highlighted in violet) and anthracene. Comparison of reversed phase C18 analytical HPLC chromatogram of the freshly isolated heteroleptic complex **26** sample (black line 0 h), homoleptic complex **26a** and anthracene during 15 h (yellow line). (a) Zoomed anthracene signal; (b) Zoomed homoleptic complex **26a** signal; (c) Zoomed heteroleptic complex **26** signal.

To exclude that the fast degradation of compound **26** is not enhanced during the evaporation of the solvent, we decided to directly inject the solution obtained after isolation of the mixture in an analytical reversed phase HPLC (Reprosil C18) along with adding anthracene as reference. In this way quantitative analysis of the conversion to the homoleptic species can be performed, as illustrated in figure 19. The homoleptic complex **26a** is present immediately after the injection of the freshly isolated solution of **26** (black line), like the ^{1}H-NMR spectrum (figure 18), confirming the immediate decomposition of target asymmetric complex **26** into the homoleptic species. Moreover, after 15 h (yellow line) one can observe that the concentration of **26a** in the solution is increasing (figure 19, b). Through, the hydrophobic complex **26b** is not detectable since the signal seems to be very broad and lost in the noise of the background. It is also important to note that anthracene, which was added as reference compound, allow to quantitatively monitor the transformation of the heteroleptic specie, since its concentration is not changing and therefore not interacting in the solution whatsoever. The fast degradation of **26** can be explained by the preferential interaction of MeCN with the dissociated ligand, better known as ligand-solvent interaction, which stabilizes the transition state and decreases the kinetic stability of the complex. An good example of such effect was reported by Henderson and Hayward, where the stability of Fe(II)-bis(tpy) complexes was investigated in the presence of different solvents. They could observe the variation in decay rates of more than five orders of magnitude for the dissociation of k_{-2} in presence of an even more strongly binding metal ion.[145] Moreover, they could find a correlation between the rate of dissociation and the solubility of the bare ligand. In our case the solvent could not be avoided, since the heteroleptic complex **26** was only separable in a MeCN/water mixture on the reversed phase HPLC (Reprosil C18).

Stability of Heteroleptic Co(III)-Based Complex 27

Co(III)-based bis(tpy) complexes are known to be kinetically inert, as can show the work done by Henderson and Hayward, who studied the substitution effect on their stability by introducing electron-withdrawing or -donating groups at the position 4' on tpys.[126] This strong binding behaviour between the cobalt center and the tpy ligand can be attributed to the change of oxidation state from (II) to (III), which induces an enhanced electrostatic attraction. Moreover, the molecular geometry is changing form a distorted d^7 to a straight octahedral d^6 complex, increasing the stability of the structure.
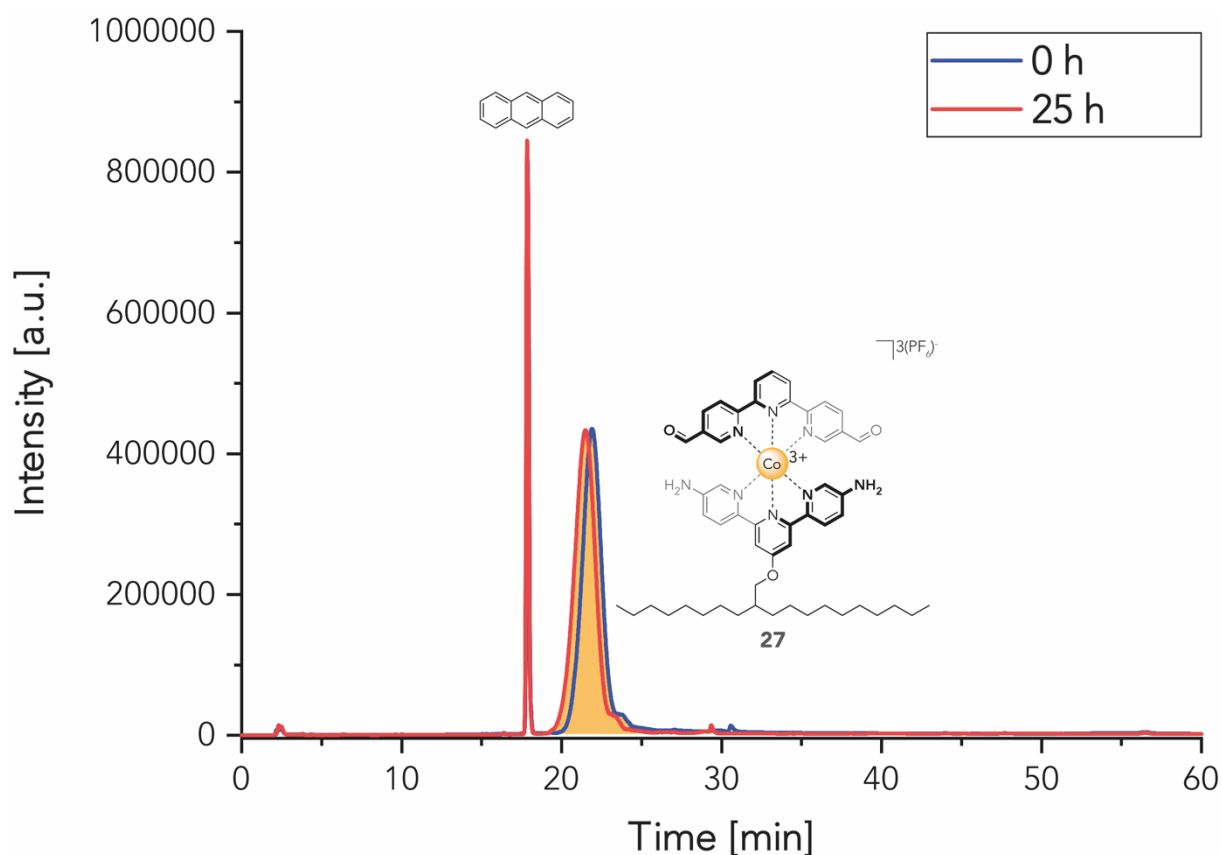
Figure 20: Molecular structures of **27** (highlighted in orange) and anthracene. Comparison of reversed phase C18 analytical HPLC chromatogram of the fresh isolated heteroleptic complex **27** sample (blue line) at 0 h and after 25 h (red line).

The investigation of the stability of molecule **27** was performed by injecting a freshly prepared solution of the asymmetric Co(III)-complex and anthracene for the quantitative analysis of its transformation into the homoleptic specie (**27b**). As illustrated in figure 20, no new peak was detectable after 25 h and the area of heteroleptic compound **27** (highlighted in orange) normalized to the area of anthracene did not change. To make sure that the peak did not disappeared in the baseline, because of the tailing behaviour of homoleptic complex **27b** (see figure 14), ^{1}H-NMR and MS-analysis were also performed and confirmed the stability of complex **27** for at least 4 weeks.

Stability of Heteroleptic Ru(II)-Based Complex **30**

Ru(II)-bis(tpy) complexes are known to have high binding constants (*K*), resulting in kinetically inert system.[141,146–148] This is also the case for the synthesized Ru(II)-based complex **30**, as one can see in figure 21. The ^{1}H-NMR spectrum of **30** was recorded in intervals of 24 h, in acetonitrile-d_3 at room temperature. As the spectra obtained remained unchanged, we conclude that the heteroleptic compound **30** is not degrading into other species (figure 21). The asymmetric complex **30** was synthesized as an important reference compound for understanding the amphiphilic behaviour of the designed molecules at the air-water interface, as the compound is not degrading at all. Though, we could not use it for further investigations in the target 2D-molecular textile, since it is only possible to remove the metal from its complex form by using harsh conditions, as described by Schubert and collaborators.[147]
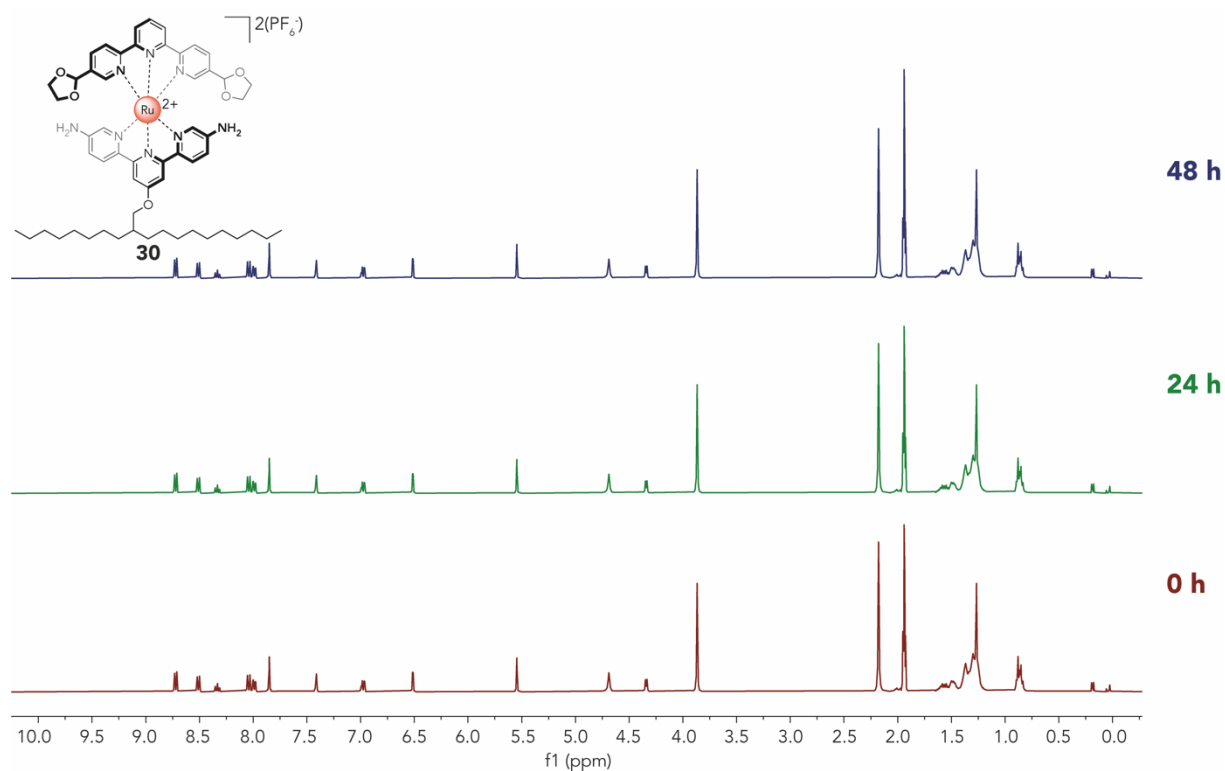
Figure 21: Molecular structure and ^{1}H-NMR spectra of **30** recorded over 48 h, showing the stability of the Ru(II)-based heteroleptic bis(tpy) complex.

Polymerisation Strategy - *Schiff* Base Condensation

Schiff bases are molecules containing an azomethine functional group, better known as imine[149] with the general formula RCH=N–R^1, where R and R^1 are either aliphatic or aromatic groups (scheme 20). Named after the German chemist Hugo Schiff,[150] these molecules can be obtained via a condensation reaction between primary amines and carbonyl compounds like aldehydes or ketones. The reversible reaction starts by the nucleophilic addition of a primary amine to an electrophilic carbonyl species, resulting in an unstable carbinolamine (hemiaminal), which immediately dehydrates and produce an imine. The last step of the reaction, the conversion of the carbinolamine to the imine via dehydration (rate determinant step), can be acid-catalyzed. The conversion has been studied either in organic solvents[151–154] or aqueous solutions[155–159] where the pH should not be too acidic. Indeed, since amines have a basic character

and a protonated amine species ($-NH_3^+$) loses its nucleophilicity, the equilibrium is pushed towards the reactants side without forming the hemiaminal. If a *Schiff* base is involved in a nucleophilic addition by a water molecule, the two starting materials are reobtained, and the starting conditions are restored.
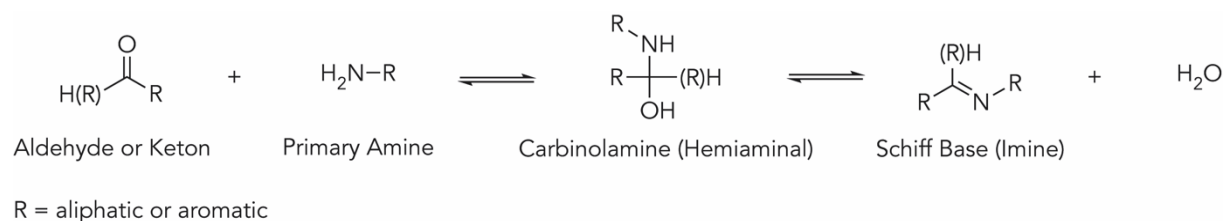
Scheme 20: Molecular structures and synthesis of *Schiff* bases

Schiff bases are very established compounds because of their ease of preparation and their wide application potential in different fields of chemistry. For the pharmaceutical research for example, they represent an interesting moiety for the design of antimalarial agents[160], antibacterial agents[161], antifungal agents[162] or antiviral agents[163]. In supramolecular chemistry also, they give access to structures like covalent organic frameworks (COFs)[164–168] or different type of knots[169–171]. The "proof-reading" or "self-healing" element of *Schiff* bases, due to their reversible nature, are extensively used in contemporary chemistry and are part of the most essential features for the so-called dynamic covalent chemistry[164,172–176] (DCC) strategy.

In this project we wanted to benefit from the *Schiff* bases properties and therefore designed both tpy ligands with a primary amine and an aldehyde at position 5 and 5''. As mentioned in the subchapter "Design of the Building Blocks and Assembly Strategy", we aimed at performing the polymerisation at an air/water interface. To simulate the conditions on the interface, we first used water as solvent and performed the following polymerisation reactions in such a way that they can be transferred in a LB trough. This excludes the use of dried agents or reflux conditions. Preliminary tests were performed to investigate the compatibility of the chosen functional groups and

establish the best conditions for the *Schiff* base condensation in water. 3-Aminopyridine and 3-pyridinecarboxaldehyde were used as reference compounds, yielding the literature known compound N-(3-pyridinemethylene)-3-pyridinimine (**17**). The reactions were performed in three different solvents and a catalytic amount of TFA was added in condition i), iii) and v).
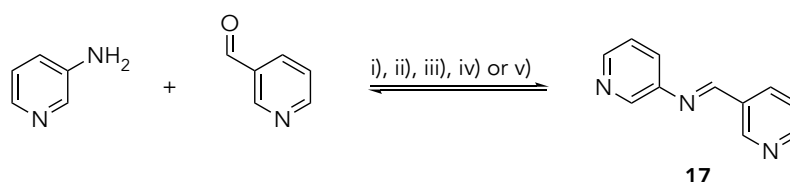
Scheme 21: Molecular structures and synthesis of preliminary *Schiff* base condensation to obtain **17**. i) TFA cat., CHCl$_3$, rt, 3 h, 71 %; ii) THF, rt, 3 h, 36 % iii) TFA cat., THF, rt, 3 h, 69 %; iv) H$_2$O, rt, 3 h, 0%; v) TFA cat., H$_2$O, rt, 3 h, 54 %.

Four out of five reaction conditions worked with a decent yield comprised between 36 - 71 %. All the entries employing catalytic amount of TFA pushed the equilibrium to the *Schiff* base and increased the yield at least by 30 %. In the case of entry iv), compound **17** was not formed due to the insolubility of the starting materials in water. After adding catalytic amounts of acid, the solids started solubilizing and the initially colourless solution immediately took a yellowish shade. This observation can be rationalized by the protonation of the pyridine unit, which leads to a more water-soluble species.[177] The ^{1}H-NMR spectrum shows the typical singlet at 8.53 ppm arising from the proton on the imine functional group (−N=CHR) proton.[178] Also, the infrared (IR) spectrum reveals the characteristic stretching band for the conjugated imine bond (−N=C−) at 1625 cm^{-1}.[178] With these preliminary experiments, one could confirm that the chosen substitution position on the pyridine is reactive enough for the synthesis of the *Schiff* base **17** using the conditions mentioned. Furthermore, we succeeded in performing the condensation in water, with acceptable yields. To extend this study, we decided to investigate the *Schiff* base condensation reaction on a tpy unit, reacting the "hydrophilic" tpy **4** with two equivalents of 3-aminopyridine forming [2,2':6',2''- terpyridine]-5,5''-diyl)bis(N-(pyridine-3-yl)methanimine (**14**) (scheme 22).

64
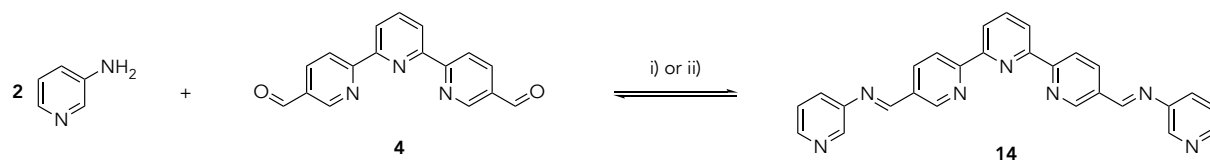
Scheme 22: Molecular structures and synthesis of *Schiff* base condensation on tpy **4** leading to **14**. i) TFA cat., THF, rt, 8 h, 65 %; ii) TFA cat., H_2O, rt, 8 h, 49 %.

In both cases, the desired compound could be isolated with a decent yield comprised between 49 – 65 %. Those results are similar to the one presented earlier, and only a yield difference of 16 % is noted. This discrepancy can be explained by the equilibrium existing between the starting materials, the mono condensate *Schiff* base and **14**, caused by the reactivity of the imine bonds with water. This prevents the reaction to go to completion. The IR spectrum of compound **14** shows the before-mentioned characteristic stretching band located at 1624 cm^{-1} and the appropriate singlet from the ^{1}H-NMR spectrum located at 8.62 ppm. The *Schiff* base condensation was also performed with the hydrophobic tpy **22**, in order to investigate its reactivity towards 3-pyridinecarboxaldehyde and therefore form *Schiff* base **23** (scheme 23).
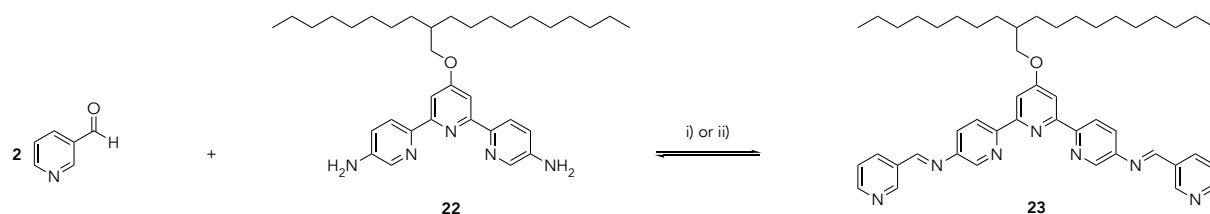
Scheme 23: Molecular structures and synthesis of *Schiff* base condensation on tpy **22** leading to **23**. i) TFA cat., THF, rt, 8 h, 33 %; ii) TFA cat., H_2O, rt, 8 h, 25 %.

Tpy **23** was obtained using both conditions with yields comprised between 25 – 33 %. The IR spectrum obtained for this compound shows the typical stretching band located at 1627 cm^{-1} and the ^{1}H-NMR singlet signal located at 8.62 ppm for the imine moiety. In those cases, one can observe that the equilibrium is pushed towards the reactant side as the yields are lower compared with the other preliminary tests. It is well-known that nucleophilic additions are disfavoured on position 3 and 5 of the pyridine ring. The same reaction was then performed with two equivalents of

benzaldehyde to study the potential effects of the aldehyde moiety reactivity over the outcome of the reaction (scheme 24). By introducing a more electrophilic species, the yield was increased by 10 % in both entries. In the IR spectrum, one can find the imine stretching band located at 1625 cm^{-1} and a singlet located at 8.57 ppm was observed in the ^{1}H-NMR.
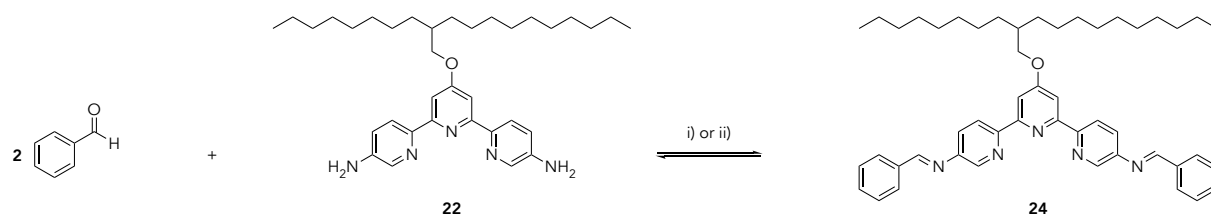
Scheme 24: Molecular structures and synthesis of Schiff base condensation on tpy **22** leading to **24**. i) TFA cat., THF, rt, 8 h, 46 %; ii) TFA cat., H$_2$O, rt, 8 h, 37 %.

To finalize the preliminary tests for the *Schiff* base condensation, homoleptic complex **27b** was let react with four equivalents of 3-pyridinecarboxaldehyde to form *Schiff* base **51b** (Scheme 25).
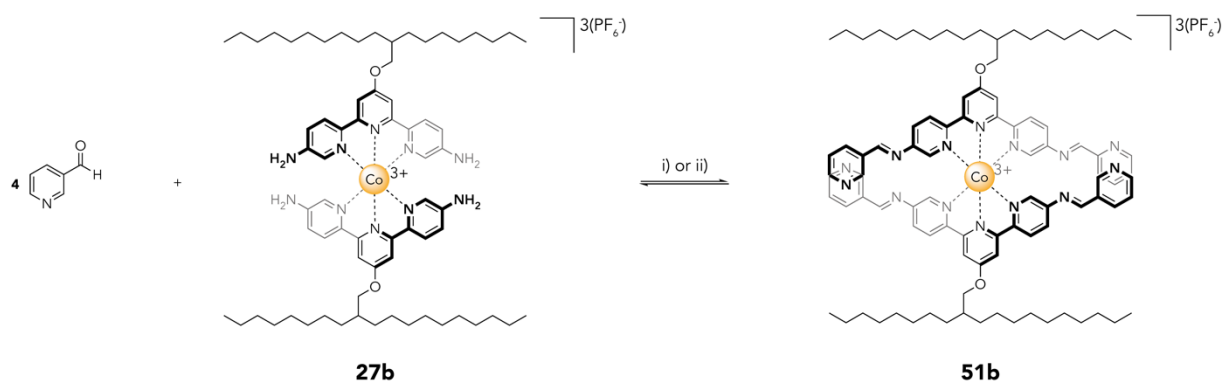
Scheme 25: Molecular structures and synthesis of *Schiff* base condensation on tpy complex **27b** leading to **51b**. i) TFA cat., H$_2$O, rt, 7 d; ii) TFA cat., CHCl$_3$, rt, 7 d.

Though, the desired compound **51b** was not formed using condition i). This can be explained by the hydrophobic nature of molecule **27b**, which makes it insoluble in water and therefore unavailable for the reaction. On the other hand, when the same

reaction was done in CHCl₃ the mono-, di-and the tri-condensate species could be detected by Di-ESI-MS (see figure 22). Unfortunately, compound **51b** could still not be detected, most probably due to the reverse reaction of the desired compound with the water formed in *situ*. Despite not having gained access to the four-fold substituted product, the results obtained with those test reactions were encouraging enough to extend them on the LB trough. Furthermore, the interlinking chemistry involved for this project is very dynamic and the conditions explored here do not rigorously represent the ones that can be found in a molecular film. Therefore, we decided to use the *Schiff* base condensation as polymerisation strategy for the heteroleptic bis(tpy) complexes **27**.
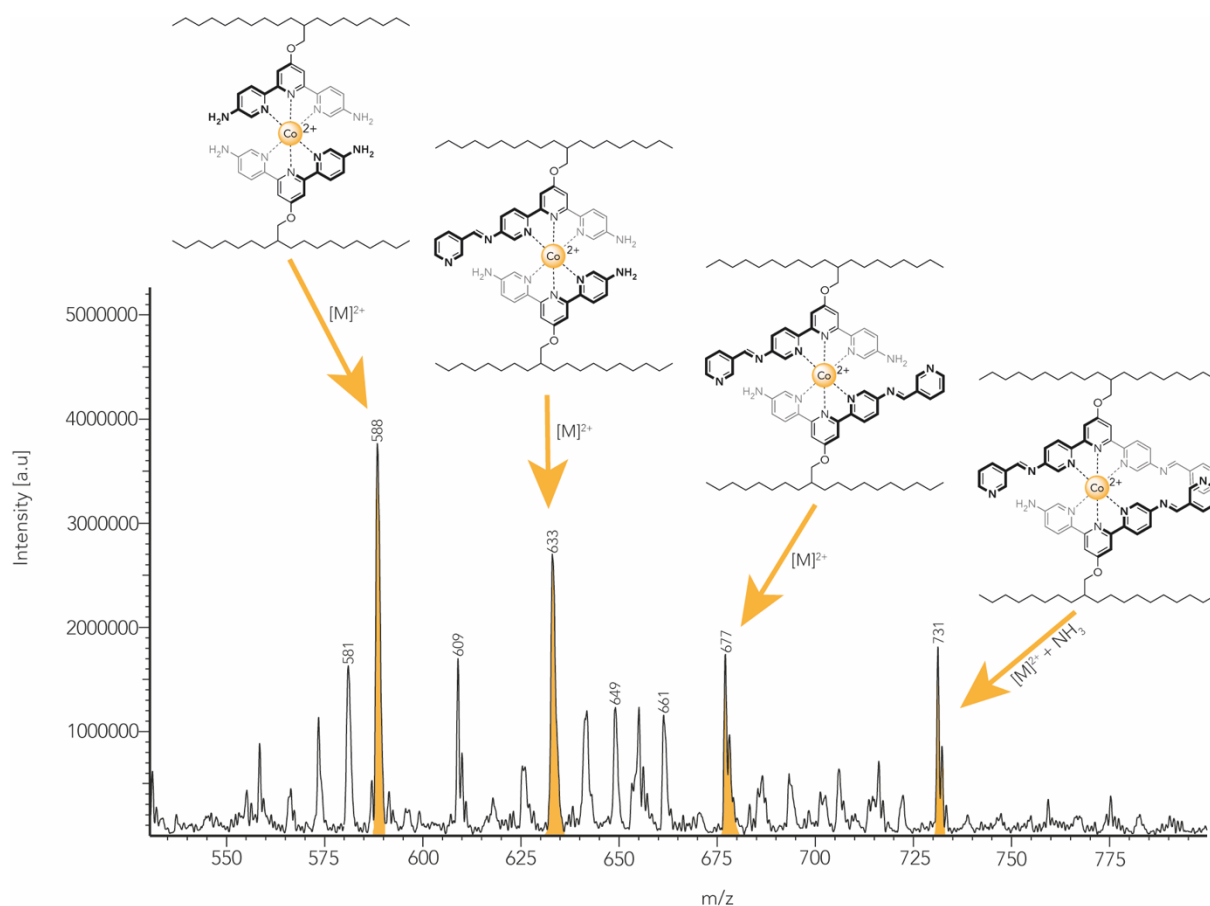
Figure 22: Molecular structures and Di-ESI-MS spectrum of the *Schiff* base condensation product obtained for molecule **27b** showing the mono-, di-, tricondensate species.

Schiff Base Condensation on Heteroleptic Complex **27**

This subchapter will focus on the *Schiff* base condensation between neighbouring complexes of **27**, which leads to the formation of a polymer as displayed in scheme 26.
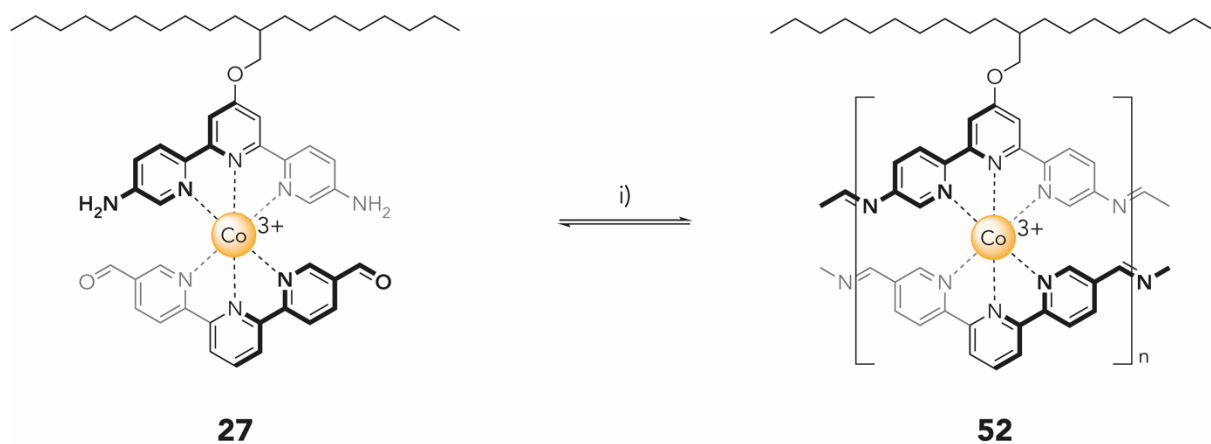
Scheme 26: Molecular structures and synthesis of *Schiff* base condensation on heteroleptic complex **27** leading to polymer **52**. i) 1,4-Dioxane, TFA-d cat., MeCN-d^3, rt, 100 h.
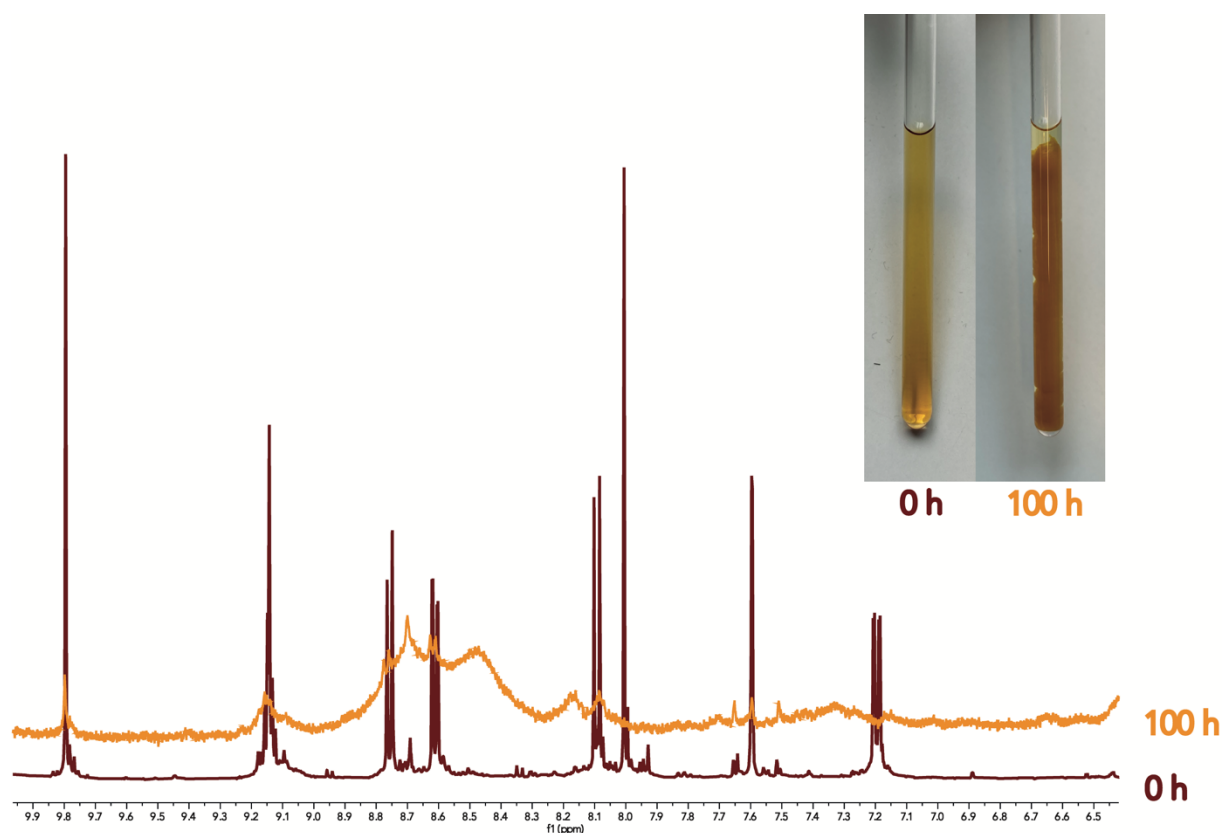
Figure 23: Comparison of the aromatic region ^{1}H-NMR spectrum and NMR tube of **27** at 0 h (highlighted in bordeaux red) and 100 h (highlighted in orange).

The polymerisation reaction of asymmetric complex **27** was performed in an NMR tube charged with 1,4-dioxane as internal standard, catalytic amounts of deuterated TFA (0.01%) and acetonitrile-d$_3$ at room temperature. The composition of the reaction mixture was analysed by ^{1}H-NMR spectroscopy every hour up to 4 h at the beginning and then every 4 h. Figure 23 illustrates the transformation of a well resolved ^{1}H-NMR spectrum of complex **27** (0 h, highlighted in bordeaux red) to a very broad one (100 h, highlighted in orange). Also, a solid was formed out of the clear solution of the NMR tube after 100 h. To our delight, the aldehyde peak located at 9.8 ppm can be used as control signal to follow the reaction, since the singlet is downfield shifted in a region where nothing else is present. In figure 24 one can observe the obviously decrease in intensity of the singlet arising from the aldehyde within 72 h (the full ^{1}H-NMR spectrum of the sample can be found in chapter 3, General Remarks, Polymerization of Complex **27**, figure 54).

Time [h]	Integral of aldehyde Signal of **27** relative to 1,4-dioxane	Normalize amount of aldehyde Signal of **27**
0	0.72	1.0000
1	0.58	0.8056
2	0.53	0.7361
3	0.47	0.6528
4	0.44	0.6111
8	0.37	0.5139
12	0.33	0.4583
16	0.29	0.4028
20	0.26	0.3611
24	0.19	0.2639
28	0.17	0.2361
32	0.17	0.2361
36	0.14	0.1944
40	0.11	0.1528
44	0.10	0.1389
48	0.10	0.1389
52	0.09	0.1250
56	0.09	0.1250
60	0.08	0.1111
64	0.07	0.0972
68	0.07	0.0972
72	0.05	0.0694
76	0.05	0.0694
80	0.04	0.0556
84	0.05	0.0694
88	0.04	0.0556
92	0.04	0.0556
96	0.04	0.0556
100	0.02	0.0278

Figure 24: Comparison of ^{1}H-NMR spectra of aldehyde signal of **27** within 72 h and ratio of aldehyde signal of heteroleptic complex **27** integral to that of 1,4-dioxane. Colours are highlighting the reaction time (red = 0 h; green = 24 h; turquoise = 48 h; blue = 72 h).

1,4-Dioxane was added as internal standard to determine the relative concentration of **27** as displayed in figure 24 (table). The table shows the ratio of the aldehyde signal of complex **27** integral to that of the internal standard. The rate of concentration in heteroleptic complex **27** decrease, can be best fitted with an exponential decay (see Chapter 3, Polymerization of Complex **27**, figure 53) suggesting a half-life for the reaction of $t_{1/2}$ = 12.5 h, i. e. when 50 % of the starting material **27** is polymerized. After 100 h the heteroleptic complex **27** was not detectable anymore in the Di- ESI- MS, confirming the observation made in ^{1}H-NMR. The solid formed was also analysed in the MS-devise, but no *m/z* signals could be assigned to the starting material or small oligomers. To gain more information about the molecular structure of the solid formed, IR spectroscopy was performed (figure 25).

In figure 25, the IR spectrum of heteroleptic complex **27** and the presumably formed polymer **52** were compared. The disappearing of the characteristic stretching band for the primary amine (N-H) at 3639 cm^{-1} and 3570 cm^{-1} and the carbonyl stretching band for the aldehyde (C=O) at 1625 cm^{-1}, confirms the transformation of the asymmetric complex **27**. Furthermore, one can observe the apparition of new vibration bands at 1700 and 1602 cm^{-1} that would fit with the characteristic imine bonds (-C=N-) stretching frequency.[178] By combining our preliminary tests outcome (Subchapter: Schiff Base Condensation as Polymerisation Strategy) and these results, we can conclude that the functional groups of **27** are not present anymore in the new species and that the chosen polymerisation strategy seems to be efficient.
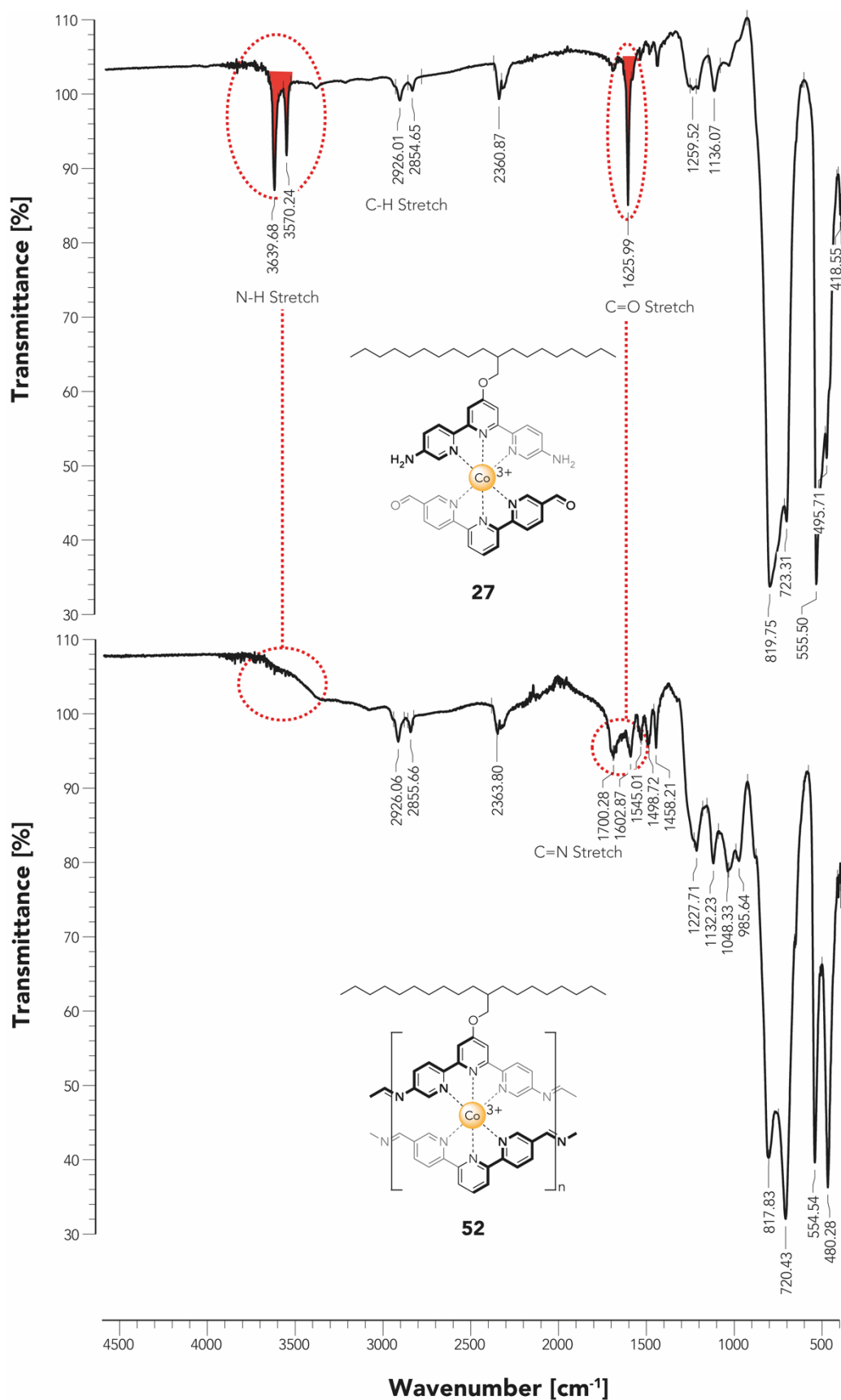
Figure 25: Comparison of molecular structure and IR spectra of complex **27** and the formed solid (presumably polymer **52**). Primary amine signal (N-H stretch) and aldehyde (C=O stretch) are highlighted with red dots.

Amphiphilic Behaviour at the Air/Water Interface of Heteroleptic Complexes

Amphiphilic molecules, also known as amphiphiles are compounds containing both hydrophilic (water-loving) and hydrophobic (water-hating) components. Lipids, fatty acids or phospholipids are all chemical compounds possessing a non-polar tail made of saturated or unsaturated hydrocarbon chains and a polar head made of non-ionic or ionic functional groups.[179] The presence of polar (polyoxyethylene, salts) and non-polar (hydrocarbon chains) components in one molecule gives it the remarkable property of self-assembly or a so called surface activity.[180] This property allows the pre-organisation of the amphiphiles at an air-water interface in such a way that the hydrophobic component (non-polar group, tail) is oriented to the air and the hydrophilic part (polar groups, head) interacts with the water. The investigation of such pre-organized and self-assembling systems on an interface is a very hot topic in the field of biochemistry, nanotechnology, material sciences or medicinal chemistry as reviewed in several reports.[179–182] The target heteroleptic complex developed for this work was designed in such a way, that it would self-assemble at an air-water interface thanks to a hydrophobic ligand **22** and the cationic property of the charged complex itself. A powerful tool for producing and deposit self-assembled monolayers (SAM)[183–185] or multilayers, is the LB trough. Through the LB trough, one can appreciate the surface activity of an amphiphile by compressing the molecules together and form a monolayer (2D) or a multilayer (3D) at an air/liquid or a liquid/liquid interface. This is achieved by controlling the changing surface tension of the medium in presence of the amphiphile. In a typical surface-pressure-area isotherm, the surface pressure (Π) is defined as the difference in interfacial tension between a clean interface (γ_0) and an interface with an amphiphile (γ) (equation 2).[186]

$$\Pi = \gamma_0 - \gamma$$

Equation 2: Surface pressure Π, where γ_0 is the surface tension of pure water and γ is the surface tension of the coated air-water interface.

During the compression of the amphiphilic molecules on the water surface, several transition phases were formed, similarly to the three most common phases of matter (solids, liquids, and gases). Figure 26 is illustrating a surface-pressure-area isotherm of a hypothetical organic amphiphile possessing a long aliphatic chain creating a monolayer. In the gaseous phase (G), the molecules are not organized on the surface, and they are not interacting with each other. During the compression phase the surface area is decreasing, and the molecules start to interact with each other and enter in the expanded or the so-called liquid phase (E). The transition between phase G and E is accompanied by a change in the isotherm plot. By compressing the molecules further, the condensed phase (C) may appear and the amphiphile is then perfectly arranged at the air/water interface.
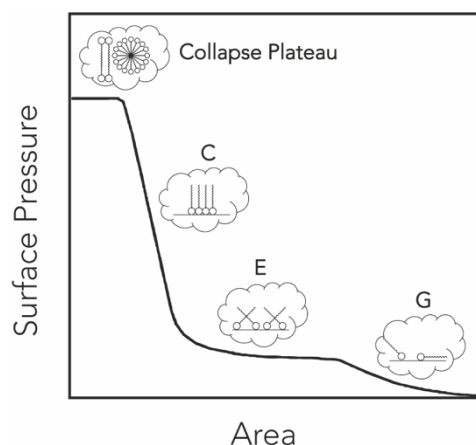
Figure 26: Surface-pressure-area isotherm of a hypothetical organic amphiphile possessing long aliphatic chains, showing all the possible phase transformations; C = Condensed Phase; E = Expanded or Liquid Phase; G = Gaseous Phase.

If the monolayer is compressed even further, the arrangement will then collapse and a collapse plateau will be formed, testifying for the creation of multilayers or micelles. The observation of the different phase transitions of a monolayer is depending on several parameters such us as the temperature of the interface, the compression speed, the resting time and the concentration of the spread sample.[187] In this subchapter we will explore the amphiphilic behaviour of the heteroleptic complexes

26, **27** and **30** synthesized, by investigating of their surface-pressure-area isotherm in a Kibron G1 LB microtrough on an air/water interface. Later, we will analyse and discuss about the different phase transitions observed and the data obtained.

Amphiphilic Behaviour at the Air/Water Interface of Complex **26**

As discussed earlier, Fe(II)-based heteroleptic complex **26** is immediately dissociating in its corresponding homoleptic complexes (**26a** and **26b**) and its concentration could therefore not be determined exactly. However, an impure sample of complex **26** was dissolved in a MeCN:CHCl$_3$ (1:10) mixture and was drop-casted on the water surface. To ensure the full evaporation of the solvent mixture used, every measurement was started after 15 min and a compression speed of 20 mm/min at 20 °C (water temperature) was used.
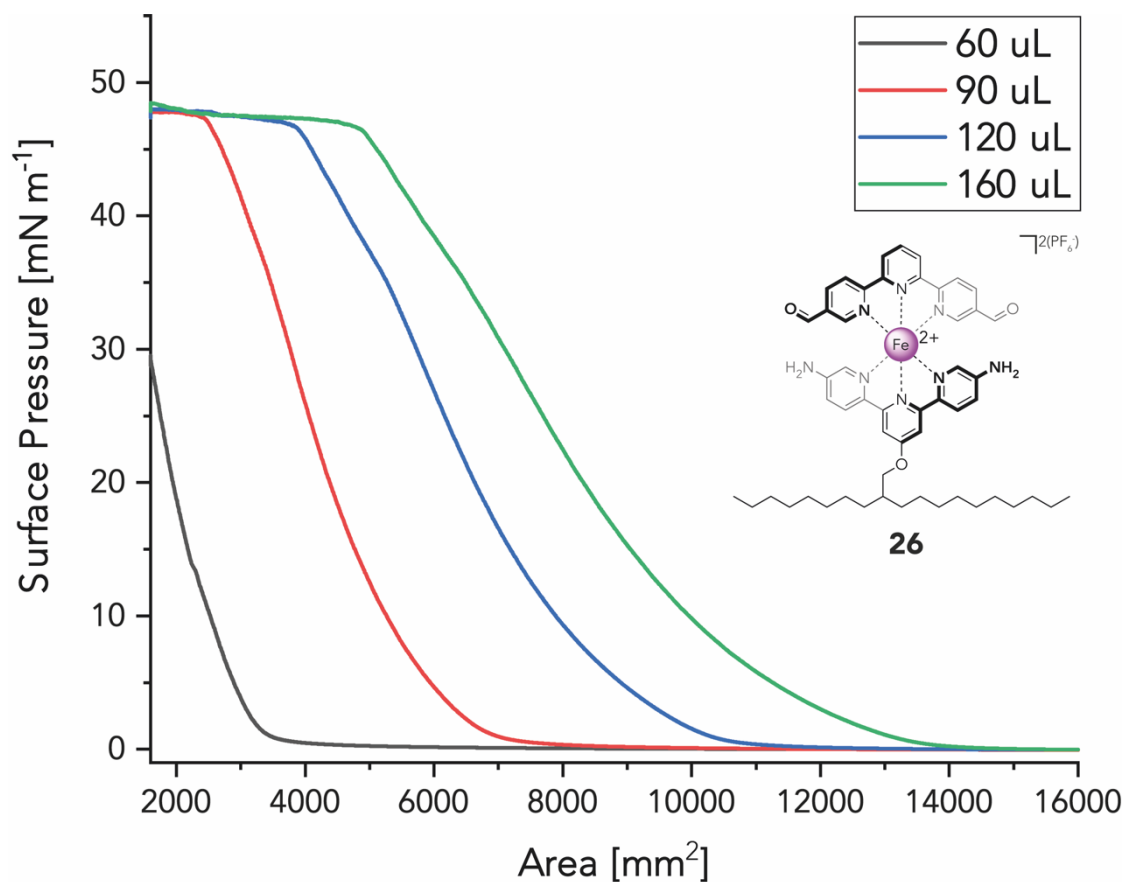
Figure 27: Molecular structure and comparison of the surface-pressure-area isotherm of an impure Fe(II)-based heteroleptic complex **26** sample using different amount of solution, highlighted in several colours.

As illustrated in figure 27, the asymmetric complex **26** is exhibiting a surface pressure confirming that the molecules are floating between the interfaces. The compression area is increasing along with the amount of solution spread, since a larger area is demanded by the presence of a higher quantity of matter. In these measurements, one can observe the phase transition G - E and from E to the collapse plateau at a surface pressure of 47 mN/m, hiding the breaking point of the C phase. Several parameters that can modulate the properties of the self-assembled structure such as the temperature of the subface, the compression speed, the resting time and the concentration[180] were changed in order to try and find the breaking point of the C phase, in vain.

Amphiphilic Behaviour at the Air/Water Interface of Complex **27**

The kinetically inert Co(III)-based heteroleptic complex **27** was dissolved in a MeCN/CHCl$_3$ (1:10) mixture to obtain a solution with a concentration of 0.00067 M and it was directly drop-casted on the water surface. After 15 min the solvents were considered evaporated and the surface area was compressed by a Teflon barrier at 20 mm/min, at 20 °C (water temperature) and the surface-pressure-area isotherm was recorded (Figure 28a).
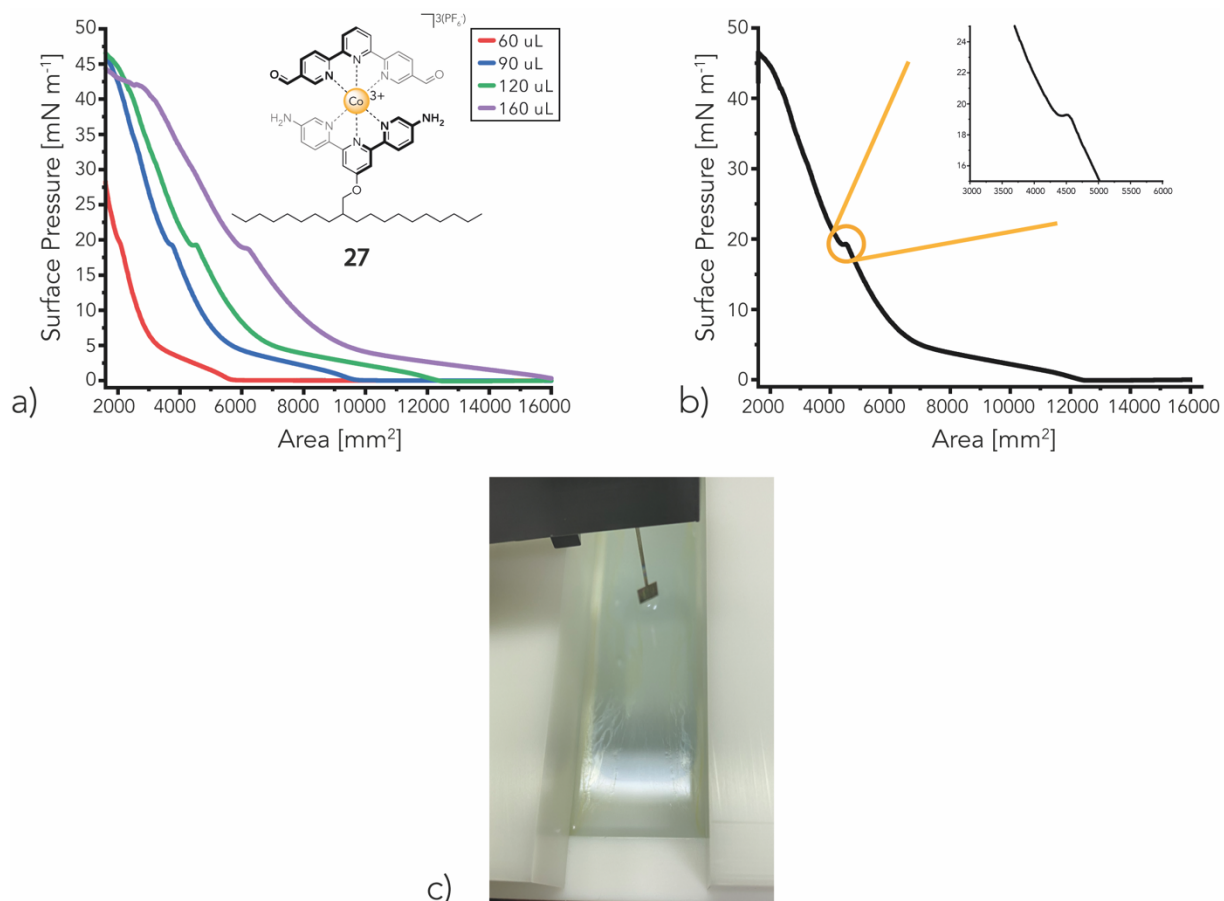
Figure 28: Molecular structure and comparison of the surface-pressure-area isotherm of a complex **27** sample. (a) Comparison of the surface-pressure-area isotherm with different amount of solution used, highlighted in several colours; (b) Single plot highlighting in orange the collapse point of the monolayer at a surface pressure of 19 mN/m. (c) Film formed at the interface when compressing the molecules over 19 mN/m.
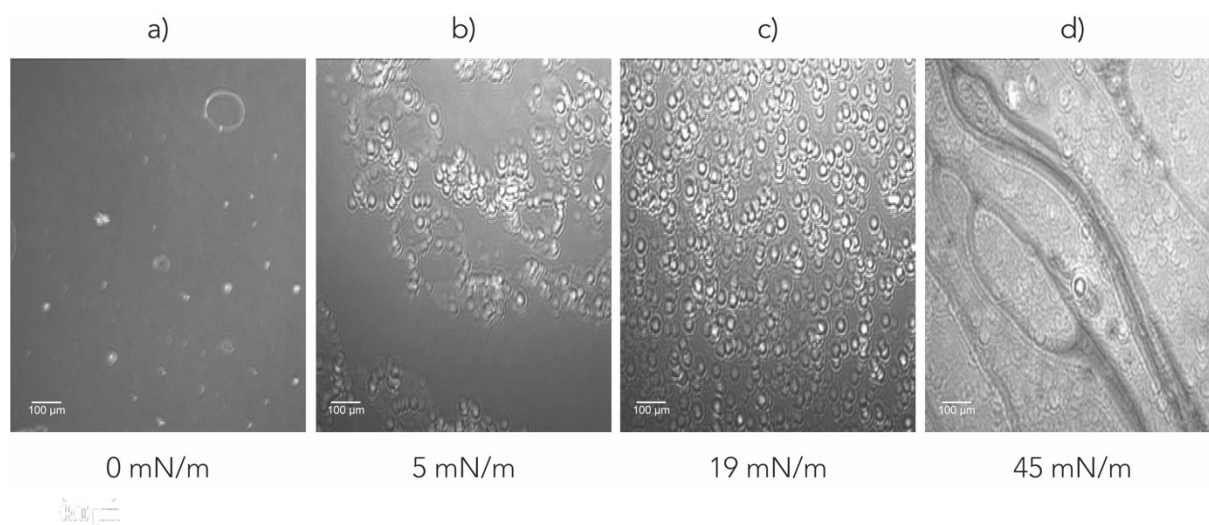
Figure 29: BAM images of the drop-casted heteroleptic complex **27** sample at different surface pressures: (a) at 0 mN/m; (b) at 5 mN/m; (c) at 19 mN/m; (d) at 45 mN/m.

76

As it is seen in figure 28a/b, when the area of the surface is compressed the surface pressure increases. To our delight, one can perfectly observe the different phase transitions (figure 28b) in this case. In the surface-pressure-area isotherm, one can also see the transformation of the G – E phase and the the E – C phase. At a surface pressure of 19 mN/m, one can clearly observe a step, indicating that a compact layer collapses. The further reduction of the surface area induces the breaking of the layer formed, and an overlapping occurs as the surface pressure is collapsed for a short period due to the formation of multilayers.
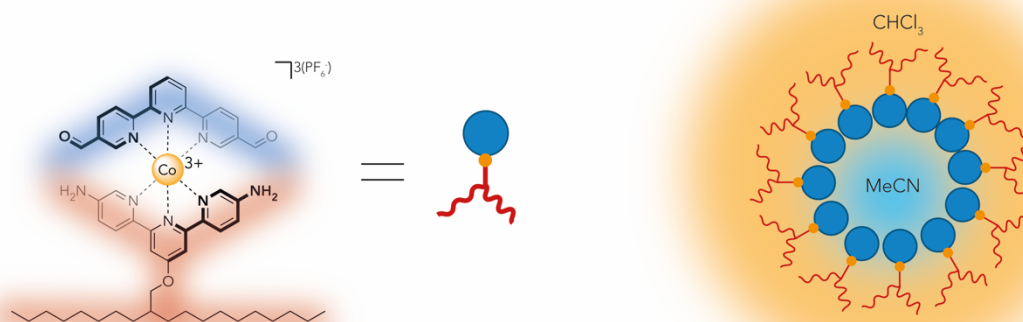
Figure 30: Chemical structure and hypothetical composition of the spherically shaped structures on the BAM, that could form some micelles. The drawing on the right side is illustrating the self-assembling of the amphiphile around the MeCN solvent. The size and the shape of the solvents is only qualitative for the illustration.

With these results, we were able to understand at which surface pressure the monolayer is builded-up and collapsed. Furthermore, the interface was monitored in real-time by Brewster angle microscopy (BAM) in order to investigate the phase transformations even deeper. Figure 29 displays the BAM images of the drop-casted solution of **27** at the air/water interface at different surface pressures on the LB trough. During the compression of the amphiphile spread, the complexes get closer to each other and form cluster like or spherical shaped aggregates (see figure 29b/c. It is not perfectly clear if a layer is formed under the aggregates detected even though the surface-pressure-area isotherm (Figure 28b) shows a breaking point at 19 mN/m

corresponding to a self-assembled compact layer. However, at a surface pressure of 45 mN/m, an amorphous film can be detected and thus confirms the presence of the amphiphilic heteroleptic complex **27** at the interface, as illustrated in figure 28c and 29d. From the BAM pictures obtained, one could assume that the spherically shaped structures are micelles, that can be formed during the dissolving process of the solid heterolpetic tpy complex **27**. As mentioned at the beginning of this subchapter, compound **27** was dissolved in a MeCN/CHCl$_3$ (1:10) mixture and therefore, one could hypothesize that the amphiphilic complex **27** is self-assembling around MeCN molecules by forcing the hydrophilic part to point towards the centre and arranging the hydrocarbon chains to the outside forming some micelles, as illustrated in figure 30. Therefore, the step observed at 19 mN/m (figure 28b) could be the breaking point of a monolayer created by micelles.

Amphiphilic Behaviour at the Air/Water Interface of Complex **30**

The Ru(II)-based heteroleptic complex **30** is the only compound with acetal protected aldehydes in the structure. Molecule **30** was dissolved in a MeCN/CHCl$_3$ (1:10) mixture to obtain a solution with a concentration of 0.00068 M and it was drop-casted to the water surface of the LB trough. To ensure the evaporation of the used solvent mixture, every measurement was started after 15 min using a compression speed of 20 mm/min at 20 °C (water temperature).

As one can see in figure 31 the surface-pressure-area isotherm looks very similar to the plot obtained for complex **26**. The transition phase G is transformed to the phase E and the collapsed phase (C) is not visible at all. The collapse plateau is formed in all the measurements at a surface pressure of 44 mN/m near the values of complex **26** and **27**. Moreover, for the experiments where 120 µL (blue line) and 160 µL (green line) were spread, a new phase transition seems to be generated.
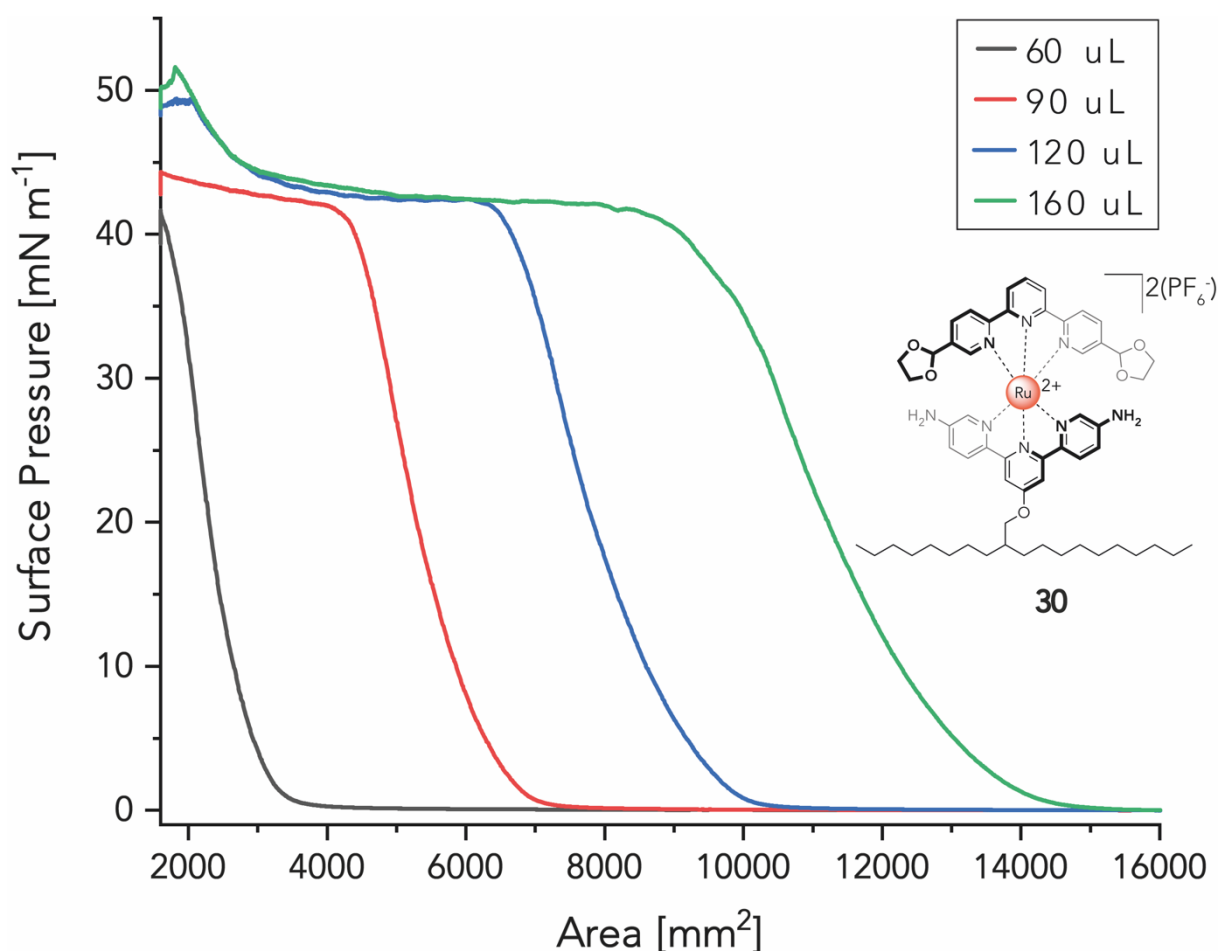
Figure 31: Molecular structure and comparison of the surface-pressure-area isotherm of Ru(II)-based heteroleptic complex **30** using different amount of solution, highlighted in several colours.

To summarize this subchapter, all the complexes synthesized (**26**, **27** and **30**) behaves as amphiphiles, since all of them could exhibit a surface pressure at an air/water interface. In the surface-pressure-area isotherm of compound **26** and **30**, the collapse of the monolayer was not visible. This can be explained by the coexistence of the liquid-expanded and liquid-condensed phases, where the transition phases are overlapping each other. As a result, the critical point (breaking point of the monolayer) is not easily accessible as described by Crane and collaborators.[188] In the case of complex **27**, the formation of a compact layer could be observed at a surface pressure of 19 mN/m, which indicated the self-assembling of a monolayer. The real-time observation via BAM, could only prove the amphiphilic behaviour of the designed compound **27** and not elucidate the formation of a monolayer. Furthermore,

spherically shaped aggregates (or not identified micelles) which could be formed during the dissolving process of **27** before the sample is drop casted on the air/water interface of the LB trough, could be observed via BAM. The step observed at 19 mN/m could be the breaking point of a monolayer made by micelles. However, this statement is still a hypothesis and should be confirmed by more experiments.

Contact Angle Measurements of Deposited Complex 27

The amphiphilic heteroleptic Co(III) complex **27** was deposited at a surface pressure of 18 mN/m on different support surfaces using the LB trough.
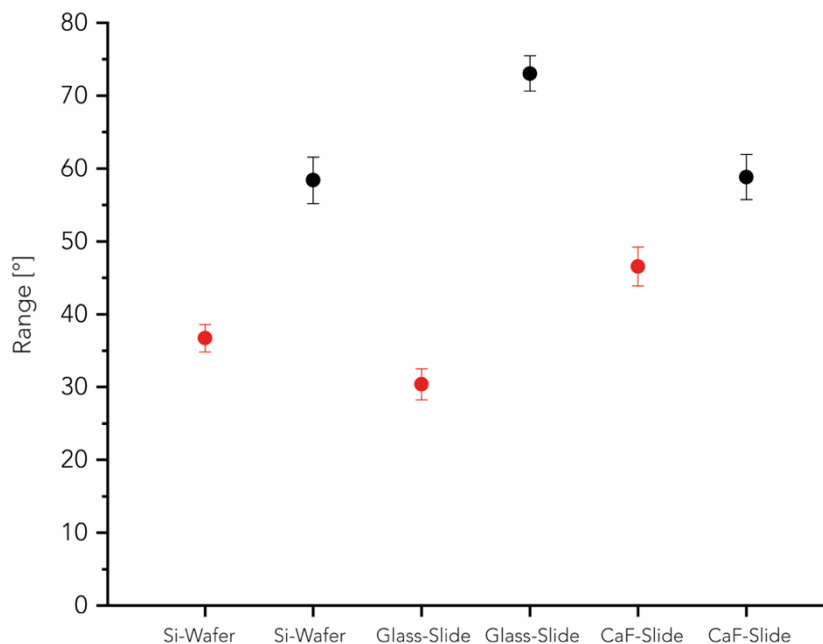
Figure 32: Contact angle measurements plotted on different support surfaces: Bare surface (red circle) and surface coated with **27** (black circle).

Figure 32 displays the average value of 6 measurements (see Chapter 3, General Remarks, Contact Angle Measurements, tables 4-6) including the standard deviation of different contact angle measurements made on several surface supports. The asymmetric complex **27** was deposited using the Y-type LB film deposition modes[189] for the hydrophilic surfaces (Si-Wafer and Glass-slide), and the X-type deposition

mode[189], for the hydrophobic surface support (CaF-Slide). The Y-type deposition is a head-to-head deposition method, where the hydrophilic substrate is raised through the subphase during the deposition and therefore placed in the water phase before the amphiphile is spread. The X-type deposition method is a head-to-tail deposition method, where the hydrophobic substrate is immersed through the subphase during the deposition. The contact angle of the bare Si-wafer (red circle) was 36.7 ± 2 ° and that of the film transferred on the Si-wafer (black-circle) was 58.4 ± 3 °. In the case of the bare glass-slide (red circle) the contact angle was 30.4 ± 2 ° and that of the coated glass-slide (black circle) was 73.1 ± 3 °. The contact angle for the hydrophobic bare CaF-slide (red circle) was 46.5 ± 2 ° and that of the treated CaF-slide (black circle) was 58.8 ± 3 °. It is clearly visible that the hydrophobicity of the coated Si-wafer and that of the glass-slide is increased, which is expected since the Y-type deposition is pre-ordering the aliphatic chain in the air. The treated CaF-slide shows an increased contact angle, which is surprising since the X-type deposition should arrange the amphiphile aliphatic chain in pointing towards the support surface. One explanation for this could be that the amphiphile overturns under water, which leads to arranging of the hydrophilic tail to the air interface, as described by Honig[190]. A second hypothesis could be the creation of a double layer where the polar heads are interacting with each other, and the hydrophobic tails are looking towards the air. A third hypothesis would be the self-assembly of circularly shaped micelles, where all the hydrophobic components of the amphiphile are pointing to the outwards and the hydrophilic moieties are pointing towards the centre of the micelles. This hypothesis would support the results observed in the BAM, discussed in the previous subchapter (Amphiphilic Behaviour at the Air/Water Interface of Complex 27).

X-Ray Photoelectron Spectroscopy (XPS) of Deposited Complex **27**

To study the films, and particularly, to see if the deposition process is working, XPS experiments were carried out. To do so, the heteroleptic Co(III) complex **27** was

transferred from the air/water interface onto a Si-wafer. Figure 33 compares the XPS survey spectra of a bare Si-wafer (red line) and that of the film coated Si-wafer (black line).
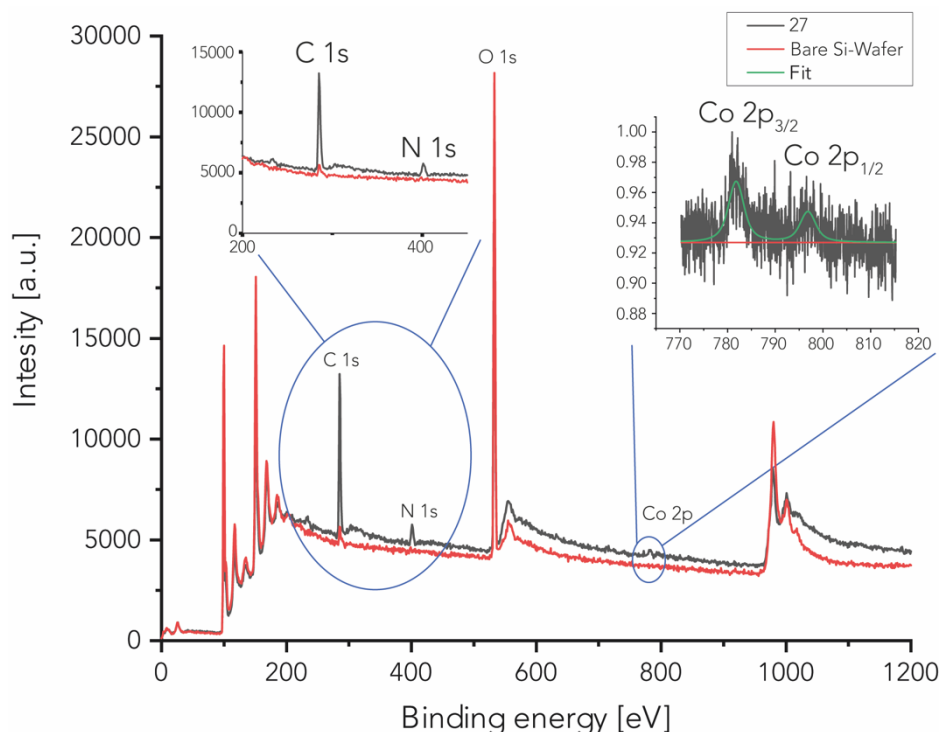
Figure 33: Comparison of XPS survey spectra of **27** on Si-wafer (black line) and bare Si-wafer (red line), highlighting in blue the binding energies of C 1s, N 1s and Co 2p.

The characteristic Co $2p_{3/2}$ and Co $2p_{1/2}$ binding energies at 781 eV and at 796 eV are displayed in the core level spectrum. The split of 15 eV observed is comparable with the literature values given for Co(III) species.[191–194] Moreover, one can spot the binding energies of the more common elements O 1s at 532 eV, N 1s at 401 eV and C 1s at 285 eV. All elements involved in the molecular structure of the species could be detected on the Si-wafer surface by XPS, thus confirming the successful transfer of the film. Motivated by these promising results, we polymerized heteroleptic complex **27** on the LB trough and transferred the film formed on a Si-wafer to characterize the film by XPS experiment. The XPS survey appeared quite similar (see Figure 34) to the one obtained initially. The binding energies of Co 2p are not changing (Co $2p_{3/2}$ = 781 eV and Co $2p_{1/2}$ = 796 eV), the N 1s has a binding energy of 400 eV, which is shifted by

1 eV and the binding energy of C 1s (285 eV) is also not significantly shifted. The XPS studies could not unequivocally prove that the monomer polymerizes to give a 2D polymer, since the binding energies measured are quite similar. However, Dash investigated several *Schiff* base dioxime ligands complexed with Co(II) and Co(III) and reported comparable binding energies for the imine (399 - 401 eV).[195]
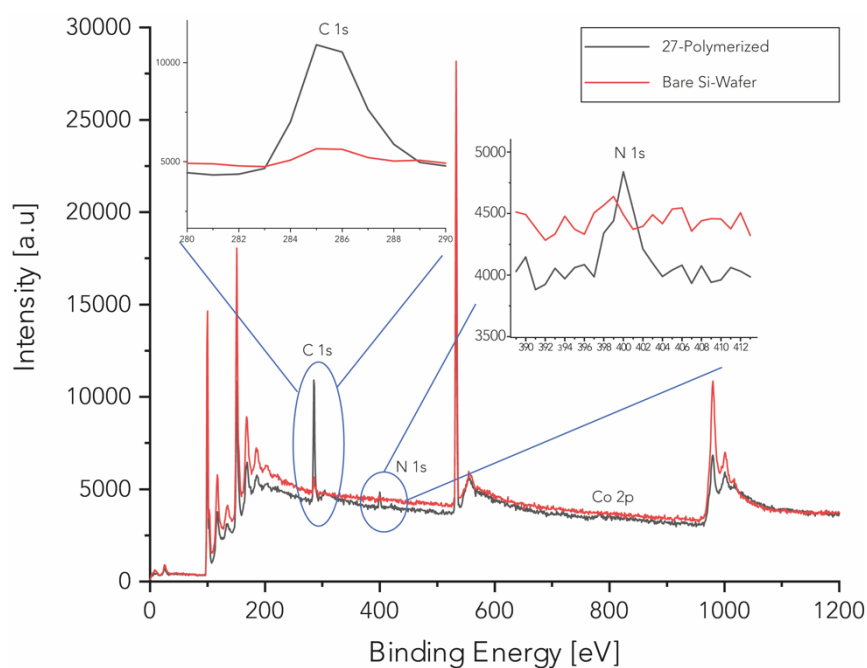
Figure 34: Comparison of XPS survey spectra of interfacial polymerized and deposited film of **27** on Si-wafer (black line) and bare Si-wafer (red line), highlighting in blue the binding energies of C 1s, N 1s.

Atomic Force Microscopy (AFM) of Deposited Complex **27**

Preliminary non-contact AFM (nc-AFM) measurements were performed to elucidate the molecular orientation and the thickness of the films transferred on the different support surfaces. The question of whether or not the film is a monolayer is fundamental for this project, as the main goal is to produce a planar 2D molecular textile. The height of the monolayer was estimated to be 2.23 nm, by taking the distance between C4' of the "hydrophilic" ligand and the last carbon atom of the aliphatic chain of complex **27** structure optimized by DFT calculations at the ωB97X-D/6-31G level of theory. The AFM height analysis was carried out after transferring

the interfacial polymerized heteroleptic complex **27** using the LB method onto different support surfaces.
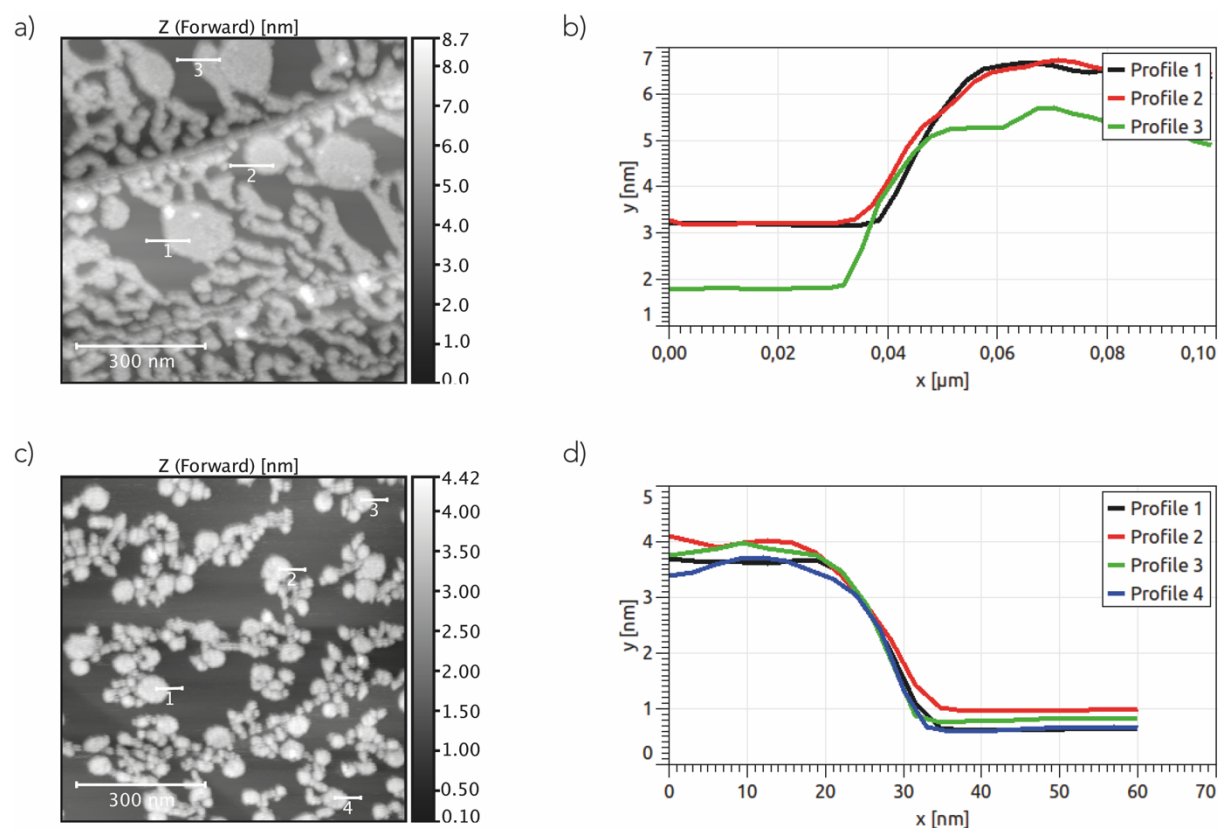
Figure 35: nc-AFM images of transferred polymerized complex **27** transferred on HOPG support surface at RT (a) and annealed at 100 °C (c). Height curves recorded at different locations on the HOPG surface at RT (b) and annealed at 100 °C (d).

Figure 35a is displaying the topography nc-AFM image of complex **27** deposited on a highly oriented pyrolytic graphite (HOPG) surface, at room temperature under ultra-high vacuum (UHV) conditions after 12 h. One can recognise some interconnected circle-like molecular islands, which could be an indication for the successful polymerisation between monomers in the form of elongated molecular aggregates. Moreover, one can clearly see the HOPG step edges which separates large terraces. The molecular islands probed have the same thickness, as one can see in figure 35b, indicating that the same material is observed. The annealing of the sample helps to purify the surface and to rearrange the molecular orientation of the film. In the case

84

of the annealed sample, the interconnected molecular islands seem to become more spherical and compact, like micelles (see Figure 35c). Furthermore, the thickness of the aggregates (~3.2 nm) is not significantly changing. These results are confirming the stability over the anneallation process, since the film height is not affected. Additionally, the height obtained is around 1.0 nm higher than the estimated monolayer height (2.23 nm). This is indicating that the spherically shaped aggregates are too high to be monolayers. Intrigued by these results and the data obtained for the contact angle and the XPS measurements, we decided to transfer the polymerized film onto a Si-wafer and examinate its surface by nc-AFM (see Figure 36 and 37).
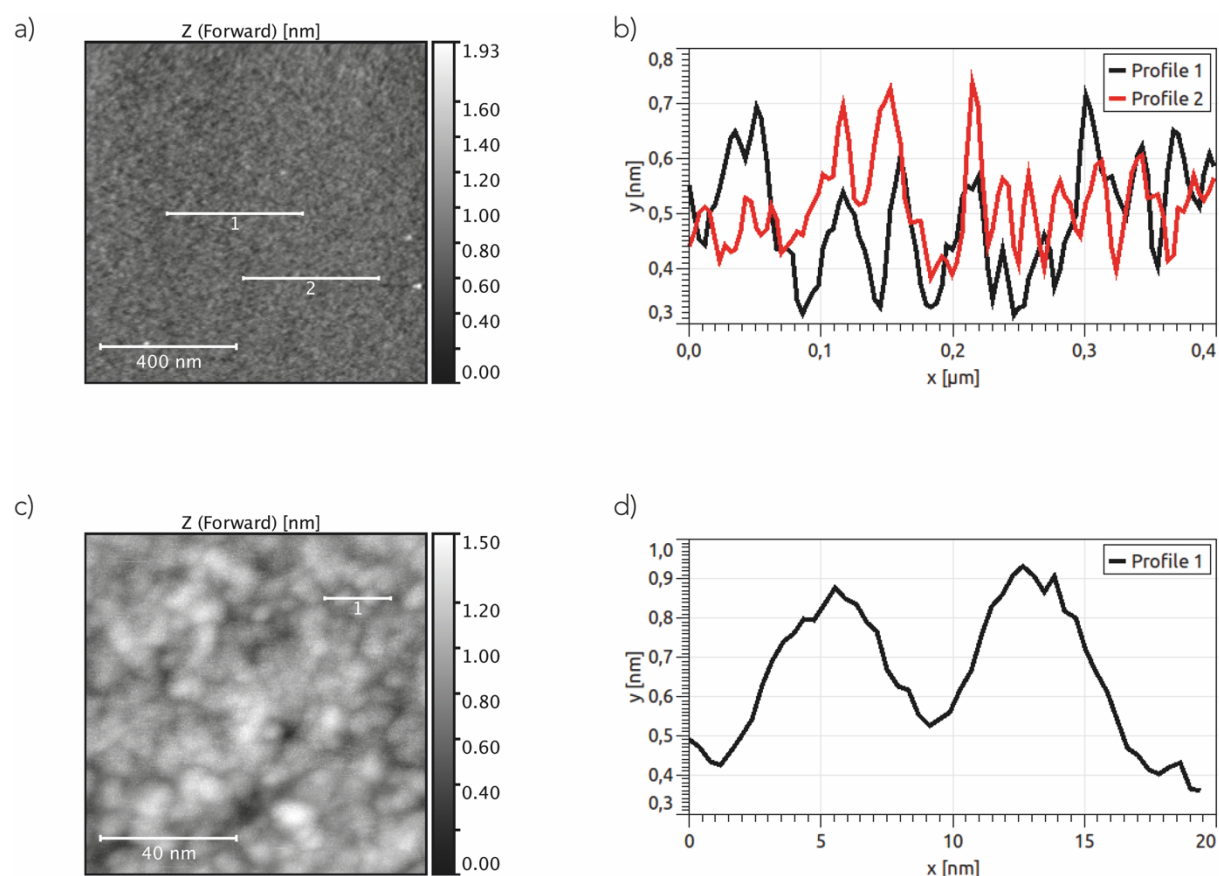
Figure 36: nc-AFM images of the polymerized complex **27** transferred on Si-wafer support surface at RT and height curves. (a) Large scale nc-AFM topography.; (b) Height curves recorded at different locations of large scale nc-AFM topograpghy.; (c) Zoomed nc-AFM topography.; (d) Height curve of recorded zoom nc-AFM topography.

The large scale nc-AFM topography image of interfacial polymerized **27**, seems to be very homogeneous and without any formation of higher molecular islands or defects on the surface (See Figure 36a). The molecular packing of the film is tighter and the circle-like structures are closer to each other as one can see in the zoomed image (Figure 36c). The profile of the sample indicates that the surface is nearly flat, since the height variation is small (~0.4 nm), but the corrugation is very high (Figure 36b and 36d). Figure 37 shows the nc-AFM topography image of the same sample annealed at 200 °C for 1 h. Compared to the non-annealed surface, the annealed film is not significantly changed (see figure 37a) and the height profile is confirming the planarity of the film (see figure 37c). Sadly, the internal structure of the compressed film could not be resolved with enough resolution. However, the fact that the surface was unaffected by annealing indicates that a stable assembly is formed, as the high temperature would have impacted the distribution of the molecules or would have cleaned them out of the support surface.
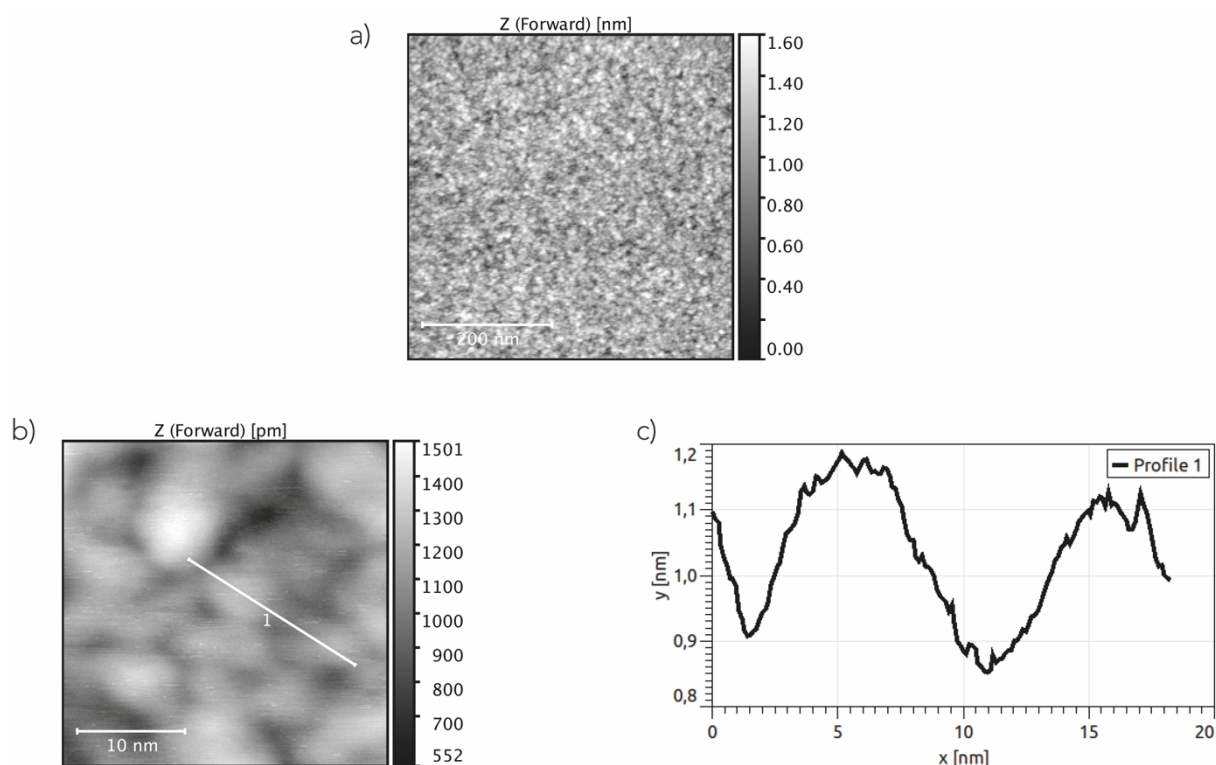
Figure 37: nc-AFM images of the polymerized complex **27** transferred on Si-wafer support surface after anneallation at 200 °C for 1 h and height curve. (a) Large scale nc-AFM topography.; (b) Zoomed nc-AFM topography.; (c) Height curve of recorded zoom topography.

These preliminary results are confirming that on the hydrophobic support surface more spherically shaped aggregates were observed, which is supporting our hypothesis about the formation of stable micelles during the dissolving process of compound **27**. The height of the formed aggregates is around 3.2 nm, which is a higher value than the calculated height of the heterloptic complex **27** (2.23 nm), indicating that the formed aggregates are not islands of the desired monolayer. Since the circle-like aggregates seems to be very stable after the annellation process, one could imagine that the polymerisation reaction takes place on the prea-arranged micelle, forming a stable interwoven circle shaped supramolecule. It is important to mention, that the length and the height of the observed spherically shaped structures on the AFM pictures are not corresponding to a sphere. One reason of this mismatch could be explained by the deforming process of the spherical micelle to a more ellipsoidal structure or the collapse of the circle-like structure. In the case of the hydrophilic Si-wafer, one could observe a planar and regular surface with high corrugation, as expected for a 2D molecular textile. However, even though the polymerisation of the monomers into a network is not fully confirmed or proved yet, the AFM images obtained are pointing towards the formation of very stable aggregates (HOPG surface) or films (Si-Wafer), since no significant changes were observed after high temperature anneallation. Furthermore, the interlinked elongated structures of the film transferred onto HOPG is also suggesting a covalently bonded species, indicating the formation of a network.

Conclusion and Outlook

In this work, three different "hydrophilic" and one hydrophobic tpy based ligands were successfully synthesized and characterized. We showed that these compounds are suitable for the preparation of an amphiphilic kinetically stable heteroleptic tpy complex for the self-assembly of a 2D molecular textile, and were engaged in further polymerisation reactions. The most suitable ligands **4** and **22**, were successfully combined in a heteroleptic complex with three different transition metals. Their stability over degradation to the homoleptic species was investigated and their amphiphilic behaviour was studied at an air/water interface on the LB trough.

Heteroleptic tpy complex **27** was the most promising candidate for the realisation of the desired 2D interwoven fibre, since the Co(III)-based asymmetric complex was proven to be kinetically inert over weeks thanks to ^{1}H-NMR, 18C reversed phase HPLC and MS-analysis. Furthermore, the acid-catalysed *Schiff* base condensation as interlinking strategy was investigated by ^{1}H-NMR and FT-IR spectroscopy. The formation of a polymer was notably characterized by the disappearing of the precursor stretching bands (amine and aldehyde) and the appearing of new target stretching bands (imine).

The amphiphilic behaviour of **27** was then investigated at an air/water interface using the LB tool and a very promising step was observed at 19 mN/m, indicating for the creation of a compact layer. The interfacial activity of complex **27** was investigated with a BAM and spherical aggregates were observed at all surface pressures, indicating the spontaneous formation of micelles during the preparation of the sample. We were able to transfer the compressed film onto different surface supports, and an increase in the surface hydrophobicity could be observed via contact angle measurements. The hypothesis about the formation of self-assembled micelles was supported with the contact angle results obtained for the samples deposited on the hydrophobic substrate, since an increase in hydrophobicity was observed. The

transferred film was characterized by XPS, which allowed to confirm the presence of the expected elements on polymerized and non-polymerized support slides.

Preliminary nc-AFM topography images were performed to elucidate the molecular orientation and the thickness of the films transferred onto the different support surfaces. In the case of the HOPG support surface, elongated molecular aggregates could be observed adopting a circle-like shape. The height of the formed aggregates is around 3.2 nm, which is a higher value than the calculated height of the heterloptic complex **27** (2.23 nm). Moreover, the spherically shaped molecular assembly seem to be temperature stable. This is indicating the presence of covalently bonded species that could potentially be resembling an interwoven sphere. However, the length and the height of the observed spherically shaped structures on the AFM pictures are not corresponding to a spherically micelle. On the other hand, nc-AFM topography images of the interfacial polymerized film, transferred on a Si-wafer, showed a completely different surface. The spherically shaped aggregates are smaller and closer packed to each other on the Si-wafer, indicating that a totally different transfer process from the LB trough to the substrate is involved. The fully covered surface appeared homogeneous with high corrugation as expected for a 2D polymer. However, the solid-phase characterisation of the film is still not entirely confirming the presence of a monolayer and at that point, high-resolution images are required.

These results, combined to the contact angle measurements and the BAM investigation, lead to the conclusion that the deposition on a hydrophobic support surface is more challenging than expected, as the polymerized molecules are organizing in spherically shaped aggregates like micelles, instead of a regular and planar film. To avoid the formation of micelles during the preparation of the sample, a third solvent such as THF could be used, to prevent the self-assembling around a MeCN molecule(s). However, the preparation of interwoven micelles would be very interesting and the results obtained should be further investigated to confirm the proposed supermolecule. The deposition onto hydrophilic support surfaces seems to

be more suitable and preliminary nc-AFM images are indicating the presence of a homogeneous film. Nevertheless, it is important to mention, that the presented results should be further investigated, as many questions regarding the orientation, the thickness and the packing of the solid phase remain to be answered.

The investigation of thin monolayer films (1-3 nm), and in particular the ones obtained from an air/water interface self-assembly, remains very challenging, infrastructure dependent and time consuming. There is not yet an established process to follow for the investigation and characterisation of such films, which would significantly help in the progress of this fascinating research field of 2D interwoven materials. The fundaments of this particularly challenging characterisation task should be guided by a specialised analytical team with the right infrastructure. This would definitely accelerate and qualitatively improve the outcome of such a challenging and exciting project.

For the outlook of this project, different spectroscopic techniques would be required to confirm and elucidate the molecular structure of the desired films. To study the formation and the size of the molecular textile at the air/water interface in real-time, high-resolution BAM could be applied. With the help of a spectroscopic ellipsometry, one could also determine the surface roughness or thickness, as well as investigate the optical properties of the film. Other powerful tools for the investigation of the film surface structure include the scanning electron microscopy (SEM) or the transmission electron microscopy (TEM), which could reveal the regular lateral patterns in the sample in combination with the detection of electrons diffraction pattern. With the help of scanning tunnelling microscopy (STM) and AFM in combination with tip-enhanced Raman spectroscopy (TERS), one could obtain high resolution images and have a hold on a sensitive spectroscopic analysis of the 1-3 nm thin film.

Any other spectroscopic tools combining sensitive spectroscopic analysis such as ellipsometry and UV-Vis coupled with high resolution microscopes (AFM or STM) would also be of particular interest.

Furthermore, the chemical reduction of the reversible imine bonds to amines on the LB trough or on the support surface would further stabilize the 2D molecular textile. Moreover, the demetallation process of the interlinked molecular fibre, which is still very troublesome, should be investigated. Chemically, this could be achieved by reducing first Co(III) to Co(II) and then protonating the tpys, or by introducing ligands with higher affinity with metallic ions such as potassium cyanide. Electrochemistry could also be considered as a powerful and reliable tool for reducing the (strongly binding) Co(III) moieties. The successfully synthesized and characterized tpy ligand **10** would also be a suitable ligand for the creation of a 2D molecular textile. Indeed, since the ligand is elongated by one benzyl per branch and the unit cell would only have a bigger cavity in the unit cell (see figure 38b). This comparative element would be of particular interest for the investigation of mechanical properties. This include for example the measurement of the 2D material's elasticity by Youngs`s modulus, or its for filtering ability as suggested recently by Leigh and collaborators.[196]
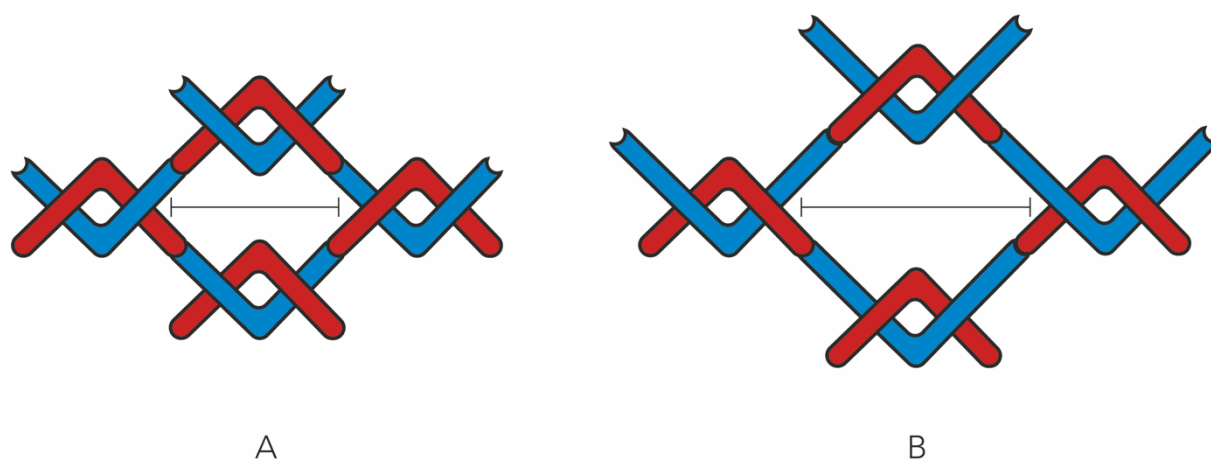
Figure 38: Comparison of unit cell cavity. (a) Using ligands of equal length.; (b) Using ligands of unequal length.

Chapter 2

Photolabile Ruthenium(II) Polypyridyl Complexes as Charge Carrier for Biomolecules in the Gas-Phase
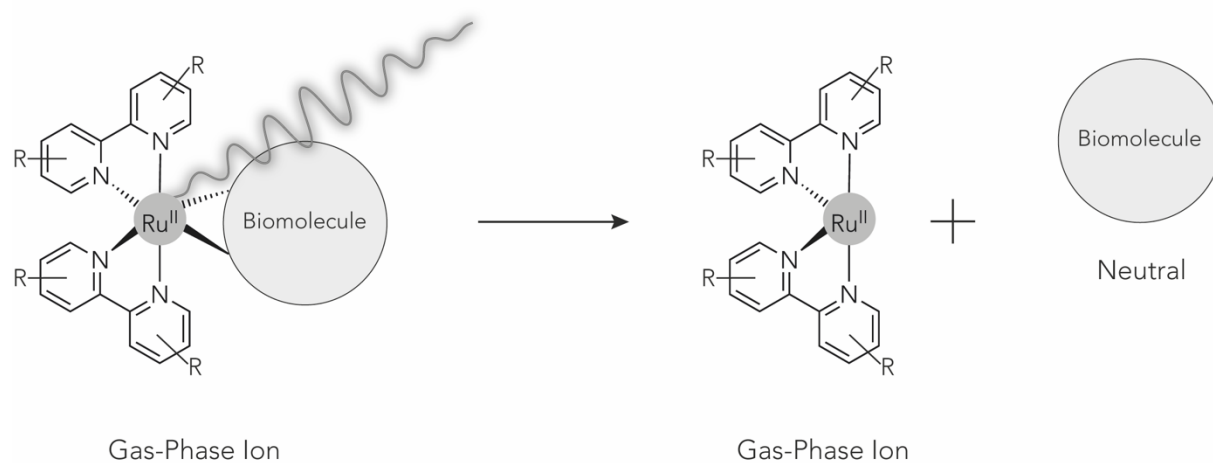
Introduction

Biomolecules in the Gas-Phase

Electrospray ionization (ESI)[197] and matrix-assisted laser desorption ionization (MALDI)[198,199] are two established techniques, which are used to transfer charged macromolecules into the gas phase for mass spectrometry. Both techniques are known for their very gentle and soft ionisation process, since usually no fragmentation of the analyte is observed.[200] In a very simplified way , in ESI the biomolecules are dissolved in solution and are ionized through an electric field, creating a continuous beam of multiply charged biomolecules after passing a small capillary.[201] In the case of MALDI, the analyte is mixed with a matrix, that can absorb the laser light before transferring the macromolecules into the gas-phase, preventing the degradation of target molecules and forming mostly singly charged species.[200] Both mentioned ionization techniques revolutionized the characterisation and the investigation of heavy biomolecules in the gas-phase.

The volatilization of peptides, proteins or other biological composites are not only interesting for the determination of the molecular-weight, but also to get information about the sequence[202] or for mapping extracellular matrix proteins[203]. Furthermore, the study of such molecules which are predominantly found in an aqueous environment will additionally elucidate our knowledge about their structural properties. The study of neutral biomolecular beams would be desirable, as perturbation generated by charge effects could be excluded. The investigation of neutral bio composites would be very interesting for physicochemical characteristics such as the measurements of molecular electronic properties[204], the optical and magnetic properties[205,206]. Furthermore, infrared absorption spectra could be measured under controlled and non-interacting conditions.[207] However, the

preparation or the control of specifically charged or neutral biomolecular beams remains very challenging, and the development of further techniques is required.[208]

Applications of Photocages in the Gas-Phase

Photocleavable groups, also known as photocages allow excellent spatio-temporal control in the release of complex biomolecules via photo irradiation. Furthermore, the utilisation of photocages is currently investigated for several applications in photoactivated drug delivery and photochemotherapy.[209] A well designed photocage needs to fulfil several criteria for its efficient application in biological systems, as reported by Adams and Tsien: i) The photocages should mask and deactivate the active side of the biomolecule; ii) the photo-induced release of the coupled compound is expected to be quantitative and fast; iii) the photoproducts should not interact or interfere with the released species.[210]

The spatio-temporal control over the release of complex biomolecules could be an advantage for controlling the charge state of a biomolecule in the gas phase.

Debiossac and collaborators reported about the efficient photo-induced cleavage of nitroaryl based photocleavable tags (PCTs) attached to polypeptides in the gas-phase.[211] As illustrated in scheme 27, the formation of two possible photoproducts could be observed after the irradiation at 266 nm: i) the heterolysis and ii) H-transfer. The authors observed that the small peptides can undergo heterolytic photocleavage under charge transfer and that longer peptides follows a dissociation path involving a H-transfer, without leaving an additional charge on the cleaved peptide chain. Additional charge decoration of the leaving groups (LG) by Schätti and co-workers enabled the charge reduction and even neutralization of human insulin in high vacuum via photocleavage of nitroaryl-based PCTs.[212] A drawback of the nitroaryl-based PCTs is their absorption area, which overlaps with the absorption of aromatic amino acid side chains such as phenyalanine, tyrosine or tryptophan absorbing between 255 – 280 nm[213]. It is important to mention, that the charge decoration of a

biomolecular composite is not only interesting for the mentioned purpose, but it can be used as volatilisation method in mass spectrometry, which enables the detection of not ionizable compounds.
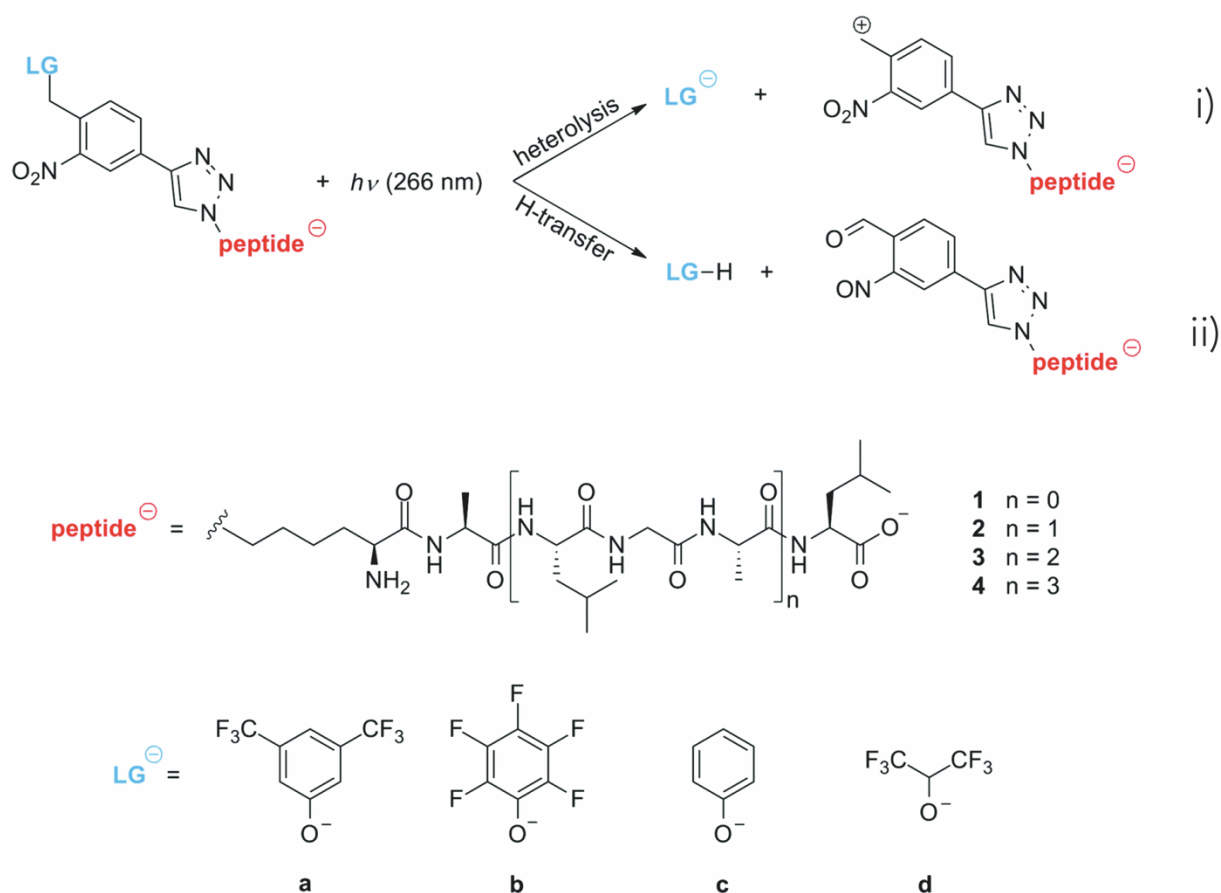
Scheme 27: Reaction scheme of nitroaryl-based photocleavable tags (PCTs) for oligopeptides reported by Debiossac and collaborators. The structures can either undergo heterolytic cleavage (i) or dissociation with simultaneous H-transfer (ii). Adapted from ref [211] with permission from the Royal Society of Chemistry.

Photolabile Ru(II)-based polypyridyl complexes are attractive candidates for the photo-induced manipulation of biopolymers in the gas-phase, since they have been successfully developed as photocages in solution.[209] Their MLCT band can be tuned to lower absorptions energies for ligand dissociation and advantageously, additional charge decoration of the complexes is not required since the Ru(II) complexes are already charged.

The reader of this thesis will find in the next subchapters an introduction about $[Ru(bpy)_3]^{2+}$ complex and why photolabile Ru(II)-polypyridyl complexes are suitable candidates for the photo-induced spatio-temporal controlled release of biomolecules in the gas-phase.

$[Ru(bpy)_3]^{2+}$ Complex

In 1936, the first article presenting the synthesis and some optical properties of $[Ru(bpy)_3]^{2+}$ was published by Francis Burstall.[214] It was noted that the prepared Ru(II)-based complex is significantly more stable than the Fe(II) and Ni(II) analogues and that two enantiomers were formed, the Δ- and Λ-enantiomers, as illustrated in figure 39.
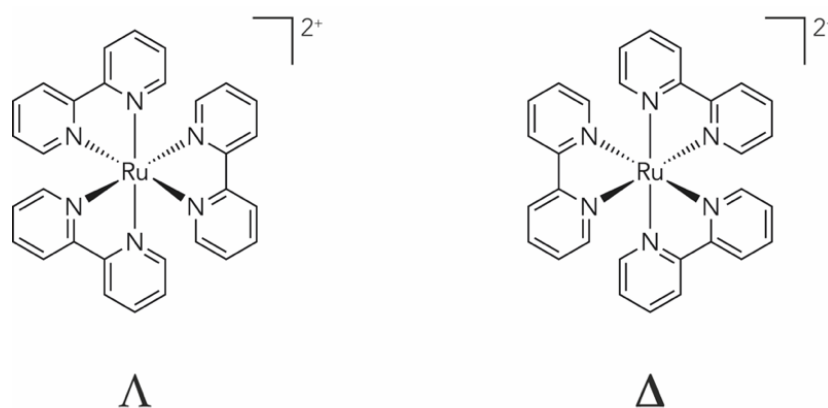
Figure 39: Molecular structure of $[Ru(bpy)]^{2+}$ Δ- and Λ-enantiomers.

The luminescence of $[Ru(bpy)_3]^{2+}$, which results from a charge transfer within the complex, was reported around 20 years later by Paris and Brandt.[215]

$[Ru(bpy)_3]^{2+}$ has become a model compound for scientist who were attracted by several properties, such as the chemical stability, the redox properties, the excited-state reactivity, the excited-state lifetime or the luminescence emission.[216–220] The overall knowledge about this fascinating compound was used as comparative element for the variety of Ru(II) polypyridyl complexes that have been investigated in the last decades.[219,220]

The absorption spectrum of $[Ru(bpy)_3]^{2+}(PF_6^-)_2$ is shown in figure 40.
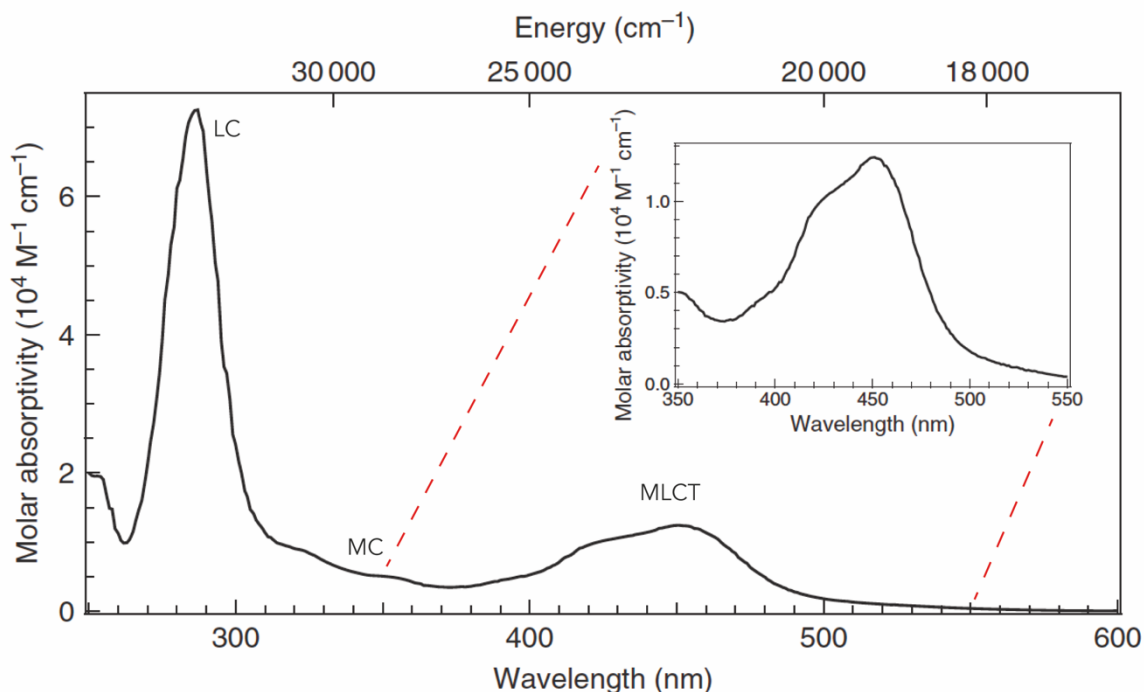
Figure 40: The absorption spectrum of $[Ru(bpy)_3]^{2+}(PF_6^-)_2$ in MeCN at RT. The inset shows the MLCT band. Adapted from ref. [216] with permission from Springer Nature.

The dominant absorption band at 285 nm corresponds to a spin-allowed LC π-π* transition located on the bpys, which has been assigned by comparison with the absorption spectrum of the protonated bpy ligand.[221] The intense band at 450 nm can be assigned to the spin allowed MLCT d-π* transition.[216]

The shoulders at 322 and 344 nm are attributed to the MC transitions, also known as ligand field (LF) or d-d transition, which involves the displacement of the electron density from one d molecular orbital to another one, higher in energy.[216] The population of this non-bonding orbital leads to a geometrical perturbation around the metal center and weakens the metal-ligand bond. One of the first quantitative studies about the photo-induced ligand dissociation of the $[Ru(bpy)_3]^{2+}$ complex to form

[Ru(bpy)$_2$Cl$_2$] in chlorinated solvents was reported by Gleria and collaborators in 1978.[222] A few years later, Meyer and co-workers studied this photochemical process by irradiating several [Ru(bpy)$_2$(L)$_2$]$^{2+}$ complexes at 436 nm, in coordinating and non-coordinating solvents.[223] They proposed the formation of a pentacoordinate intermediate (PCI), which is subsequently coordinated by a solvent molecule, as illustrated in scheme 28.
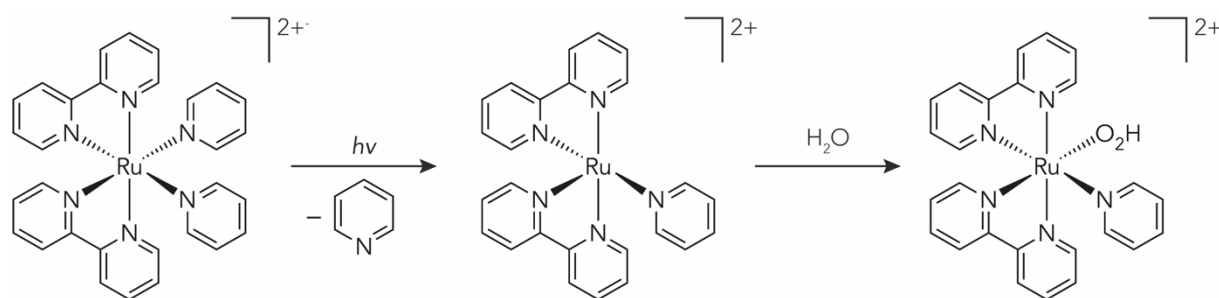
Scheme 28: Proposed mechanism for photo-induced ligand exchange, by Meyer and co-workers.

Meyer and co-workers discussed the process with the help of an energy diagram, to rationalize the photo dissociation as shown in figure 41.[224]
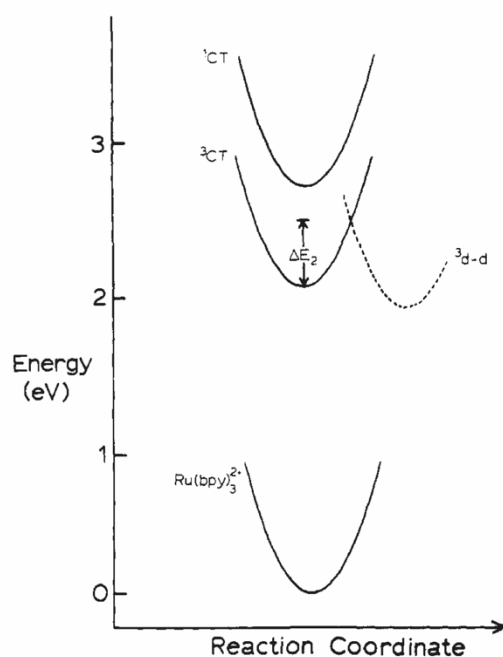
Figure 41: Proposed energy diagram of Ru(bpy)$_3^{2+}$, showing the ^{1}CT, ^{3}CT and ^{3}d-d excited states. Reproduced from ref. [224] with permission of ACS Publications.

The energy diagram displays the [1]MLCT ([1]CT) transition band, which is coupled to two triplet states, the [3]MLCT ([3]CT) and the anti-bonding orbital [3]MC ([3]d-d). The energy diagram proposed was further confirmed by DFT calculations[225]. These first discoveries motivated scientists to further investigate this photo-induced phenomenon to a variety of Ru(II)-based polypyridyl complexes to understand the involved exited-states and to elucidate the mechanism behind this photosubstitution reaction.[226]

Photo-Induced Ligand Exchange in Ru(II) Polypyridyl Complexes

The generally accepted model for the photo-induced ligand exchange process in Ru(II)-based polypyridyl complexes is illustrated in figure 42. After excitation of the singlet ground state ([1]GS) to the [1]MLCT state, the subsequent fast (14 - 40 fs)[227,228] and efficient (quantum yield = $\Phi \approx 1$) intersystem crossing (ISC) leads to the energetically lowest and relatively long lived (580 ns in H_2O)[229] excited state of Ru(II) polypyridyl complexes, the [3]MLCT state. The energetically slightly higher [3]MC state, which has a significant antibonding character, will be thermally populated and as consequence, the electron density will be promoted from a metal d-orbital to another d-orbital with more σ^* character. The population of the [3]MC state leads to the dissociation of the ligand since the N-Ru bond becomes labile and destabilized. Recent investigations have confirmed the relatively long-lived (~170 ps) PCI in $[Ru(bpy)_2(L)_2]^{2+}$ systems, which precedes coordination with water, as reported by Simon and collaborators.[230] The tuning of this photochemical process can be achieved by shifting the MLCT band to lower absorption energies. This can be accomplished relatively simple, introducing electron-poor functional groups or ligands with an extended π-system and stabilized π*-orbitals relative to those of bpy derivatives, such as 2,2'-biquinoline (biq) or 1,1'-biisoquinoline. Shifting the MLCT band to lower energies will increase the energy gap (ΔE) between the [3]MLCT and [3]MC, leading to scarce crossovers and poor Φ.
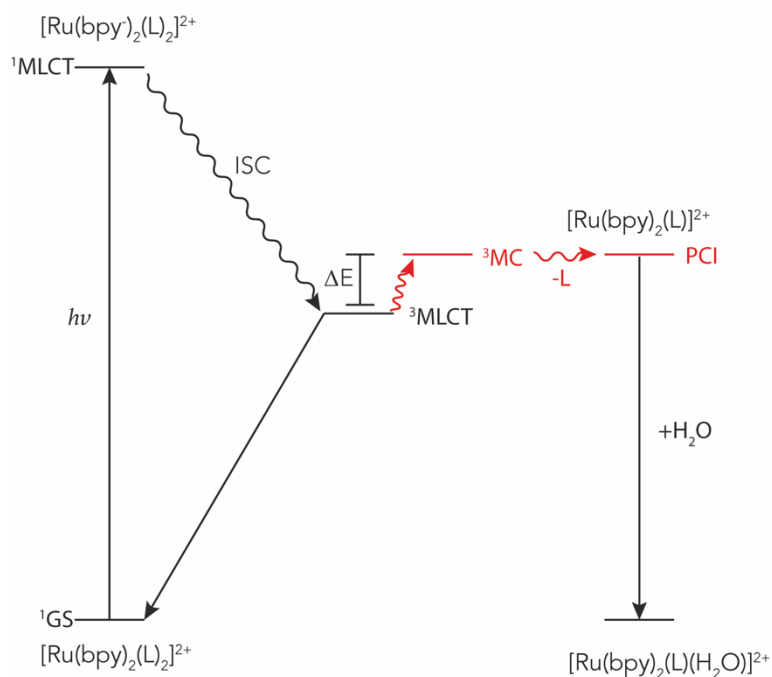
Figure 42: Jablonski diagram showing the electronic states for the photo-induced dissociation of Ru(II)-based polypyridyl complexes in water.

The energy gap between the two excited states can be reduced by introducing steric bulk to the system, perturbating the pseudo-octahedral geometry around the Ru(II) metal center. This distortion of the structural geometry leads to an elongation of the Ru-N bonds and stabilizes the ^{3}MC state(s) to lower energies, thereby facilitating the dissociation process. This phenomenon was reported by Glazer and co-workers, who observed the above mentioned process with [Ru(biq)$_2$(phen)]$^{2+}$ complex (phen = phenantroline).[231] Ligand exchange with water molecules was achieved by irradiating the dissolved complex at 650 nm. Another synthetic strategy that can be used for increasing the steric bulk strain is to methylate the bpy ligands. As reported by Turro and research group, the Φ for the pyridine exchange could be increased by more than 1000 times (from 0.0001 to 0.16) using 6,6'-dimethyl-2,2'-bpy instead of 2,2'-bpy.[232]

Bipyridines

In 1888, the first publication concerning the synthesis of 2,2'-bipyridine (bpy, figure 5) was presented by Fritz Blau, who reported about the dry distillation of copper(II) pyridine-2-carboxylate, and produced volatile hydrogen cyanide along with a distillation mixture constituted of pyridine and small amounts of bpy.[233] One year later, Blau published a more detailed procedure for the dry-distillation of copper(II) pyridine-2-carboxylate, which yielded 17 % of the 2,2'-bpy and reported about the formation of an intense red coloration when bpy is reacted with Fe(II) salts.[234]
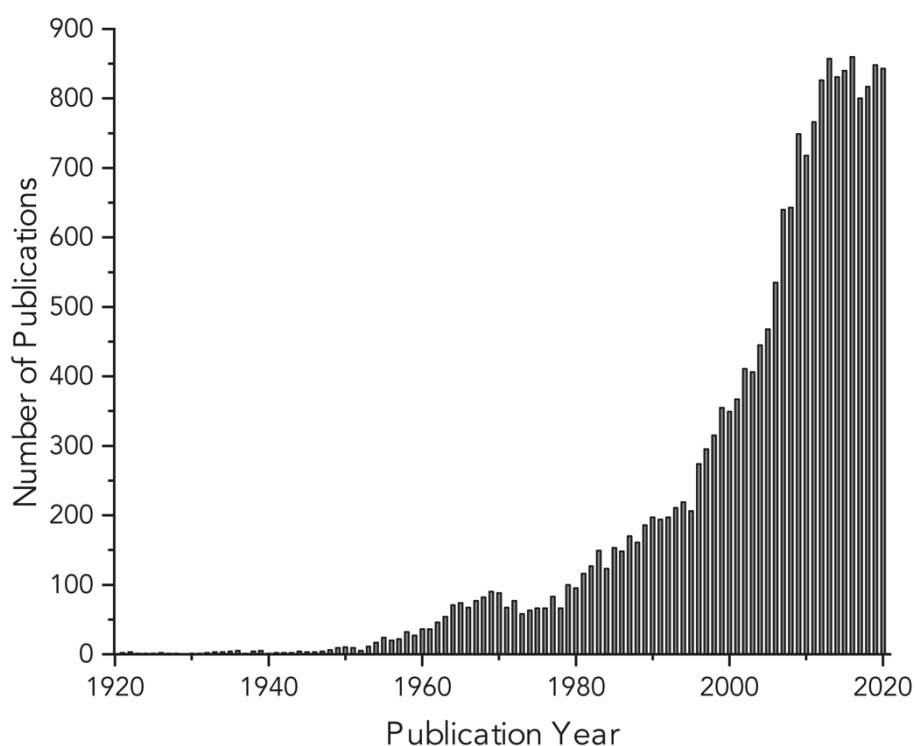
Figure 43: Histogram of the number of publications containing the term "bipyridine" using SciFinder™ (search performed on the 10th August 2021).

As illustrated in figure 43, it took almost 80 years from the first report about bpys for the scientific community to realize the importance and the huge potential of this bidentate ligand. Bpy complexes of various redox-active metal ions show interesting electrochemical behaviour and variable photophysical and photo optical properties.[235,236] Furthermore, it became also a very popular ligand in supramolecular

and macromolecular chemistry.[237,238] The increased interest in bpy derivatives was also fuelled by the progress made in analytical chemistry, which enabled the identification of natural products containing bpy building blocks like caerulomycins or collismycins.[239]

Synthetic Approaches
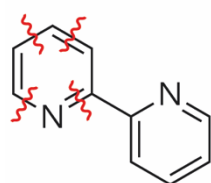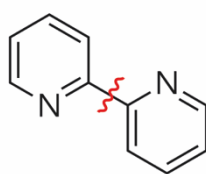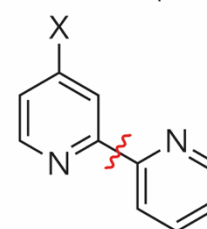
Figure 44: The three basic methods for the synthesis of 2,2'-bpys: (a) ring-assembly approach; (b) homo-coupling approach; (c) cross-coupling approach.

For the preparation of bpy-based structures, there are three basic synthetic approaches: the ring-assembly, the transition metal-catalyzed homo-coupling and the transition metal-catalyzed cross-coupling, as illustrated in figure 44. In the ring-assembly process, a pyridine ring will be formed in a cyclisation reaction most famously exemplified in the Kröhnke methodology. In the transition metal-catalyzed homo-couplings, two identical pyridine units will be connected by forming a new C-C bond at the position 2. The transition metal-catalyzed cross-coupling is suitable for the preparation of asymmetric bpys, since two different pyridine rings can be coupled together. This subchapter outlines the most common procedures for the synthesis of bpy derivatives.

Ring-Assembly Approach

Several methods have been developed for the preparation of bpy derivatives by employing the ring-assembly strategy for one of the pyridyl unit, and the most common ones are illustrated in scheme 29.
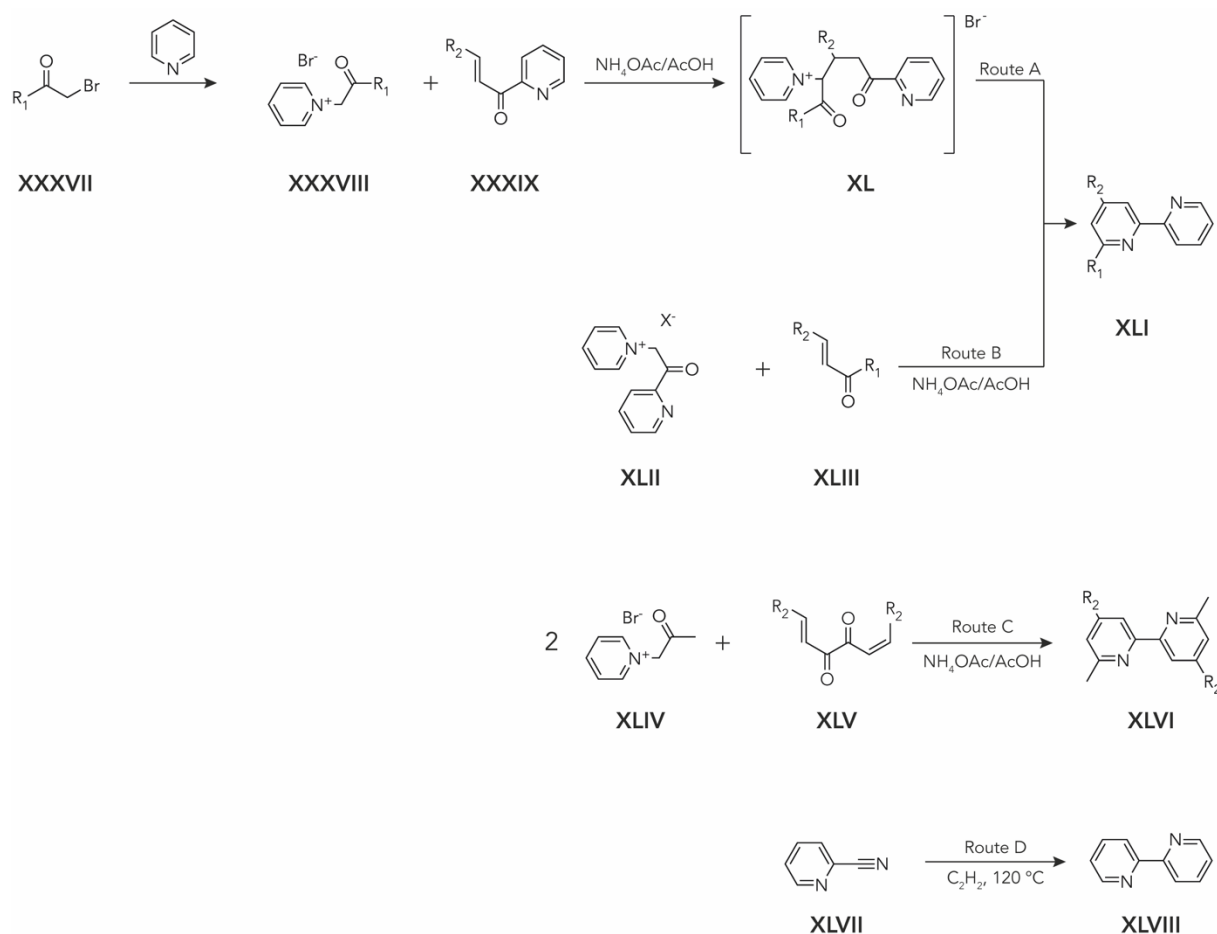
Scheme 29: An overview of the most common ring-assembly approaches: Kröhnke condensation (route a, b and c) and Brinkmann`s protocol (route d).

One of the most well-known methodologies is the Kröhnke approach, where a pyridinium salt reacts with an unsaturated ketone to form a bpy derivative (Scheme 29, route a). This strategy involves the preparation of a pyridinium salt **XXXVIII** (X = Br or I), which can be obtained via an Ortoleva-King reaction[48] between a bromomethyl ketone **XXXVII** and a pyridine. The unsaturated ketone **XXXIX** can be

prepared in a classical aldol condensation, starting from an aldehyde building block and 2-acetylpyridine. The 1,5-diketonte intermediate (**XL**) results from a Michael addition between pyridinium salt **XXXVIII** and unsaturated ketone **XXXIX**. The subsequent ring-closure with an appropriate ammonia source leads to the substituted bpy derivative **XLI**. Another Kröhnke method for the preparation of derivative **XLI** employs the condensation of an unsaturated ketone **XLIII** with pyridinium salt **XLII**, which has more acidic methylene hydrogen atoms compared to an α, β-unsaturated ketone (scheme 29, route b). The last Kröhnke approach outlined in scheme 29 is route c, where two equivalents of pyridinium salt **XLIV** are reacted with the doubly unsaturated ketone **XLV** to form the poly substituted bpy derivative **XLVI**. It is important to mention that the efficiency of route c is very low, as reported by Kröhnke.[47] An alternative strategy for the ring-assembly approach is the high yielding procedure reported by Brinkmann (scheme 29, route d).[240] In this case, 2-cyanopyridine (**XLVII**) is reacted with acetylene at 120 °C in the presence of a cobalt(I) catalyst, and bpy **XLVIII** can be isolated in 95 % yield.

Transition Metal-Catalyzed Homo-Coupling Approach

The transition metal-catalyzed homo-coupling of two identical pyridyl rings was used in most of the earlier works for the preparation of bpy derivatives.[241] This approach allows the direct coupling of two identical pyridyl rings, by generating a new C-C bond at the position 2. A fundamental advantage of this method is that the unreacted starting material can be easily recovered and recycled. However, the harsh reaction conditions necessary and the low efficiency featured by the homo-couplings remains a general drawback. As illustrated in scheme 30a, the utilisation of Raney nickel or Pd/C catalysts can induce the homo-coupling between two pyridine rings (**XLIX**) which yields substituted bpy **L**. Several routes were developed by Sasse and collaborators for the preparation of bpy derivatives using Raney nickel as catalyst.[242–244] The "classical" copper catalysed Ullmann reaction gave access to differently substituted

bpys[245], as exemplified by the homo-coupling of halopyridine **LI** yielding 3,3'-dimethyl-bpy (**LII**) reported by Nakamaru (scheme 30b)[246]. A timelier method for the preparation of bpy derivatives is the homo-coupling of 2-halopyridines (**LIII**) using a transition-metal catalyst.

R= H, CH$_3$, CH$_2$CH$_3$, C$_6$H$_5$, COCH$_3$, CN, CO$_2$Et

X = Br, Cl   R$_1$= H, COOCH$_3$ R$_2$= H, OCH$_3$
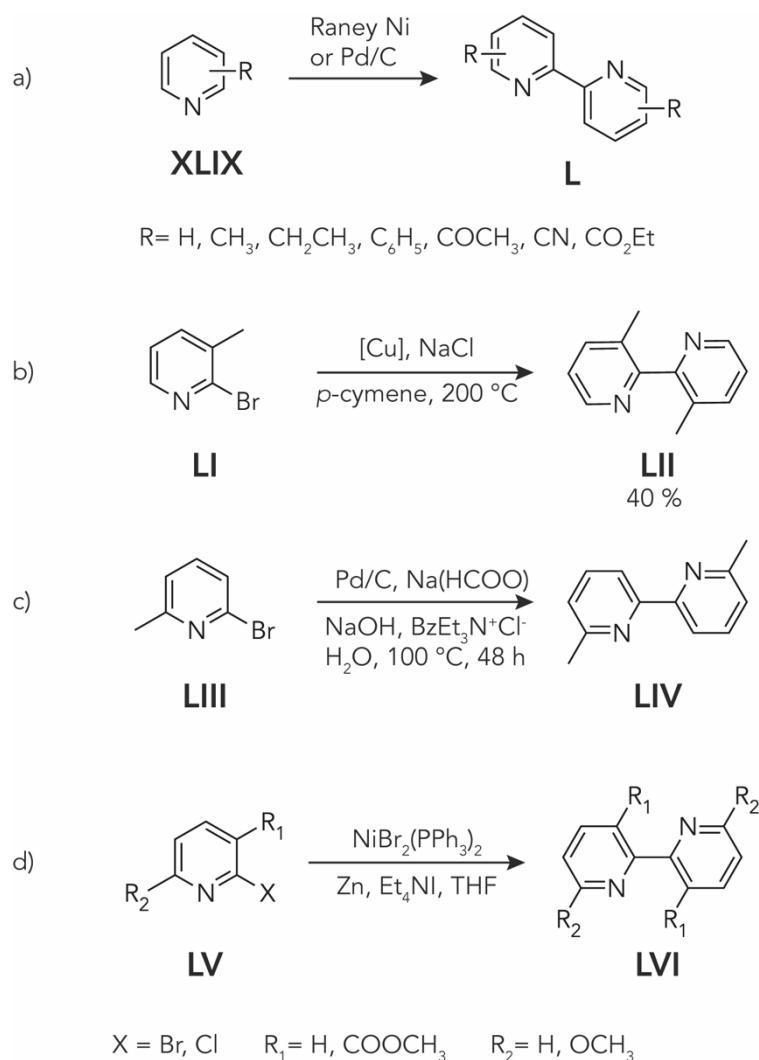
Scheme 30: Transition metal-catalyzed homo-couplings of pyridine derivatives.

However as illustrated in scheme 30c, the improvements in this field were achieved by introducing phase transfer conditions and other catalytic systems, and allowed for example to prepare 6,6'-dimethyl-2,2'-bpy (**LIV**) in a multi-hundred-gram scale.[247,248] The development of milder coupling conditions compared to the Ullmann reaction,

gave the possibility to produce a variety of multi substituted bpy derivatives in good to moderate yields, as reported by Iyoda and collaborators.[249] In their publication, the authors used a Ni(II)-complex along with zinc as a reducing agent and tetraethylammonium iodide for the homo-coupling of multifunctional halopyridines **LV**, thereby synthesizing various substituted 2,2'-bpy derivatives **LVI**, as displayed in scheme 30d.

Transition Metal-Catalysed Cross-Coupling Approach

The need for unsymmetrical substituted and functionalized bpy ligands could be satisfied by the synthetically progress made in Pd^0- or Ni^0-catalysed cross-coupling reactions.
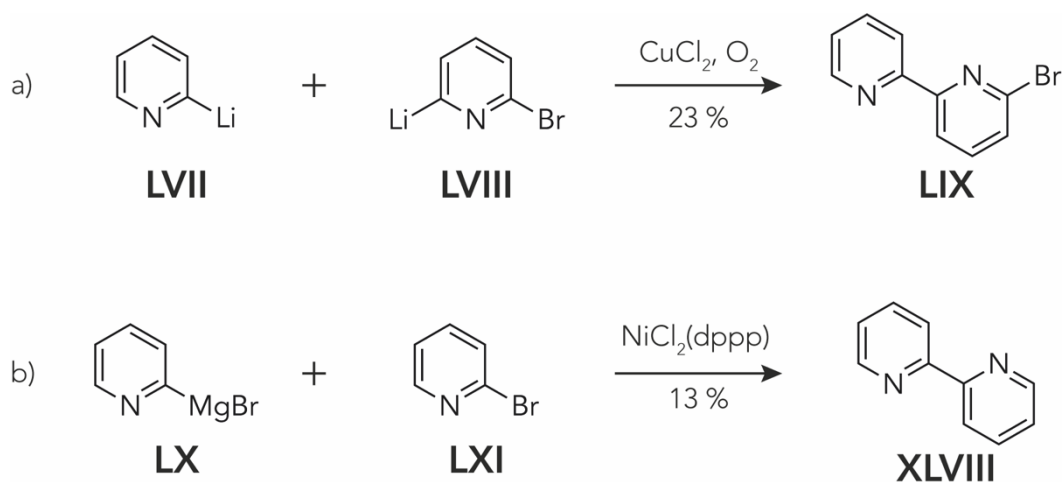
Scheme 31: Synthesis of 2,2'-bpy derivatives via traditional cross-coupling procedures. (a) Cross-coupling between lithiated pyridines; (b) Ni-catalysed Grignard coupling.

As displayed in scheme 31, initial cross-coupling methods involved the preparation of organometallic pyridines species. For example, lithiated pyridines could be coupled in the presence of copper species, resulting in unsymmetrical bpy **LIX** (scheme 31a) or bpy could be obtained from the Grignard reagent using a Ni-catalyzed coupling (scheme 31b).[250,251] It is important to mention that both methods are restricted in the

functionalities that can be employed and the low yields provided by the reaction are not suitable for upscaling processes. Fraser and collaborators published an efficient and high yielding procedure for the synthesis of asymmetrical bpy derivatives based on a Negishi cross-coupling (scheme 32a).[95] This approach involves the lithium/halogen exchange of 2-bromopyridine (**LXI**) and subsequent transmetallation with zinc chloride. The last step consists in the C-C coupling reaction between triflate **LXII** and the previously prepared pyridyl zinc reagent, yielding a variety of different methyl substituted bpy derivatives **LXIII**.
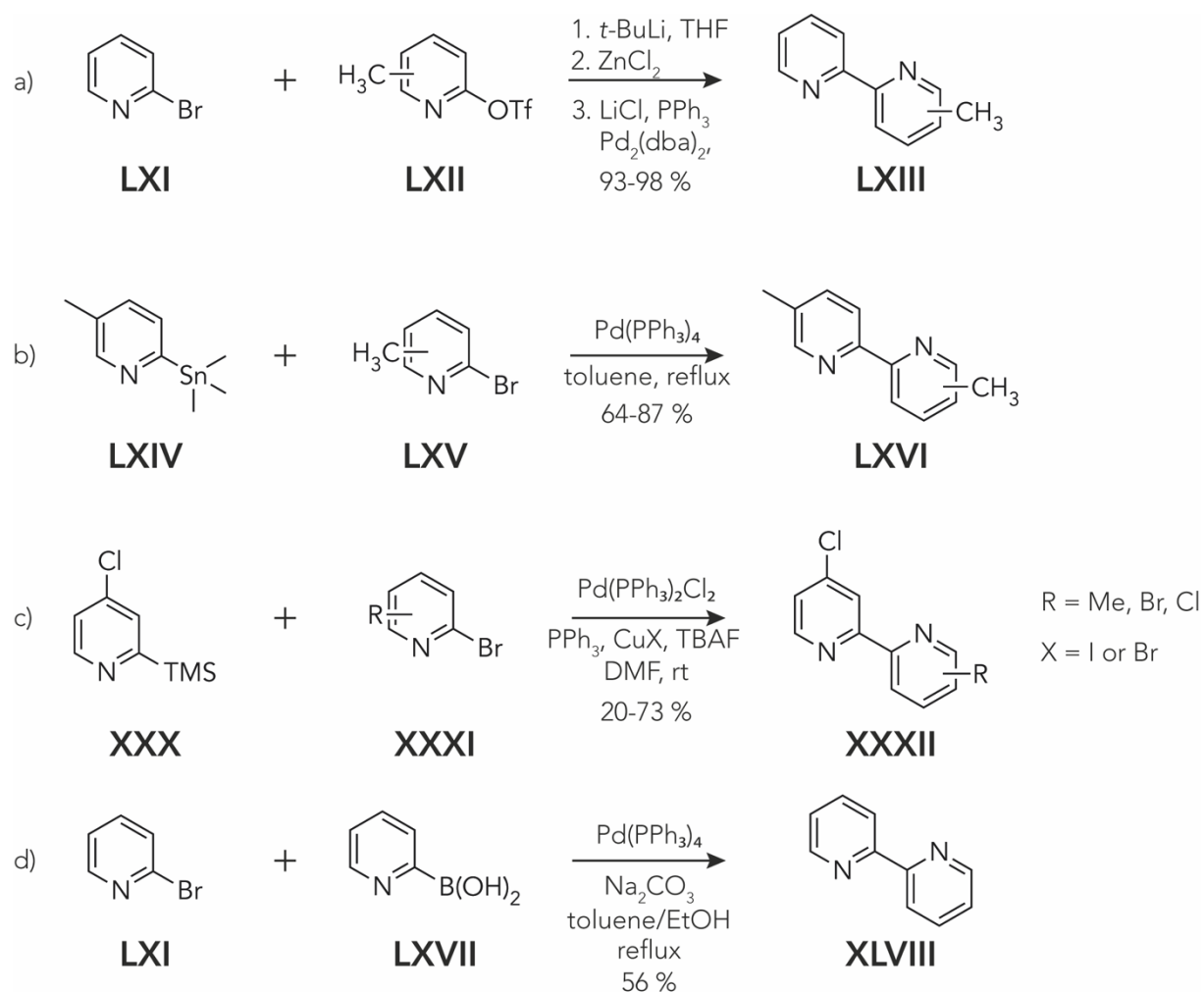
Scheme 32: Most common used cross-coupling procedures for the synthesis of bpy derivatives. (a) Negishi cross-coupling; (b) Stille cross-coupling; (c) Hiyama cross-coupling; (d) Suzuki-Miyaura cross-coupling.

Scheme 32b displays the Stille cross-coupling between trimethyltin reagent **LXIV** and 2-bromo pyridine derivative **LXV** that leads to a variety of methylated bpys **LXVI**, as reported by Yamamoto and co-workers.[252] This path has the disadvantage of requiring challenging purification processes for the organotin reagents and in particular, the handling of the highly toxic and volatile tin by-products formed during the transmetallation step. An alternative Pd^0-catalyzed approach for the formation of the C-C bond between the two pyridyl rings at the position 2 is the Hiyama cross-coupling procedure reported by Louërat and collaborators (scheme 32c).[93] 4-Chloro-2-trimethylsilylpyridine (**XXX**) was reacted with differently substituted halopyridines **XXXI** in a copper-mediated Hiyama cross-coupling reaction, yielding a variety of 4-chloro-substituted bpy derivatives **XXXII**. Another suitable method for the preparation of substituted bpy derivatives is the Suzuki-Miyaura cross-coupling as outlined in scheme 32d. In this Pd^0-catalyzed cross-coupling, a halopyridine **LXI** and an appropriate boronic acid **LXVII** are reacted to form bpy derivatives in moderate yields, as reported by Matondo and his research team.[253] It is important to mention that the Suzuki-Miyaura cross-coupling is very challenging and inefficient due to the unstable boronic acid moiety in pyridines derivatives, which suffers from facile proton-deboronation. The so-called 2-pyridyl problem was indeed recently reported by Willis and collaborators.[254] Nevertheless, the further improvements in the Suzuki-Miyaura cross-coupling for the preparation of bpy derivatives is needed and conditions for specific systems are reported.[255,256]

Aim of this Work

The aim of this project was to design and synthesize new PCTs based on Ru(II) polypyridyl complexes. The main purpose of these tailor-made tags is to chemically and optically enable the volatilisation of complex biopolymers via electrospray ionisation, to control their motion in the gas-phase thanks to electric and magnetic fields, and to control their charge at a given time and position by photo-induced ligand dissociation at 532 nm.

The project was motivated by the preliminary studies made on photocleavable *ortho*-nitrobenzylether derivatives, reported by Debiossac and collaborators in 2018.[257,258] In the report, the dissociation of *ortho*-nitrobenzylether derivatives was accomplished by utilizing UV irradiation at 266 nm. To generalize the method, suitable PCTs that can be triggered outside of the absorption profile of biomolecules were needed.
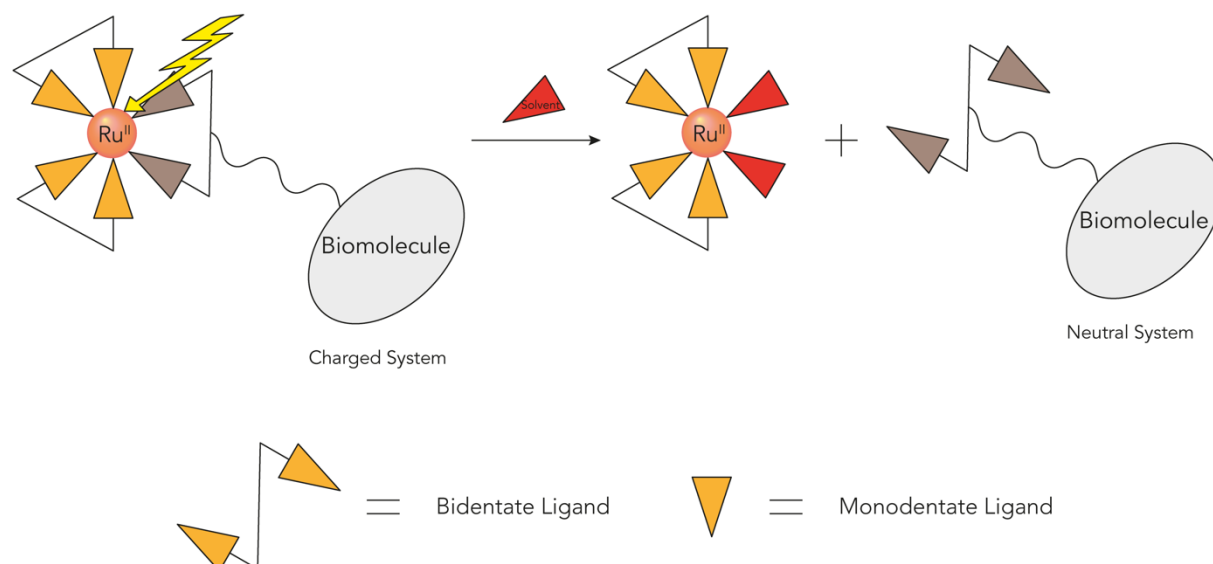
Figure 45: Sketch of the concept in solution, were the photocleavable bidentate ligand bearing a polypeptide can be exchanged with solvent molecules (monodentate) after irradiation at a specific wavelength. The resulting two species have a different oxidation state.

As illustrated in figure 45, the main goal was to find a Ru(II)-based chromophore that can dissociate a bidentate ligand at a specific wavelength. After cleavage, the biomolecule will be in a different charged state due to the loss of the charged Ru(II)-fragment. It is important to mention, that the cleavage experiments are performed in the high vacuum chamber of a customized mass spectrometer and not in solution. If successful, this more general approach might enable the charge control of more complex biomolecules that can be introduced in high vacuum.

The photocleavage experiments at 532 nm were performed by the group of Prof. M. Arndt at the University of Vienna and will not be discussed in detail within this doctoral thesis.

Design and Synthetic Strategy of the Polypyridyl Complexes

As mentioned in the introduction of this chapter, Ru(II)-based polypyridyl complexes were commonly used as photocages for aromatic heterocycles in bioactive systems.[259] It is important to mention that to do so, the coordinated compounds should be kinetically inert, highly soluble either in polar solvents or water, and that the ligands can be modified for convenient coupling with polypeptides.[260]

Therefore, 5 Ru(II)-based polypyridyl complexes were designed as model compounds to investigate their potential as photolabile component in high vacuum, as illustrated in figure 46.
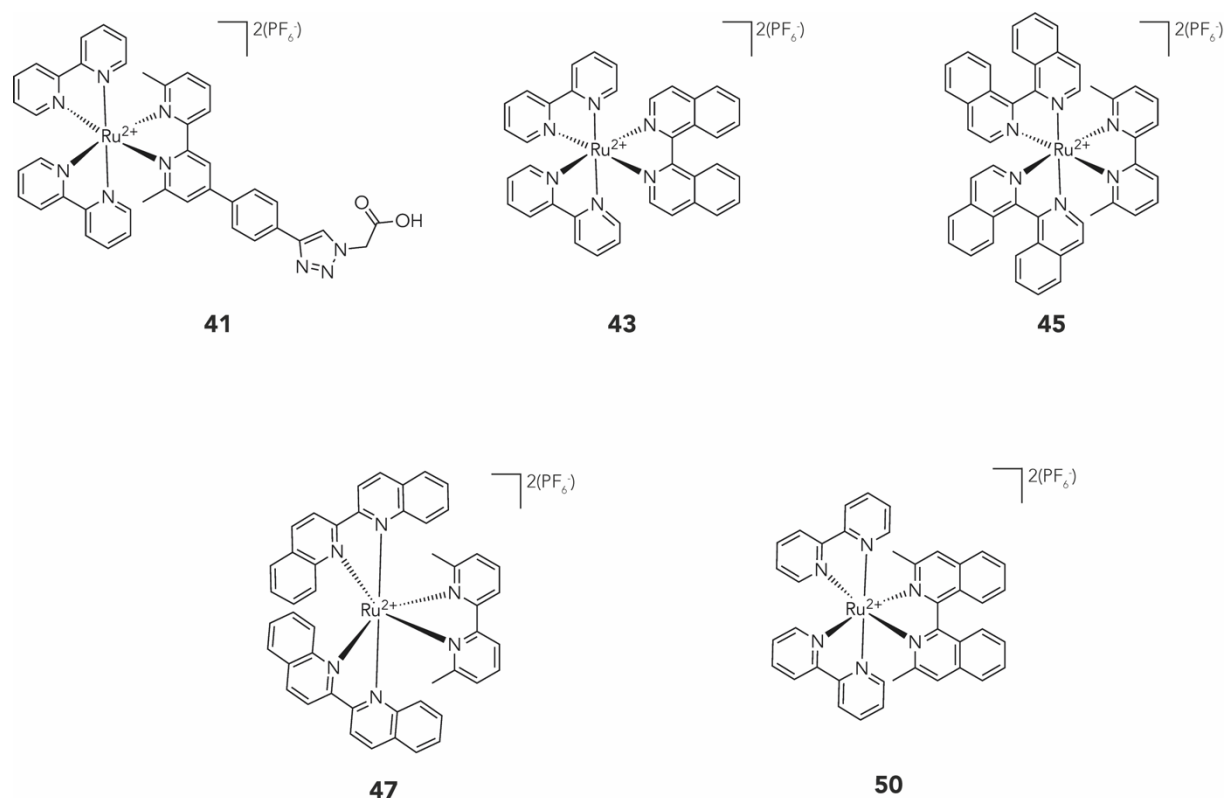
Figure 46: Molecular structures of the designed Ru(II)-based polypyridyl complexes for photo-induced ligand dissociation in high vacuum.

Tris bpy complex **41** is the first compound that was designed for the mentioned purpose, and it incorporates a 6,6'-dimetyl-bpy ligand. It is known that the introduction of steric bulk to the ligand present in Ru(II) complexes brings a distortion to the pseudo-octahedral geometry around the metal and enhances the efficiency of the ligand exchange.[261,262] The distortion of the geometry around the metal center lowers the energy of a dissociative ^{3}MC state, allowing its thermal population from the lower lying ^{3}MLCT state. The population of the ^{3}MC state then allows the ejection of a ligand.[263–266]

The absorption cross-section at 532 nm is expected to be weak for complex **41** as it should behave like $[Ru(bpy)_3]^{2+}$. Therefore, steric bulk was introduced to enhance the efficiency of the photo dissociation process. Furthermore, complex **41** is equipped with a carboxylic acid, which is convenient for potential coupling with peptide moieties.

Complexes **43**, **45**, **47** and **50** are optimized for the absorption at 532 nm, since the replacement of at least one bpy ligand with 1,1'-biisoquinolines or biq derivatives leads to a strong bathochromic shift in their excitation spectrum.[267–269] Complex **43** and **50** are structurally very similar and in both cases, the 1,1'-biisoquinolines ligands are expected to dissociate due to their steric bulk. Complex **47** and **50** are bearing both bis-methylated bpy ligands, which are the one expected to dissociate from the metal center.

It is important to note, that these structures are not yet adapted for the coupling with polypeptides, but are designed as model compounds for the investigation of the photo-induced dissociation process in high vacuum at a wavelength of 532 nm.

Retrosynthesis of Bpy Ligand 39
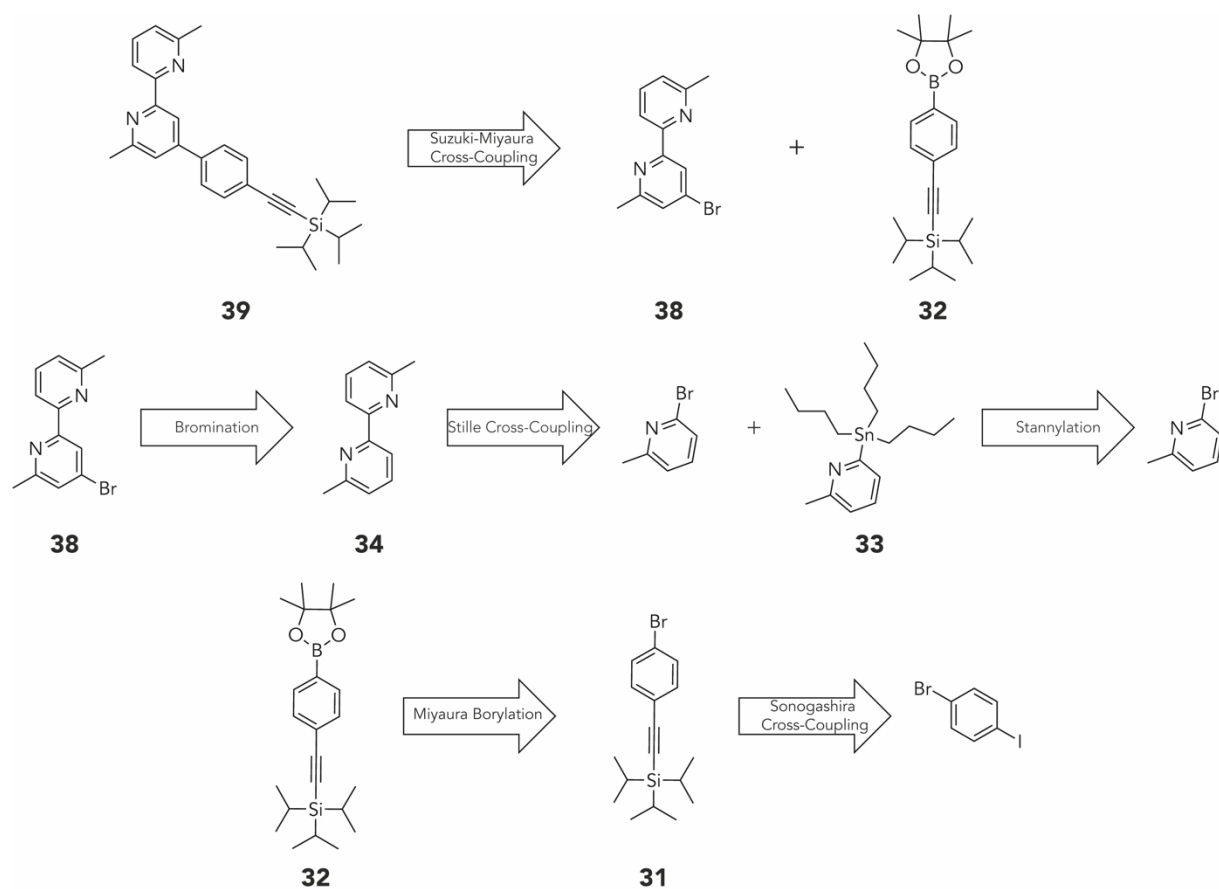
Scheme 33: Retrosynthetic analysis of bpy ligand **39**.

Following the retrosynthetic strategy illustrated in scheme 33, bpy ligand **39** can be obtained by Suzuki-Miyaura cross-coupling between 4-bromo-6,6'-dimethyl-2,2'-bpy (**38**) and the appropriate boronic ester **32**. Bpy **38** can be accessed by the bromination at position 4 of 6,6'-dimethyl-2,2'-bpy (**34**), which itself should be obtained by a Stille cross-coupling, between 2-methyl-6-(tributhylstannyl)pyridine (**33**) and commercially available 2-methyl-6-bromine pyridine. The tin reagent **33** can be synthesized by the stannylation of 2-methyl-6-bromopyridine. The boronic ester derivative **32** can be accessed via Pd⁰-catalyzed Miyaura borylation of ((4-bromophenyl)ethynyl)triisopropylsilane (**31**). Finally, the brominated compound **31**

can be obtained via Sonogashira cross-coupling of commercially available 1,4-bromoiodobenzene and mono protected tri*iso*propylsilyl (TIPS) acetylene.

Retrosynthesis of Complex 41
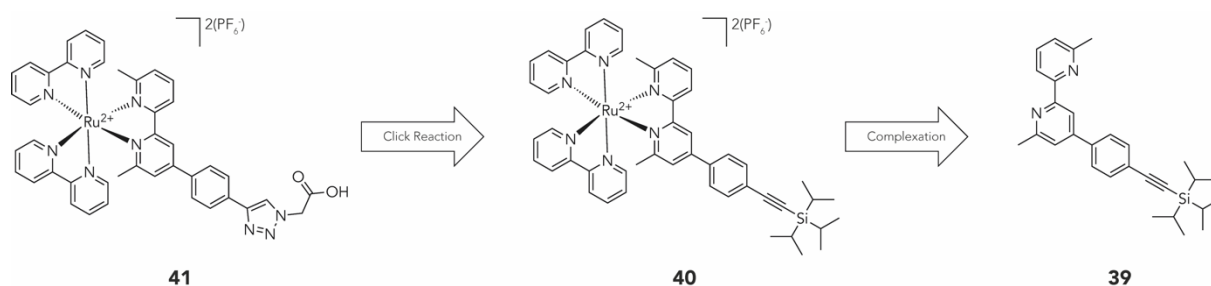
Scheme 34: Retrosynthetic analysis of complex **41**.

Retrosynthetically, complex **41** can be obtained via copper-catalyzed "click" reaction with the TIPS protected alkyne derivative **40**. The Ru(II)-based tris bpy complex **40** can be accessed by the complexation of bpy **39** with commercially available *cis*-bis(2,2'-bpy)dichlororuthenium(II) hydrate, as illustrated in scheme 34.

Retrosynthesis of Complex 43
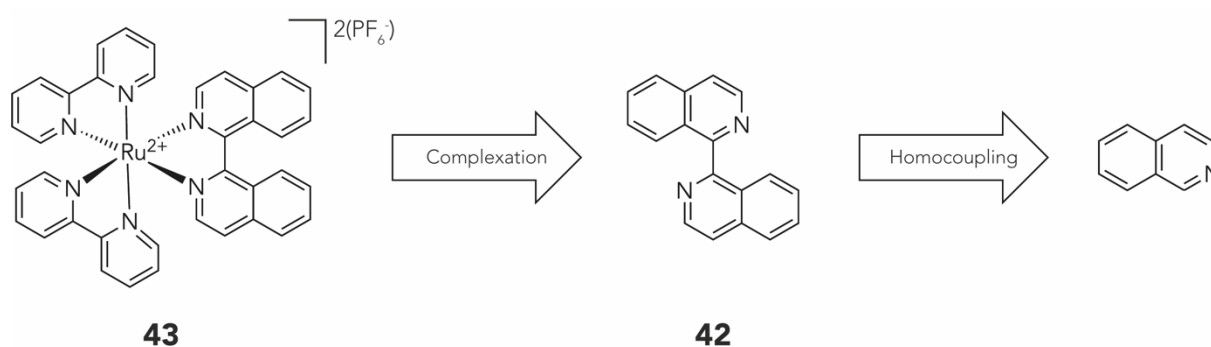
Scheme 35: Retrosynthetic analysis of complex **43**.

Following the retrosynthetic strategy illustrated in scheme 35, Ru(II)-based complex **43** can be accessed via the complexation of *cis*-bis(2,2'- bpy)dichlororuthenium(II)

hydrate and 1,1'-biisoquinoline (**42**). Molecule **42** can be obtained by the homocoupling of two isoquinolines.

Retrosynthesis of Complex **45**
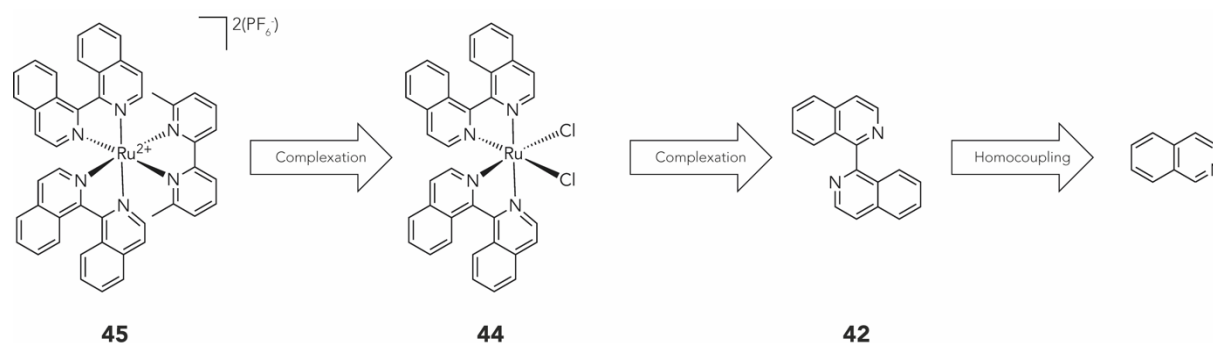
Scheme 36: Retrosynthetic analysis of complex **45**.

Retrosynthetically, complex **45** can be obtained by the complexation of commercially available dimethylated bpy **34** with Ru(II)-based complex **44**, as illustrated in scheme 36. *Cis*-bis(1,1'-biisoquinoline)dichlororuthenium (**44**) can be synthesized via complexation of ligand **42** with a commercially available Ru(III) salt. The retrosynthetic approach for the synthesis of compounds **42** and **34** were presented in the previous subchapters.

Retrosynthesis of Complex **47**
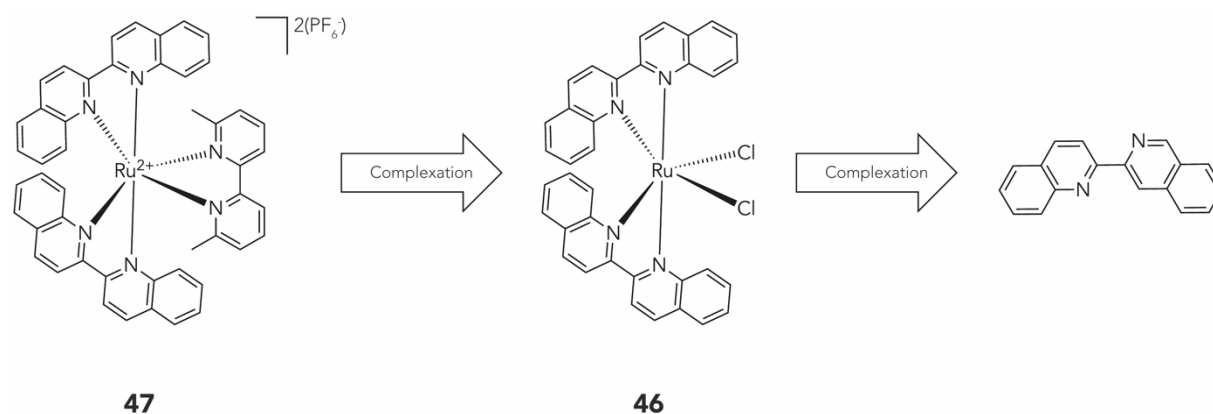
Scheme 37: Retrosynthetic analysis of complex **47**.

Following the retrosynthesis displayed in scheme 37, Ru(II)-based complex **47** can be accessed via complexation reaction of bpy **34** with *cis*-complex **46**, which itself can be obtained by the complexation of commercially available biq with a Ru(III) salt.

Retrosynthesis of Complex **50**

Retrosynthetically, complex **50** can be synthesized via complexation reaction of *cis*-bis(2,2'- bpy)dichlororuthenium(II) hydrate and 3,3'-dimethyl-1,1'-biisoquinoline (**49**), as illustrated in scheme 38.
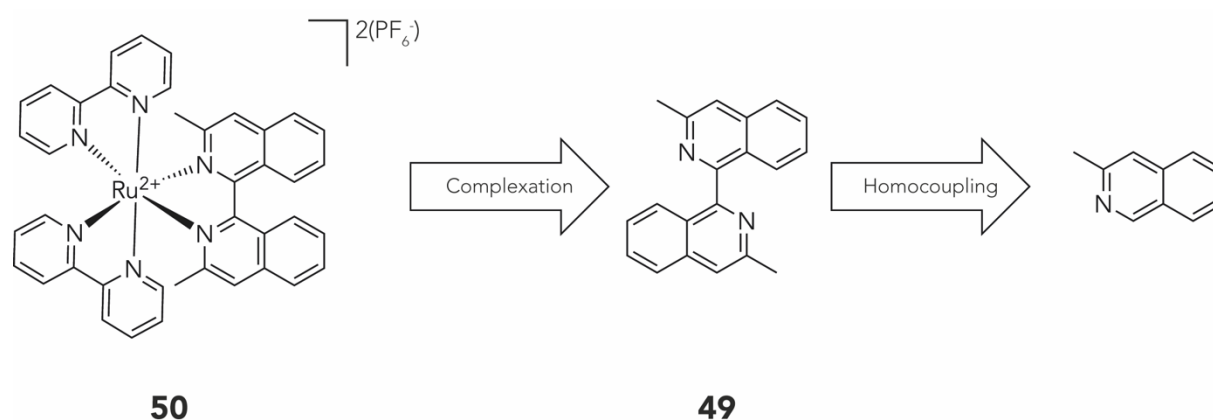
Scheme 38: Retrosynthetic analysis of complex **50**.

The homocoupling of 3-methylisoquinoline at the position 1 should form the desired 1,1'-biisoquinoline derivative **49**.

Results and Discussion

Synthesis of Bpy ligand 39
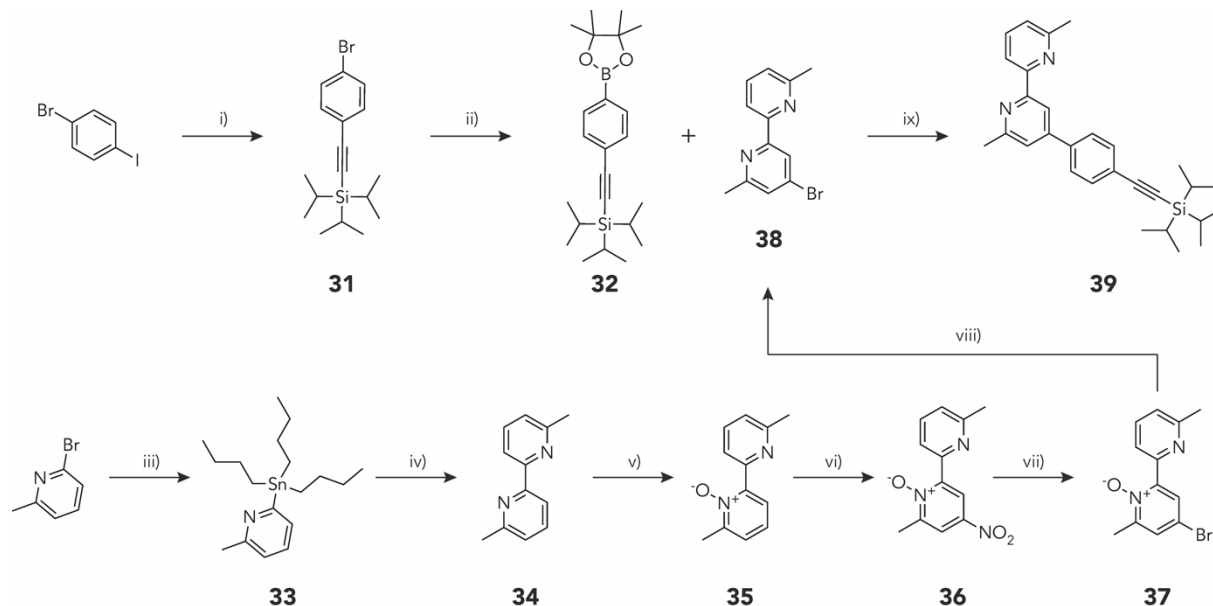
Scheme 39: Molecular structure and synthesis of bpy ligand **39**. i) TIPS acetylene, Pd(PPh$_3$)$_2$Cl$_2$, CuI, THF/NEt$_3$, RT, 0.25 h, quant.; ii) B$_2$pin$_2$, Pd(dppf)Cl$_2$, 1,4-dioxane, 100 °C, 1 h, 94 %; iii) *n*-BuLi, SnBu$_3$Cl, THF, - 78 °C – RT, 12 h, 98 %; iv) PPh$_3$, Pd(PPh$_3$)$_4$, toluene, 130 °C, 12 h, 68 %; v) *m*-CPBA, CHCl$_3$, 0 °C – RT, 2 h, 75 %; vi) H$_2$SO$_4$, HNO$_3$, 100 °C, 1 h, 60 %; vii) acetyl bromide, acetic acid, 80 °C, 2 h, 53 %; viii) PBr$_3$, CHCl$_3$, 70 °C, 2 h, 93%; ix) Pd(PPh$_3$)$_2$Cl$_2$, K$_2$CO$_3$, EtOH/H$_2$O, 100 °C, 2 h, 97 %.

Scheme 39 illustrates the synthetic procedure used for the synthesis of bpy ligand **39**. Commercially available 1,4-bromoiodobenzene and TIPS acetylene were reacted in a classical regioselective Sonogashira cross-coupling using adopted conditions of Roos and collaborators[270], to quantitatively provide brominated compound **31**. The synthesis of boronic ester **32** starting from compound **31** was already reported from Höger and collaborators.[271,272] By introducing the pinacol boronic ester via lithium-halogen exchange, they managed to isolate 62 – 71 % of compound **32**. We could prepare compound **32** via Pd^0-catalyzed Miyaura borylation cross-coupling using 1 equivalent of bis(pinacolato)diboron, 0.05 equivalent of dichloro[1,1'-bis(diphenylphophino)ferrocene]palladium(II) (Pd(dppf)Cl$_2$) as catalyst and

10 equivalents of K_2CO_3 as base. The reaction was conducted at room temperature and yielded 94 % of the desired boronic ester **32**. The unsymmetric 4-brominated bpy **38** was synthesized according the multistep synthesis described by Marsura and co-workers.[273] The bpy **38** and the synthesized boronic ester **32** were merged by performing a Suzuki-Miyaura cross-coupling under argon using 0.07 equivalents of *trans*-dichloro-(triphenylphosphine)palladium(II) (Pd(PPh$_3$)$_2$Cl$_2$) as catalyst and 5 equivalents of K_2CO_3 as base, providing asymmetric bpy **39** in 97 % yield.

Synthesis of Complex **41**
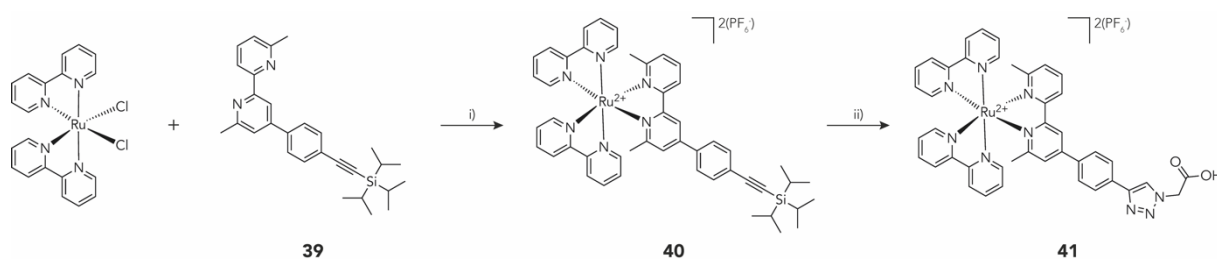
Scheme 40: Molecular structure and synthesis of complex **41**. i) Microwave, ethylene glycol, 200 °C, 10 min 2) sat. NH$_4$PF$_6$ (aq.), RT, 92 %.; ii) 2-Azidoacetic acid, TBAF, CuSO$_4$, L(+)-sodium ascorbate, THF/H$_2$O, RT, 4 h, 45 %.

Scheme 40 outlines the synthetic approach used for the preparation of the model complex **41**. In a microwave reaction, commercially available *cis*-bis(2,2'-bpy)dichlororuthenium(II) hydrate was reacted with the synthesised bpy ligand **39** at 200 °C, yielding 92 % of the target Ru(II)-based complex **40**. The conditions used were adopted from Glazer and collaborators.[274] The TIPS protecting group present on the acetylene of complex **40** was removed in situ by using tetrabutylammonium fluoride (TBAF), and subsequently, 2-azidoacetic acid, CuSO$_4$ and L(+)-sodium ascorbate were added and initiated the Cu(I) catalysed "click"-reaction affording 45 % of target compound **41**.

Synthesis of Complex 43

Scheme 41: Molecular structure and synthesis of complex **43**. i) TMPMgCl, TMEDA, toluene, 60 °C, 12 h, 69 %; ii) 1) Microwave, ethylene glycol, 200 °C, 10 min 2) sat. NH₄PF₆ (aq.), RT, racemic mixture 84 %.

Complex **43** was prepared as shown in scheme 41. 1,1'-Biisoquinoline (**42**) was synthesized according to the conditions reported by Xie and collaborators.[275] The synthesis of the racemic mixture of compound **43** was reported by Grafton and co-workers in 1994.[276] They refluxed *cis*-bis(2,2'- bpy)dichlororuthenium(II) hydrate and ligand **42** in a pressure tube under N₂ atmosphere for 6 h and obtained 75 % of the racemic mixture. We modified those conditions by preforming the reaction in the microwave at 200 °C for 10 min, and we could obtain 84 % of the target complex **43** (as racemic mixture). The different enantiomers were not separated, as it is not crucial for the target photodissociation experiments.

Synthesis of Complex 45

Scheme 42: Molecular structure and synthesis of complex **45**. i) RuCl₃, L-ascorbic acid, LiCl, ethylene glycol, 160 °C, 3 h, 62 %; ii) 1) Microwave, ethylene glycol, 200 °C, 10 min, 2) sat. a NH₄PF₆ (aq.), RT, 31 %.

The *cis*-complex **44** was synthesized based on the report published by Yang and collaborators, who first tried to perform the reaction in DMF at 140 °C and formed several by-products.[268] By modifying the solvent and the temperature used for the reaction, we could obtain the desired *cis*-complex **44** with a very decent yield, as illustrated in scheme 42. Through, the purification of **44** was very challenging and not possible with the common techniques such as flash column chromatography. The crude mixture of **44** was then complexed with bpy **34** via microwave irradiation using the same conditions as the one used for the synthesis of polypyridyl Ru(II) complexes, which yielded 31 % of compound **45**.

Synthesis of Complex **47**
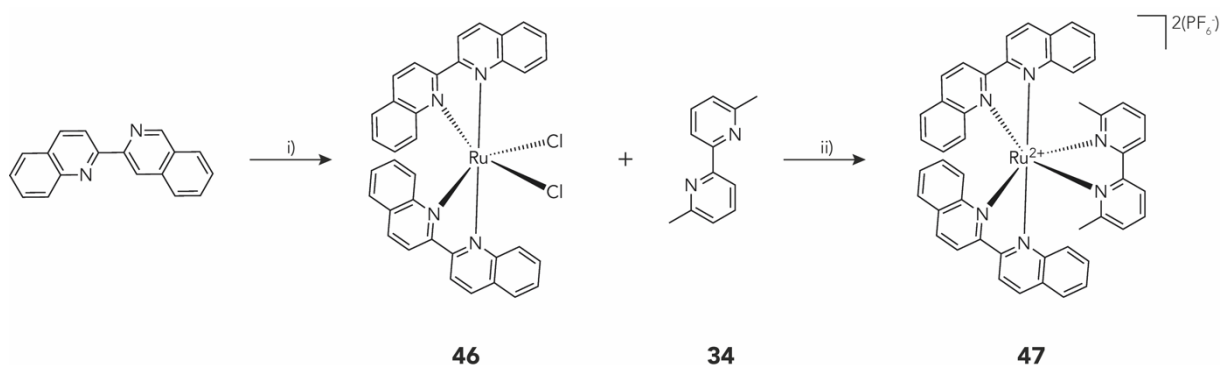
Scheme 43: Molecular structure and synthesis of complex **47**. i) RuCl$_3$, L-ascorbic acid, LiCl, ethylene glycol, 160 °C, 3 h, 72 %; ii) Microwave, ethylene glycol, 200 °C, 10 min, 2) sat. NH$_4$PF$_6$ (aq.), RT, 8 %.

The synthesis of the *cis*-complex **46** was performed by adapting the general conditions for the preparation of *cis*-bis(2,2'- bpy)dichlororuthenium(II) hydrate described by Meyer and co-workers.[277] The complexation of target complex **47** was using an excess of the bpy ligand **34** in a microwave at 200 °C for 10 min, yielding only 8 % of the desired complex. The low yield obtained can be explained either by the fact that the complex immediate photodissociates during or because it decompose on the static-phase of the column during the purification process, as reported by Klassen[278].

Synthesis of Complex **50**
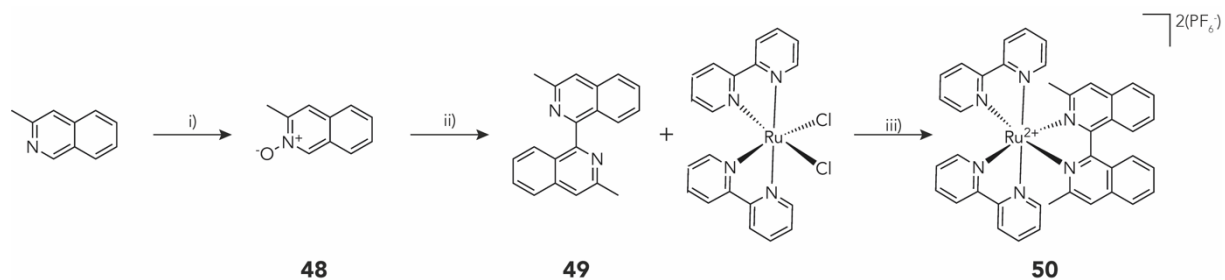
Scheme 44: Molecular structure and synthesis of complex **50**. i) *m*-CPBA, DCM, 0 °C- RT, 2 h, 99 %; ii) AIBN, KO*t*-Bu, MeTHF, 65 °C, 2 h, 40 %; iii) 1) Microwave, ethylene glycol, 200 °C, 10 min 2) sat. NH$_4$PF$_6$ (aq.), RT, 34 %.

The synthesis of complex **50** is outlined in scheme 44. 3-Methylisoquinoline was transformed to the more reactive N-oxide specie **48**, rendering the heteroaromatic compound more electrophilic.[279] The dimerization of the heterocyclic N-oxide **48** to ligand **49** was described by Larionov and collaborators and was performed using the same conditions as the ones reported.[280] The complexation of *cis*-bis(2,2'-bpy)dichlororuthenium(II) hydrate and **49** was performed in a microwave at 200 °C, in the presence of ethylene glycol for 10 min, and 34 % of target complex **50** was isolated.

Optical Investigation of polypyridyl Ru(II) Complexes

In this subchapter we will discuss optical properties of the polypyridine Ru(II)-based complexes synthesized. The UV-Vis spectra of the complexes prepared throughout the present subchapter were recorded at several concentrations, in MeCN and at room temperature. The averaged absorbances were converted into the corresponding extinction coefficients ε, following the *Beert-Lambert* law (Equation 1, chapter 1) and plotted against the respective wavelengths λ.

Figure 47 illustrates the characteristic MLCT bands of the Ru(II)-based polypyridyl complexes **41**, **43**, **45**, **47** and **50** in the 430 to 540 nm region. The MLCT transitions arises from the excitation of an electron from a molecular orbital that is primarily-metal based (dπ-orbital) into the LUMO π*-orbital of the ligand (e.g. bpy, phenanthroline and other heterocyclic aromatic ligands).[134] Furthermore, the characteristic bands in the UV region comprised between 260 and 290 nm arise from the ligand-centered (LC) π-π* transitions of the bpys.[281]

Table 3 compares the λ_{max}- and the corresponding ε-values of the MLCT-bands and the ε-values at 532 nm obtained for the Ru(II)-based complexes synthesized and those of the reference compound [Ru(bpy)$_3$]$^{2+}$ [282].
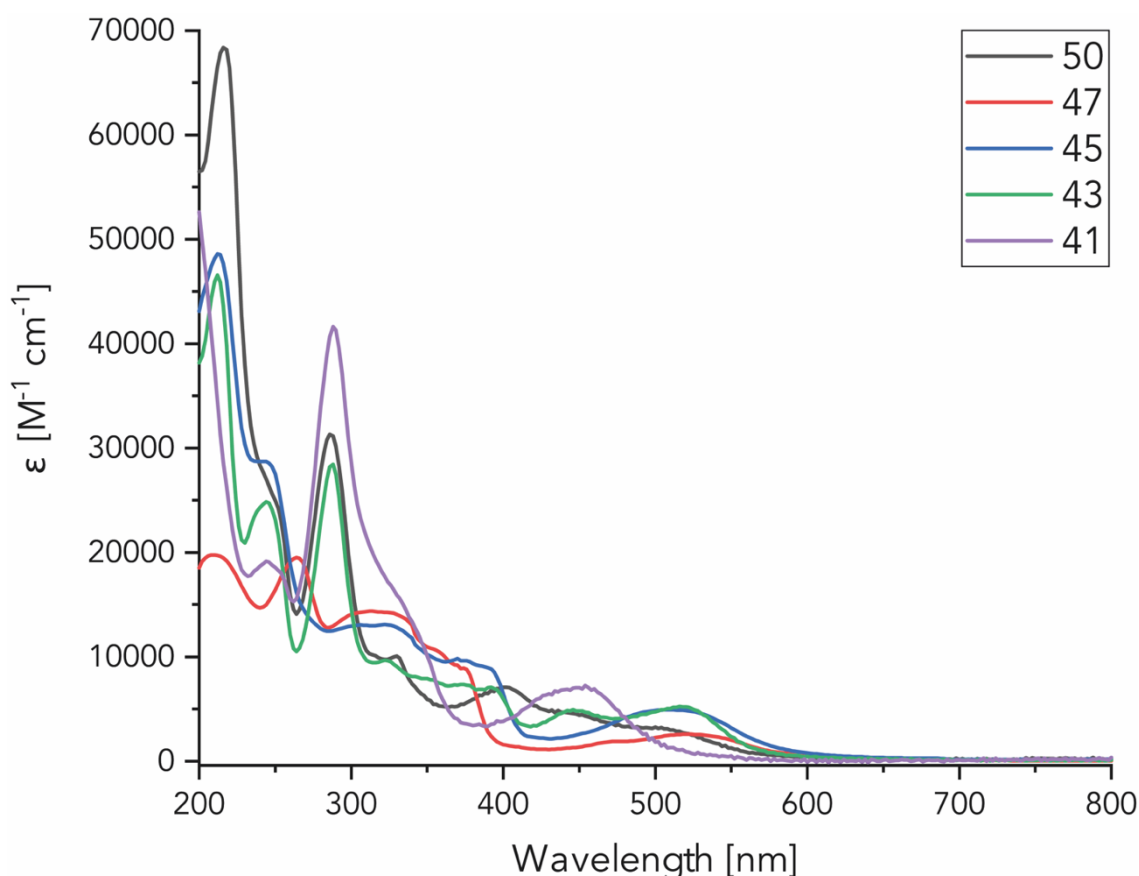
Figure 47: UV-Vis absorption spectra of Ru(II) polypyridyl complexes **41**, **43**, **45**, **47** and **50**.

Complex	λ_{max} (MLCT) [nm]	ε [M^{-1} · cm^{-1}]	λ[nm]	ε [M^{-1} · cm^{-1}]
Ru(bpy)$_3^{2+}$	452	130000	-	-
41	448	7055	532	570
43	516	5265	532	4435
45	510	4950	532	3990
47	520	2580	532	2375
50	500	3250	532	2170

Table 3: Summary of Photophysical Properties of synthesized complexes **41 – 50** and reference compound [Ru(bpy)$_3$](PF$_6$)$_2$ [282].

The MLCT absorption peak of complex **41** at 448 nm (ε = 7055 M^{-1}·cm^{-1}) exhibits a small hypsochromic shift of 4 nm compared to that of the parent [Ru(bpy)$_3$]$^{2+}$ complex. A more dominant bathochromic shift comprised between 48 and 68 nm can be observed in complexes **43**, **45**, **47** and **50**. The red shifts observed can be explained by the more extended π-system provided by the 1,1'-biisoquinoline and biq moieties, in comparison with that of bpy. Indeed, this leads to an energetic stabilization of the ligand-based LUMO π*-orbital and therefore in an increase of the absorption wavelength maxima. Furthermore, a hyperchromic shift ranging from 1600 to 3865 M^{-1}·cm^{-1} is observable for the same complexes at 532 nm, thus confirming the successful tuning of their electronic properties towards the targeted ones.

Photodissociation Experiment in Solution of Precursor **40**

In this subchapter, we will discuss about the preliminary investigation of the photo-induced dissociation of precursor **40** in solution, as illustrated in figure 48.

A freshly prepared solution of complex **40** dissolved in MeCN was injected in a reversed phase analytical HPLC (Reprosil C18), using an appropriate gradient mixture of H$_2$O/MeCN (figure 48b, orange line). Subsequently, the sample was irradiated with

sunlight at room temperature for 10 min and was re-injected in the reversed phase analytical HPLC using the same adapted gradient (figure 48b, red line). Figure 48b compares the HPLC chromatogram of the non-irradiated (orange line) and the irradiated (red line) solution of molecule **40**. After irradiation, complex **40** is not anymore detectable, since the bidentate ligand is successfully substituted with MeCN molecules, forming bpy ligand **39** (retention time = 11 min) and $[Ru(bpy)_2(MeCN)_2]^{2+}$ (retention time = 4 min). These results were further confirmed by mass spectrometry. Furthermore, as depicted in figure 48c, a change in the sample color before and after irradiation can already be observed by eye.
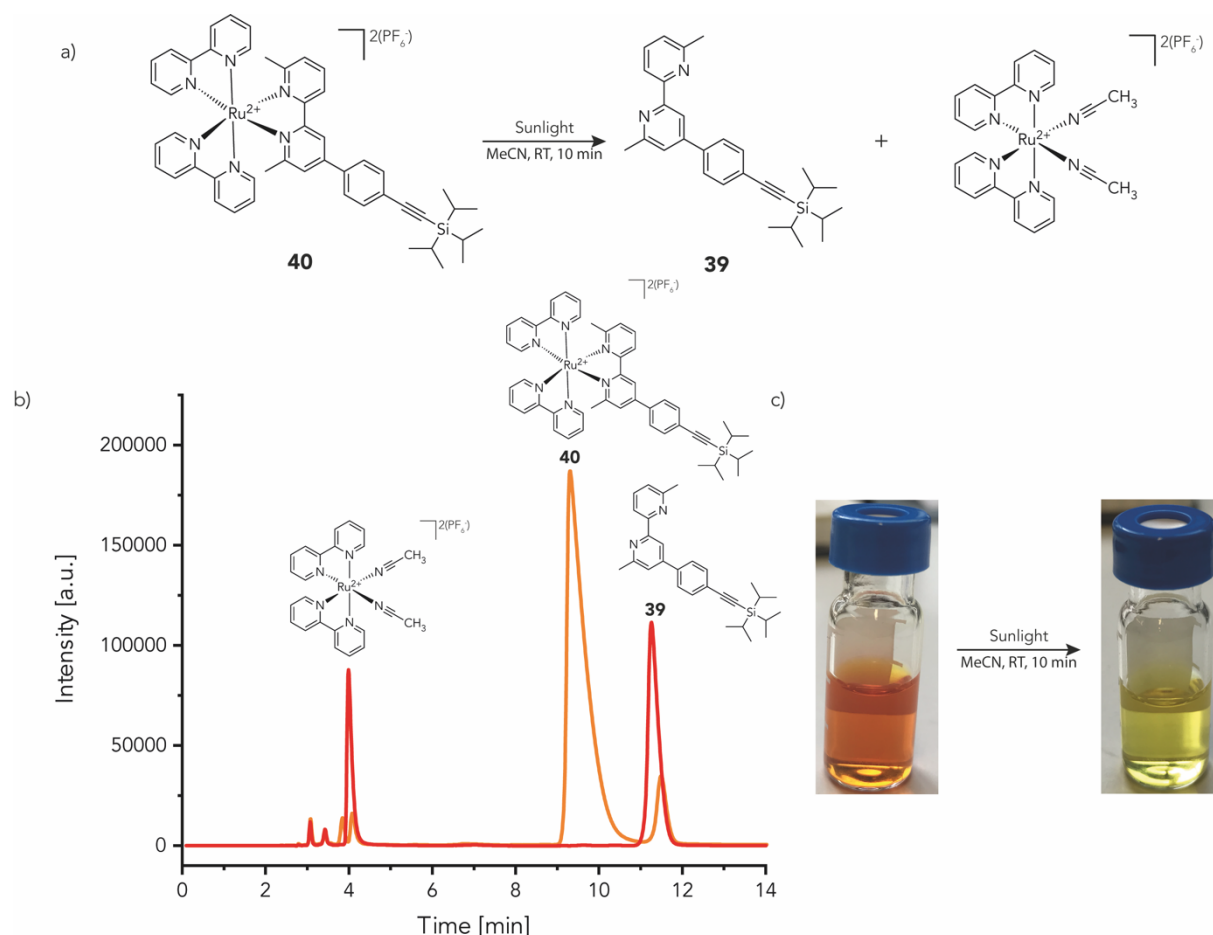
Figure 48: Photo-induced ligand exchange in solution: (a) molecular structure and dissociation reaction; (b) molecular structures and reversed phase HPLC chromatogram of **40** at 254 nm. The HPLC trace of: in orange, the solution containing precursor **40** before irradiation and in red, after 10 min of sunlight irradiation; (c) Irradiated solution of dissolved compound **40**, before irradiation (left side) and after 10 min of sunlight irradiation (right side).

Photodissociation Experiments in High Vacuum at 532 nm

The set-up for the photocleavage experiments was build and put into operation in the research group of Prof. M. Arndt at the University of Vienna. The detailed description of the device is not included in this thesis as it represents a completely different matter.

All the 5 complexes synthesized were tested and after irradiation at 532 nm, no dissociation of mass selected signals or cleavage products could be observed. The operators of the device could only follow the detachment of an PF_6^- counter-ion, from the cluster [**41**-PF_6^+]. Through, the dissociation of a PF_6^- anion shows that the gas-phase irradiation and absorption took place. Potentially, the fragmentation of non-covalently bounded clusters might provide an alternative approach to the given objectives. Furthermore, as reported by Balzani, the PF_6^- ion should be photoinert.[219] These results were surprising, since the ligand dissociation worked qualitatively well in solution, as discussed in the previous subchapter.

The anti-performance of the complexes in vacuum can be attributed to the missing exchange ligands or coordinating solvent, that play an important role in the photodissociation process. As outlined in scheme 45, the thermally activated ^{3}MC excited state leads to the cleavage of a Ru-N bond under formation of a pentacoordinate square pyramidal species. In the absence of a coordinating ligand or solvent, the pentacoordinate complex can revert back to the hexacoordinated complex in solution-phase, as reported in the studies conducted by Balzani and collaborators.[219]
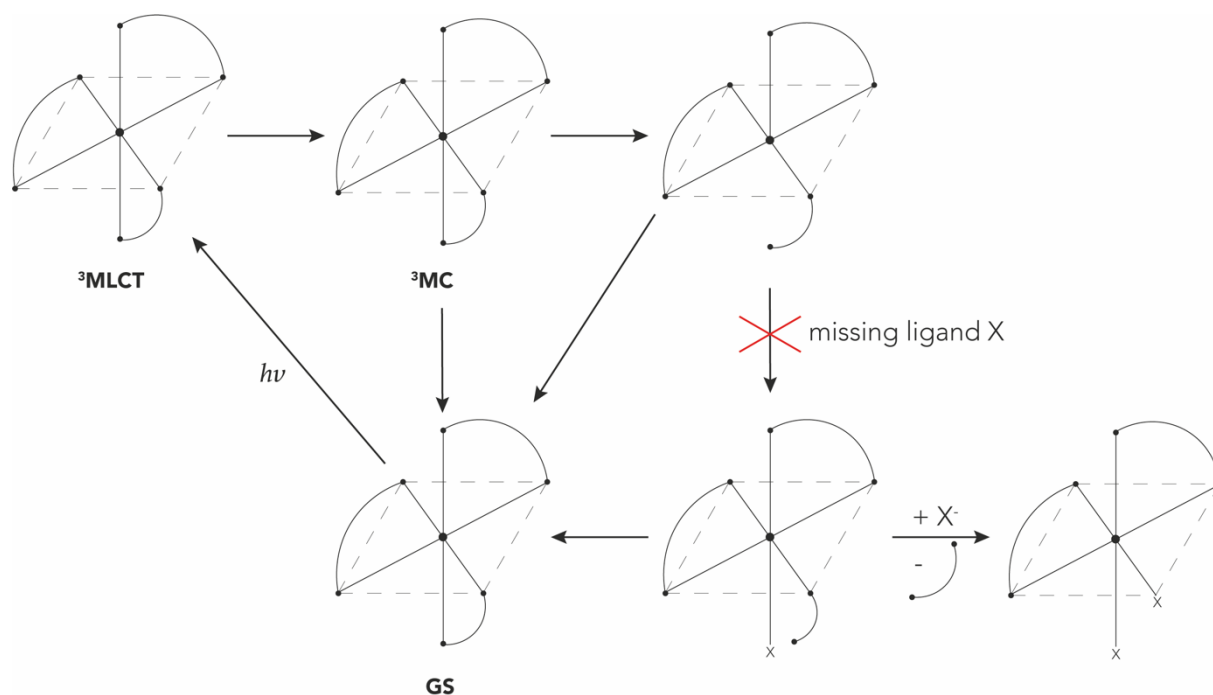
Scheme 45: Scheme of the proposed mechanism for the failed ligand dissociation in high vacuum.

It is important to mention, that all the reported photocages are studied in water or polar solvents, which leads in the case of photocleavable complexes in water to a photoaquation of the complex.[283] Another factor could be the relatively low absorption cross section at 532 nm. Despite having been optimized, the extinction coefficients remain rather low at 532 nm for the synthesized complexes (table 3).

Conclusion and Outlook

Within this project, 5 different Ru(II)-based polypyridyl complexes suitable for photo-induced ligand exchange, were successfully synthesized and characterized. By introducing ligands with more extended π-system such as 1,1'-biisoquinoline and biq derivatives in the complexes, we successfully red-shifted their absorption maxima to higher wavelength. Additionally, the ligands were equipped with methyl groups in order to increase the steric bulk around the metal center, and therefore enhance the ligand exchange process upon excitation due to the perturbation of the geometrical arrangement. Furthermore, we demonstrated that the dissociation process could be performed in solution for the Ru(II) polypyridyl complex **40** by irradiating a sample with sunlight for 10 min. The reaction was monitored with reverse phased analytical HPLC and mass analysis, which showed full conversion of the starting material to the photocleaved ligand and $[Ru(bpy)_2(MeCN)_2]^{2+}$. Unfortunately, the other synthesized complexes **41**, **43**, **45**, **47** and **50** did not behaved as intended in the photocleavage experiment under high vacuum and irradiation at 532 nm. The gas-phase photocleavage experiments were performed in the group of Prof. Arndt at the University of Vienna.

As a conclusion, we gained more insights on the synthesis and the optical behaviour of photo-labile Ru(II) polypyridyl complexes in the gas phase and therefore, new designs can now be considered. As discussed in the previous subchapter, the general mechanism for the ligand exchange in solution is exclusively dissociative, and a bidentate ligand can dissociate only if the pentacoordinate intermediate is not reverted to the hexacoordinated complex (figure 49a). When two mono-dentate ligands are used (instead of one bidentate ligand), the dissociation would take place immediately without the possibility for the complex to rearrange (figure 49b).
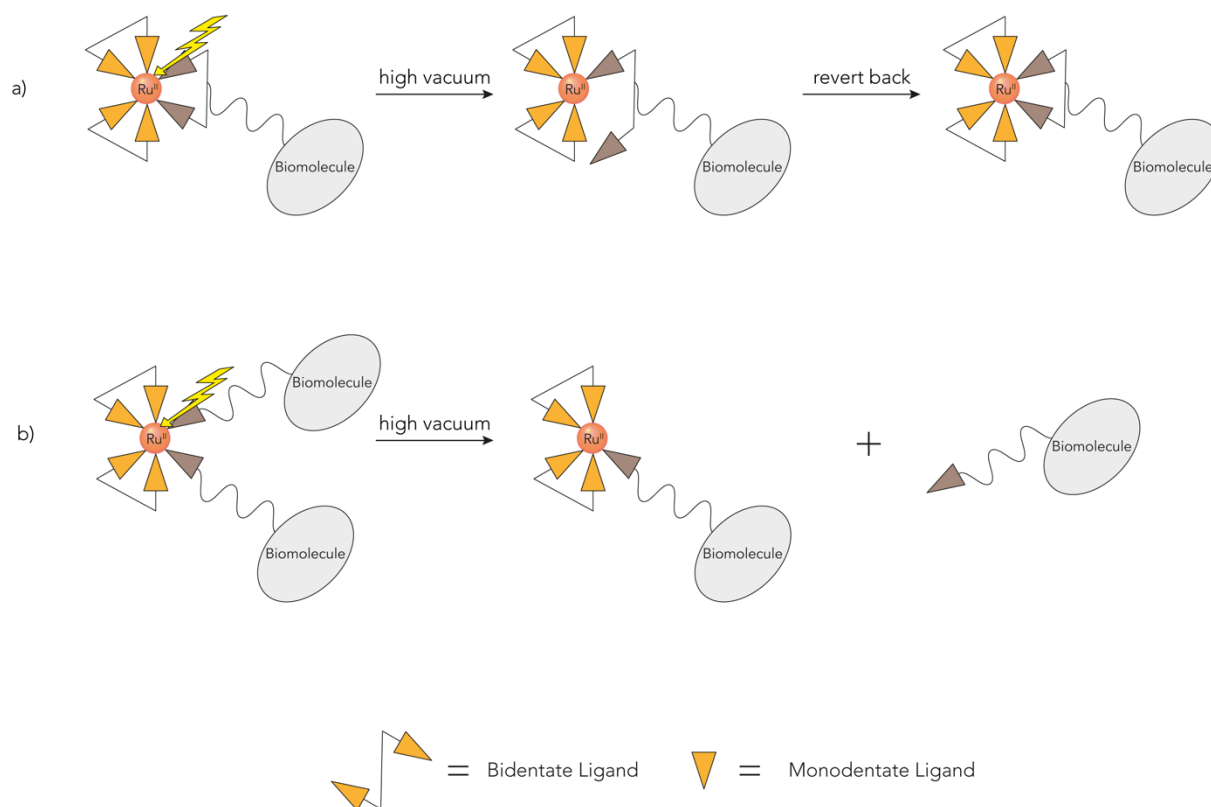
Figure 49: Sketch of the ligand dissociation process in high vacuum, comparing the dissociation of a bidentate ligand with a monodentate ligand; a) the biomolecule is attached on a bidentate ligand, after the irradiation the pentacoordinate intermediate is formed and subsequently rearrangement will restore the hexacoordinate complex; b) the biomolecule is attached on a monodentate ligand and will immediately dissociate from the metal centre.

This argument would rationalise the results hereby this work and lays the foundation for successfully studying the new photo-labile complexes proposed in figure 50.
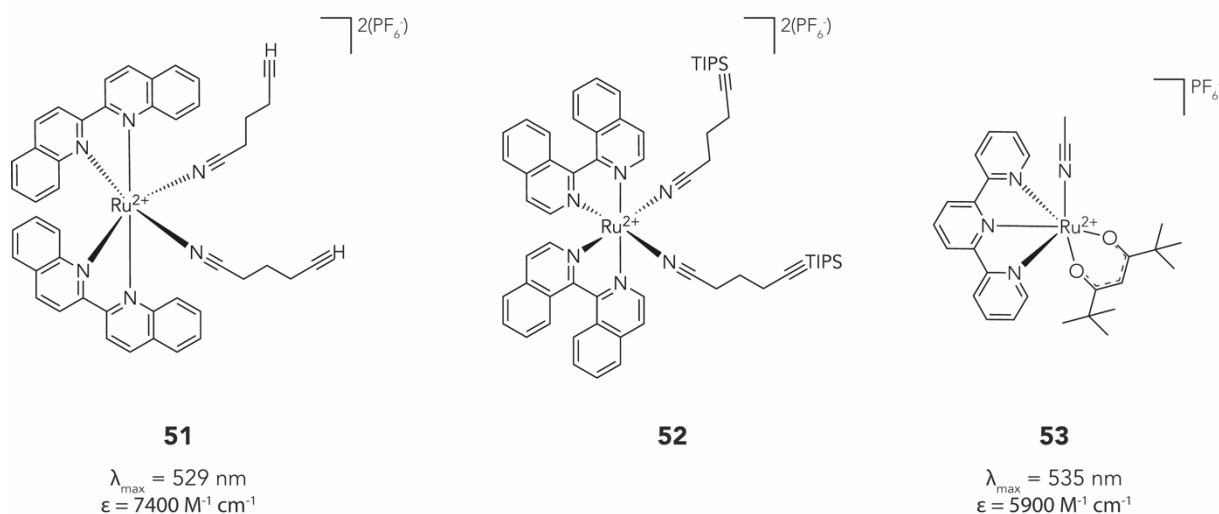
Figure 50: Molecular structure of proposed photo labile complexes, suitable for the photocleavage at 532 nm.

The Ru(II) based complexes **51**-**53** are all suitable candidates for the photo-induced dissociation in the gas-phase as the direct cleavage of a mono-dentate ligand, which should be faster and does not require the support of an additional ligand such as a solvent molecule, is expected to happen upon.

Furthermore, photo-labile complexes **51** and **53** are optimized for the cross-sections at 532 nm (figure 50) and both compounds can perform a ligand exchange with water molecules after irradiation in water.[284,285] These complexes are therefore perfect test-compounds for the investigation of the dissociative process in the gas-phase and could lay the groundwork for further improvements in the molecular design.

An alternative strategy, which employs a partially associative cleavage process could be achieved by a covalently attached latent ligand, as illustrated in figure 51.
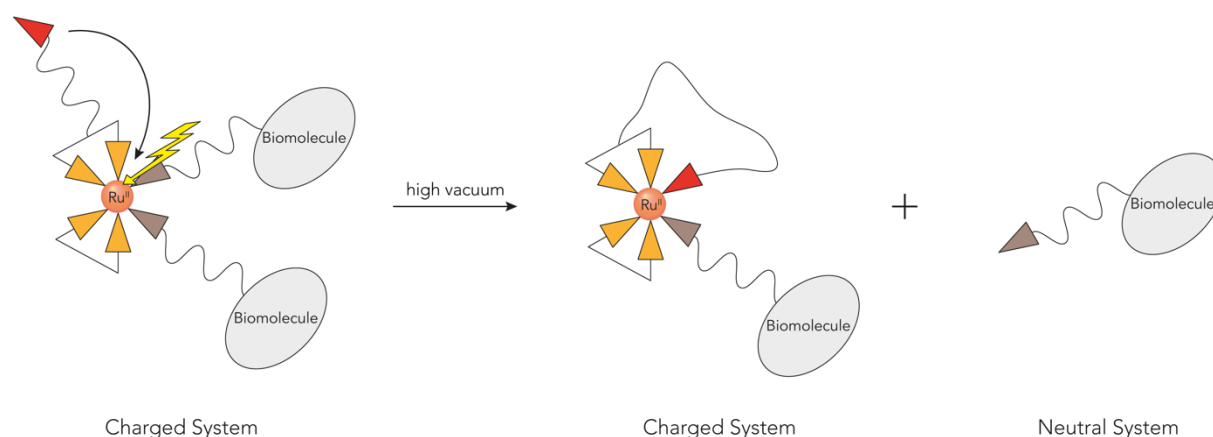
Figure 51: Sketch of a supportive ligand exchange process: (red triangle) is a coordinating moyeti that is covalently linked to a bidentate ligand and can interact with the Ru(II) metal; The ligand exchange will take place between the biomolecule modified ligand (grey triangle) and the tethered latent ligand (red triangle).

Figure 51 outlines the main idea: The photoexcitation of a Ru(II)-based chromophore leads to the dissociation of a monodentate ligand (grey triangle) under concurrent interaction of a latent coordinating group (red triangle). This would require that the ligand exchange process is not exclusively dissociative but has an associative

component. The obtained photoproducts should consist of the newly assembled Ru-complex and the dissociated ligand coupled to a biomolecule.
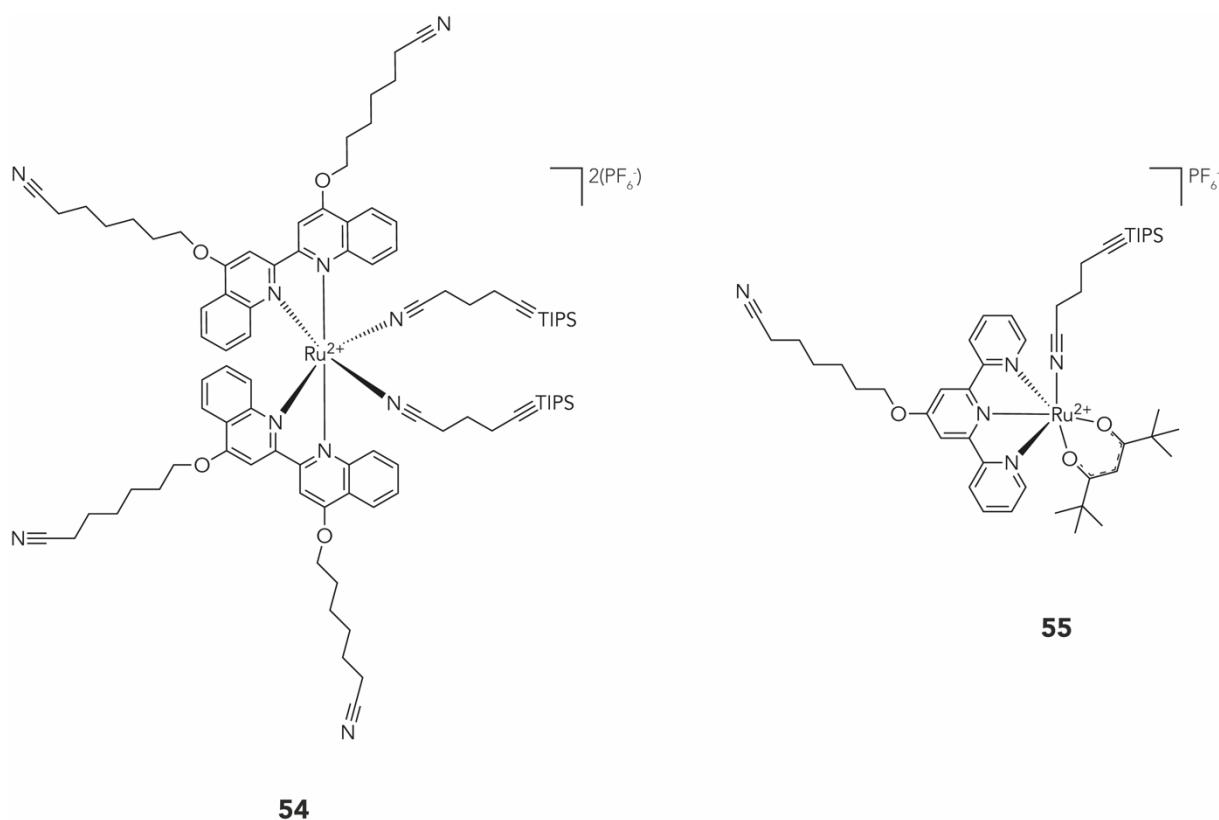
Figure 52: Molecular structure of complexes **54** and **55**.

Figure 52 outlines the molecular structures proposed for the solvent free ligand dissociation in the gas-phase. Complex **54** is composed of biq derivatives equipped with nitrile groups, that can act as coordinating units during the photo-induced ligand exchange. The nitrile groups can be introduced after the complexation reaction, if concurrent complexation during the synthesize of complex **54** is observed. The same strategy could be used for complex **55**, which bears the supporting nitrile on the position 4' of a tridentate tpy ligand.

Chapter 3

Experimental Part

General Remarks

All chemicals and solvents, if commercially available, were purchased either from, *Acros Organics*, *Activate Scientific*, *Alfa Aesar*, *ABCR*, *Apollo Scientific*, *Combi-Blocks*, *Fluorochem*, *Fluka*, *Merck, Sigma-Aldrich*, *TCI* or *VWR* and were used as received unless otherwise stated. Dry solvents were purchased from *Acros Organics* and *Sigma-Aldrich* and used as crown cap. For an inert atmosphere Argon 4.8 from *PanGas* was used. Oxygen-sensitive reactions were performed under inert atmosphere using regular Schlenk-techniques in oven-dried glassware. For this purpose, dry solvents were used which were additionally degassed with argon for at least 15 minutes.

Fourier Transform Infrared Spectroscopy (FT-IR)

Fourier transform infrared (FT-IR) spectra were measured with a IRTracer-100 from *Shimadzu*, in the region of 4500-300 cm^{-1}. The spectra were recorded at room temperature with 150 scans and with a resolution of 2.0 cm^{-1}.

Ultraviolet-Visible Absorption Spectroscopy (UV/Vis)

UV/Vis measurements were recorded on a *Jasco* V-770 spectrophotometer using 117.100F-QS cuvettes from *Hellma Analytics* with 10 mm light path. The wavelength of maxima absorption maxima (λ_{max}) are reported in nm.

Nuclear Magnetic Resonance (NMR) Spectroscopy

NMR measurements were recorded using a *Bruker* DPX-400 (400 MHz for ^{1}H and 101 MHz for ^{13}C), a *Bruker* DRX-500 (500 MHz for ^{1}H and 101 MHZ for ^{13}C) or a *Bruker* Ascend Avance III HD (600 MHz for ^{1}H and 151 MHz for ^{13}C) spectrometer at 298 K if not stated otherwise. Solvents for NMR were purchased from *Cambridge Isotope Laboratories*, *Sigma-Aldrich* or *Fluorochem*. Chemical shifts are given in ppm relative to trimethylsilane (TMS) or the residual proton signal of the deuterated solvent (CDCl$_3$: 7.26 ppm, CDCl$_2$: 5.33 ppm, CD$_3$CN: 1.94 ppm, DMSO-d$_6$: 2.50 ppm, THF-d$_8$: 3.58 ppm) for ^{1}H spectra or the carbon signal of the solvent (CDCl$_3$: 77.1 ppm, CDCl$_2$: 53.8 ppm, CD$_3$CN: 118.2 ppm, DMSO-d$_6$: 39.5 ppm, THF-d$_8$: 67.5 ppm) for ^{13}C spectra. The coupling constants (J) are given in Hertz (Hz), the multiplicities are denoted as: *s* (singlet), *d* (doublet), *t* (triplet), *q* (quartet), m (multiplet) and *br* (broad).

Mass Spectrometry (MS)

MS measurements were recorded either on a *Shimadzu* LC-MS 2020 with a *Dr. Maisch* Reprosher 100 C18-Aqua, 2 mm x 125 mm, 5 µm column or a *Shimadzu* direct injection MS 8040 for Electron Spray Ionization (ESI). MS spectra were measured in *m/z* (%). Gas chromatography-mass spectrometry (GC-MS) was performed on a *Shimadzu* GCMS-QP2010 SE gas chromatography system with a ZB-5HT inferno column (30 m x 0.25 m x 0.25 m), at 1 mL/min He-flow rate (split = 20:1) with a *Shimadzu* mass detector (EI 70 eV). Direct analysis in real time mass spectrometry (DART-MS) was measured on a *IonSense* DART-SVP100 (He, 450°C) connected to a *Shimadzu* LC-MS 2020. High-resolution mass spectra (HRMS) were measured as HR-ESI-ToF-MS with a *Bruker* Maxis 4G instrument or HR-MALDI-FTICR with a *Bruker* solariX 94.

Thin Layer Chromatography (TLC)

TLC was performed on a 0.25 mm precoated glass plate (silica gel 60 F_{254}) from *Merck*. Substances were detected at 254 nm by fluorescence quenching or at 366 nm by self-fluorescence. If necessary, the plates were stained with $KMnO_4$, ninhydrin or $FeSO_4$.

Column Chromatography (CC)

For normal phase CC SilicaFlash® P60 (particle size 40 – 63 μm) from *SiliCycle* was used.

High-Performance Liquid Chromatography (HPLC)

HPLC was performed on a *Shimadzu* LC-20AD and a LC-20AT HPLC, respectively, was used equipped with a diodearray UV/Vis detector (SPD-M10A VP from *Shimadzu*, λ = 200 – 600 nm) and a column oven from *Shimadzu* CTO-20AC. The used column for analytical reverse phase was a Reprosil 100 C18, 5 μm, 4.6 mm x 250 mm from *Dr. Maisch GmbH*, for preparative reverse phase was a Reprosil 100 C18, 10 μm, 250 x 30 mm from *Dr. Maisch GmbH*.

Langmuir-Blodgett (LB)

LB assembly and deposition was performed on a *Kibron* Microtrough G1 with trough inner dimensions of 5 mm x 80 mm x 260 mm and a Dip Coater LayerX 90 at 298 K if not stated otherwise. The trough and the barriers were rinsed first with deionised water, then with ethanol and finally with chloroform. The used deionised water was provided from a Milli-Q water dispenser.

Polymerization of Complex **27**

The data set (Table 4) was fitted with an exponential decay equation (see fit below)
giving $y = 0.779\ e^{-x/18.116} + 0.0656$.
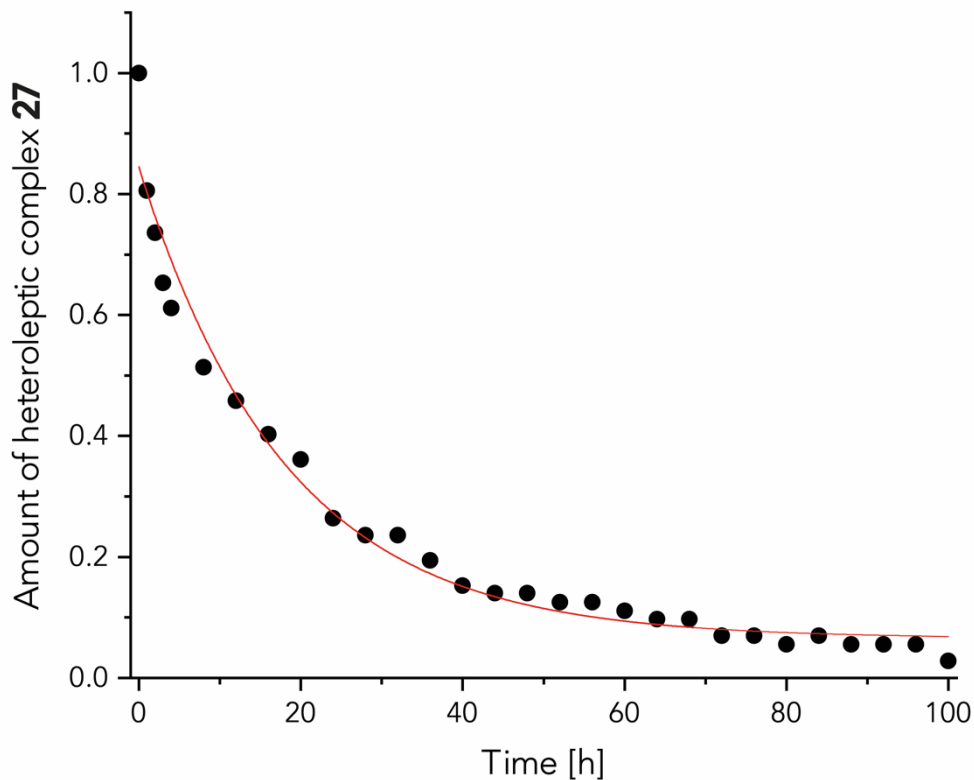
Figure 53: Plotted amount of heteroleptic complex **27** versus time, fitted with an exponential decay (red line).

The decrease in concentration of heteroleptic complex **27** can be best fitted with an
exponential decay (red line) suggesting a half-life $t_{1/2}$ of 12.5 h for the reaction (i. e.
when 50 % of the starting material is consumed).
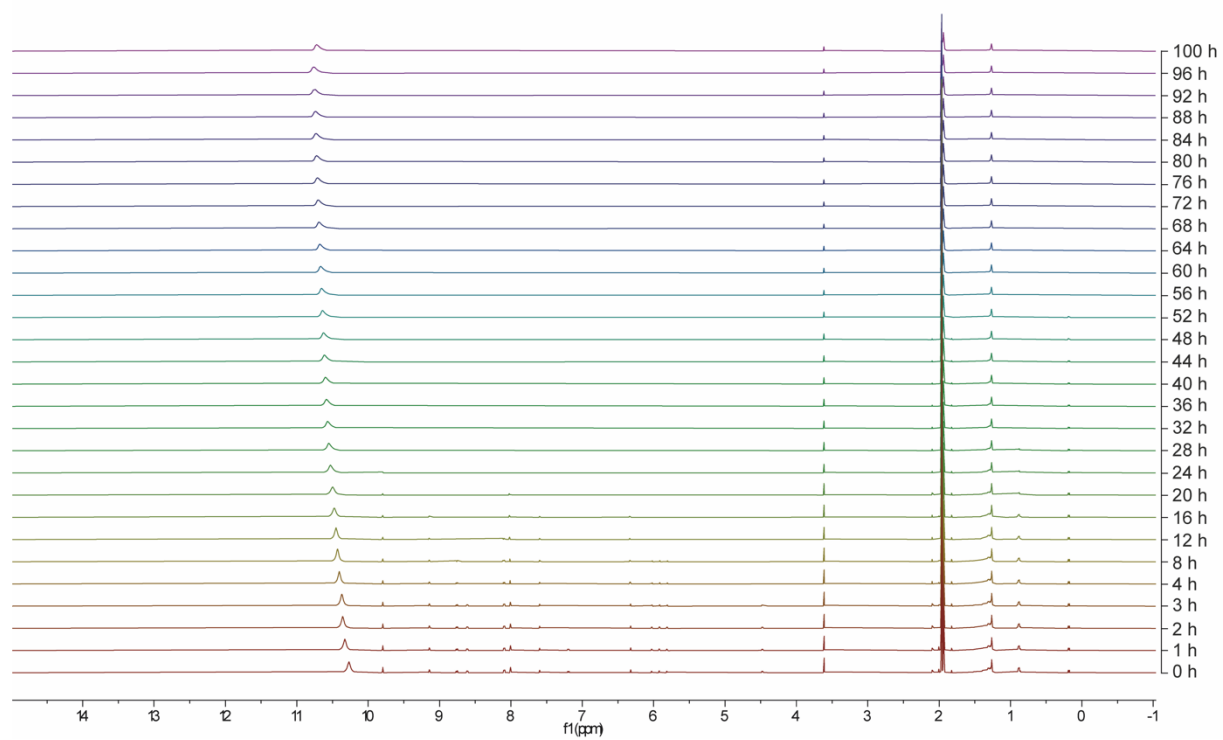
Figure 54: Polymerization reaction of compound **27** monitored over 100 h by ^{1}H-NMR.

Contact Angle Measurements

Contact angle measurements were performed using 2 µL from a Milli-Q water dispenser. The droplets were recorded on a *Krüss* FM40 EasyDrop Machine and were analysed with Drop Shape Analysis for Windows software from *Krüss*. Pictures for the contact angle measurements were only considered if the focus assistant did show a value of more than 90.

Contact angle on bare Glass-Slide [°]	Contact angle of deposited **27** film on Glass-Slide [°]
30	72.4
33.8	74
28.9	76.1
27.8	73.2
31.7	68.8
30.1	73.8

Table 4: Contact angle measurements of bare glass-slide and deposited **27** on glass-slide.

Contact angle of bare Si-Wafer [°]	Contact angle of deposited **27** film on Si-Wafer [°]
39.2	57
38.7	57.9
35.4	53.9
36.4	58.4
34.5	59.6
36.0	63.6

Table 5: Contact angle measurements of bare Si-wafer and deposited **27** on Si-wafer.

.

Contact angle of bare CaF-Slide[°]	Contact angle of deposited **27** film on CaF-Slide [°]
49.8	61.4
47.4	57.5
43.6	58.1
47	57.6
48.4	54.9
43.1	63.5

Table 6: Contact angle measurements of bare CaF-slide and deposited **27** on CaF-slide.

Brewster Angle Microscope (BAM)

Brewster angle microscope (BAM) experiments were performed with the EP3SW system (*Nanofilm Technologie GmbH*, Göttingen, Germany) equipped with a ND:YAG laser at λ = 532 nm, a long distance objective (*Nikon*, 20x), and a monochrome CCD camera. The size of the BAM image corresponds to 220 x 250 µm^2 , with a resolution of 1 µm.

Atomic Force Microscopy (AFM)

Non-contact Atomic Force Microscopy (nc-AFM) measurements were performed with a custom-built non-contact atomic force microscope (AFM) from the department of Physics of the University of Basel. The microscope is working at room temperature under ultra high vacuum (UHV) conditions. The microscope is controlled via a *Nanonis* electronics RC5. PPP-NCL cantilevers (*Nanosensor*) were used as sensor (typical resonance frequency of f 1 = 170 kHz, oscillation amplitude A 1 = 2–5 nm, and f2 = 1 MHz, A2 = 400–800 pm. Their preparation consisted of annealing for 1 h at 400 K followed by tip Ar + sputtering for 90 s at 680 eV at an Ar + pressure of 3 × 10^{-6} mbar. The base pressure of the UHV system during AFM measurements is maintained at 2 × 10^{-11} mbar

X-Ray Photoelectron Spectroscopy (XPS)

The prepared support surfaces were dried on a Schlenk line under a vacuum of 1×10^{-2} mbar for 18 h and directly transferred to the UHV XPS chamber without baking the vacuum. The pressure in the XPS chamber was kept in the range of ~2- 4×10^{-9} mbar. The UHV chamber was equipped with a monochromatic Al-Kα X-ray source (hν = 1486.6 eV) and a photoelectron spectroscopy analyser (VG ESCALAB 210) with an energy resolution of 0.5 eV at 20 eV pass energy. Surveys and

high resolution core level spectra were measured using 10 scans at a pass energy of 100 eV and 60 scans at a pass energy of 20 eV, respectively. The Au $4f^{7/2}$ peak was set to 84 eV for electron binding energy (BE) calibration. Fitting of the core level lines was performed using DoniachSunjic functions[286] after a Shirley or Tougaard background subtraction[287], using *UNIFIT* for Windows (Version 2015) software[288]. The intensities were corrected using Scofield sensitivity factors and the transmission function measured with our system as described by Scofield[289]. Wafers that were exposed to XPS measurement were not further used to prevent falsification of the results by a damaged monolayer due to X-ray irradiation during the XPS measurement.[290]

Synthetic Procedures

"Hydrophilic" Tpy Ligand

1
C$_8$H$_8$BrNO$_2$
230.06 g/mol
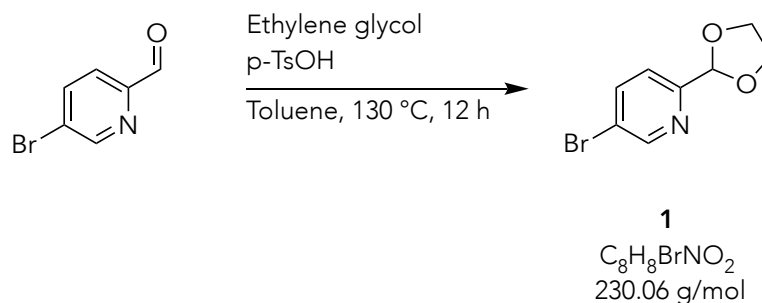
5-bromo-2-(1,3-dioxolane-2-yl)pyridine (1): A 250 mL round-bottomed flask with a Dean-Stark apparatus was charged with 5-bromopicolinaldehyde (5.00 g, 26.9 mmol, 1.0 eq), ethylene glycol (3.00 mL, 53.8 mmol, 2.0 eq.), *p*-toluenesulfonic acid monohydrate (102 mg, 54.0 µmol, 2 mol%) and toluene (100 mL). The reaction mixture was refluxed for 12 h and after the TLC confirmed full conversion of the starting material, the reaction was cooled to room temperature, quenched with a saturated aqueous solution of sodium bicarbonate (20 mL) and the aqueous phase was washed three times with EtOAc. The combined organic fractions were dried over MgSO$_4$, filtered and concentrated under reduced pressure. The crude was subjected to column chromatography (EtOAc:cyclohexane = 1:4) to afford compound **1** as a yellowish oil (6.14 g, 26.9 mmol, quant.).

Analytical data for 1:

^{1}H NMR (500 MHz, CDCl$_3$, 25 °C) **δ** = 8.45 (d, J = 2.5 Hz, 1H), 7.64 (dd, J = 8.2, 2.4 Hz, 1H), 7.49 (d, J = 8.2 Hz, 1H), 5.81 (s, 1H), 4.14 – 3.96 (m, 4H).

^{13}C NMR (126 MHz, CDCl$_3$, 25 °C) **δ** = 148.86, 142.96, 136.91, 133.26, 127.99, 101.37, 65.55 ppm.

HRMS (ESI-ToF, MeOH, positive mode): calc. for [C$_8$H$_9$NBrO$_2$]$^+$ 229.9811; found 229.9815.

2
$C_{20}H_{35}NO_2Sn$
440.22 g/mol
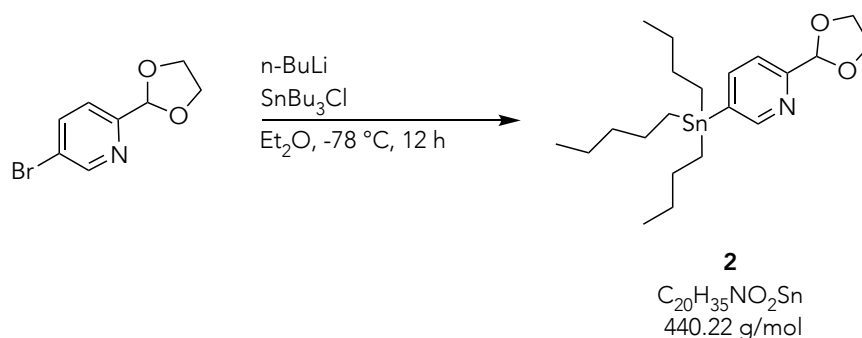
2-(1,3-dioxolan-2-yl)-5-(tributylstannyl)pyridine (2): In an oven-dried 100 mL Schlenk tube under argon flow 5-bromo-2-(1,3-dioxolane-2-yl)pyridine (**1**, 10.4 g, 45.2 mmol, 1.0 eq.) and dry Et_2O (60 mL) were added. The reaction mixture was cooled to -78 °C, before *n*-BuLi (2.5 M in hexane, 20 mL, 64.1 mmol, 1.1 eq.) was added dropwise. After 30 minutes, $SnBu_3Cl$ (15.0 mL, 49.7 mmol, 1.1 eq.) was added and the reaction mixture was stirred at -78 °C gradually warming up to room temperature overnight. The reaction was quenched with H_2O (20 mL) and then extracted with EtOAc (3 x 40 mL). The combined organic phases were dried over $MgSO_4$, filtered and concentrated under reduced pressure. The residue was purified by flash column chromatography (EtOAc:cyclohexane = 1:4) to give the desired compound as a yellow oil (5.45 g, 12.6 mmol, 98 %).

Analytical data for 2:

¹H NMR (500 MHz, $CDCl_3$, 25 °C) **δ** = 8.82 (d, J = 2.2 Hz, 1H), 7.59 (dd, J = 7.7, 2.3 Hz, 1H), 7.43 (d, J = 7.7 Hz, 1H), 5.81 (s, 1H), 4.15 – 3.99 (m, 4H), 1.58 – 1.52 (m, 6H), 1.35 – 1.29 (m, 6H), 1.13 – 1.09 (m, 6H), 0.87 (t, J = 7.3 Hz, 9H).

¹³C NMR (126 MHz, $CDCl_3$, 25 °C) **δ** = 175.64, 148.99, 131.99, 131.62, 131.29, 102.53, 65.55, 29.19, 27.47, 13.81, 9.98 ppm.

HRMS (ESI-ToF, MeOH, positive mode): calc. for $[C_{20}H_{36}NO_2Sn]^+$ 442.1766; found 442.1766.

3
C₂₁H₁₉N₃O₄
377.40 g/mol
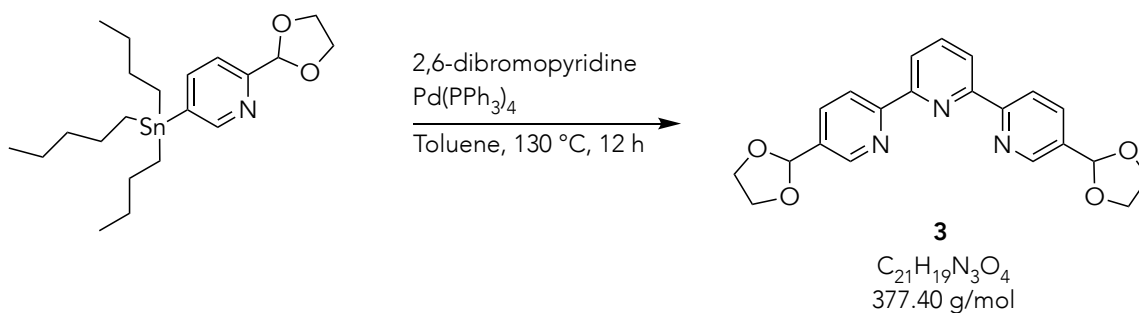
5,5''-di(1,3-dioxolan-2-yl)-2,2':6',2''-terpyridine (3): An oven-dried 50 mL two-necked round-bottomed flask was purged with argon and charged with 2,6-dibromopyridine (367 mg, 1.55 mmol, 1.0 eq.), 2-(1,3-dioxolan-2-yl)-5-(tributylstannyl)pyridine (**2**, 1.50 g, 3.41 mmol, 2.2 eq.) and toluene (20 mL). The mixture was degassed with argon for 15 minutes and then Pd(PPh₃)₄ (179 mg, 1 %mol, 0.1 eq.) was added and further degassed for 5 minutes. The reaction mixture was heated to reflux for 12 h. After TLC showed full conversion of the starting material, the reaction was stopped by cooling down at room temperature and the solvent was removed under reduced pressure. The residue was plugged by short flash column chromatography (SiO₂, 10% K₂CO₃) (DCM) to remove the toxic tin byproducts. The crude was purified by flash column chromatography (acetone:cyclohexane = 1:5 + 0.1% NH₄OH) to give the titled compound as a yellowish solid (510 mg, 1.55 mmol, 87 %).

Analytical data for 3:

¹H NMR (500 MHz, CDCl₃, 25 °C) **δ** = 8.75 (d, J = 2.2 Hz, 2H), 8.59 (d, J = 8.2 Hz, 2H), 8.44 (d, J = 7.8 Hz, 2H), 7.91 (dt, J = 8.2, 2.1 Hz, 3H), 5.90 (s, 2H), 4.14 – 3.98 (m, 8H).

¹³C NMR (126 MHz, CDCl₃, 25 °C) **δ** = 156.90, 155.06, 147.73, 137.91, 135.09, 133.62, 121.37, 120.75, 101.99, 65.41 ppm.

HRMS (ESI-ToF, MeOH/MeCN, positive mode): calc. for [C₂₁H₂₀N₃O₄]⁺ 378.1448; found 378.1455.

4
$C_{17}H_{11}N_3O_2$
289.29 g/mol
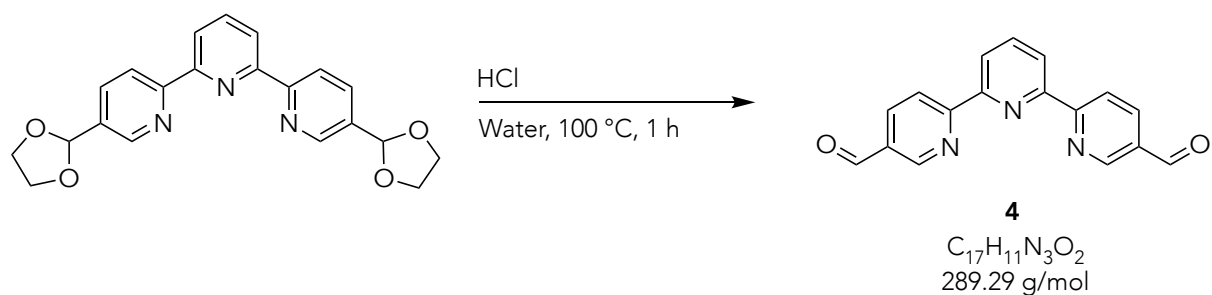
[5,5''-diformyl-2,2':6',2''-terpyridine (4): A 100 mL round-bottomed flask was charged with 5,5''-di(1,3-dioxolan-2-yl)-2,2':6',2''-terpyridine (**4**, 509 mg, 1.35 mmol, 1.0 eq.), hydrochloric acid (37 %, 10 mL) and water (40 mL). The reaction mixture was heated to reflux and stirred for 1 h. Afterwards the mixture was allowed to cool down at room temperature and precipitation was filtered, washed with Et_2O (2 x 10 mL) and dried under reduced pressure. The hydrochloride specie was suspended in EtOH and the pH was adjusted to 8 with an aqueous solution of sodium hydroxide (aq. 10%) and an aqueous solution of sodium bicarbonate. The aqueous phase was washed with EtOAc. The combined organic layers were washed with brine, dried over $MgSO_4$, filtered and concentrated under reduced pressure. The solid was purified by column chromatography (acetone:cyclohexane = 1:1 + 0.1 % NH_4OH) to yield the desired product as an off white solid (350 mg, 1.21 mmol, 90 %).

Analytical data for 4:

¹H NMR (500 MHz, $CDCl_3$, 25 °C) **δ** = 10.21 (s, 2H), 9.16 (dd, J = 2.2, 0.9 Hz, 2H), 8.81 (d, J = 8.2 Hz, 2H), 8.64 (d, J = 7.8 Hz, 2H), 8.35 (dd, J = 8.2, 2.2 Hz, 2H), 8.06 (t, J = 7.8 Hz, 1H).

¹³C NMR (126 MHz, $CDCl_3$, 25 °C) **δ** = 190.68, 160.50, 154.56, 151.96, 138.52, 136.96, 131.45, 123.39, 121.50 ppm.

HRMS (ESI-ToF, MeOH, positive mode): calc. for $[C_{17}H_{11}N_3NaO_2]^+$ 312.0743; found 312.0745.

5

$C_{17}H_{30}BrNSn$

447.05 g/mol
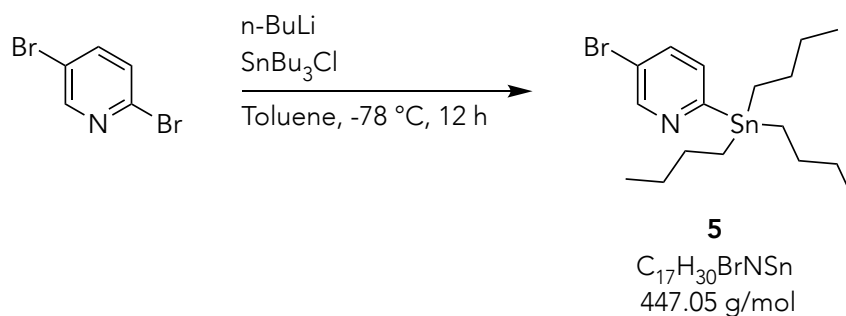
5-bromo-2-(tributylstannyl)pyridine (5): In an oven-dried 100 mL Schlenk tube under argon flow 2,5-dibromopyridine (8.00 g, 33.8 mmol, 1.0 eq.) and dry toluene (40 mL) were added. The reaction mixture was cooled to -78 °C, before *n*-BuLi (2.5 M in hexane, 15.0 mL, 37.2 mmol, 1.1 eq.) was added dropwise. After 30 minutes, SnBu₃Cl (90 %, 11.2 mL, 37.2 mmol, 1.1 eq.) was added and the reaction mixture was stirred at -78 °C gradually warming up to room temperature overnight. The reaction was quenched with H_2O (20 mL) and then extracted with EtOAc (3 x 30 mL). The combined organic phases were dried over $MgSO_4$, filtered and concentrated under reduced pressure. The residue was purified by flash column chromatography (EtOAc: cyclohexane = 1:4) to give the desired compound as a yellowish oil (13.80 g, 30.8 mmol, 91 %).

Analytical data for 5:

¹H NMR (500 MHz, $CDCl_3$, 25 °C) **δ** = 8.81 (dd, J = 2.3, 0.8 Hz, 1H), 7.63 (dd, J = 7.9, 2.4 Hz, 1H), 7.29 (dd, J = 8.0, 0.8 Hz, 1H), 1.59 – 1.50 (m, 6H), 1.35 – 1.26 (m, 6H), 1.14 – 1.05 (m, 6H), 0.90 – 0.86 (m, 12H).

¹³C NMR (126 MHz, $CDCl_3$, 25 °C) **δ** = 172.21, 151.41, 135.84, 133.01, 120.42, 29.01, 27.30, 13.66, 9.94 ppm.

HRMS (ESI-ToF, MeOH, positive mode): calc. for $[C_{17}H_{31}BrNSn]^+$ 448.0648; found 448.0654.

6
$C_{15}H_9Br_2N_3$
391.07 g/mol
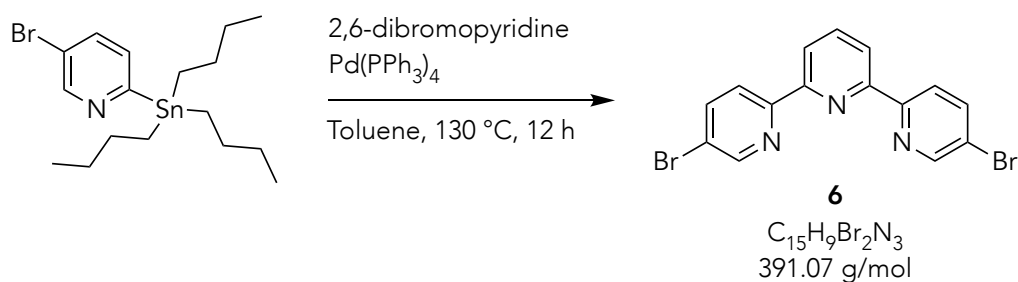
5,5''-dibromo-2,2':6',2''-terpyridine (6): An oven-dried 100 mL two-necked round-bottomed flask was purged with argon and charged with 2,6-dibromopyridine (1.32 g, 5.59 mmol, 1.0 eq.), 5-bromo-2-(tributylstannyl)pyridine (**5**, 6.50 g, 14.5 mmol, 2.6 eq.) and dry toluene (50 mL). The mixture was degassed with argon for 15 minutes and then Pd(PPh₃)₄ (323 mg, 5 %mol, 0.05 eq.) was added and further degassed for 5 minutes. The reaction mixture was heated to reflux for 24 h. After TLC showed full conversion of the starting material, the reaction was stopped by cooling down at room temperature and the solvent was removed under reduced pressure. The residue was plugged by short flash column chromatography (SiO₂, 10% K₂CO₃) (DCM) to remove the toxic tin byproducts. The crude was purified by flash column chromatography (acetone:cyclohexane = 1:10 + 0.1 % NH₄OH) to give the titled compound as a white solid (1.05 g, 2.69 mmol, 48 %).

Analytical data for 6:

¹H NMR (500 MHz, CDCl₃, 25 °C) **δ** = 8.74 (dd, J = 2.4, 0.7 Hz, 2H), 8.48 (dd, J = 8.5, 0.8 Hz, 2H), 8.43 (d, J = 7.8 Hz, 2H), 7.99 – 7.94 (m, 3H).

¹³C NMR (126 MHz, CDCl₃, 25 °C) **δ** = 154.66, 154.64, 150.36, 139.63, 138.29, 122.53, 121.41, 121.37 ppm.

HRMS (ESI-ToF, MeOH, positive mode): calc. for [C₁₅H₉Br₂N₃Na]⁺ 411.9055; found 411.9060.

7
C$_9$H$_9$IO$_2$
276.07 g/mol
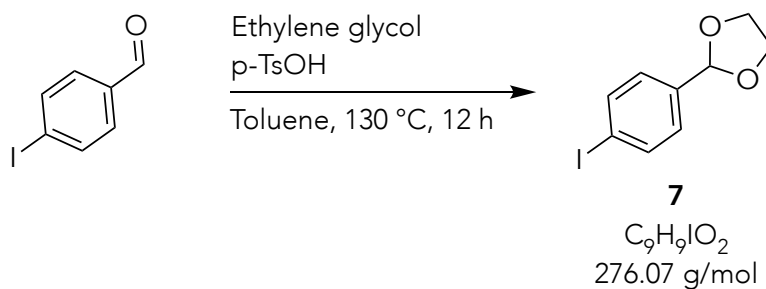
2-(4-iodophenyl)-1,3-dioxolane (7): A 250 mL round-bottomed flask with a Dean-Stark apparatus was charged with 4-iodobenzaldehyde (8.27 g, 35.7 mmol, 1.0 eq), ethylene glycol (20.0 mL, 357 mmol, 10.0 eq.), *p*-toluenesulfonic acid monohydrate (136 mg, 0.75 mmol, 2 mol%) and toluene (100 mL). The reaction mixture was heated to reflux for 12 h. After the TLC confirmed full conversion of the starting material, the reaction was cooled to room temperature, quenched with a saturated aqueous solution of sodium bicarbonate (20 mL) and the aqueous phase was extracted with EtOAc (3 x 20 mL). The combined organic layers were dried over MgSO$_4$, filtered and concentrated under reduced pressure. The crude was purified with column chromatography (EtOAc:cyclohexane = 1:7) to afford compound **7** as a yellowish oil (9.75 g, 35.3 mmol, 99 %).

Analytical data for 7:

¹H NMR (500 MHz, CDCl$_3$, 25 °C) **δ** = 7.72 (d, J = 8.4 Hz, 2H), 7.22 (d, J = 8.2 Hz, 2H), 5.76 (s, 1H), 4.10 – 4.03 (m, 4H).

¹³C NMR (126 MHz, CDCl$_3$, 25 °C) **δ** = 137.62, 136.61, 128.48, 103.26, 95.24, 65.45 ppm.

GCMS (EI⁺, 70 eV): *m/z* [ion, intensity (%)] = 276.7 (M⁺, 4), 149.0 (M⁻ -I, 65).

8

C$_{21}$H$_{36}$O$_2$Sn

439.23 g/mol
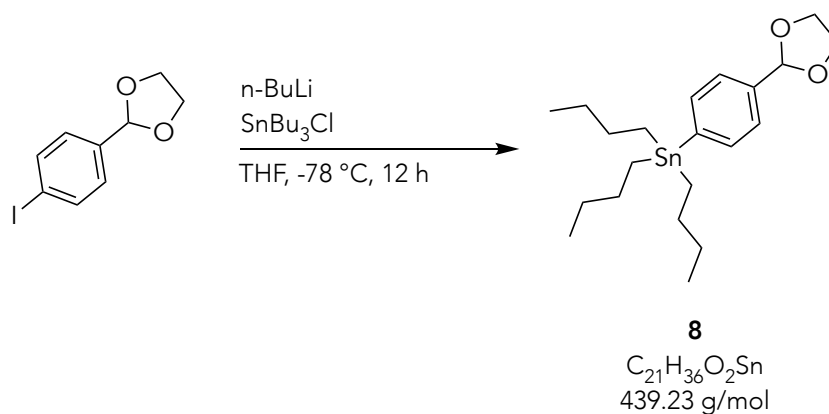
(4-(1,3-dioxolan-2-yl)phenyl)tributylstannane (8): In an oven-dried 100 mL Schlenk tube under argon flow (2-(4-iodophenyl)-1,3-dioxolane (**7**, 10.2 g, 37.1 mmol, 1.0 eq.) and dry THF (40 mL) were added. The reaction mixture was cooled to -78 °C, before *n*-BuLi (1.6 M in hexane, 25.5 mL, 40.8 mmol, 1.1 eq.) was added dropwise. After 30 min, SnBu$_3$Cl (90 %, 14.5 mL, 48.2 mmol, 1.3 eq.) was added and the reaction mixture was stirred at -78 °C gradually warming up to room temperature overnight. The reaction was quenched with H$_2$O (20 mL) and then extracted with EtOAc (3 x 30 mL). The combined organic phases were dried over MgSO$_4$, filtered and concentrated under reduced pressure. The residue was purified by flash column chromatography (EtOAc:cyclohexane = 1:8) to give the desired compound as a yellow oil (12.5 g, 28.4 mmol, 77 %).

Analytical data for 8:

^{1}H NMR (500 MHz, CDCl$_3$, 25 °C) **δ** = 7.49 (d, J = 8.0 Hz, 2H), 7.43 (d, J = 8.0 Hz, 2H), 5.80 (s, 1H), 4.15 – 4.03 (m, 4H), 1.67 – 1.44 (m, 6H), 1.33 (d, J = 7.2 Hz, 6H), 1.07 – 1.04 (m, 6H), 0.88 (t, J = 7.2 Hz, 12H).

^{13}C NMR (126 MHz, CDCl$_3$, 25 °C) **δ** = 143.57, 137.57, 136.61, 125.92, 104.05, 65.46, 29.20, 27.50, 17.66, 13.80, 9.71.ppm.

GCMS (EI$^+$, 70 eV): *m/z* [ion, intensity (%)] = 382.7 (M$^+$ - C$_4$H$_{10}$, 86), 326.7 (M$^+$ -2 C$_4$H$_{10}$, 68), 268.7 (M$^+$ -3 C$_4$H$_{10}$, 87).

9
C₃₃H₂₇N₃O₄
529.60 g/mol
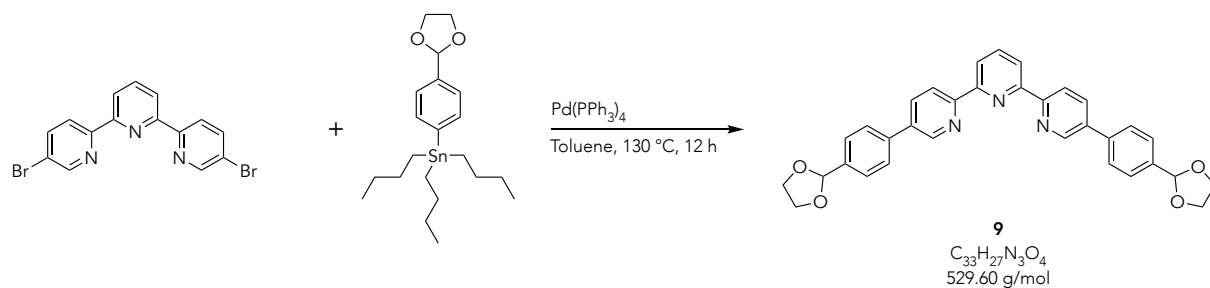
5,5''-bis(4-(1,3-dioxolan-2-yl)phenyl)-2,2':6',2''-terpyridine (9): An oven-dried 100 mL two-necked round-bottomed flask was purged with argon and charged with 5,5''-dibromo-2,2':6',2''-terpyridine (**6**, 400 mg, 1.02 mmol, 1.0 eq.), (4-(1,3-dioxolan-2-yl)phenyl)tributylstannane (**8**, 2.69 g, 6.12 mmol, 6.0 eq.) and dry toluene (30 mL). The mixture was degassed with argon for 15 min and then Pd(PPh₃)₄ (118 mg, 0.1 mmol, 0.1 eq.) was added and further degassed for 5 min. The reaction mixture was heated to reflux for 24 h. After TLC showed full conversion of the starting material, the reaction was stopped by cooling down at room temperature and the solvent was removed under reduced pressure. The residue was plugged by short flash column chromatography (SiO₂, 10 % K₂CO₃) (DCM) to remove the toxic tin byproducts. The crude was purified by flash column chromatography (acetone: cyclohexane = 1:5 + 0.1 % NH₄OH) and automated recyclable GPC to give the titled compound as a white solid (66.0 mg, 125 µmol, 12 %).

Analytical data for 9:

¹H NMR (500 MHz, CDCl₃, 25 °C) **δ** = 8.94 (dd, J = 2.4, 0.8 Hz, 2H), 8.71 (dd, J = 8.2, 0.8 Hz, 2H), 8.50 (d, J = 7.8 Hz, 2H), 8.07 (dd, J = 8.2, 2.4 Hz, 2H), 7.99 (t, J = 7.8 Hz, 1H), 7.69 (s, 2H), 7.64 (s, 2H), 5.91 (s, 2H), 4.18 – 4.08 (m, 8H).

¹³C NMR (126 MHz, CDCl₃, 25 °C) **δ** = 155.38, 155.29, 147.80, 138.74, 138.15, 138.09, 136.30, 135.36, 127.40, 127.30, 121.25, 121.17, 103.55, 65.55 ppm.

HRMS (ESI-ToF, MeOH, positive mode): calc. for [C₃₃H₂₈N₃O₄]⁺ 530.2074; found 530.2081, calc for [C₃₃H₂₈N₃NaO₄]⁺ 552.1894, found 552.1890.

10
C$_{29}$H$_{19}$N$_3$O$_2$
441.49 g/mol
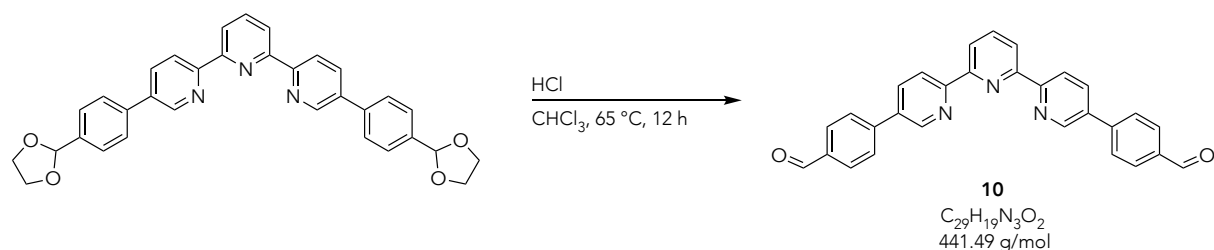
4,4'-([2,2':6',2''-terpyridine]-5,5''-diyl)dibenzaldehyde (10): A 20 mL round-bottomed flask was charged with 5,5''-bis(4-(1,3-dioxolan-2-yl)phenyl)-2,2':6',2''-terpyridine (**9**, 10 mg, 18.9 µmol, 1.0 eq.), hydrochloric acid (37 %, 1.00 mL) and CHCl$_3$ (10 mL). The reaction mixture was heated to reflux 1 h. After the TLC showed full conversion of the starting material, the reaction was stopped by cooling down at room temperature. Afterwards the pH was adjusted to 8 with an aqueous solution of sodium hydroxide (10 %) and a saturated aqueous solution of sodium bicarbonate. The aqueous phase was extracted with DCM (3 x 10 mL) and the combined organic layers were washed with brine, dried over MgSO$_4$, filtered and concentrated under reduced pressure. The solid was purified by column chromatography (acetone:cyclohexane = 1:4 + 0.1 % NH$_4$OH) to yield the desired product as an off white solid (8.00 mg, 18.0 µmol, 96 %).

Analytical data for **10**:

^{1}H NMR (500 MHz, CDCl$_3$, 25 °C) **δ** = 10.12 (s, 2H), 9.48 (d, J = 1.9 Hz, 2H), 8.98 (dd, J = 8.5, 2.2 Hz, 2H), 8.84 (d, J = 8.6 Hz, 2H), 8.59 (d, J = 7.7 Hz, 2H), 8.49 (dd, J = 8.6, 7.3 Hz, 1H), 8.23 (d, J = 8.4 Hz, 4H), 7.97 (d, J = 8.3 Hz, 4H).

^{13}C NMR (126 MHz, CDCl$_3$, 25 °C) **δ** = 195.04, 146.65, 145.90, 145.74, 142.39, 141.27, 140.79, 138.71, 137.14, 132.20, 128.40, 126.09, 125.33 ppm.

HRMS (ESI-ToF, MeOH, positive mode): calc. for [C$_{29}$H$_{20}$N$_3$O$_2$]$^+$ 442.1550; found 442.1547.

11
$C_{18}H_{33}NSn$
382.18 g/mol
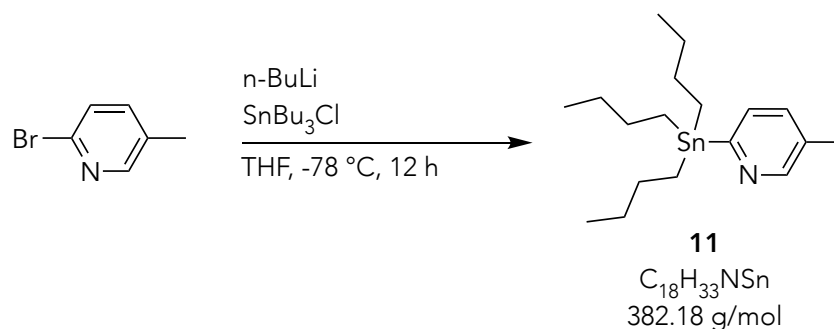
5-Methyl-2-(tributylstannyl)pyridine (11): In an oven-dried 100 mL Schlenk tube under argon flow 2-bromo-5-methylpyridine (5.0 g, 29.1 mmol, 1.0 eq.) and dry THF (40 mL) were added. The reaction mixture was cooled to -78 °C, before *n*-BuLi (2.5 M in hexane, 12.8 mL, 32.0 mmol, 1.1 eq.) was added dropwise. After 30 min, SnBu₃Cl (95 %, 9.1 mL, 32.0 mmol, 1.1 eq.) was added and the reaction mixture was stirred at - 78 °C gradually warming up to room temperature overnight. The reaction was quenched with H_2O (20 mL) and then extracted with EtOAc (3 x 30 mL). The combined organic phases were dried over MgSO₄, filtered and concentrated under reduced pressure. The residue was purified by flash column chromatography (EtOAc: cyclohexane = 1:10) to give the desired compound as a yellowish oil (10.9 g, 29.1 mmol, 98 %).

Analytical data for **11**:

¹H NMR (500 MHz, CDCl₃, 25 °C) **δ** = 8.59 (s, 1H), 7.33 – 7.28 (m, 2H), 2.28 (q, J = 0.9 Hz, 3H), 1.59 – 1.51 (m, 6H), 1.32 (dq, J = 14.3, 7.3 Hz, 5H), 1.13 – 1.08 (m, 6H), 0.87 (t, J = 7.3 Hz, 9H).

¹³C NMR (126 MHz, CDCl₃, 25 °C) **δ** = 169.71, 151.43, 134.11, 131.96, 131.37, 29.22, 27.47, 18.62, 13.80, 9.87 ppm.

HRMS (ESI-ToF, MeOH, positive mode): calc. for $[C_{18}H_{34}NSn]^+$ 384.1711; found 384.1716.

12
C_{17}H_{15}N_3
361.33 g/mol
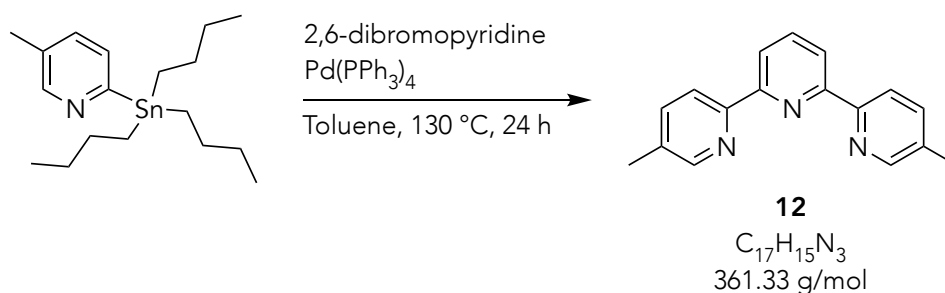
5,5''-Dimethyl-2,2':6',2''-terpyridine (12): An oven-dried 100 mL two-necked round-bottomed flask was purged with argon and charged with 2,6-dibromopyridine (275 mg, 1.16 mmol, 1.0 eq.), 5-methyl-2-(tributylstannyl)pyridine (**11**, 1.33 g, 3.48 mmol, 3.0 eq.) and dry toluene (20 mL). The mixture was degassed with argon for 15 min and then Pd(PPh_3)_4 (134 mg, 10 %mol, 0.1 eq.) was added and further degassed for 5 min. The reaction mixture was heated to reflux for 24 h. After TLC showed full conversion of the starting material, the reaction was stopped by cooling down at room temperature and the solvent was removed under reduced pressure. The residue was plugged by short flash column chromatography (SiO_2, 10 % K_2CO_3) (DCM) to remove the toxic tin byproducts. The crude was purified by flash column chromatography (acetone:cyclohexane = 1:10 + 0.1 % NH_4OH) to give the titled compound as a white solid (200 mg, 1.16 mmol, 66 %).

Analytical data for 12:

^{1}H NMR (500 MHz, CDCl_3, 25 °C) δ = 8.53 – 8.48 (m, 4H), 8.38 (d, J = 7.8 Hz, 2H), 7.92 (t, J = 7.8 Hz, 1H), 7.65 (ddd, J = 8.1, 2.4, 0.9 Hz, 2H), 2.41 (s, 6H).

^{13}C NMR (126 MHz, CDCl_3, 25 °C) δ = 155.56, 153.98, 149.70, 137.92, 137.51, 133.52, 120.83, 120.50, 18.55 ppm.

HRMS (ESI-ToF, MeOH, positive mode): calc. for [C_{17}H_{16}N_3]$^+$ 162.1339; found 262.1337.

13
$C_{17}H_{11}N_3O_4$
321.29 g/mol
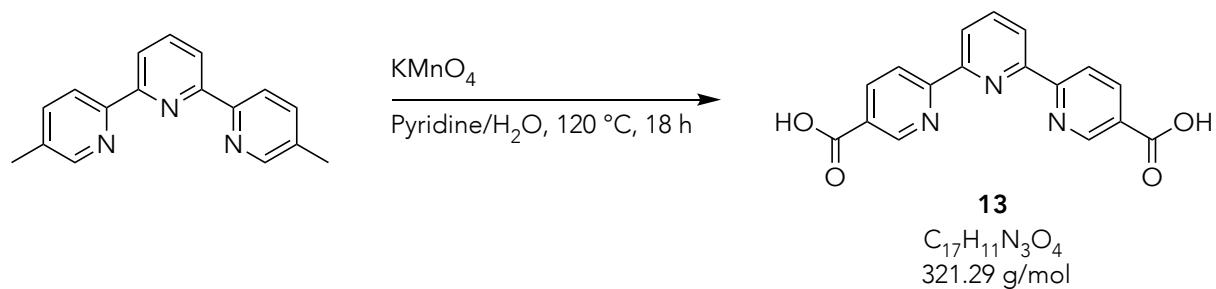
[2,2':6',2''-terpyridine]-5,5''-dicarboxylic acid (13): 5,5''-Dimethyl-2,2':6',2''-terpyridine (**12**, 1.00 g, 3.83 mmol, 1.0 eq.) was dissolved in pyridine/H_2O (60 mL/20 mL), $KMnO_4$ (7.41 g, 46.0 mmol, 12.0 eq.) was added and the reaction mixture was refluxed overnight. After LCMS showed the mono oxidized species, more $KMnO_4$ (3.70 g, 23.0 mmol, 6.0 eq.) was added and refluxed until LCMS showed full conversion in the desired compound. The reaction mixture was cooled to room temperature, quenched with EtOH (10 mL) and the $KMnO_4$ residue was filtered off. An aqueous solution of HCl (1M) was added to the filtrate to adjust the pH to 6 and a white precipitate was formed. The precipitate was filtered, washed with H_2O (3 x 30 mL) and dried in vacuo to afford the desired compound as a white solid (900 mg, 3.83 mmol, 73 %).

Analytical data for 13:

¹H NMR (500 MHz, DMSO-d_6, 25 °C) **δ** = 13.52 (s, 2H), 9.19 (d, J = 2.1 Hz, 2H), 8.74 (d, J = 8.1 Hz, 2H), 8.55 (d, J = 7.8 Hz, 2H), 8.47 (dd, J = 8.2, 2.0 Hz, 2H), 8.19 (q, J = 8.0 Hz, 1H).

¹³C NMR (126 MHz, DMSO-d_6, 25 °C) **δ** = 166.10, 158.01, 154.05, 150.21, 138.98, 138.32, 126.78, 122.26, 120.53 ppm.

HRMS (ESI-ToF, MeOH, positive mode): calc. for $[C_{17}H_{11}N_3NaO_4]^+$ 344.0642; found 344.0638.

14
C₂₇H₁₉N₇
441.50 g/mol
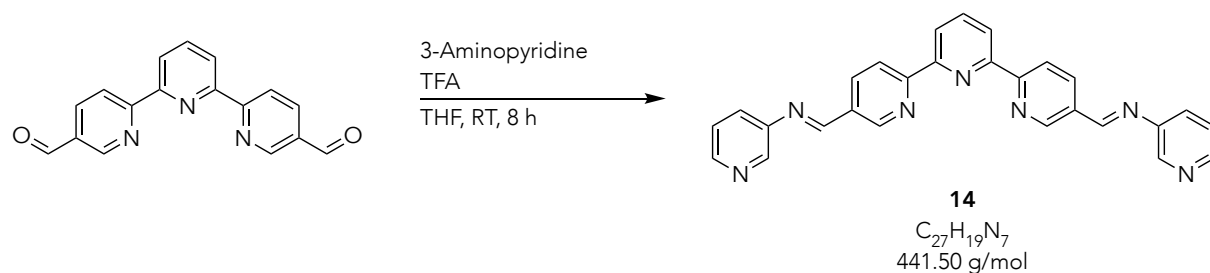
[2,2':6',2''-terpyridine]-5,5''-diyl)bis(N-(pyridine-3-yl)methanimine (14): An oven dried 5 mL round-bottomed flask was charged with 3-aminopyridine (9.80 mg, 104 µmol, 3.0 eq.), [2,2':6',2''-terpyridine]-5,5''-dicarbaldehyde (**4**, 10.0 mg, 34.6 µmol, 1.0 eq.), THF (3 mL) and TFA (1.00 µL, 13.5 µmol, 0.3 eq.). The mixture was stirred for 8 h at room temperature. After TLC confirmed full consumption of the starting materials, the reaction was stopped by removing the solvent under reduced pressure. The crude mixture was first purified by Kugelrohr distillation to remove the unreacted 3-aminopyridine and then purified via manual gel-permeation chromatography (Biobeads SX-3, in DCM) yielding the titled compound as a yellowish solid (10.0 mg, 23.0 µmol, 65 %).

Analytical data for 14:

¹H NMR (500 MHz, CDCl₃, 25 °C) **δ** = 9.12 (dd, J = 2.2, 0.8 Hz, 2H), 8.79 (d, J = 8.4 Hz, 2H), 8.62 (s, 2H), 8.60 (d, J = 7.8 Hz, 2H), 8.57 (d, J = 2.6 Hz, 2H), 8.54 (dd, J = 4.8, 1.6 Hz, 2H), 8.49 (dd, J = 8.3, 2.2 Hz, 2H), 8.04 (t, J = 7.8 Hz, 1H), 7.60 (ddd, J = 8.1, 2.6, 1.5 Hz, 2H), 7.37 (dd, J = 4.8, 0.8 Hz, 2H).

¹³C NMR (126 MHz, CDCl₃, 25 °C) **δ** = 159.00, 158.66, 154.93, 150.90, 147.88, 147.52, 142.81, 138.32, 136.18, 131.53, 128.03, 123.92, 122.52, 121.41 ppm.

HRMS (ESI-ToF, MeOH, positive mode): calc. for [C₂₇H₁₉N₇]⁺ 442.1775; found 442.1780 .

15
C$_{29}$H$_{21}$N$_5$
439.52 g/mol
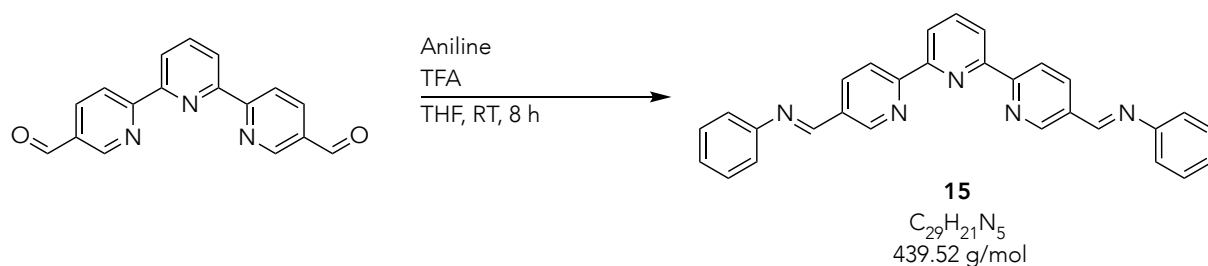
[2,2':6',2''-terpyridine]-5,5''-diyl)bis(N-(phenylmethanimine) (15): An oven dried 5 mL round-bottomed flask was charged with aniline (9.70 mg, 104 μmol, 3.0 eq.), [2,2':6',2''-terpyridine]-5,5''-dicarbaldehyde (**4**, 10.0 mg, 34.6 μmol, 1.0 eq.), THF (3 mL) and TFA (1.00 μL, 13.5 μmol, 0.3 eq.). The mixture was stirred for 8 h at room temperature. After TLC confirmed full consumption of the starting materials, the reaction was stopped by removing the solvent under reduced pressure. The crude mixture was first purified by Kugelrohr distillation to remove the unreacted aniline and then purified via manual gel-permeation chromatography (Biobeads SX-3, in DCM) yielding the titled compound as a yellowish solid (7.2 mg, 16.0 μmol, 47 %).

Analytical data for 15:

¹H NMR (500 MHz, CDCl$_3$, 25 °C) **δ** = 9.10 (dd, J = 2.1, 0.8 Hz, 2H), 8.77 (d, J = 8.2 Hz, 2H), 8.60 (s, 2H), 8.58 (d, J = 7.8 Hz, 2H), 8.48 (dd, J = 8.3, 2.2 Hz, 2H), 8.02 (t, J = 7.8 Hz, 1H), 7.44 (dd, J = 8.3, 7.4 Hz, 4H), 7.31 – 7.27 (m, 6H).

¹³C NMR (126 MHz, CDCl$_3$, 25 °C) **δ** = 158.24, 157.25, 155.05, 151.74, 150.71, 138.23, 135.97, 132.00, 129.43, 126.73, 122.28, 121.37, 121.10 ppm.

HRMS (ESI-ToF, MeOH, positive mode): calc. for [C$_{29}$H$_{22}$N$_5$]$^+$ 440.1874; found 440.1870 .

16
C$_{27}$H$_{23}$N$_{7}$
445.53 g/mol
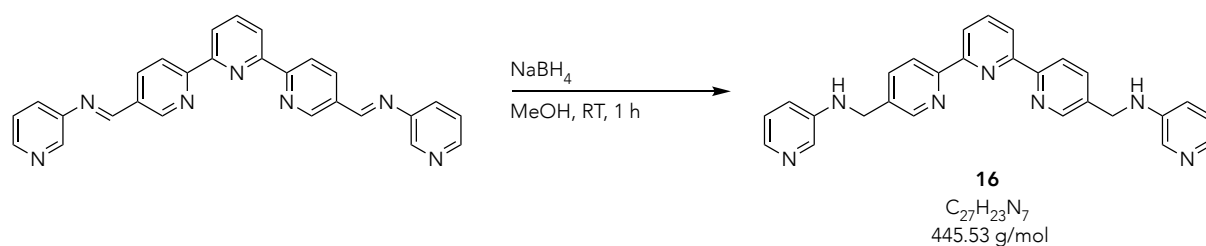
N,N' **–([2,2':6',2''-terpyridine]-5,5''-diylbis(methylene))bis(pyridine-3-amine) (16)**: An oven dried 10 mL round-bottomed flask was charged with [2,2':6',2''-terpyridine]-5,5''-diyl)bis(N-(phenylmethanimine) (**14**, 20.0 mg, 45.3 µmol, 1.0 eq.) and MeOH (6 mL). Afterwards sodium borohydride (17.0 mg, 453 µmol, 10 eq.) was added and the mixture was stirred for 1 h at room temperature. After the TLC confirmed full consumption of the starting materials, the reaction was quenched with H$_2$O (5 mL) and then extracted with EtOAc (3 x 10 mL). The combined organic phases were dried over MgSO$_4$, filtered and concentrated under reduced pressure. The titled compound was isolated as yellowish solid (19.4 mg, 44.0 µmol, 96 %).

Analytical data for 16:

¹H NMR (500 MHz, MeOD, 25 °C) **δ** = 8.67 (d, J = 1.5 Hz, 2H), 8.55 (d, J = 0.8 Hz, 2H), 8.33 (d, J = 7.8 Hz, 2H), 8.02 – 7.95 (m, 5H), 7.81 (dd, J = 4.8, 1.3 Hz, 2H), 7.25 (ddd, J = 8.5, 4.8, 0.7 Hz, 2H), 7.19 (ddd, J = 8.5, 2.9, 1.3 Hz, 2H), 4.50 (s, 4H).

¹³C NMR (126 MHz, MeOD, 25 °C) **δ** = 156.45, 156.37, 149.38, 146.91, 139.27, 137.74, 136.64, 136.55, 134.03, 126.03, 122.57, 122.10, 122.03, 45.21 ppm.

HRMS (ESI-ToF, MeOH, positive mode): calc. for [C$_{27}$H$_{24}$N$_7$]$^+$ 446.2088; 446.2081 found.
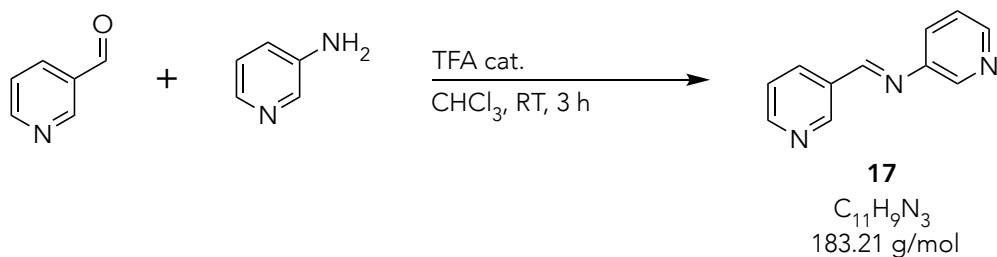
N-(3-pyridinemethylene)-3-pyridinimine (17): An oven dried 25 mL round-bottomed flask was charged with 3-pyridinecarboxaldehyde (100 mg, 934 µmol, 1.0 eq.), 3-aminopyridine (88.0 mg, 934 µmol, 1.0 eq.), CHCl$_3$ (10 mL) and TFA (1.00 µL, 13.5 µmol, 0.01 eq.). The mixture was stirred for 3 h at room temperature. After the TLC confirmed full consumption of the starting materials, the reaction was stopped by removing the solvent under reduced pressure. The crude mixture was purified via manual gel-permeation chromatography (Biobeads SX-3, in DCM) yielding the titled compound as an off white solid (122 mg, 666 µmol, 71 %).

Analytical data for 17:

¹H NMR (500 MHz, CDCl$_3$, 25 °C) **δ** = 9.04 (d, J = 2.3 Hz, 1H), 8.54 – 8.48 (m, 3H), 8.31 (dt, J = 8.0, 2.0 Hz, 1H), 7.57 – 7.53 (m, 1H), 7.44 (dd, J = 8.0, 4.8 Hz, 1H), 7.35 (dd, J = 8.1, 4.8 Hz, 1H).

¹³C NMR (126 MHz, CDCl$_3$, 25 °C) **δ** = 159.16, 152.68, 151.28, 147.84, 147.39, 142.68, 135.25, 131.51, 127.96, 124.04, 123.90 ppm.

The analytical data are in agreement with the ones reported in ref. [291].

Hydrophobic Terpyridine Ligand

18
$C_{15}H_{10}Br_2N_2O_3$
426.06 g/mol
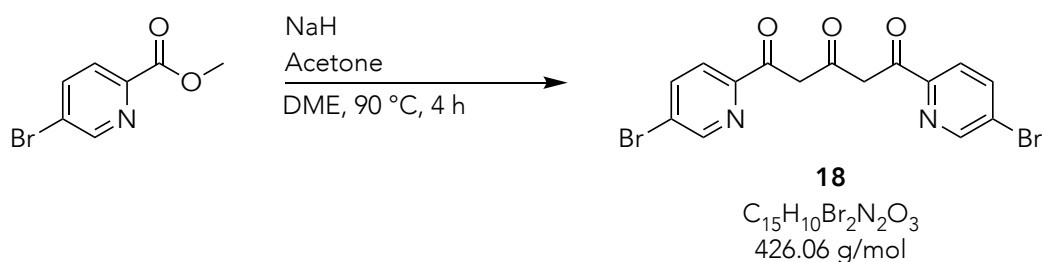
1,5-bis(5-bromopyridin-2-yl)pentane-1,3,5-trione (18): An oven dried 250 mL two-necked round-bottomed flask under argon was charged with sodium hydride (60 % dispersion in mineral oil, 2.22 g, 55.8 mmol, 4.0 eq.) and 1,2-dimethoxyethane (50 mL). A solution of dry acetone (0.8 mL, 11.2 mmol, 0.8 eq.), methyl-5-bromopyridine-2-carboxylate (6.03 g, 27.9 mmol, 2.0 eq) and 1,2-dimethoxyethane (50 mL) was added to the suspension of sodium hydride. The reaction mixture was stirred under argon at room temperature until an intense evolution of gas was observed and a yellow suspension was obtained. The yellow solution was heated carefully to reflux for 2 h and the solvent was removed under reduced pressure. The crude was treated with H_2O (50 mL), acidified to pH 7 and the precipitate was filtrated and washed with water until the washing appeared clean. The filtrate was dried under reduced pressure to give the title compound as a yellow solid (4.52 g, 10.6 mmol, 76 %). The titled compound was used without further purification steps.

Analytical data for (18):

HRMS (ESI-ToF, MeOH, positive mode): calc. for $[C_{15}H_{11}Br_2N_2O_3]^+$ 424.9125; found 424.9131.

19

$C_{15}H_9Br_2N_3O$

407.07 g/mol
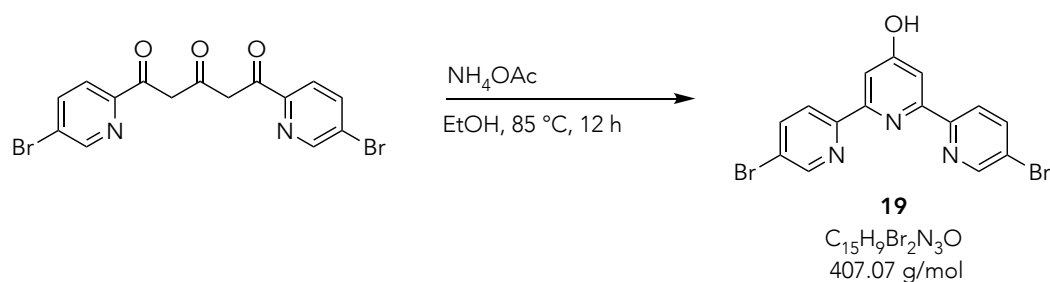
5,5''-dibromo-[2,2':6',2''-terpyridin]-4'(1'*H*)-one (19): A two-necked round-bottomed flask was charged with 1,5-bis(5-bromopyridin-2-yl)pentane-1,3,5-trione (**18**, 1.00 g, 2.35 mmol, 1.0 eq.), ammonium acetate (1.27 g, 15.5 mmol, 7.0 eq.) and EtOH (40 mL). The mixture was heated to reflux for 12 h. Afterwards the solution was cooled down at 10 °C and the precipitation was filtered and washed with Et_2O (2 x 20 mL). The resultant organic fraction was concentrated to give a second crop of precipitate. The solid residue were combined and dried under reduced pressure and purified by column chromatography (acetone:cyclohexane = 1:1 + 1 % NH_4OH) to yield the desired product as an off white solid (580 mg, 2.35 mmol, 61 %).

Analytical data for **19**:

¹H NMR (500 MHz, DMSO-d_6, 25 °C) **δ** = 11.09 (s, 1H), 8.82 (dd, J = 2.4, 0.7 Hz, 2H), 8.52 (dd, J = 8.5, 0.7 Hz, 2H), 8.22 (dd, J = 8.5, 2.4 Hz, 2H), 7.83 (s, 2H).

¹³C NMR (126 MHz, DMSO-d_6, 25 °C) **δ** = 166.16, 155.64, 153.81, 149.94, 139.89, 122.53, 120.98, 108.37 ppm.

HRMS (ESI-ToF, MeOH, positive mode): calc. for $[C_{15}H_{10}Br_2N_3O]^+$ 405.9185; found 405.9188.

20
C₃₅H₄₉Br₂N₃O
687.61 g/mol
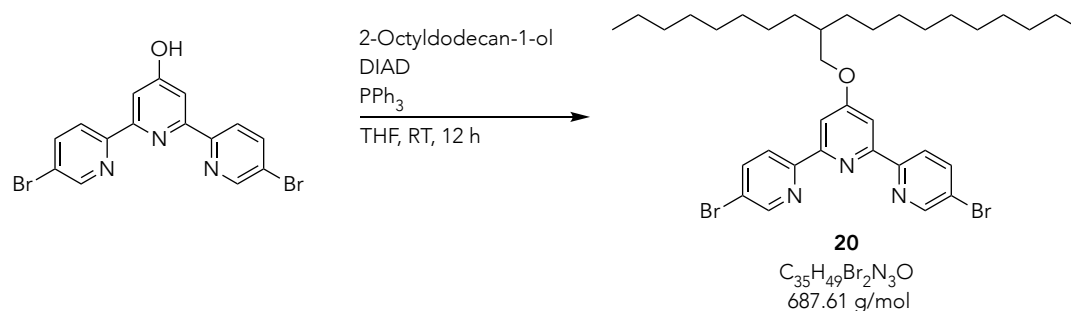
6,6'-(5-((2-octyldodecyl)oxy)-1,3-phenylene)bis(3-bromopyridine) (20): An oven dried 50 mL round-bottomed flask under argon was charged with 5,5''-dibromo-[2,2':6',2''-terpyridin]-4'(1'H)-one (**19**, 602 mg, 1.48 mmol, 1.0 eq.), 2-octyldodecan-1-ol (0.58 mL, 1.63 mmol, 1.1 eq.), triphenylphosphine (466 mg, 1.78 mmol, 1.2 eq.) and dry THF (20 mL). The reaction mixture was cooled to 0 °C and DIAD (0.35 mL, 1.78 mmol, 1.2 eq.) was added dropwise. The reaction was allowed to warm to room temperature and stirred for 12 h. After TLC confirmed full conversion of the starting materials the solvent was removed under reduced pressure and the remaining residue was purified by column chromatography (acetone:cyclohexane = 1:5 + 0.1 % NH₄OH) to yield the desired product as a brownish oil (835 mg, 1.48 mmol, 82 %).

Analytical data for 20:

¹H NMR (400 MHz, CDCl₃, 22 °C) **δ** = 8.71 (d, J = 2.3 Hz, 2H), 8.45 (d, J = 8.5 Hz, 2H), 7.96 (s, 2H), 7.93 (dd, J = 8.5, 2.4 Hz, 2H), 4.07 (d, J = 5.5 Hz, 2H), 1.87 – 1.77 (m, 1H), 1.55 – 1.39 (m, 4H), 1.31 – 1.18 (m, 30H), 0.90 – 0.84 (m, 6H).

¹³C NMR (101 MHz, CDCl₃, 22 °C) **δ** = 167.75, 156.17, 154.64, 150.14, 139.45, 122.67, 121.32, 107.72, 71.16, 38.01, 32.06, 32.05, 31.44, 30.14, 29.82, 29.79, 29.78, 29.74, 29.50, 29.48, 27.02, 27.01, 22.83, 22.82, 14.25 ppm.

HRMS (ESI-ToF, MeOH, positive mode): calc. for [C₃₅H₅₀Br₂N₃O]⁺ 686.2315; found 686.2315.

21
$C_{61}H_{69}N_5O$
888.26 g/mol
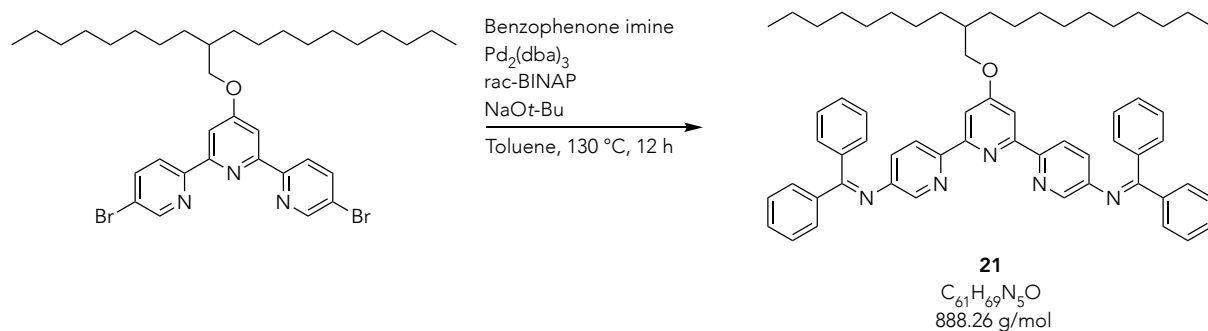
_N,N'_-(4'-((2-octyldodecyl)oxy)-[2,2':6',2''-terpyridine]-5,5''-diyl)bis(1,1-diphenylmethanimine) (21): An oven-dried 25 mL Schlenk-tube was purged with argon and charged with 6,6'-(5-((2-octyldodecyl)oxy)-1,3-phenylene)bis(3-bromopyridine) (**20**, 400 mg, 0.58 mmol, 1.0 eq.), benzophenone imine (247 mL, 1.40 mmol, 2.4 eq.), sodium _t_-butoxide (161 mg, 1.63 mmol, 2.8 eq.) and dry toluene (8 mL). The mixture was degassed with argon for 15 min and then rac-BINAP (236 mg, 0.38 mmol, 0.65 eq.) and tris(dibenzylideneacetone)dipalladium(0) (266 mg, 29.0 mmol, 0.5 eq.) were added. The reaction mixture was degassed with argon for 5 min and heated to reflux for 12 h. After TLC confirmed full consumption of the starting material, the reaction was stopped by removing the solvent under reduced pressure. The remains were eluted with EtOAc (10 ml) and again concentrated on Celite to purify the crude product via flash column chromatography (acetone:cyclohexane = 1:10 + 0.1 % NH_4OH) to obtain a brownish oil (399 mg, 58.0 mmol, 77 %).

Analytical data for 21:

¹H NMR (400 MHz, CDCl₃, 23 °C) **δ** = 8.49 (d, J = 8.4 Hz, 2H), 8.20 (d, J = 2.4 Hz, 2H), 7.93 (s, 2H), 7.91 – 7.86 (m, 4H), 7.63 – 7.57 (m, 2H), 7.52 (dd, J = 8.3, 6.6 Hz, 4H), 7.41 – 7.33 (m, 6H), 7.30 – 7.19 (m, 6H), 4.13 (d, J = 5.3 Hz, 2H), 1.92 – 1.83 (m, 1H), 1.61 – 1.43 (m, 4H), 1.36 (s, 30H), 0.97 (d, J = 6.7 Hz, 6H).

¹³C NMR (101 MHz, CDCl₃, 22 °C) **δ** = 170.41, 167.58, 156.71, 151.20, 147.63, 141.74, 139.18, 135.68, 131.37, 129.64, 129.54, 129.22, 129.02, 128.44, 121.11, 106.52,

70.77, 53.53, 38.04, 32.04, 32.02, 31.44, 30.12, 29.79, 29.75, 29.70, 29.46, 29.45, 27.00, 26.99, 22.81, 22.80, 14.25, 14.24 ppm.

HRMS (ESI-ToF, MeOH/DCM, positive mode): calc. for $[C_{61}H_{70}N_5O]^+$ 888.5575; found 888.5572.

22
C₃₅H₅₃N₅O
559.84 g/mol
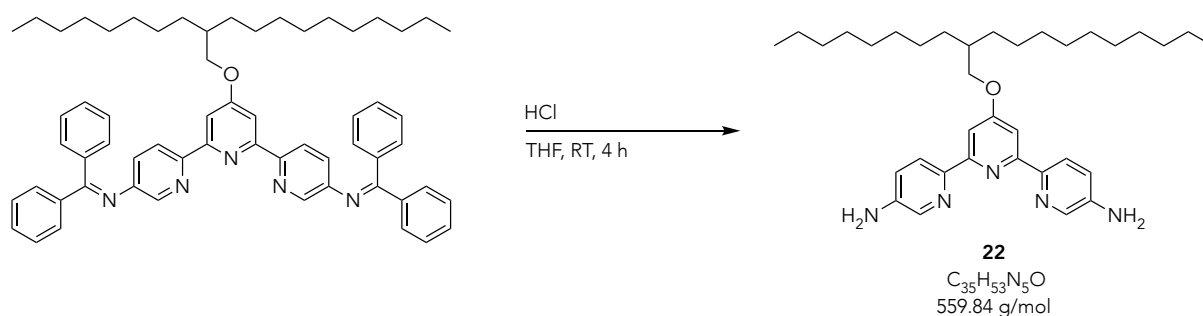
4'-((2-octyldodecyl)oxy)-[2,2':6',2''-terpyridine]-5,5''-diamine (22): A 25 mL round-bottomed flask was charged with N,N'-(4'-((2-octyldodecyl)oxy)-[2,2':6',2''-terpyridine]-5,5''-diyl)bis(1,1-diphenylmethanimine) (**21**, 2.00 g, 2.25 mmol, 1.0 eq.), aqueous hydrochloric acid (37 %, 1 mL) and THF (10 mL). The reaction mixture was stirred at room temperature for 4 h. The precipitate obtained was filtered and washed with Et₂O (2 x 10 mL) and dried under reduced pressure. The hydrochloride was suspended in EtOH and the pH was adjusted to 8 with aqueous sodium hydroxide (aq. 10%) and a saturated aqueous sodium bicarbonate solution. The organic material was extracted from the aqueous layer with EtOAc (3 x 20 mL). The combined organic layers were washed with brine, dried over MgSO₄, filtered and concentrated under reduced pressure. The solid was purified by column chromatography (acetone:cyclohexane = 1:10 + 1 % NH₄OH) to yield the desired product as an brownish oil (1.15 g, 2.25 mmol, 91 %).

Analytical data for 22:

¹H NMR (500 MHz, CDCl₃, 25 °C) **δ** = 8.40 (d, J = 8.5 Hz, 2H, *H5/H5''*), 8.15 (d, J = 2.8 Hz, 2H, *H2/H2''*), 7.76 (s, 2H, *H3'/H5'*), 7.11 (dd, J = 8.5, 2.8 Hz, 2H, *H4/H4''*), 4.06 (d, J = 5.4 Hz, 2H, *OCH₂*), 3.84 (s, 4H, *NH₂/NH₂''*), 1.83 – 1.77 (m, 1H, *CH (Aliphatic)*), 1.50 – 1.42 (m, 2H, *CH₂ (Aliphatic)*), 1.44 – 1.30 (m, 2H, *CH₂ (Aliphatic)*), 1.31 – 1.18 (m, 27H, *CH₂ (Aliphatic)*), 0.87 (t, J = 6.8 Hz, 6H, *CH₃ (Aliphatic)*).

¹³C NMR (126 MHz, CDCl₃, 25 °C) **δ** = 167.56 (C4', 1C), 157.07 (C2'/C6', 2C), 147.49 (C6/C2'', 2C), 142.86 (C3/C5'', 2C), 136.44 (C2/C6'', 2C), 122.14 (C5/C3'', 2C), 122.04

(C4/C4'', 2C), 105.17 (C3'/C5', 2C), 70.73 (C_{ether}, 1C), 38.08 (C_t, 1C), 32.06 (C_{ethyl}, 1C), 32.05 (C_{ethyl}, 2C), 31.47 (C_{ethyl}, 2C), 30.17 (C_{ethyl}, 2C), 29.83 (C_{ethyl}, 1C), 29.79 (C_{ethyl}, 2C), 29.75 (C_{ethyl}, 1C), 29.49 (C_{ethyl}, 2C), 27.02 (C_{ethyl}, 2C), 22.83 (C_{ethyl}, 2C), 22.82 (C_{ethyl}, 2C), 14.26 (C_{methyl}, 2C) ppm.

HRMS (ESI-ToF, MeOH/DCM, positive mode): calc. for $[C_{35}H_{54}N_5O]^+$ 560.4323; found 560.4328.

23
C$_{47}$H$_{59}$N$_7$O
738.04 g/mol
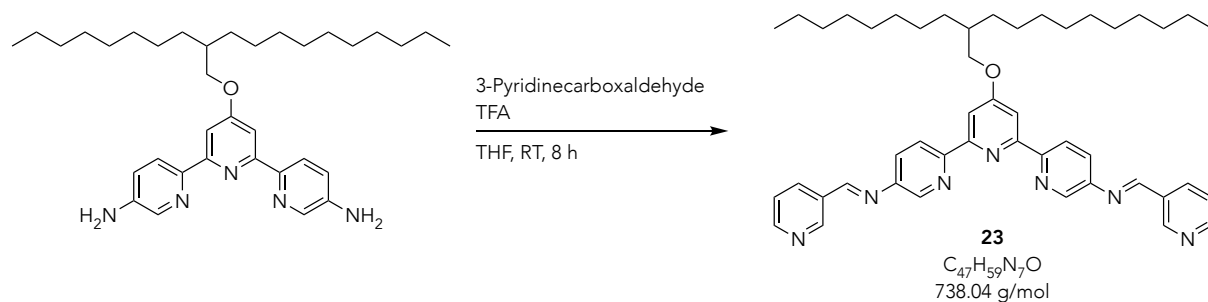
N,N'-(4'-((2-octyldodecyl)oxyl)-[2,2':6',2''-terpyridine]-5,5''-diyl)bis(1-(pyridine-3-yl-methanimine) (23): An oven dried 5 mL round-bottomed flask was charged with 3-pyridinecarboxaldehyde (13.0 mg, 121 µmol, 3.0 eq.), 4'-((2-octyldodecyl)oxy)-[2,2':6',2''-terpyridine]-5,5''-diamine (**22**, 22.6 mg, 40.4 µmol, 1.0 eq.), THF (3 mL) and TFA (1.00 µL, 13.5 µmol, 0.3 eq.). The mixture was stirred for 8 h at room temperature and after the TLC confirmed full consumption of the starting materials, the reaction was stopped by removing the solvent under reduced pressure. The crude mixture was first purified by Kugelrohr distillation to remove the unreacted aldehyde species and then purified via manual gel-permeation chromatography (Biobeads SX-3, in DCM) yielding the titled compound as a yellowish solid (10.0 mg, 14.0 µmol, 33 %).

Analytical data for 23:

¹H NMR (500 MHz, CDCl$_3$, 25 °C) **δ** = 9.08 (d, J = 1.5 Hz, 2H), 8.76 (dd, J = 4.8, 1.7 Hz, 2H), 8.70 (d, J = 0.7 Hz, 2H), 8.62 (s, 2H), 8.60 (d, J = 1.8 Hz, 2H), 8.36 (dt, J = 7.9, 2.0 Hz, 2H), 8.02 (s, 2H), 7.72 (dd, J = 8.4, 2.5 Hz, 2H), 7.46 (dd, J = 7.9, 4.8 Hz, 2H), 4.13 (d, J = 5.5 Hz, 2H), 1.89 – 1.80 (m, 1H), 1.54 – 1.46 (m, 2H), 1.45 – 1.24 (m, 30H), 0.89 – 0.84 (m, 6H).

¹³C NMR (126 MHz, CDCl$_3$, 25 °C) **δ** = 167.74, 158.86, 156.71, 154.64, 152.71, 151.37, 147.40, 142.24, 135.28, 131.62, 128.54, 124.06, 121.83, 107.43, 71.06, 38.08, 32.07, 31.49, 30.16, 29.83, 29.79, 29.75, 29.50, 27.04, 22.83, 14.27 ppm.

HRMS (ESI-ToF, MeOH, positive mode): calc. for $[C_{47}H_{60}N_7O]^+$ 738.4854; found 738.4849.

24
$C_{49}H_{61}N_5O$
736.06 g/mol
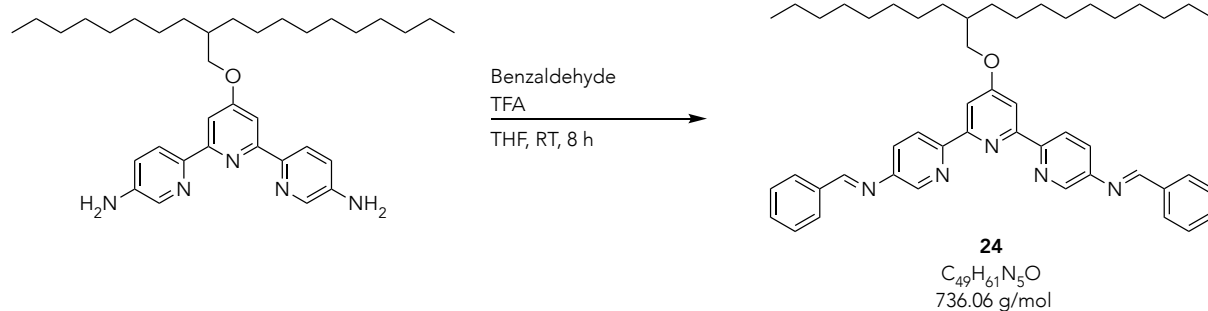
N,N'-(4'-((2-octyldodecyl)oxyl)-[2,2':6',2''-terpyridine]-5,5''-diyl)bis(1-phenylmethanimine) (24): An oven dried 5 mL round-bottomed flask was charged with benzaldehyde (11.4 mg, 107 µmol, 3.0 eq.), 4'-((2-octyldodecyl)oxy)-[2,2':6',2''-terpyridine]-5,5''-diamine (**22**, 20.0 mg, 35.7 µmol, 1.0 eq.), THF (3 mL) and TFA (1.00 µL, 13.5 µmol, 0.3 eq.). The mixture was stirred for 8 h at room temperature and after the TLC confirmed full consumption of the starting materials, the reaction was stopped by removing the solvent under reduced pressure. The crude mixture was first purified by Kugelrohr distillation to remove the unreacted aldehyde species and then purified via manual gel-permeation chromatography (Biobeads SX-3, in DCM) yielding the titled compound as a yellowish solid (12.0 mg, 16.0 µmol, 46 %).

Analytical data for 24:

^{1}H NMR (500 MHz, CDCl$_3$, 25 °C) **δ** = 8.69 (d, J = 0.7 Hz, 2H), 8.58 (dd, J = 2.6, 0.7 Hz, 2H), 8.57 (s, 2H), 8.01 (s, 2H), 7.97 (dd, J = 7.6, 1.9 Hz, 4H), 7.70 (dd, J = 8.4, 2.6 Hz, 2H), 7.55 – 7.51 (m, 6H), 4.13 (d, J = 5.4 Hz, 2H), 1.51 (q, J = 6.7 Hz, 1H), 1.37 – 1.23 (m, 30H), 0.87 (td, J = 6.9, 3.2 Hz, 6H).

^{13}C NMR (126 MHz, CDCl$_3$, 25 °C) **δ** = 167.72, 161.99, 156.84, 154.14, 148.05, 142.17, 135.99, 132.13, 129.26, 129.06, 128.64, 121.79, 107.20, 71.01, 38.10, 32.06, 31.50, 30.18, 29.84, 29.80, 29.76, 29.51, 27.05, 22.84, 14.27 ppm.

HRMS (ESI-ToF, MeOH, positive mode): calc. for $[C_{49}H_{62}N_5O]^+$ 736.4949; found 736.4955.

25
C$_{47}$H$_{63}$N$_7$O
742.07 g/mol
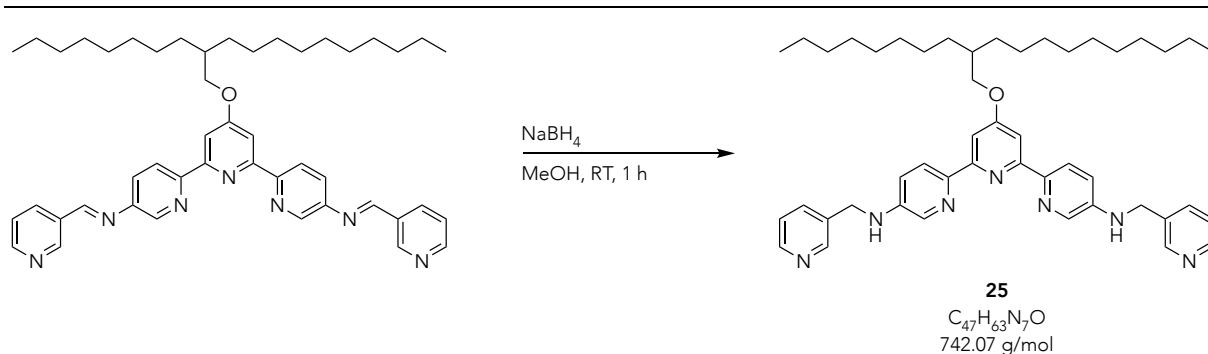
***N,N'*-dibenzyl-4'-((2-octyldodecyl)oxyl)-[2,2':6',2''-terpyridine]-5,5''-diamine (25):** An oven dried 10 mL round-bottomed flask was charged with [2,2':6',2''-terpyridine]-5,5''-diyl)bis(N-(phenylmethanimine) (**24**, 15.0 mg, 20.3 μmol, 1.0 eq.) and MeOH (6 mL). Afterwards sodium borohydride (8.00 mg, 203 μmol, 10 eq.) was added and the mixture was stirred for 1 h at room temperature and after the TLC confirmed full consumption of the starting materials, the reaction was quenched with H$_2$O (5 mL) and then extracted with EtOAc (3 x 10 mL). The combined organic phases were dried over MgSO$_4$, filtered and concentrated under reduced pressure. The titled compound was isolated as yellowish oil (14.8 mg, 20.0 μmol, 98 %).

Analytical data for 25:

¹H NMR (500 MHz, CDCl$_3$, 25 °C) **δ** = 8.62 (s, 2H), 8.46 (d, J = 4.8 Hz, 2H), 8.31 (s, 2H), 7.99 (s, 2H), 7.78 (d, J = 7.8 Hz, 2H), 7.38 – 7.34 (m, 2H), 7.22 (d, J = 6.9 Hz, 2H), 7.01 (d, J = 8.8 Hz, 2H), 4.49 (s, 4H), 4.11 (s, 2H), 1.86 – 1.77 (m, 1H), 1.48 – 1.36 (m, 4H), 1.31 – 1.15 (m, 28H), 0.90 – 0.81 (m, 6H).

¹³C NMR (126 MHz, CDCl$_3$, 25 °C) **δ** = 170.72, 158.30, 155.77, 152.01, 148.89, 147.29, 146.31, 135.57, 135.55, 134.06, 123.91, 122.81, 104.08, 84.87, 44.78, 37.94, 32.03, 32.02, 31.22, 30.12, 29.82, 29.77, 29.47, 26.96, 22.80, 14.24 ppm.

HRMS (ESI-ToF, MeOH, positive mode): calc. for [C$_{47}$H$_{64}$N$_7$O]$^+$ 742.5167; 742.5154 found.

Amphiphilic Heteroleptic Complexes

26a
$C_{34}H_{22}FeN_6O_4P_2F_{12}$
924.03 g/mol

26
$C_{55}H_{64}FeN_8O_3P_2F_{12}$
1194,37 g/mol

26b
$C_{70}H_{106}FeN_{10}O_2P_2F_{12}$
1464,71 g/mol
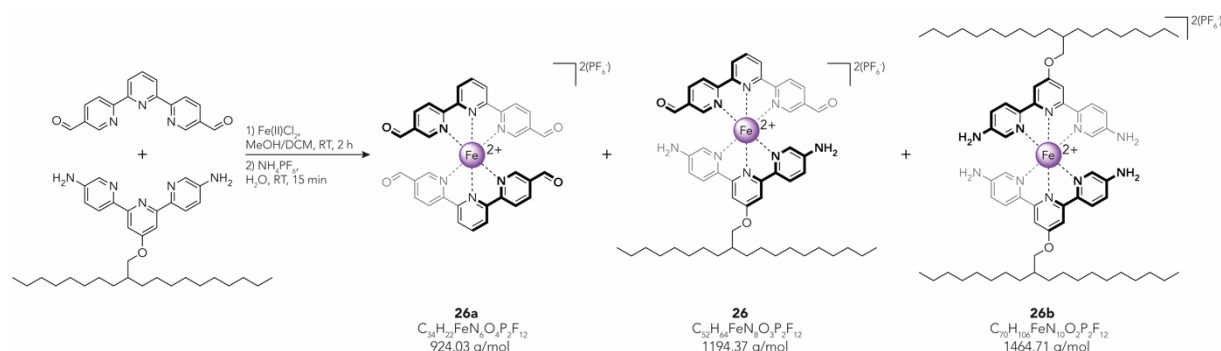
[Fe(22)(4)]$^{2+}$[2(PF$_6$)]$^-$ (26): A 100 mL round-bottomed flask was charged with 4'-((2-octyldodecyl)oxy)-[2,2':6',2''-terpyridine]-5,5''-diamine (**22**, 88.0 mg, 157.0 µmol, 1.0 eq.), [2,2':6',2''-terpyridine]-5,5''-dicarbaldehyde (**4**, 45.0 mg, 157.0 µmol, 1.0 eq.), iron(II) chloride (21.9 mg, 173.0 µmol, 1.1 eq.), MeOH (30 mL) and DCM (30 mL). The reaction mixture was stirred for 2 h at room temperature. The solvents were removed under reduced pressure, water was added and the aqueous phase was washed with EtOAc to remove organic impurities. Afterwards, an aquoeos solution of ammonium hexafluorophosphate (20 mL) was added and the mixture was stirred at room temperature for 15 min in order to exchange the counter ion and make it soluble in organic solvents. The aqueous phase was extracted with EtOAc. The combined organic layers were dried over MgSO$_4$, filtered and concentrated under reduced pressure. The crude product contained the homoleptic complexes **26a**, **26b** and the heteroleptic complex **26**. To obtain the desired heteroleptic target complex **26,** the crude mixture was purified via preparative reversed-phase HPLC using an optimized isocratic solvent system (H$_2$O:MeCN = 10:90 + 0.1 % TFA, 40 mL/min) yielding the target compound **26** as purple solid (83.0 mg, 69.0 µmol, 44 %). Homoleptic compound **26a** was isolated as purple solid (38.0 mg, 41.1 µmol, 26 %) and homoleptic compound **26b** was isolated as red/purple solid (65.0 mg, 44.4 µmol, 28 %). The yield of this complexation is not accurateenough, since the heteroleptic complex **26** is degrading immediately in the corresponding homoleptic species.

Analytical data for **26**:

HRMS (ESI-ToF, MeCn, positive mode): calc. for $[C_{52}H_{64}FeN_8O_3]^{2+}$ 452.2220; found 452.2225.

Analytical data for **26a**:

^{1}H NMR (500 MHz, CD$_3$CN, 25 °C) **δ** = 9.63 (s, 4H), 9.13 (d, J = 8.1 Hz, 4H), 8.86 (t, J = 8.1Hz, 2H), 8.65 (d, J = 8.2 Hz, 4H), 8.27 (dd, J = 8.2, 1.8 Hz, 4H), 7.39 (d, J = 1.9 Hz, 4H).

^{13}C NMR (126 MHz, CD$_3$CN, 25 °C) **δ** = 189.81, 162.23, 160.73, 156.43, 139.55, 138.74, 134.44, 127.12, 125.17 ppm.

HRMS (ESI-ToF, MeCn, positive mode): calc. for $[C_{34}H_{22}FeN_6O_4]^{2+}$ 317.0521; found 317.0522.

Analytical data for **26b**:

^{1}H NMR (500 MHz, CD$_2$Cl$_2$, 25 °C) **δ** = 7.92 (d, J = 8.7 Hz, 4H), 7.84 (s, 4H), 6.97 (dd, J = 8.7, 2.6 Hz, 4H), 6.43 (d, J = 2.4 Hz, 4H), 4.39 (d, J = 5.5 Hz, 4H), 4.17 (s, 8H), 2.05 (p, J = 6.1 Hz, 2H), 1.70 – 1.46 (m, 8H), 1.40 – 1.29 (m, 56H), 1.07 - 0.90 (m, 12H).

^{13}C NMR (126 MHz, CD$_2$Cl$_2$, 25 °C) **δ** = 168.02, 160.82, 147.48, 146.27, 139.25, 123.84, 121.85, 106.81, 73.18, 38.43, 32.36, 31.64, 30.50, 30.19, 30.12, 30.08, 29.81, 27.33, 23.12, 14.30 ppm.

HRMS (ESI-ToF, MeCn, positive mode): calc. for $[C_{70}H_{106}FeN_{10}O_2]^{2+}$ 587.3920; found 587.3912.

27
C$_{52}$H$_{64}$CoN$_8$O$_3$P$_3$F$_{18}$
1342.34 g/mol

27b
C$_{70}$H$_{106}$CoN$_{10}$O$_2$P$_3$F$_{18}$
1612,68 g/mol
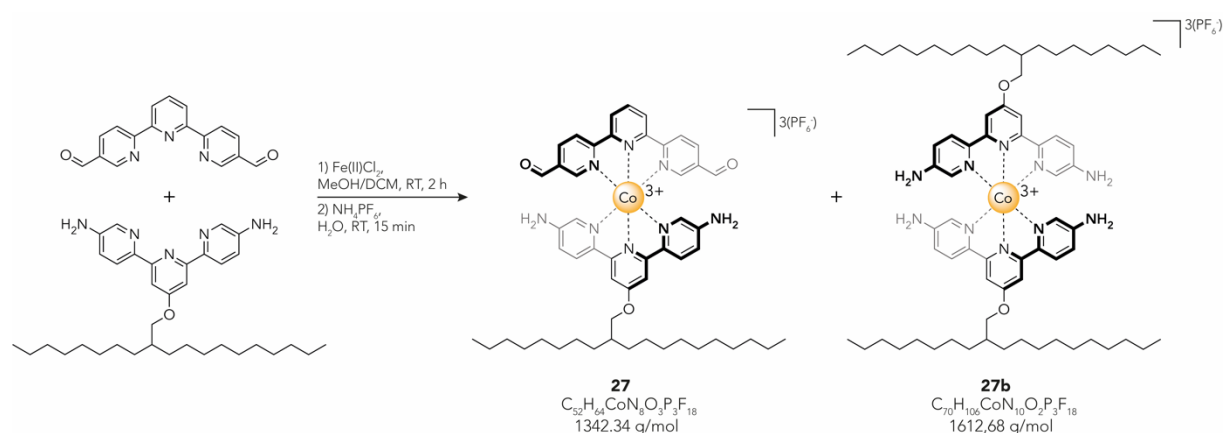
[Co(22)(4)]$^{3+}$[3(PF$_6$)]$^-$ (27): A 100 mL round-bottomed flask was charged with 4'-((2-octyldodecyl)oxy)-[2,2':6',2''-terpyridine]-5,5''-diamine (**22**, 39.0 mg, 68.9 μmol, 1.0 eq.), [2,2':6',2''-terpyridine]-5,5''-dicarbaldehyde (**4**, 20.0 mg, 68.9 μmol, 1.0 eq.), cobalt(II) chloride hexahydrate (20.0 mg, 82.7 μmol, 1.2 eq.), MeOH (5 mL) and DCM (5 mL). The reaction mixture was stirred for 2 h at room temperature. The solvent was removed under reduced pressure, water was added and the aqueous phase was washed with EtOAc to remove organic impurities. Afterwards, an aqueous solution of ammonium hexafluorophosphate (10 mL) was added and the mixture was stirred at room temperature for 15 min in order to exchange the counter ion and make it soluble in organic solvents. The aqueous phase was extracted with EtOAc. The combined organic layers were dried over MgSO$_4$, filtered and concentrated under reduced pressure. The crude product contained one homoleptic complexe **27b** and the heteroleptic complex **27**, the homoleptic complex **27a** was not detected. To obtain the desired heteroleptic target complex **27**, the crude mixture was purified via preparative reversed-phase HPLC using an optimized solvent gradient ranging from (H$_2$O:MeCN = 60:40 to H$_2$O:MeCN = 10:90 + 0.1 % TFA, 40 mL/min) yielding the product **27** as brownish solid (40.0 mg, 33.0 μmol, 49 %). Homoleptic compound **27b** was isolated as brownish solid (26.0 mg, 18.0 μmol, 26 %).

Analytical data for 27:

¹H NMR (500 MHz, CDCl$_3$, 25 °C) **δ** = 9.81 (d, J = 0.5 Hz, 2H, *H*$_{Aldehyde\ Hydrophilic}$), 9.20 – 9.08 (m, 3H, *H3/H4'/H5''*$_{Hydrophilic}$), 8.76 (d, J = 8.1 Hz, 2H, H3'/H5'$_{Hydrophilic}$), 8.62 (dd, J = 8.2, 1.6 Hz, 2H, H4/H4''$_{Hydrophilic}$), 8.07 (d, J = 8.9 Hz, 2H, H5/H3''$_{Hydrophobic}$), 8.00 (s, 2H, *H3'/H5'*$_{Hydrophobic}$), 7.59 (dd, J = 1.7, 0.6 Hz, 2H, *H6/H2'*$_{Hydrophilic}$), 7.18 (dd, J = 8.9, 2.4 Hz, 2H, *H4/H4''*$_{Hydrophobic}$), 6.32 (d, J = 2.3 Hz, 2H, *H2/H6''*$_{Hydrophobic}$), 5.27 (s, 4H, *NH2*), 4.48 (d, J = 5.7 Hz, 2H, *OCH$_2$*), 2.11 – 2.06 (m, 1H, CH$_{Aliphatic}$), 1.53 – 1.48 (m, 4H, *CH$_{2\ Aliphatic}$*), 1.44 – 1.22 (m, 28H, *CH$_{2\ Aliphatic}$*), 0.94 – 0.85 (m, 6H, *CH$_{3\ Aliphatic}$*).

¹³C NMR (126 MHz, CDCl$_3$, 25 °C) **δ** = 188.95 (C$_{Aldehyd}$, 2C), 173.29 (C4'$_{Hydrophobic}$, 1C), 160.04 (C2/C6''$_{Hydrophilic}$, 2C), 158.39 (C2'/C6'$_{Hydrophobic}$, 2C) 156.44 (C2'/C6'$_{Hydrophilic}$, 2C), 154.66 (C6/C2''$_{Hydrophilic}$, 2C), 150.70 (C3/C5''$_{Hydrophobic}$, 2C), 146.72 (C4'$_{Hydrophilic}$, 1C), 144.50 (C6/C2''$_{Hydrophobic}$, 2C), 142.97 (C4/C4'$_{Hydrophilic}$, 2C), 137.91 (C2/C6''$_{Hydrophobic}$, 2C) 137.12 (C5/C3''$_{Hydrophilic}$, 2C), 130.30 (C3'/C5'$_{Hydrophilic}$, 2C), 128.40 (C3/C5''$_{Hydrophilic}$, 2C), 128.20 (C5/C3''$_{Hydrophobic}$, 2C), 124.25 (C4/C4''$_{Hydrophobic}$, 2C), 110.38 (C3'/C5'$_{Hydrophobic}$, 2C), 75.33 (C$_{ethyl}$, 1C), 38.57 (C$_t$, 1C), 32.69 (C$_{ethyl}$, 2C), 31.79 (C$_{ethyl}$, 1C), 30.73 (C$_{ethyl}$, 1C), 30.44 (C$_{ethyl}$, 2C), 30.41 (C$_{ethyl}$, 2C), 30.37 (C$_{ethyl}$, 2C), 30.12 (C$_{ethyl}$, 2C), 27.46 (C$_{ethyl}$, 2C), 23.44 (C$_{ethyl}$, 2C), 23.42 (C$_{ethyl}$, 2C), 14.43 (C$_{methyl}$, 1C) ppm.

HRMS (ESI-ToF, MeOH, positive mode): calc. for [C$_{52}$H$_{64}$CoN$_8$O$_3$]$^{2+}$ 453.7211; found 453.7214.

Analytical data for 27b:

¹H NMR (500 MHz, CDCl$_3$, 25 °C) **δ** = 8.06 (d, J = 8.8 Hz, 4H, *H5/H3''*), 7.93 (s, 4H, *H3'/H5'*), 7.21 (dd, J = 8.9, 2.4 Hz, 4H, *H4/H4''*), 6.50 (d, J = 2.3 Hz, 4H, *H2/H6'*), 4.41 (d, J = 5.9 Hz, 4H, OCH$_2$), 2.09 – 2.01 (m, 2H, CH$_{(Aliphatic)}$), 1.62 – 1.49 (m, 8H, CH$_2$ $_{(Aliphatic)}$), 1.37 – 1.23 (m, 56H, CH$_{2\ (Aliphatic)}$), 0.91 – 0.86 (m, 12H, CH$_{3\ (Aliphatic)}$).

¹³C NMR (126 MHz, CDCl₃, 25 °C) **δ** = 172.92 (C4', 2C), 157.98 (C2'/C6', 4C), 150.43 (C3/C5'', 4C), 144.42 (C6/C2'', 4C), 137.40 (C2/C6'', 4C), 127.42 (C5/C3'', 4C), 124.13 (C4/C4'', 4C), 109.72 (C3'/C5', 4C), 75.15 (C_{ethyl}, C2), 38.56 (C_t, 2C), 32.62 (C_{ethyl}, 4C), 31.75 (C_{ethyl}, 2C), 31.72 (C_{ethyl}, 2C), 30.67 (C_{ethyl}, 4C), 30.29 (C_{ethyl}, 4C), 30.05 (C_{ethyl}, 4C), 27.38 (C_{ethyl}, 4C), 27.33 (C_{ethyl}, 4C), 23.36 (C_{ethyl}, 4C), 14.36 (C_{methyl}, 1C) ppm.

HRMS (ESI-ToF, MeOH, positive mode): calc. for $[C_{70}H_{106}CoN_{10}O_2]^{3+}$ 392.5939; found 392.5943.

28
C$_{35}$H$_{53}$Cl$_3$N$_5$ORu
767.3 g/mol
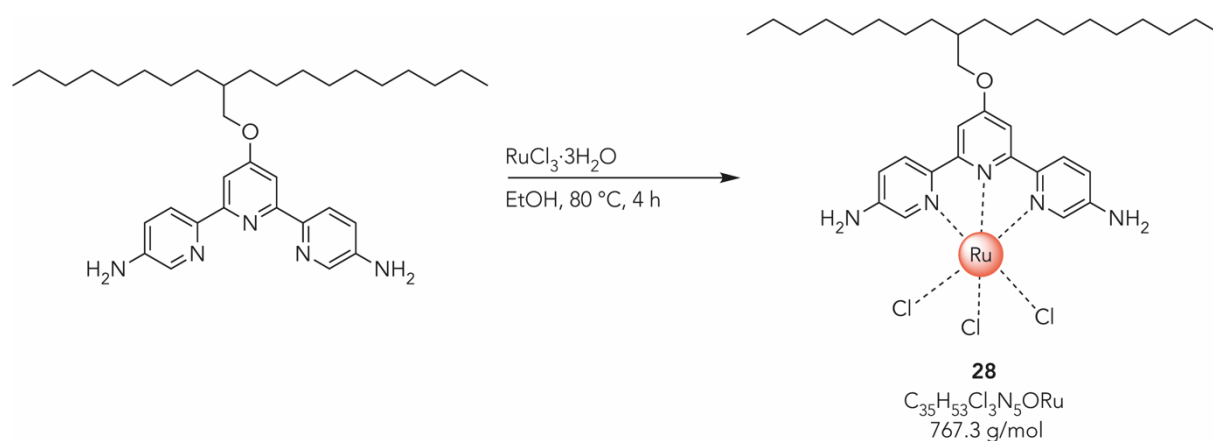
[Ru(22)]³⁺[3Cl⁻] (28): A 50 mL two-necked round-bottomed flask was purged with argon and charged with 4'-((2-octyldodecyl)oxy)-[2,2':6',2''-terpyridine]-5,5''-diamine (**22**, 116 mg, 207 µmol, 1.0 eq.), ruthenium(III) chloride trihydrate (54.0 mg, 207 µmol, 1.0 eq.) and EtOH (10 mL). The reaction mixture was refluxed for 4 h. The crude was allowed to cool at room temperature, followed by the formation of a dark precipitate. The precipitate was filtered, washed with water (3 x 10 mL), Et$_2$O (3 x 10 mL) and dried under reduced pressure, yielding the desired product as crude (112 mg, 146 µmol, 70 %). The titled compound was used for the next synthetic step without any further purification.

29
C$_{52}$H$_{68}$N$_8$O$_3$RuP$_2$F$_{12}$
1244.38 g/mol
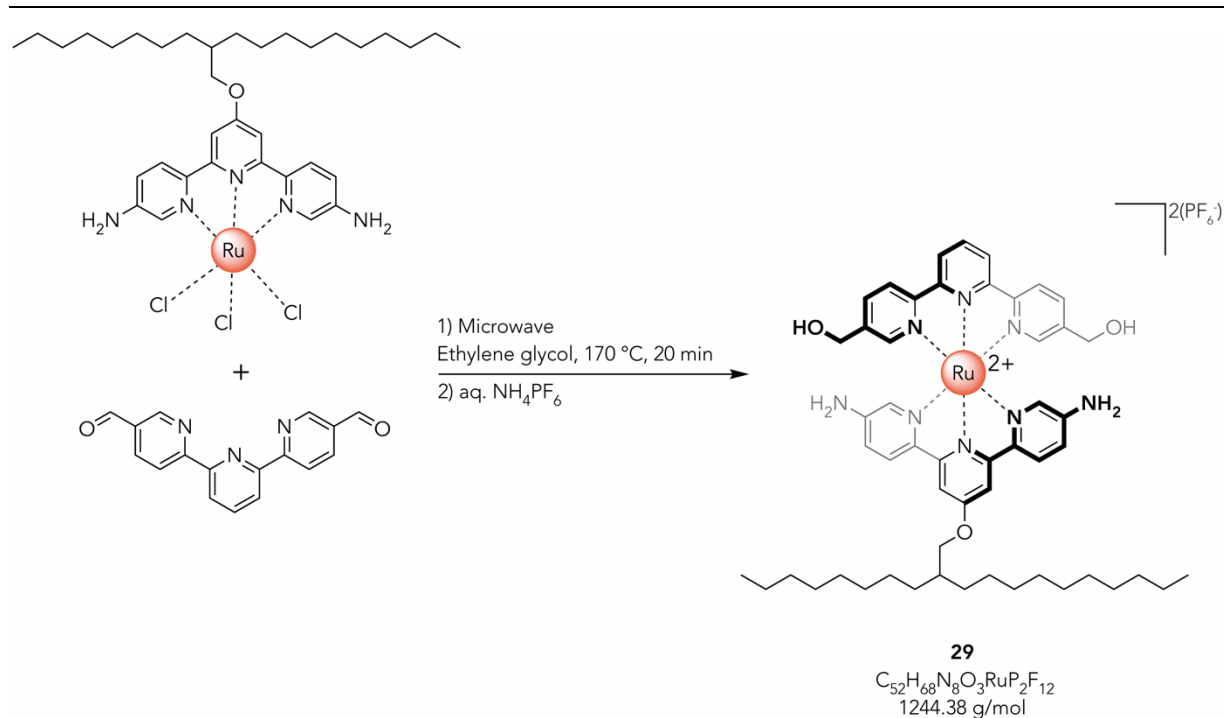
[Ru(22)([2,2':6',2''-terpyridine]-5,5''-diyldimethanol (29): An 25 mL oven-dried microwave vessel was purged with argon and charged with [Ru(**22**)]$^{3+}$[3Cl$^-$] (**28**, 112 mg, 146 µmol, 1.0 eq), [2,2':6',2''-terpyridine]-5,5''-dicarbaldehyde (**4**, 42.0 mg, 146 µmol, 1.0 eq.), triethylamine (4 drops) and ethylene glycol (15 mL). The mixture was degassed with argon for 15 min. The vessel was closed and heated to 170 °C for 20 min. After cooling down to room temperature, an aqueous solution of ammonium hexafluorophosphate (10 mL) was added to the mixture in order to exchange the counter ion and make it soluble in organic solvents. The precipitate was filtered and washed with water (30 mL). The filtrate was solved in EtOAc (20 mL) and washed with water. The combined organic layers were dried over MgSO$_4$, filtered and concentrated under reduced pressure to obtain a dark red powder (110 mg, 89.0 µmol, 61 %).

Analytical data for 29:

¹H NMR (500 MHz, CD$_3$CN, 25 °C) **δ** = 8.65 (d, J = 8.2 Hz, 2H), 8.45 (d, J = 8.3 Hz, 2H), 8.30 (t, J = 8.1 Hz, 1H), 8.04 (d, J = 8.8 Hz, 2H), 7.93 – 7.77 (m, 4H), 7.33 (d, J = 1.8 Hz, 2H), 6.98 (dd, J = 8.9, 2.5 Hz, 2H), 6.55 (d, J = 2.6 Hz, 2H), 4.68 (s, 2H), 4.38

(d, J = 5.7 Hz, 2H), 4.33 (d, J = 5.6 Hz, 2H), 2.03 – 1.98 (m, 1H), 1.64 – 1.47 (m, 4H), 1.38 – 1.25 (m, 28H), 0.90 – 0.80 (m, 6H).

¹³C NMR (126 MHz, CD$_3$CN, 25 °C) **δ** = 167.48, 157.94, 156.97, 156.89, 150.63, 148.22, 146.98, 143.11, 138.88, 136.41, 125.73, 124.56, 123.72, 121.09, 107.08, 73.64, 61.17, 38.65, 32.69, 31.95, 30.74, 30.70, 30.43, 30.36, 30.15, 27.48, 23.44, 23.41, 14.40 ppm.

HRMS (ESI-ToF, MeOH, positive mode): calc. for $[C_{52}H_{68}RuN_8O_3]^{2+}$ 477.2230; found 477.2225.

30
$C_{56}H_{72}N_8O_5RuP_2F_{12}$
1328.40 g/mol
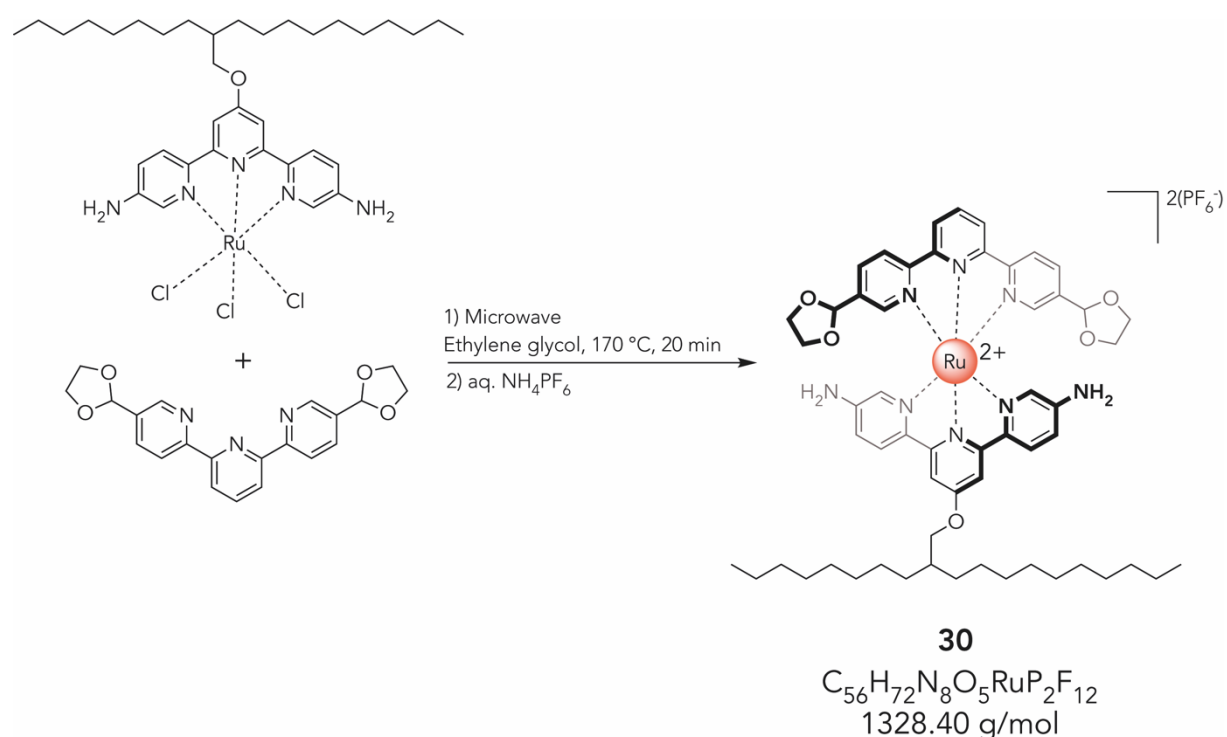
[Ru(22)(3)] (30): An 25 mL oven-dried microwave vessel was purged with argon and charged with [Ru(**22**)]$^{3+}$[3Cl$^-$] (**28**, 47.0 mg, 61.0 µmol, 1.0 eq), 5,5''-di(1,3-dioxolan-2-yl)-2,2':6',2''-terpyridine (**3**, 23.0 mg, 61.0 µmol, 1.0 eq.), triethylamine (4 drops) and ethylene glycol (15 mL). The mixture was degassed with argon for 15 min. The vessel was closed and heated to 170 °C for 20 min. After cooling down to room temperature, an aqueous solution of ammonium hexafluorophosphate (10 mL) was added to the mixture in order to exchange the counter ion and make it soluble in organic solvents. The precipitate was filtered and washed with water (30 mL). The filtrate was solved in EtOAc (20 mL) and washed with water. The combined organic layers were dried over MgSO$_4$, filtered and concentrated under reduced pressure to obtain a dark red powder (40 mg, 30.0 µmol, 49 %).

Analytical data for 30:

^{1}H NMR (500 MHz, CD$_3$CN, 25 °C) **δ** = 8.91 (d, J = 8.2 Hz, 2H), 8.70 (dd, J = 8.3, 0.7 Hz, 2H), 8.52 (t, J = 8.1 Hz, 1H), 8.23 (d, J = 8.9 Hz, 2H), 8.18 (ddd, J = 8.4, 1.9, 0.5 Hz, 2H), 8.04 (s, 2H), 7.60 (d, J = 1.8 Hz, 2H), 7.17 (dd, J = 8.9, 2.5 Hz, 2H), 6.70 (d, J

= 2.5 Hz, 2H), 5.74 (s, 2H), 4.88 (s, 4H), 4.53 (d, J = 5.7 Hz, 2H), 4.06 (s, 8H), 2.24 –
2.17 (m, 1H), 1.82 – 1.64 (m, 4H), 1.52 – 1.42 (m, 28H), 1.10 – 1.04 (m, 6H).

^{13}C NMR (126 MHz, CD$_3$CN, 25 °C) **δ** = 167.26, 159.51, 156.45, 150.36, 147.86,
146.28, 139.02, 138.78, 136.09, 134.85, 125.40, 124.52, 124.17, 120.74, 106.77,
100.41, 73.22, 65.97, 38.19, 32.28, 31.54, 31.50, 30.32, 30.27, 30.01, 29.94, 29.73,
29.69, 27.05, 23.02, 22.99, 13.98 ppm.

HRMS (ESI-ToF, MeOH, positive mode): calc. for $[C_{56}H_{72}RuN_8O_5]^{2+}$519.2337; found
519.2340.

Ruthenium(II) Polypyridyl Complexes

31
C$_{17}$H$_{25}$BrSi
336.09 g/mol
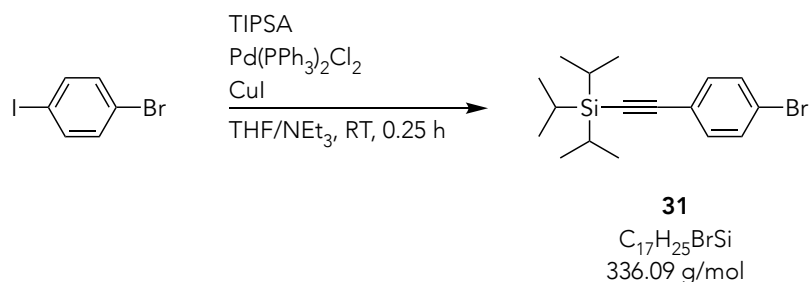
(4-bromophenyl)ethyniyl)triisopropylsilane (31): An oven-dried 100 mL Schlenk-tube was purged with argon and charged with 1,4-bromoiodobenzene (1.5 g, 5.3 mmol, 1.0 eq), bis(triphenylphosphine) palladium(II) chloride (186 mg, 265 µmol, 0.05 eq.) copper(I) iodide (103 mg, 530 µmol 0.1 eq), triethylamine (10 mL) and THF (30 mL). The mixture was degassed with argon for 15 min and then (triisopropylsilyl) acetylene (1.3 mL, 5.8 mmol, 1.1 eq) was added. The reaction mixture was stirred at room temperature for 15 min. After the TLC confirmed full consumption of the starting material, the reaction was stopped by removing the solvents under reduced pressure. The remains were eluted with DCM and again concentrated on celite to purify the crude via flash column chromatography (cyclohexane) to obtain a colorless oil (1.78 g, 5.3 mmol, quant.).

Analytical data for 31:

^{1}H NMR (500 MHz, CDCl$_3$, 25 °C) **δ** = 7.44 (d, J = 8.1 Hz, 2H), 7.35 (d, J = 8.1 Hz, 2H), 1.15 (s, 21H).

^{13}C NMR (126 MHz, CDCl$_3$, 25 °C) **δ** = 133.58, 131.57, 122.67, 122.63, 106.04, 92.16, 18.80, 11.44.ppm.

GCMS (EI$^+$, 70 eV): *m/z* [ion, intensity (%)] = 336 (8) [M+], 293 (100) [M+-C3H7], 267 (32), 251 (43), 237 (61), 223 (73), 129 (33).

32
$C_{23}H_{37}BO_2Si$
384.27 g/mol
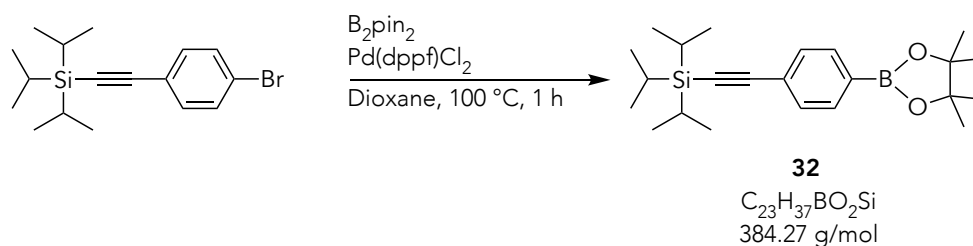
4,4,5,5-tetramethyl-2-[4-[2-[tris(1-methylethyl)silyl]ethynyl]-1,3,2-dioxaborolane (32):

An oven dried 100 mL Schlenk-tube was purged with argon and charged with ((4-bromophenyl)ethynyl)triisopropylsilane (**31**, 1.0 g, 3.1 mmol, 1.0 eq.), bis(pinacolato)diboron (0.8 g, 3.1 mmol, 1.0 eq.), potassium acetate (, 3.0 g, 31.1 mmol, 10.0 eq.), and dioxane (25mL). The mixture was degassed with argon for 15 min and then dichloro[1,1'-bis(diphenylphophino)ferrocene]palladium(II) (120.0 mg, 164 µmol, 0.05 eq.) was added. The reaction mixture was stirred at 100 °C for 1h. After the TLC confirmed full consumption of the starting material, the reaction was stopped by removing the solvent under *vaquo*. The remains were eluted with DCM and reconcentrated on celite to purify the crude via flash column chromatography (DCM:cyclohexane = 1:3) to obtain a colorless solid (1.1 g, 2.9 mmol, 94 %).

Analytical data for 32:

¹H NMR (500 MHz, CDCl$_3$, 25 °C) **δ** = 7.73 (d, J = 8.3 Hz, 2H), 7.46 (d, J = 8.3 Hz, 2H), 1.34 (s, 12H), 1.14 – 1.12 (m, 21H).

¹³C NMR (126 MHz, CDCl$_3$, 25 °C) **δ** = 134.59, 131.31, 126.37, 107.32, 92.19, 84.08, 83.65, 25.01, 18.81, 11.47 ppm.

GCMS (EI⁺, 70 eV): *m/z* [ion, intensity (%)] = 384 [5%, M⁺], 341 [100%, M⁺ - C$_3$H$_7$], 313 [27%], 299 [45%], 285 [50%], 271 [74%], 213 [15%], 171 [38%].

33
$C_{18}H_{33}NSn$
382.16 g/mol
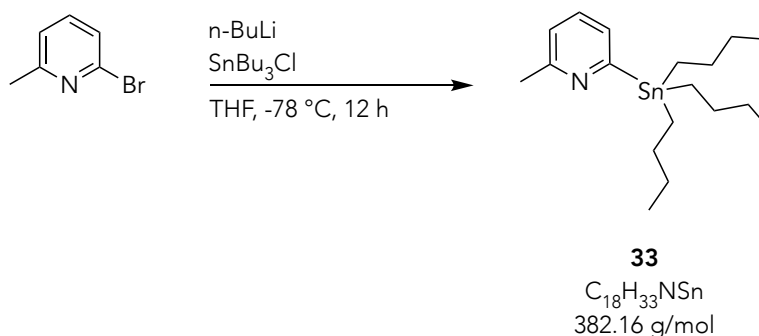
2-Methyl-6-(tributhylstannyl)pyridine (33): An oven-dried 100 mL Schlenk-tube was purged with argon and charged with 2-bromo-6-methylpyridine (1.5 g, 8.7 mmol, 1.0 eq.) and dry THF (30 mL). The reaction mixture was cooled to -78 °C, before *n-* BuLi (1.6 M in hexane, 6.00 mL, 9.6 mmol, 1.1 eq.) was added dropwise. After 30 min, SnBu₃Cl (3.5 mL, 13.1 mmol, 1.5 eq.) was added and the reaction mixture was stirred at -78 °C and was gradually warming up to room temperature overnight. The reaction was quenched with H_2O (20 mL) and then extracted with EtOAc (3 x 40 mL). The combined organic phases were dried over $MgSO_4$, filtered and concentrated under reduced pressure. The crude was purified by flash column chromatography (EtOAc :cyclohexane = 1:3) to give the title compound as a yellowish oil (3.3 g, 8.7 mmol, 98 %).

Analytical data for 33:

¹H NMR (400 MHz, CDCl₃, 22 °C) **δ** = 7.36 (t, J = 7.5 Hz, 1H), 7.18 (d, J = 7.5 Hz, 1H), 6.95 (d, J = 7.8 Hz, 1H), 2.54 (s, 3H), 1.60 – 1.52 (m, 6H), 1.37 – 1.29 (m, 6H), 1.13 – 1.07 (m, 6H), 0.93 – 0.85 (m, 9H).

¹³C NMR (101 MHz, CDCl₃, 22 °C) **δ** = 173.23, 158.74, 133.37, 129.48, 121.60, 29.23, 27.48, 25.08, 13.84, 9.99 ppm.

HRMS (ESI-ToF, MeOH, positive mode): calc. for $[C_{18}H_{34}NSn]^+$ 384.1711; found 384.1716.

34
C$_{12}$H$_{12}$N$_2$
184.10 g/mol
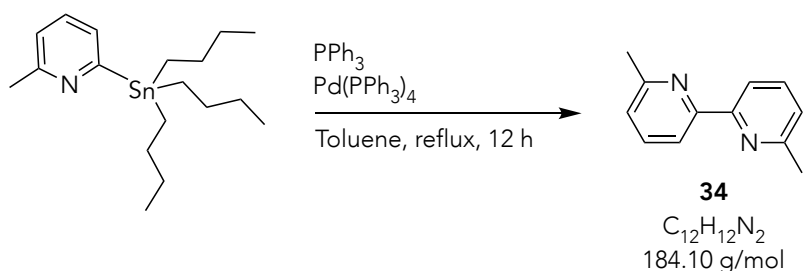
6,6'-Dimethyl-2,2'-bipyridine (34): An oven-dried 50 mL two-necked round bottomed flask purged with argon was charged with 2-methyl-6-(tributhylstannyl)pyridine (**33**, 3.7 g, 9.7 mmol 1.1 eq.), 2-bromo-6-methylpyridine (1.5 g, 8.8 mmol, 1.0 eq.), triphenylphosphine (47.0 mg, 176 µmol, 0.02 eq.) and dry toluene (20 mL). The mixture was degassed for 15 min before adding tetrakis(triphenylphosphine)palladium(0) (100 mg, 88.0 µmol, 0.01 eq.). The reaction mixture was refluxed for 12 h. After the TLC confirmed full conversion of the starting material, the reaction was quenched with H$_2$O (20 mL) and then extracted with EtOAc (3 x 15 mL). The combined organic phases were dried over MgSO$_4$, filtered and concentrated under reduced pressure. The crude was purified by flash column chromatography (EtOAc:cyclohexane = 1:5 + 0.1 % NH$_4$OH) to give the desired compound as a yellowish oil (1.1 g, 5.9 mmol, 68 %).

Analytical data for 34:

¹H NMR (500 MHz, CDCl$_3$, 25 °C) **δ** = 8.18 (d, J = 7.8 Hz, 2H), 7.68 (t, J = 7.7 Hz, 2H), 7.15 (d, J = 7.6 Hz, 2H), 2.63 (s, 6H).

¹³C NMR (126 MHz, CDCl$_3$, 25 °C) **δ** = 158.00, 156.11, 137.12, 123.18, 118.30, 24.83 ppm.

HRMS (ESI-ToF, MeOH, positive mode): calc. for [C$_{12}$H$_{13}$N$_2$]$^+$ 185.1073; found 185.1075.

35
$C_{12}H_{12}N_2O$
200.09 g/mol
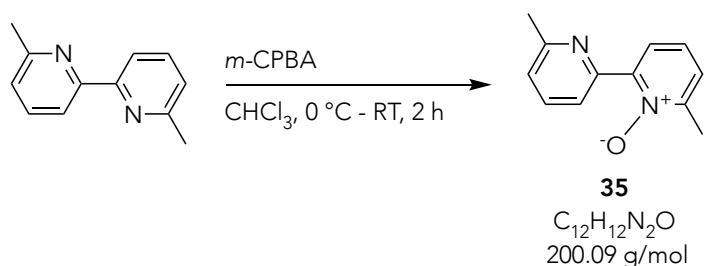
6,6'-Dimethyl-2,2'-bipyridine-1-oxide (35): A 100 mL round-bottomed flask was charged with 6,6'-dimethyl-2,2'-bipyridine (**34**, 600 mg, 3.2 mmol, 1.0 eq.) and chloroform (20 mL). The reaction mixture was cooled to 0 °C and *m*-chloroperbenzoic acid (730 mg, 3.2 mmol, 1.0 eq.) dissolved in chloroform (20 mL) was added dropwise. The solution was stirred for 2 h at room temperature. After TLC confirmed full conversion of the starting material, the reaction was quenched with H_2O (10 mL) and the aqueous phase was extracted with DCM (3 x 10 mL). The combined organic layers were washed with a saturated aqueous solution of sodium hydrogen carbonate (2 x 10 mL), water (3 x 10 mL), dried over $MgSO_4$, filtered and concentrated under reduced pressure. The crude was purified by column chromatography (EtOAc:cyclohexane = 1:5 + 0.1 % NH_4OH) to yield the desired product as a brownish solid (490 mg, 2.4 mmol, 75 %).

Analytical data for 35:

¹H NMR (400 MHz, $CDCl_3$, 22 °C) **δ** = 8.55 (d, J = 7.9 Hz, 1H), 7.97 (dd, J = 7.4, 2.8 Hz, 1H), 7.70 (t, J = 7.8 Hz, 1H), 7.30 – 7.23 (m, 2H), 7.20 (d, J = 7.6 Hz, 1H), 2.62 (s, 3H), 2.58 (s, 3H).

¹³C NMR (101 MHz, $CDCl_3$, 22 °C) **δ** = 158.07, 149.79, 149.78, 147.83, 136.27, 125.63, 125.62, 124.88, 123.59, 122.48, 24.62, 18.44 ppm.

HRMS (ESI-ToF, MeOH, positive mode): calc. for $[C_{12}H_{13}N_2O]^+$ 201.1022; found 201.1021.

36
$C_{12}H_{11}N_3O_3$
245.08 g/mol
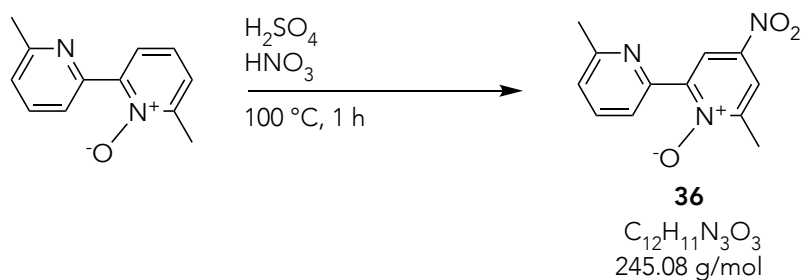
6,6'-Dimethyl-4-nitro-2,2'-bipyridine-1-oxide (36): A 100 mL round-bottomed flask was charged with 6,6'-dimethyl-2,2'-bipyridine 1-oxide (**35**, 7.5 g, 37.4 mmol, 1.0 eq.), conc. sulfuric acid (16 mL) and nitric acid (68%, 11 mL). The reaction mixture was stirred at 100 °C for 1 h. After TLC confirmed full conversion of the starting material, the reaction was poured into ice water and the pH was adjusted to 8 with an aqueous sodium hydroxide solution (10%) and a saturated aqueous sodium bicarbonate solution. The precipitate was filtered, washed with water and dried. The desired product was obtained as a yellowish solid (5.4 g, 22.3 mmol, 60 %).

Analytical data for 36:

¹H NMR (500 MHz, CDCl$_3$, 25 °C) **δ** = 8.95 (d, J = 3.3 Hz, 1H), 8.58 (d, J = 8.0 Hz, 1H), 8.11 (d, J = 3.3 Hz, 1H), 7.75 (t, J = 7.8 Hz, 1H), 7.28 (s, 1H), 2.66 (s, 3H), 2.63 (s, 3H).

¹³C NMR (126 MHz, CDCl$_3$, 25 °C) **δ** = 158.61, 151.87, 147.29, 141.45, 137.83, 125.35, 122.77, 120.42, 119.28, 29.86, 24.16, 18.86 ppm.

HRMS (ESI-ToF, MeOH, positive mode): calc. for [C$_{12}$H$_{12}$N$_3$O$_3$]$^+$ 246.0873; found 246.0874.

37
$C_{12}H_{11}BrN_2O$
278.01 g/mol
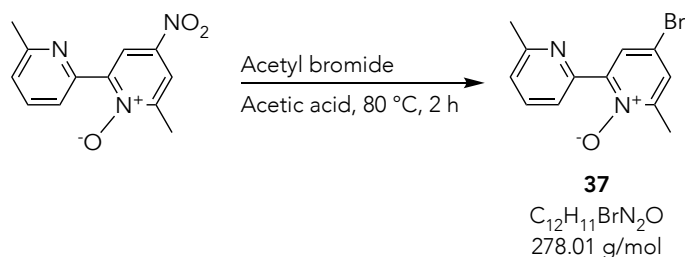
4-Bromo-6,6'-dimethyl-2,2'-bipyridine-1-oxide (37): A 100 mL round-bottomed flask was charged with 6,6'-dimethyl-4-nitro-2,2'-bipyridine-1-oxide (**36**, 2.0 g, 8.3 mmol, 1.0 eq.), acetyl bromide (16.0 mL, 216 mmol, 26.5 eq.) and acetic acid (50 mL). The reaction mixture was refluxed for 2 h. After TLC confirmed full conversion of the starting material, the reaction was poured into ice water and the pH was adjusted to 8 with an aqueous solution of sodium hydroxide (10%) and a saturated aqueous solution of sodium bicarbonate. The aqueous phase was extracted with EtOAc (3 x 15 mL). The combined organic layers were washed with brine, dried over $MgSO_4$, filtered and concentrated under reduced pressure. The crude was purified by column chromatography (acetone:toluene = 1:3) to yield the desired product as a yellow solid (1.2 g, 4.3 mmol, 53 %).

Analytical data for 37:

¹H NMR (500 MHz, CDCl3, 25 °C) **δ** = 8.62 (d, J = 7.9 Hz, 1H), 8.19 (d, J = 3.0 Hz, 1H), 7.70 (t, J = 7.8 Hz, 1H), 7.41 (d, J = 2.3 Hz, 1H), 7.21 (d, J = 7.7 Hz, 1H), 2.62 (s, 3H), 2.55 (s, 3H).

¹³C NMR (126 MHz, CDCl3, 25 °C) **δ** = 158.26, 151.08, 148.45, 136.47, 128.47, 128.29, 124.14, 122.54, 118.16, 29.70, 24.58, 18.30 ppm.

HRMS (ESI-ToF, EtOAc, positive mode): calc. for $[C_{12}H_{12}N_2OBr]^+$ 279.0128; found 279.0130.

38
C$_{12}$H$_{11}$BrN$_2$
262.01 g/mol
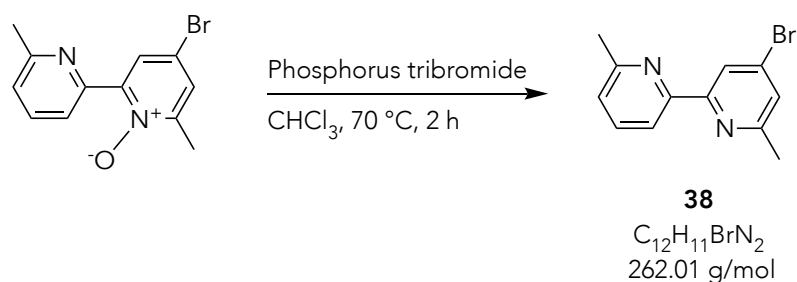
4-Bromo-6,6'-dimethyl-2,2'-bipyridine (38): A 100 mL round-bottomed flask was charged with 4-bromo-6,6'-dimethyl-2,2'-bipyridine-1-oxide (**37**, 955 mg, 3.4 mmol, 1.0 eq) and chloroform (20 mL). Phosphorus tribromide (5.0 mL, 53.3 mmol, 15.6 eq) was added and the reaction mixture was refluxed for 2 h. After TLC confirmed full conversion of the starting material, the reaction was poured into ice water and the pH was adjusted to 8 with an aqueous sodium hydroxide solution (10%) and a saturated aqueous solution of sodium bicarbonate. The aqueous phase was extracted with DCM (3 x 10 mL). The combined organic layers were washed with brine, dried over MgSO$_4$, filtered and concentrated under reduced pressure. The desired product was obtained as an off white solid (843 mg, 3.2 mmol, 93 %).

Analytical data for 38:

¹H NMR (500 MHz, CDCl3, 25 °C) **δ** = 8.42 (d, J = 1.7 Hz, 1H), 8.18 (d, J = 7.8 Hz, 1H), 7.70 (t, J = 7.7 Hz, 1H), 7.33 (d, J = 1.7 Hz, 1H), 7.18 (d, J = 7.6 Hz, 1H), 2.64 (s, 3H), 2.60 (s, 3H).

¹³C NMR (126 MHz, CDCl3, 25 °C) **δ** = 159.17, 157.98, 156.75, 154.28, 137.32, 134.00, 126.17, 123.80, 121.69, 118.60, 24.50, 24.33 ppm.

HRMS (ESI-ToF, MeOH, positive mode): calc. for [C$_{12}$H$_{12}$N$_2$Br]$^+$ 263.0178; found 263.0181.

39
C$_{29}$H$_{36}$N$_2$Si
440.26 g/mol
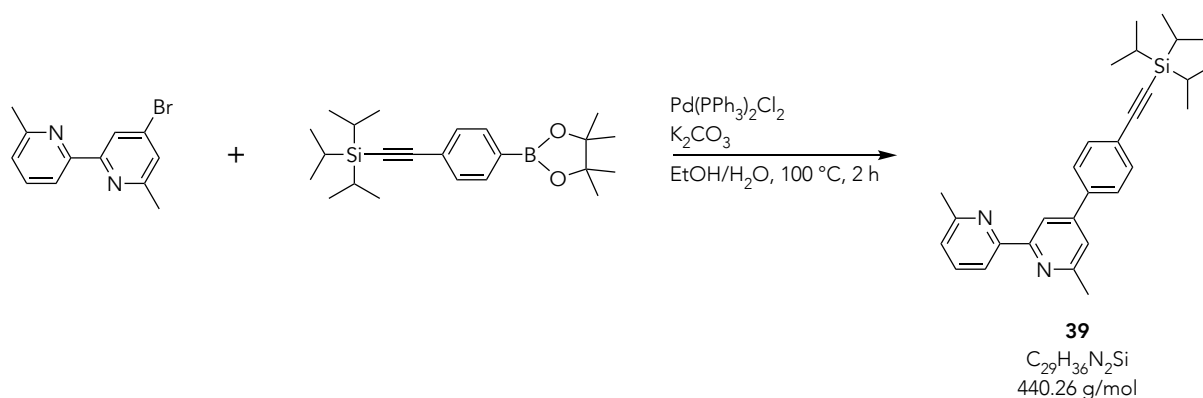
6,6'-Dimethyl-4-(4-((triisopropylsilyl)ethynyl)phenyl)-2,2'-bipyridine (39): An oven-dried 25 mL Schlenk-tube was purged with argon and charged with 4-bromo-6,6'-dimethyl-2,2'-bipyridine (**38**, 400 mg, 1.5 mmol, 1.0 eq.), 4,4,5,5-tetramethyl-2-[4-[2-[tris(1-methylethyl)silyl]ethynyl]phenyl]-1,3,2-dioxaborolane (**32**, 700 mg, 1.8 mmol, 1.2 eq.), potassium carbonate (1.0 g, 7.6 mmol, 5.0 eq), EtOH (30 mL) and H$_2$O (10 mL). The mixture was degassed with argon for 15 min before adding trans-dichloro-(triphenylphosphine)palladium(II) (80.0 mg, 113 µmol, 0.07 eq). The reaction mixture was stirred at 100 °C for 2 h. After TLC confirmed full consumption of the starting material, the reaction was stopped by removing the solvent under reduced pressure. The remains were eluted with DCM and again concentrated on celite to purify the crude via flash column chromatography (acetone:cyclohexane = 1:30 + 1 % NH$_4$OH) to obtain a yellow powder (650 mg, 1.4 mmol, 97 %).

Analytical data for **39**:

¹H NMR (500 MHz, CDCl3, 25 °C) **δ** = 8.43 (s, 1H), 8.23 (d, J = 7.8 Hz, 1H), 7.72 – 7.68 (m, 3H), 7.59 (d, J = 8.4 Hz, 2H), 7.37 (d, J = 1.7 Hz, 1H), 7.18 (d, J = 7.7 Hz, 1H), 2.70 (s, 3H), 2.66 (s, 3H), 1.15 (s, 21H).

¹³C NMR (126 MHz, CDCl3, 25 °C) **δ** = 158.59, 158.09, 149.00, 138.55, 137.35, 132.75, 127.12, 124.31, 123.52, 121.07, 118.76, 116.55, 106.78, 92.46, 27.07, 24.81, 24.76, 18.84, 17.85, 11.49 ppm.

HRMS (ESI-ToF, MeOH, positive mode): calc. for $[C_{29}H_{37}N_2Si]^+$ 441.2721; found 441.2723.
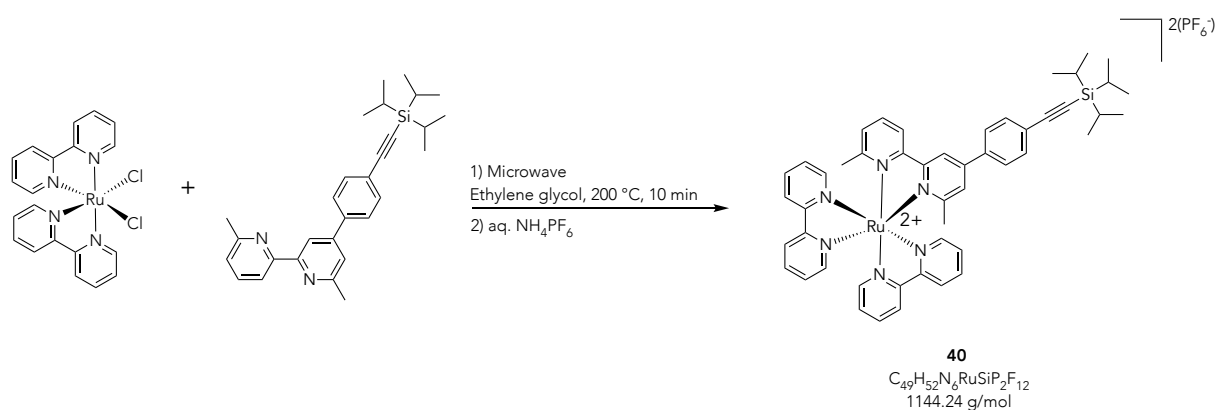
40
$C_{49}H_{52}N_6RuSiP_2F_{12}$
1144.24 g/mol

(6,6'-dimethyl-4-(4-((triisopropylsilyl)ethynyl)phenyl)-2,2'-bipyridine)-bis(bipyridine)ruthenium(II) hexafluorophosphate (40): An oven-dried 10 mL microwave vessel was purged with argon and charged with 6,6'-dimethyl-4-(4-((triisopropylsilyl)ethynyl)phenyl)-2,2'-bipyridine (**39**, 300 mg, 681 µmol, 1.1 eq) and ethylene glycol (5 mL). The mixture was degassed with argon for 15 min before cis-bis(2,2'- bipyridine)dichlororuthenium(II) hydrate (310 mg, 619 µmol, 1.0 eq) was added. The vessel was closed and heated to 200 °C for 10 min. After cooling down to room temperature, an aqueous solution of potassium hexafluorophosphate was added to the mixture in order to exchange the counter ion and make it soluble in organic solvents. The precipitate was filtered and washed with water. The filtrate was solved in DCM (20 mL) and washed with water. The combined organic layers were dried over MgSO₄, filtered and concentrated under reduced pressure. The crude was purified by flash column chromatography (acetone:cyclohexane = 1:10 + 1 % NH₄OH) to obtain a red powder (650 mg, 620 µmmol, 92 %).

Analytical data for 40:

¹H NMR (500 MHz, CD₃CN, 25 °C) **δ** = 8.53 (d, J = 7.9 Hz, 2H), 8.49 (t, J = 7.3 Hz, 2H), 8.42 (dd, J = 13.8, 8.2 Hz, 2H), 8.11 (q, J = 8.3 Hz, 2H), 8.02 – 7.92 (m, 5H), 7.89 (d, J = 8.5 Hz, 2H), 7.68 – 7.63 (m, 4H), 7.60 (s, 1H), 7.48 (q, J = 6.1 Hz, 2H), 7.32 (d, J = 7.7 Hz, 1H), 7.24 (t, J = 6.7 Hz, 2H), 1.71 (s, 3H), 1.70 (s, 3H), 1.16 (s, 21H).

¹³C NMR (126 MHz, CD₃CN, 25 °C) **δ** = 283.78, 283.56, 277.40, 276.77, 275.60, 275.56, 275.36, 275.30, 271.09, 270.83, 269.81, 269.73, 266.32, 256.30, 255.98, 255.92, 255.79, 255.77, 255.74, 255.72, 253.42, 250.61, 250.42, 246.18, 245.45, 245.43, 245.23, 245.20, 243.15, 243.13, 242.45, 242.35, 242.26, 240.35, 237.58, 224.18, 211.35, 142.63, 142.49, 135.94, 129.04 ppm.

HRMS (ESI-ToF, MeOH, positive mode): calc. for $[C_{49}H_{52}N_6RuSi]^{2+}$ 427.1534; found 427.1533.

41
$C_{42}H_{35}N_9O_2RuP_2F_{12}$
1089.13 g/mol

2-(4-(4-(6,6'-dimethyl-[2,2'-bipyridin]-4-yl)phenyl)-1H-1,2,3-triazol-1-yl)acetic acid-bis(bipyridine)-ruthenium(II) Hexafluorophosphate (41): An oven-dried 25 mL two necked round-bottomed flask was purged with argon and was charged with (6,6'-dimethyl-4-(4-((triisopropylsilyl)ethynyl)phenyl)-2,2'-bipyridine)-bis(bipyridine)ruthenium(II) hexafluorophosphate (**40**, 200 mg, 175 µmol, 1.0 eq) and dry THF (10 mL). The solution was degassed for 15 min before TBAF (1M in THF, 260 µl, 262 µmol, 1.5 eq.) was added and the mixture was stirred for 10 min at room temperature. After TLC showed complete conversion of the starting material the reaction mixture was charged with 2-zidoacetic acid (20.0 µL, 268 µmol, 1.5 eq), an aqueous solution of L(+)-sodium ascorbate (1M, 400 µL, 401 µmol, 2.3 eq), an aqueous solution of cooper(II) sulfate (1M, 35 µL, 126 µmol, 0.2 eq) and H_2O (5 mL). The mixture was stirred for 3 h at room temperature. After LC-MS showed complete conversion of the deprotected acetylene species the mixture was diluted with H_2O (10 mL) and extracted with EtOAc (3 x 10 mL). The combined organic layers were washed with a saturated aqueous potassium hexafluorophosphate solution, water, dried over $MgSO_4$, filtered and concentrated under reduced pressure. The crude was solved in MeCN (1 mL) and a saturated aqueous solution of potassium hexafluorophosphate (10 mL) whereupon a precipitate formed. The filtrate was purified by flash column chromatography (MeCN:saturated aqueous ammonium hexafluorophospat solution =

20:1) to (MeCN:saturated aqueous ammonium hexafluorophospat solution = 5:1) to obtain a red powder (85 mg, 175 µmol, 45 %).

Analytical data for 41:

¹H NMR (500 MHz, CD$_3$CN, 25 °C) **δ** = 8.58 (d, J = 2.0 Hz, 1H), 8.53 (d, J = 8.1 Hz, 1H), 8.50 (t, J = 7.9 Hz, 2H), 8.46 – 8.39 (m, 2H), 8.27 (s, 1H), 8.14 – 8.06 (m, 4H), 8.03 (d, J = 6.5 Hz, 1H), 8.01 – 7.91 (m, 7H), 7.68 – 7.63 (m, 3H), 7.52 – 7.45 (m, 2H), 7.32 (dd, J = 7.8, 1.2 Hz, 1H), 7.24 (ddd, J = 7.3, 5.7, 1.3 Hz, 2H), 5.28 (s, 2H), 1.72 (s, 3H), 1.70 (s, 3H).

¹³C NMR (126 MHz, CD$_3$CN, 25 °C) **δ** = 168.57, 166.71, 166.58, 160.38, 159.90, 158.66, 158.62, 158.43, 158.37, 154.32, 154.18, 153.88, 153.15, 152.86, 152.78, 149.78, 147.24, 139.01, 138.81, 138.79, 138.76, 138.74, 135.77, 134.00, 129.18, 128.91, 128.50, 128.47, 128.28, 128.23, 127.32, 126.05, 125.51, 125.40, 125.38, 125.29, 123.91, 123.39, 120.51, 51.56, 25.71, 25.52 ppm.

HRMS (ESI-ToF, MeOH, positive mode): calc. for $[C_{42}H_{35}N_9O_2Ru]^{2+}$ 399.5979; found 399.5981.

42
C$_{18}$H$_{12}$N$_2$
256.10 g/mol
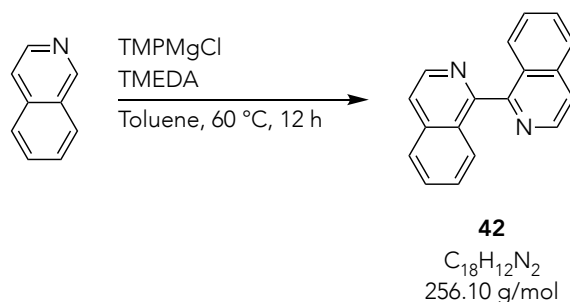
1,1'-Biisoquinoline (42): An oven-dried 100 mL Schlenk-tube was purged with argon and charged with TMPMgCl (1M in THF/Toluene, 12.8 mL, 12.8 mmol, 1.5 eq.), TMEDA (1.50 mL, 10.2 mmol, 1.2 eq.) and dry toluene (10 mL). The mixture was stirred at room temperature for 30 min before isoquinoline (1.00 mL, 8.52 mmol, 1.0 eq.) was added. The reaction mixture was stirred at 60 °C for 12 h. After TLC confirmed full consumption of the starting material, the reaction was stopped by cooling down the reaction at 0 °C adding cold water (20 mL) and extracted with DCM (3 x 15 mL). The combined organic layers were washed with water, dried over MgSO$_4$, filtered and concentrated under reduced pressure. The crude was purified by column chromatography (petroleum ether:EtOAc = 5:1) to yield the desired product as a yellow solid (750 mg, 2.9 mmol, 69 %).

Analytical data for 42:

^{1}H NMR (500 MHz, CD$_2$Cl$_2$, 25 °C) **δ** = 8.69 (d, J = 5.7 Hz, 2H), 7.98 (d, J = 8.2 Hz, 2H), 7.84 (dd, J = 5.7, 0.9 Hz, 2H), 7.75 – 7.66 (m, 4H), 7.48 (ddd, J = 8.3, 6.8, 1.2 Hz, 2H).

^{13}C NMR (126 MHz, CD$_2$Cl$_2$, 25 °C) **δ** = 158.56, 142.24, 137.22, 130.67, 128.22, 127.75, 127.50, 127.30, 121.31 ppm.

HRMS (ESI-ToF, MeOH, positive mode): calc. for [C$_{18}$H$_{13}$N$_2$]$^+$ 257.1073; found 257.1074.

The analytical data are in agreement with the ones reported in ref. [275].

43
C$_{38}$H$_{28}$N$_6$RuP$_2$F$_{12}$
960.07 g/mol
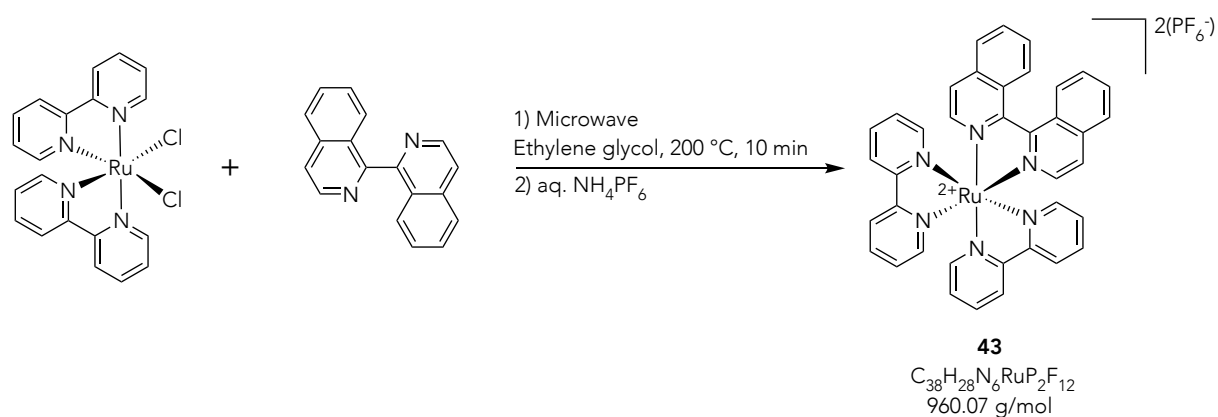
1,1'-biisoquinoline-bis-(2,2'-bipyridine)-ruthenium(II) Hexafluorophosphate (43): An oven-dried 10 mL microwave vessel was purged with argon and charged with 1,1'-biisoquinoline (**42**, 95.0 mg, 373 µmol, 1.0 eq) and ethylene glycol (5 mL). The mixture was degassed with argon for 15 minutes before cisbis(2,2'-bipyridine)dichlororuthenium(II) hydrate (150 mg, 298 µmol, 0.8 eq) was added. The vessel was closed and heated to 200 °C for 10 minutes. After cooling down to room temperature, a saturated aqueous potassium hexafluorophosphate solution (10 mL) was added to the mixture in order to exchange the counter ion and make it soluble in organic solvents. The precipitate was filtered and washed with water (3 x 5 mL). The filtrate was solved in DCM (20 mL) and washed with water. The combined organic layers were dried over MgSO$_4$, filtered and concentrated under reduced pressure. The crude was purified by flash column chromatography (MeCN: saturated aqueous ammonium hexafluorophospat solution = 5:1) to obtain the diastereomeric mixture as a red powder (300 mg, 313 µmol, 84 %).

Analytical data for 43:

LC-MS ESI, MeOH, positive mode: T$_R$ = 6.6 min, *m/z* [ion] = 334.7 [M^{+2}].

44

$C_{36}H_{24}Cl_2N_4Ru$

684.04 g/mol
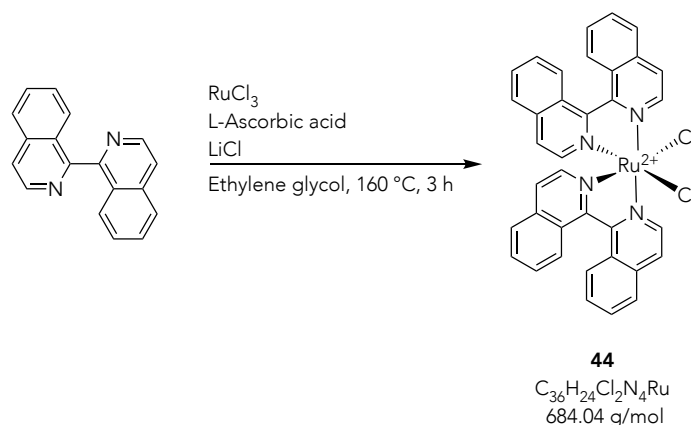
cis-Bis(1,1'-biisoquinoline)dichlororuthenium (44): A 100 mL round-bottomed flask was charged with 1,1'-biisoquinoline (**42**, 200 mg, 780 µmol, 1.0 eq.), LiCl (1.9g, 46.8 mmol, 60.0 eq.), L-ascorbic acid (96.2 mg, 546 µmol, 0.7 eq.) and DMF (10 mL). The mixture was refluxed for 30 min. Afterwards the solution was cooled down to room temperature and acetone (30 mL) was added. The mixture was stored over night at – 20 °C. The formed precipitate was filtered, washed with water (2 x 8 mL), EtOH (8 mL) and Et₂O (2 x 8 mL). The filtrate was dried in *vacuo* for 24 h to yield the titled compound as a green solid (350 mg, 486 µmol, 62 %). The titled compound was used as crude without further purification steps.

45
$C_{48}H_{36}N_6RuP_2F_{12}$
1088.13 g/mol
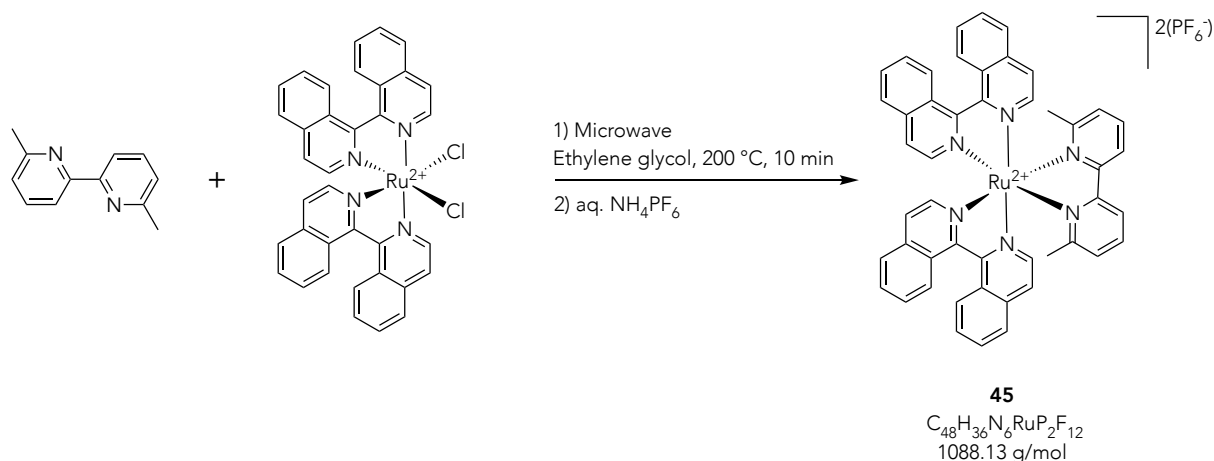
6,6'-Dimethyl-(2,2'-bipyridine)-bis(1,1'-biisoquinoline)ruthenium(II) Hexafluorophosphate (45): An oven-dried 10 mL microwave vessel was purged with argon and charged with 6,6'-dimethyl-2,2'-bipyridine (**34**, 32.0 mg, 174 µmol, 1.0 eq), and ethylene glycol (5 mL). The mixture was degassed with argon for 15 min before cis-bis(1,1'-biisoquinoline)dichlororuthenium (100 mg, 139 µmol, 0.8 eq) was added. The vessel was closed and heated to 200 °C for 10 min. After cooling down to room temperature, a saturated aqueous potassium hexafluorophosphate solution (10 mL) was added to the mixture in order to exchange the counter ion and make it soluble in organic solvents. The precipitate was filtered and washed with water (3 x 5 mL). The filtrate was solved in DCM (20 mL) and washed with water. The combined organic layers were dried over $MgSO_4$, filtered and concentrated under reduced pressure. The crude was purified by flash column chromatography (MeCN:saturated aqueous ammonium hexafluorophosphate solution = 100 : 1) to obtain the diastereomeric mixture as a violet powder (60.0 mg, 54.0 µmol, 31 %).

Analytical data for 45:

¹H NMR (500 MHz, CD_3CN, 25 °C, only the main species is listed, spectrum was difficult to interpret and contains multiple species) **δ** = 8.27 (d, J = 1.4 Hz, 2H), 8.13 (d, J = 8.3 Hz, 2H), 8.04 (d, J = 6.3 Hz, 2H), 7.99 (t, J = 9.0 Hz, 4H), 7.93 – 7.83 (m, 8H), 7.75 – 7.72 (m, 2H), 7.69 – 7.62 (m, 6H), 7.20 (d, J = 1.3 Hz, 2H), 7.15 (d, J = 5.9 Hz, 2H), 3.57 (s, 6H).

HRMS (ESI-ToF, MeOH, positive mode): calc. for $[C_{48}H_{36}N_6Ru]^{2+}$ 399.1023; found 399.1027.

46

C_{36}H_{24}Cl_2N_4Ru
684.04 g/mol
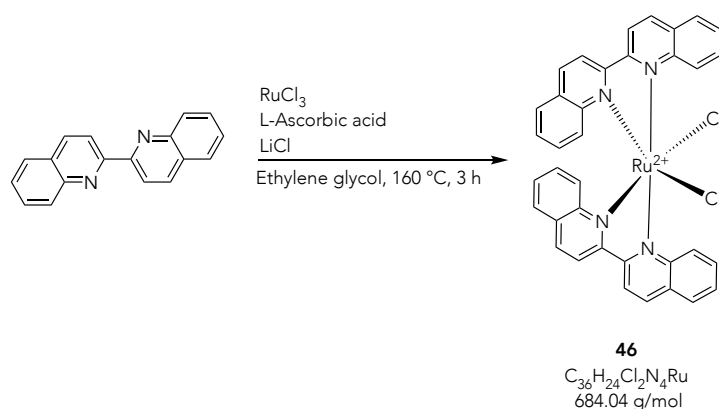
cis-Bis(2,2'-biquinoline)dichlororuthenium (46): A 100 mL round-bottomed flask was charged with 2,2'-biquinoline (600 mg, 2.34 mmol, 1.0 eq.), LiCl (5.95 g, 140 mmol, 60.0 eq.), L-ascorbic acid (289 mg, 1.64 mmol, 0.7 eq.) and DMF (20 mL). The mixture was refluxed for 30 min. Afterwards the solution was cooled down to room temperature and acetone (40 mL) was added. The mixture was stored over night at – 20 °C. The formed precipitate was filtered, washed with water (2 x 10 mL), EtOH (10 mL) and Et_2O (2 x 10 mL). The filtrate was dried in *vacuo* for 24 h to yield the titled compound as a green solid (1.21 g, 1.68 mmol, 72 %). The titled compound was used as crude without further purification steps.

47

$C_{48}H_{36}N_6RuP_2F_{12}$
1088.13 g/mol

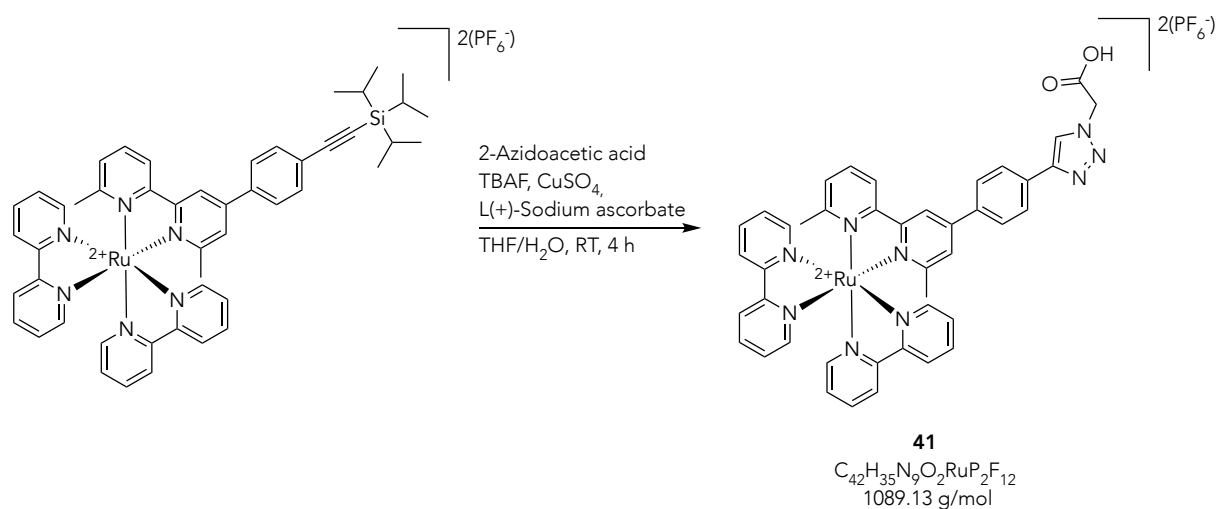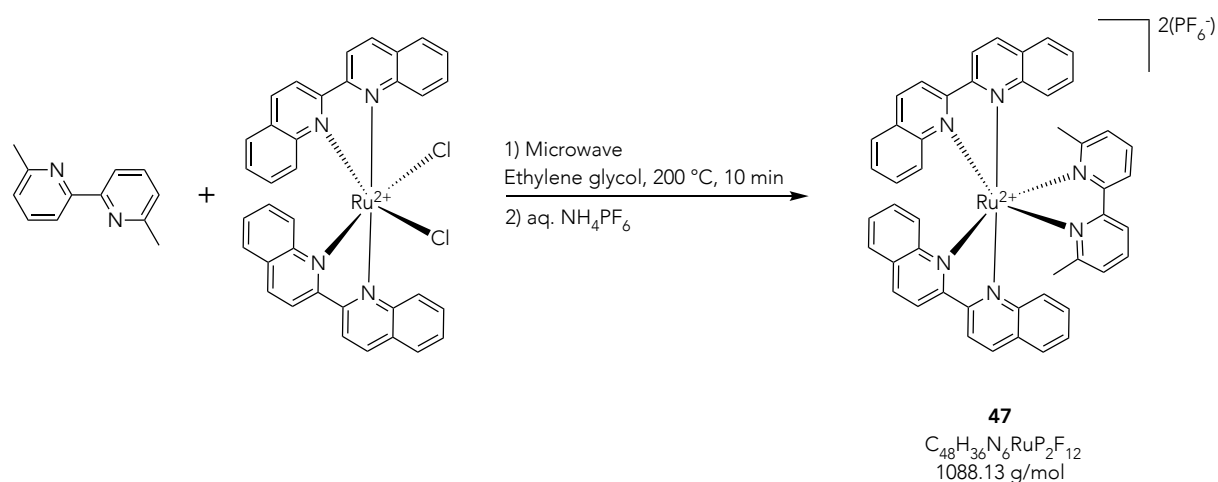**6,6'- Dimethyl- (2,2'- bipyridine)- bis(2,2'- biquinoline)ruthenium(II) Hexafluorophosphate (47):** An oven-dried 10 mL microwave vessel was purged with argon and charged with 6,6'-dimethyl-2,2'-bipyridine (**34**, 64.0 mg, 348 µmol, 1.0 eq), and ethylene glycol (5 mL). The mixture was degassed with argon for 15 min before cis-bis(2,2'-biquinoline)dichlororuthenium (200 mg, 278 µmol, 0.8 eq) was added. The vessel was closed and heated to 200 °C for 10 min. After cooling down to room temperature, a saturated aqueous potassium hexafluorophosphate solution (10 mL) was added to the mixture in order to exchange the counter ion and make it soluble in organic solvents. The precipitate was filtered and washed with water (3 x 5 mL). The filtrate was solved in DCM (20 mL) and washed with water. The combined organic layers were dried over $MgSO_4$, filtered and concentrated under reduced pressure. The crude was purified by flash column chromatography (MeCN:saturated aqueous ammonium hexafluorophosphate solution = 100 : 1) to obtain the compound **47** as a violet powder (30.0 mg, 28.0 µmol, 8 %).

Analytical data for 47:

LC-MS ESI, MeOH, positive mode: T_R = 7.2 min, m/z [ion] = 399.3 [M^{+2}].

HRMS (ESI-ToF, MeOH, positive mode): calc. for $[C_{48}H_{36}N_6Ru]^{2+}$ 399.1023; found 399.1030.

48
$C_{10}H_9NO$
159.07 g/mol
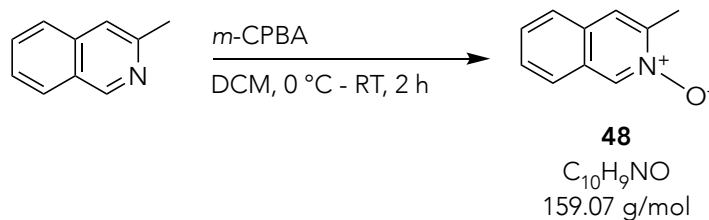
3-Methylisoquinoline-2-oxide (48): A 100 mL round-bottomed flask was charged with 3-methylisoquinoline (1.00 g, 6.98 mmol, 1.0 eq.) and DCM (20 mL). The mixture was cooled down at 0 °C before *m*-CPBA (2.00 g, 9.07 mmol, 1.3 eq.) was added in four portions. The reaction mixture was stirred for 30 min at 0 °C. Afterwards it was allowed to warm up at room temperature and was stirred for 1.5 h. After TLC confirmed full conversion of the starting material, the reaction was quenched with H_2O (20 mL) and the aqueous phase was extracted with EtOAc (3 x 20 mL). The combined organic layers were washed with water (3 x 10 mL), dried over $MgSO_4$, filtered and concentrated under reduced pressure. The crude was purified by column chromatography (EtOAc:MeOH = 2:1) to yield the desired product as an off white solid (1.10 g, 6.91 mmol, 99 %).

Analytical data for 48:

¹H NMR (500 MHz, CDCl₃, 25 °C) **δ =** 8.98 (s, 1H), 7.75 (d, J = 9.2 Hz, 2H), 7.68 (s, 1H), 7.62 – 7.54 (m, 2H), 2.68 (s, 3H).

¹³C NMR (126 MHz, CDCl₃, 25 °C) **δ =** 145.83, 137.17, 130.08, 129.61, 128.68, 128.45, 126.04, 125.12, 123.53, 17.86 ppm.

The analytical data are in agreement with the ones reported in ref. [279].

49

$C_{20}H_{16}N_2$

284.13 g/mol
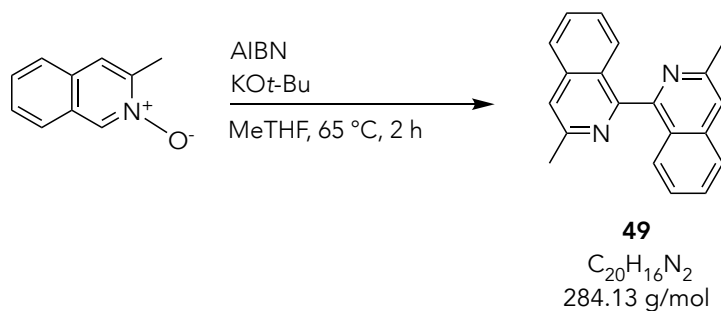
3,3'-Dimethyl-1,1'-biisoquinoline (49): An oven-dried 50 mL Schlenk-tube was purged with argon and charged with 3-methylisoquinoline-2-oxide (**48**, 300 mg, 1.88 mmol, 1.0 eq.) and degassed MeTHF (10 mL). The mixture was degassed with argon for 15 min before it was heated at 65 °C. Afterwards potassium tert-butoxide (640 mg, 5.64 mmol, 3.0 eq.) and azobisisobutyronitrile (63.0 mg, 376 µmol, 0.2 eq.) were added in four portions over 15 min. The reaction mixture was stirred at 65 °C for 2 h. After TLC confirmed full conversion of the starting material, the reaction was quenched with water (20 mL) and the aqueous phase was extracted with EtOAc (3 x 10 mL). The combined organic layers were dried over MgSO₄, filtered and concentrated under reduced pressure. The crude was purified by column chromatography (petroleum ether:EtOAc = 5:1) to yield the desired product as a solid (108.0 mg, 380 µmol, 40 %).

Analytical data for 49:

¹H NMR (500 MHz, CDCl₃, 25 °C) **δ =** 7.82 (d, J = 8.3 Hz, 2H), 7.64 – 7.59 (m, 4H), 7.52 (dd, J = 8.5, 1.0 Hz, 2H), 7.34 (ddd, J = 8.2, 6.8, 1.2 Hz, 2H), 2.79 (s, 6H).

¹³C NMR (126 MHz, CDCl₃, 25 °C) **δ =** 157.97, 151.00, 137.63, 130.35, 127.26, 126.55, 126.41, 126.16, 119.18, 24.49 ppm.

The analytical data are in agreement with the ones reported in ref. [280].

50
$C_{40}H_{32}N_6RuP_2F_{12}$
988.10 g/mol
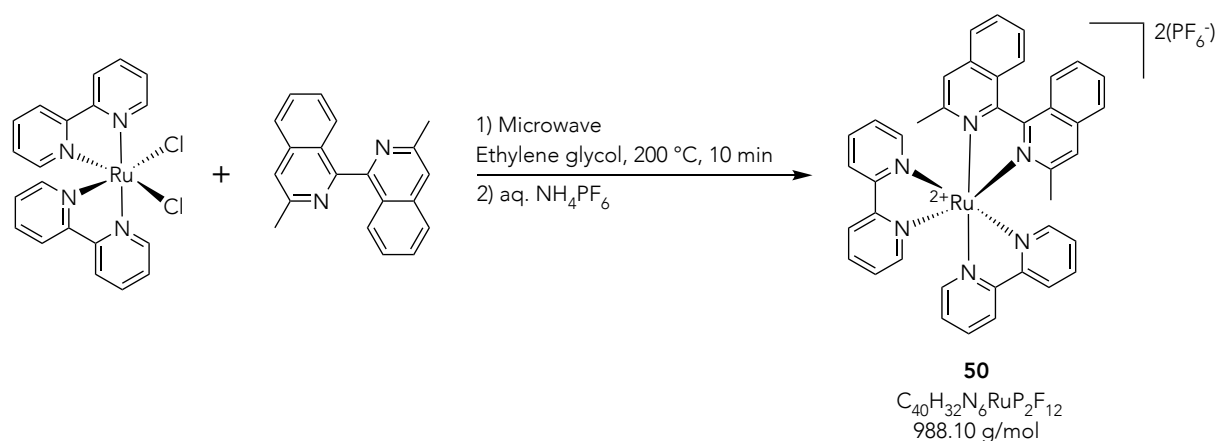
3,3'-Dimethyl-1,1'-biisoquinoline-(2,2'-bipyridine)-ruthenium(II) Hexafluorophosphate (50): An oven-dried 10 mL microwave vessel was purged with argon and charged with 3,3'-dimethyl-1,1'-biisoquinoline (**49**, 25.0 mg, 88.0 µmol, 1.0 eq) and ethylene glycol (5 mL). The mixture was degassed with argon for 15 min before cisbis(2,2′-bipyridine)dichlororuthenium(II) hydrate (35.0 mg, 70.0 µmol, 0.8 eq) was added. The vessel was closed and heated to 200 °C for 10 min. After cooling down to room temperature, a saturated aqueous potassium hexafluorophosphate solution (10 mL) was added to the mixture in order to exchange the counter ion and make it soluble in organic solvents. The precipitate was filtered and washed with water (3 x 5 mL). The filtrate was solved in DCM (20 mL) and washed with water. The combined organic layers were dried over $MgSO_4$, filtered and concentrated under reduced pressure. The crude was purified by flash column chromatography (MeCN:saturated aqueous ammonium hexafluorophospat solution = 5:1) to obtain compound **50** as red powder (30.0 mg, 29.9 µmol, 34 %).

Analytical data for 50:

¹H NMR (500 MHz, CD₃CN, 25 °C) **δ** 8.58 (ddd, J = 5.6, 1.5, 0.8 Hz, 2H), 8.43 – 8.40 (m, 4H), 7.94 (dtd, J = 16.0, 7.9, 1.5 Hz, 4H), 7.88 (dt, J = 8.5, 1.0 Hz, 2H), 7.78 (ddd, J = 8.3, 6.8, 1.1 Hz, 2H), 7.68 (s, 2H), 7.63 (ddd, J = 5.7, 1.5, 0.7 Hz, 2H), 7.55 (dd, J = 8.7, 1.0 Hz, 2H), 7.45 (ddd, J = 8.8, 6.8, 1.3 Hz, 2H), 7.25 – 7.18 (m, 4H), 1.81 (s, 6H).

¹³C NMR (126 MHz, CD₃CN, 25 °C) **δ** = 162.83, 158.55, 158.27, 156.65, 154.33, 153.53, 152.82, 151.94, 138.87, 138.80, 138.63, 138.46, 137.72, 133.54, 131.46, 128.98, 128.74, 128.67, 128.27, 128.18, 127.91, 127.70, 127.61, 127.43, 127.20, 126.73, 125.64, 125.52, 125.28, 125.14, 124.92, 119.70, 24.38 ppm.

HRMS (ESI-ToF, MeOH, positive mode): calc. for [C₄₀H₃₂N₆Ru]²⁺ 349.0866; found 349.0865.

Appendix

^{1}H-, ^{13}C-NMR (CDCl$_3$, 500/126 MHz, 25 °C) and HR-ESI-MS spectra of compound 4

^{1}H NMR (500 MHz, CDCl$_3$) δ =
10.21 (s, 2H),
9.16 (dd, J = 2.2, 0.9 Hz, 2H),
8.81 (d, J = 8.2 Hz, 2H),
8.64 (d, J = 7.8 Hz, 2H),
8.35 (dd, J = 8.2, 2.2 Hz, 2H),
8.06 (t, J = 7.8 Hz, 1H).

4

$C_{17}H_{11}N_3O_2$
289.29 g/mol

^{13}C NMR (126 MHz, CDCl$_3$) δ =
190.68, 160.50, 154.56, 151.96,
138.52, 136.96, 131.45, 123.39,
121.50.

4

$C_{17}H_{11}N_3O_2$
289.29 g/mol
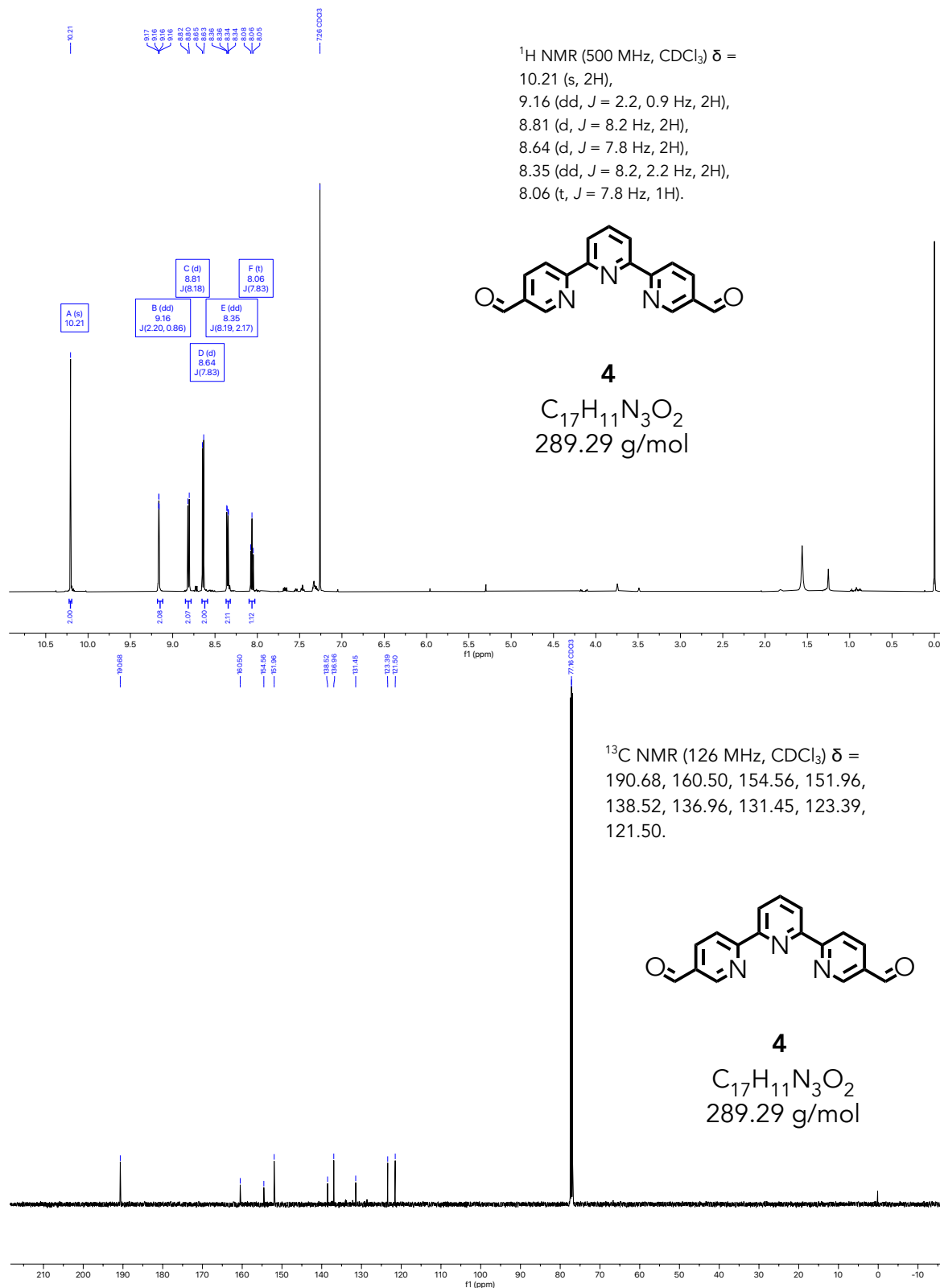
High Resolution Mass Spectrometry Report

Sample Name   **DIA-687**   Instrument   maXis 4G
Comment   Method   ms_nocolumn_mid_pos.m
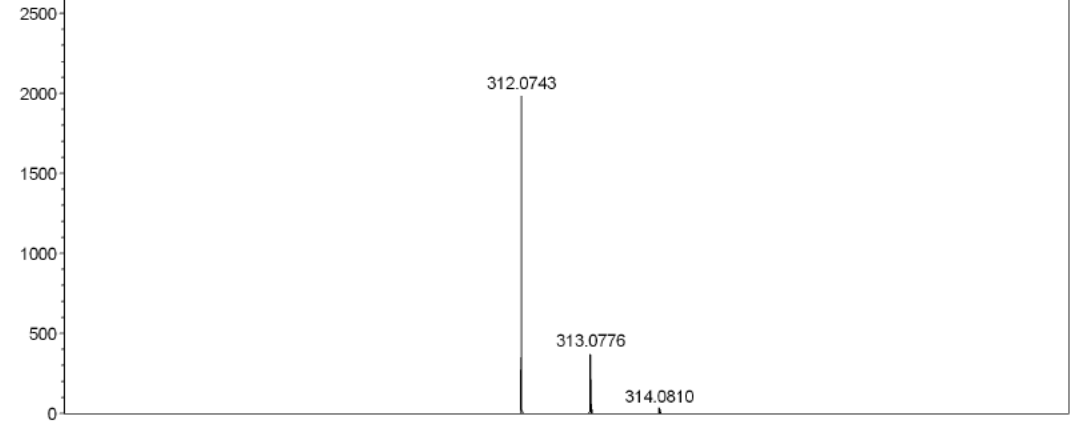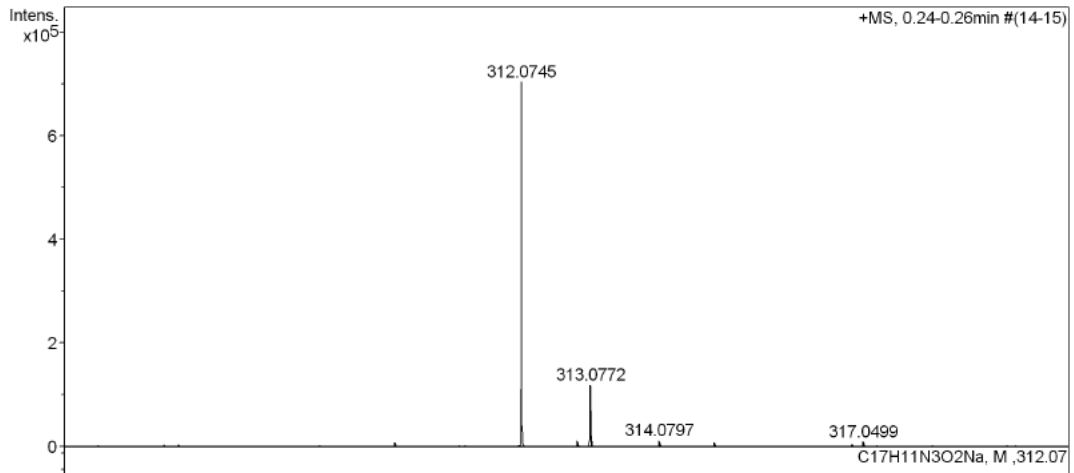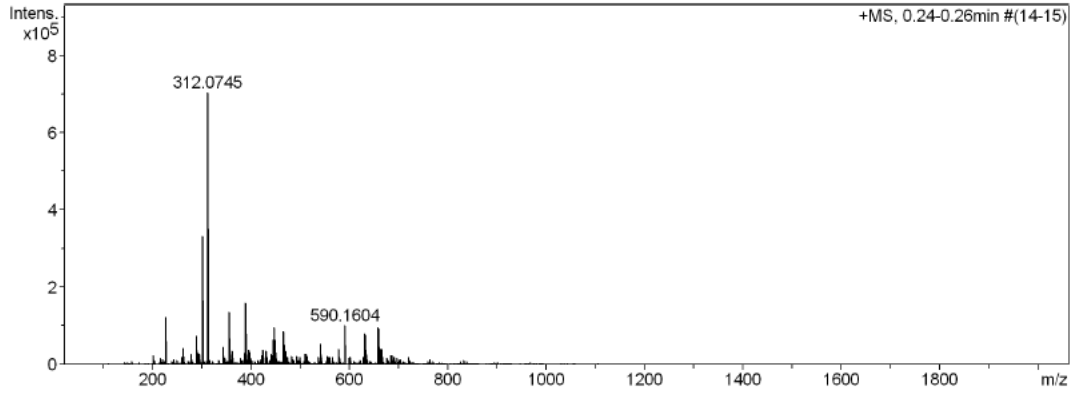
Intens.
x10⁵

+MS, 0.24-0.26min #(14-15)

312.0745

590.1604

Intens.
x10⁵

+MS, 0.24-0.26min #(14-15)

312.0745

313.0772

314.0797

317.0499

C17H11N3O2Na, M ,312.07

312.0743

313.0776

314.0810

High Resolution Mass Spectrometry Report

Measured m/z vs. theoretical m/z

Meas. m/z	#	Formula	Score	m/z	err [mDa]	err [ppm]	mSigma	rdb	e⁻ Conf	z
312.0745	1	C 17 H 11 N 3 Na O 2	100.00	312.0743	-0.1	-0.3	14.8	13.5	even	1+

Mass list

#	m/z	I %	I
1	201.1094	3.6	25171
2	217.1042	2.3	16524
3	220.9340	2.1	14690
4	226.9512	17.6	124213
5	261.1302	2.7	18825
6	263.0979	6.0	42437
7	279.0931	3.9	27274
8	288.9216	10.7	75627
9	290.0919	6.4	44783
10	293.1086	4.4	30856
11	294.9195	3.9	27829
12	301.0752	47.1	331865
13	302.0782	8.0	56625
14	312.0745	100.0	704957
15	313.0772	17.0	119551
16	344.0998	6.5	45981
17	347.0674	2.5	17414
18	356.1004	19.2	135357
19	356.9089	2.1	14924
20	357.1031	3.8	26811
21	362.9259	5.1	36148
22	379.1933	2.4	16992
23	387.9855	4.1	28937
24	388.9879	2.4	16998
25	389.1007	22.7	159821
26	389.9859	5.8	40831
27	390.1036	6.0	42061
28	391.9852	3.7	26139
29	395.9890	5.4	37828
30	397.9891	4.5	31641
31	398.0105	4.3	30315
32	400.0080	2.3	16304
33	423.2194	3.6	25209
34	424.8964	5.4	37836
35	430.0371	2.4	16794
36	430.9134	5.0	35081
37	433.1266	2.6	18305
38	442.0368	3.7	25948
39	444.0643	3.6	25324
40	445.0663	2.6	18049
41	446.0640	9.1	64338
42	447.0658	5.2	36795
43	448.0645	13.7	96643
44	448.8629	2.4	17028
45	449.0659	4.2	29578
46	450.0638	9.0	63580
47	452.0664	2.4	16769
48	465.9985	12.1	85361
49	467.0013	2.7	19045
50	467.1016	7.1	50384
51	467.2454	3.9	27524
52	467.9957	7.2	50589
53	468.1020	2.9	20553
54	468.9979	2.5	17747
55	469.9944	4.8	34057
56	473.0158	2.6	18414
57	475.0159	2.6	18258
58	481.9722	3.2	22618
59	492.8838	3.2	22888
60	498.9007	2.6	18488
61	510.0244	4.0	28264
62	511.2718	3.8	26945

Bruker Compass DataAnalysis 4.0   Acquisition Date   09.03.2021 10:37:54

High Resolution Mass Spectrometry Report

#	m/z	I %	I
63	512.0218	2.4	17087
64	513.1428	3.0	21497
65	536.1642	2.5	17966
66	541.1202	7.5	53145
67	542.1209	3.7	26425
68	543.1185	2.6	18540
69	555.2983	3.1	21766
70	557.0936	2.3	16365
71	560.8710	2.9	20322
72	566.8881	2.6	18371
73	579.1610	5.7	40246
74	580.1639	2.3	16358
75	590.1604	14.3	100853
76	591.1632	5.4	38071
77	599.3236	2.2	15774
78	601.1588	2.6	18617
79	628.8585	2.7	19330
80	631.0869	11.4	80624
81	632.0901	4.2	29837
82	633.0871	11.1	78515
83	634.0899	3.9	27397
84	634.1859	2.6	18302
85	658.0808	13.8	97116
86	659.0836	5.2	36852
87	660.0811	13.2	93236
88	661.0835	4.9	34620
89	663.0587	5.6	39275
90	664.0611	2.2	15629
91	665.0587	5.6	39691
92	666.0633	2.9	20605
93	676.0961	2.4	17228
94	685.0742	3.3	23497
95	687.0742	3.4	24151
96	690.0522	2.5	17706
97	692.0523	2.6	18641
98	696.8457	2.5	17676
99	702.8627	2.1	14711
100	720.1226	2.8	19880

Acquisition Parameter

General	Fore Vacuum	2.39e+000 mBar	High Vacuum	1.01e-007 mBar	Source Type	ESI	
	Scan Begin	75 m/z	Scan End	2000 m/z	Ion Polarity	Positive	
Source	Set Nebulizer	2.0 Bar	Set Capillary	4500 V	Set Dry Gas	8.0 l/min	
	Set Dry Heater	200 °C	Set End Plate Offset	-500 V			
Quadrupole	Set Ion Energy (MS only)	4.0 eV					
Coll. Cell	Collision Energy	8.0 eV	Set Collision Cell RF	600.0 Vpp	100.0 Vpp		
Ion Cooler	Set Ion Cooler Transfer Time	75.0 µs	Set Ion Cooler Pre Pulse Storage Time	10.0 µs			

1H-, 13C-, HMQC- HMBC-, TOCSY-NMR (CDCl3, 500/126 MHz, 25 °C) and HR-ESI-MS spectra of compound **10**

^{1}H NMR (500 MHz, CDCl$_3$) δ =
10.12 (s, 2H),
9.48 (d, J = 1.9 Hz, 2H),
8.98 (dd, J = 8.5, 2.2 Hz, 2H),
8.84 (d, J = 8.6 Hz, 2H),
8.59 (d, J = 7.7 Hz, 2H).

H (dd)
8.49
J(8.63, 7.27)

E (dd)
8.98
J(8.55, 2.16)

B (d)
8.23
J(8.41)

C (s)
10.12

D (d)
9.48
J(1.90)

F (d)
8.84
J(8.55)

A (d)
7.97
J(8.34)

G (d)
8.59
J(7.65)

10
C$_{29}$H$_{19}$N$_3$O$_2$
441.49 g/mol

^{13}C NMR (126 MHz, CDCl$_3$) δ =
195.04, 146.65, 145.90, 145.74, 142.39, 141.27,
140.79, 138.71, 137.14, 132.20, 128.40, 126.09,
125.33.

10
C$_{29}$H$_{19}$N$_3$O$_2$
441.49 g/mol
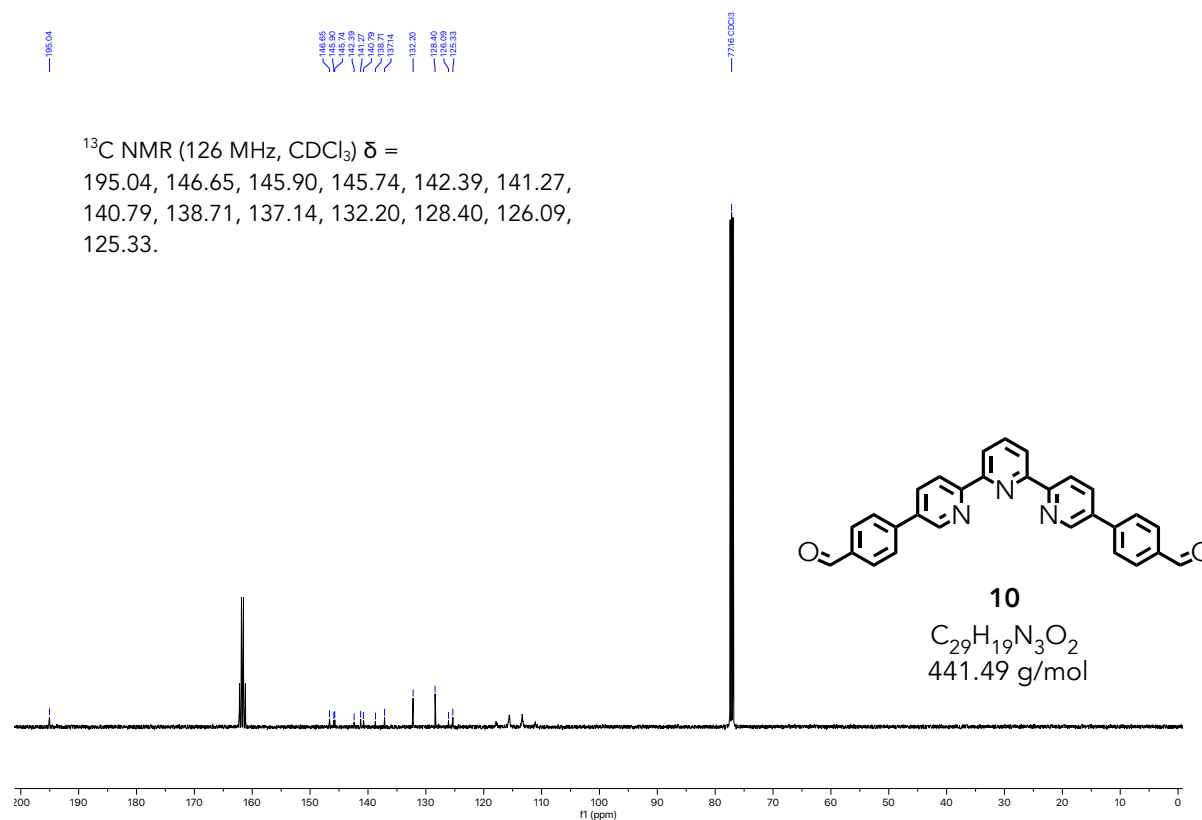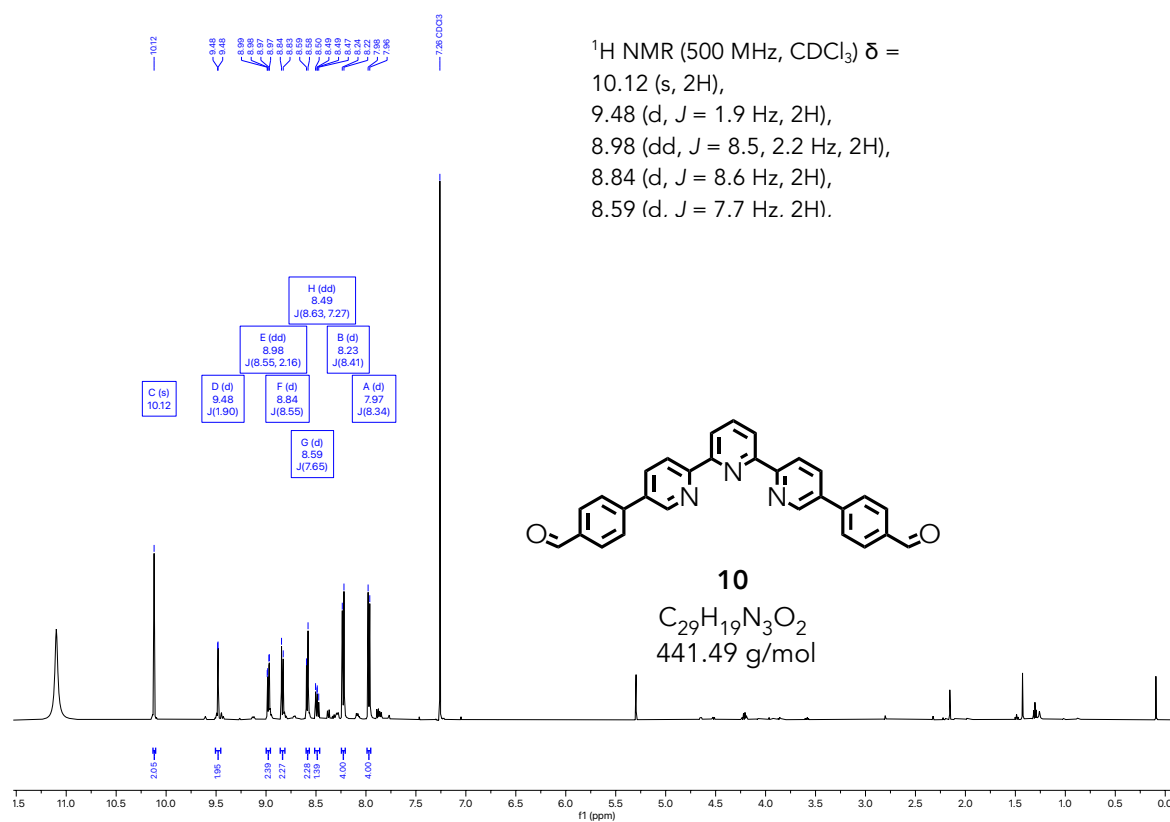
HMQC-NMR Spectrum of Compound (10)

HMBC-NMR Spectrum of Compound (10)
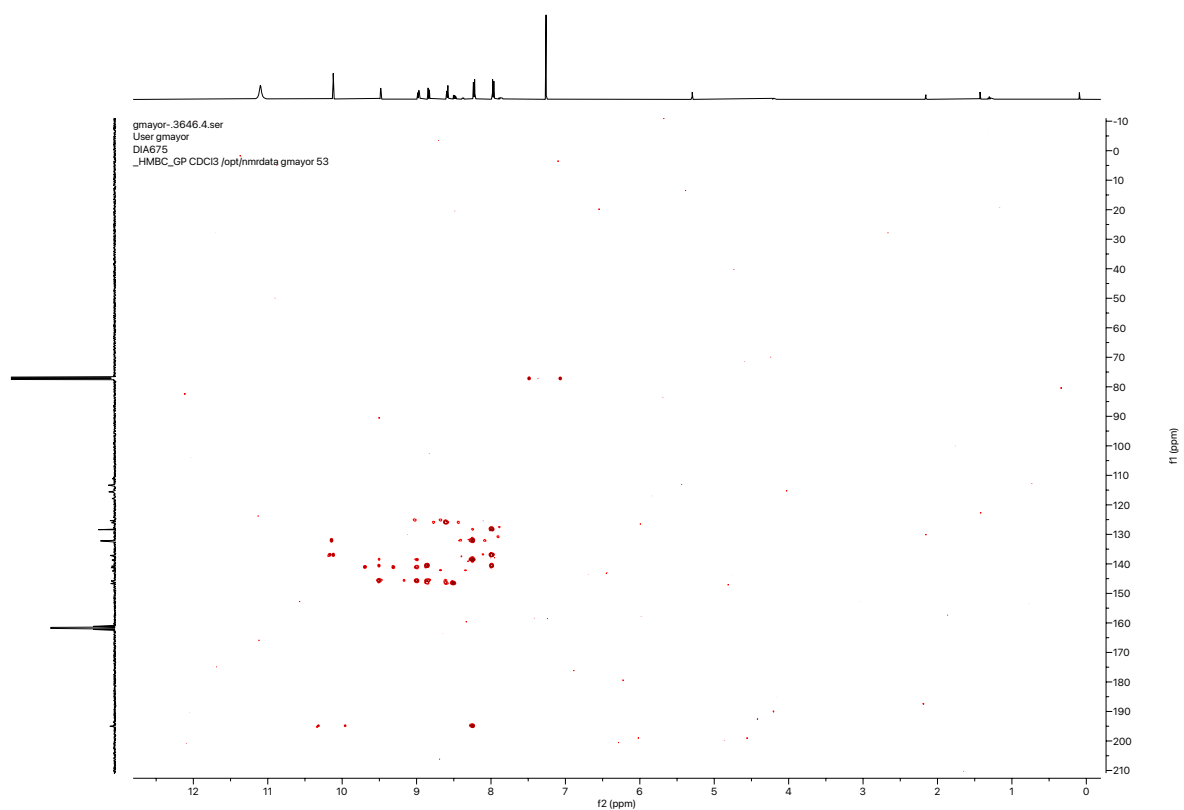
TOCSY-NMR Spectrum of Compound (10)

gmayor-.3646.6.ser
User gmayor
DIA675
_TOCSY CDCl3 /opt/nmrdata gmayor 53
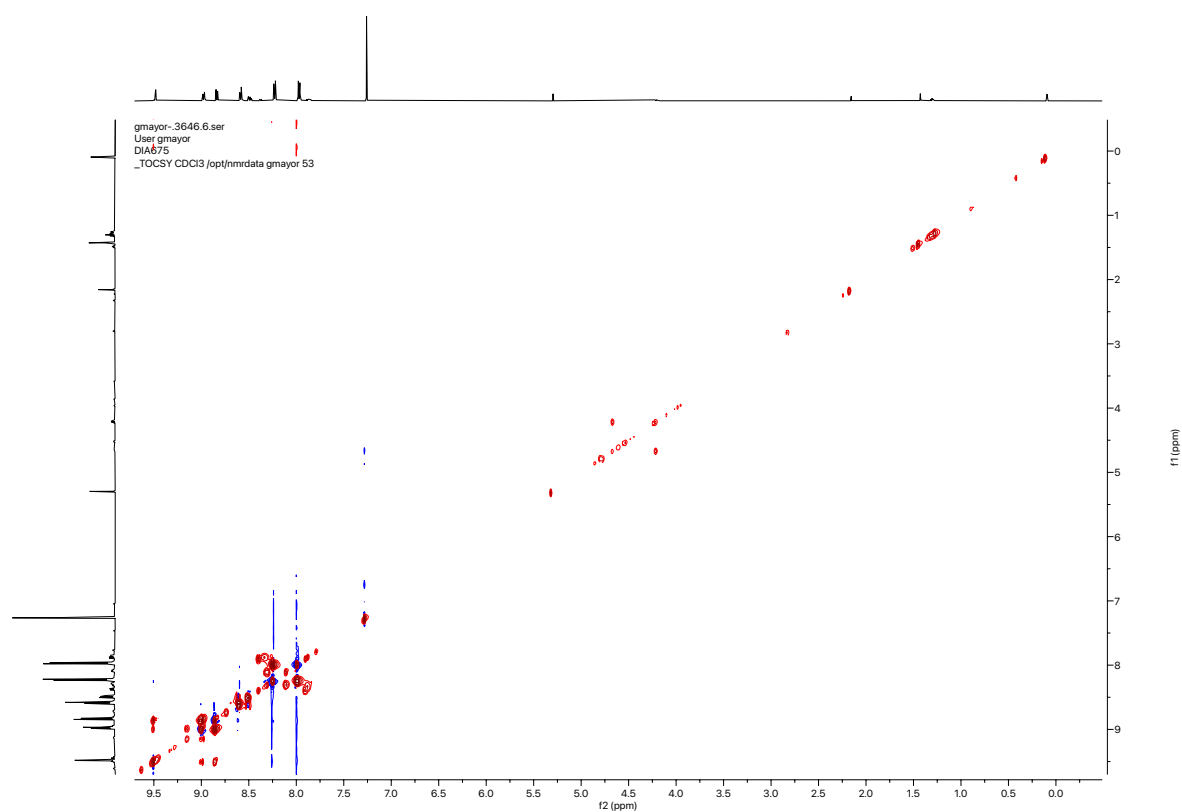
High Resolution Mass Spectrometry Report

Sample Name	**Alfredo di Silvestro / dia485**	Instrument	maXis 4G
Comment	10 ug / mL in MeCN/MeOH, analyzed in MeOH	Method	22 Direct_pos_mid.m
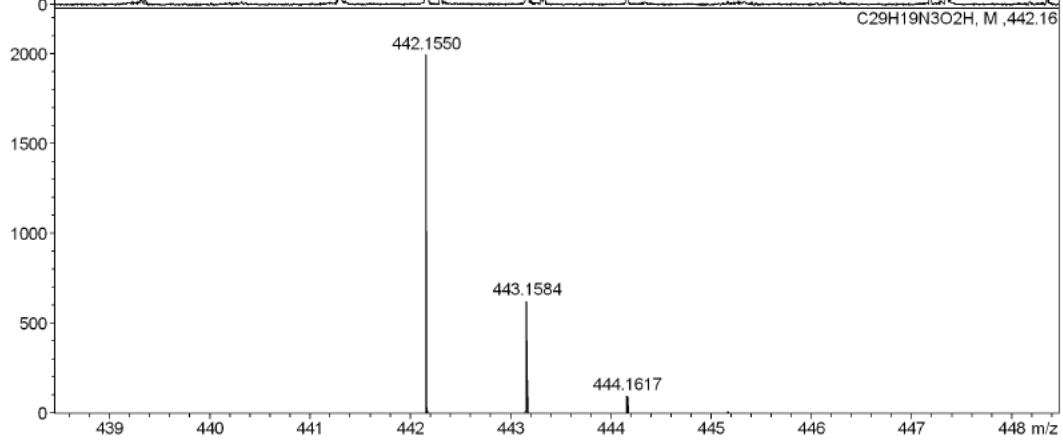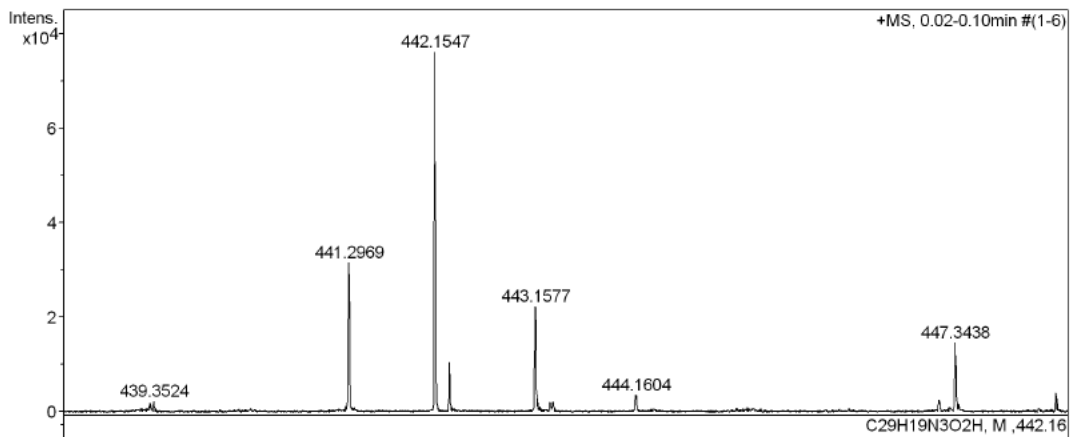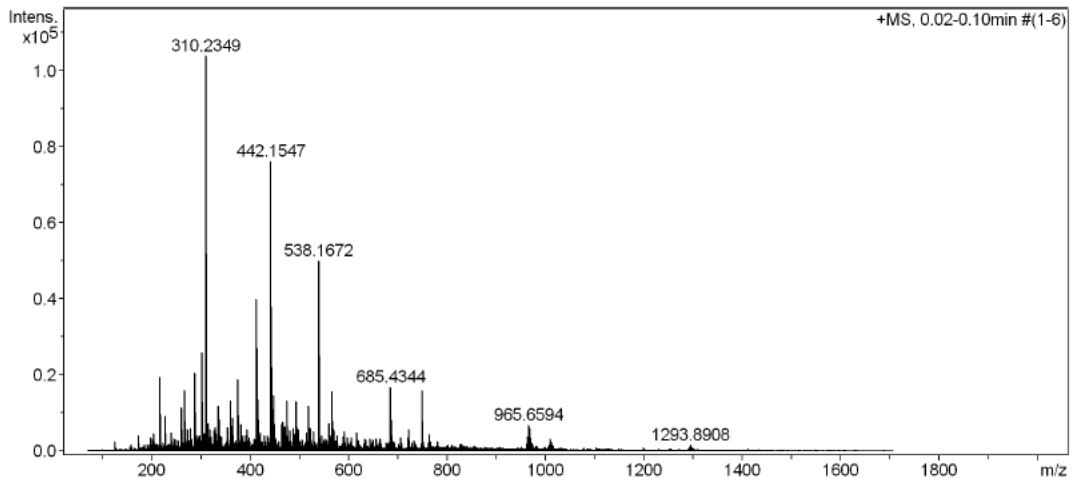
+MS, 0.02-0.10min #(1-6)

310.2349
442.1547
538.1672
685.4344
965.6594
1293.8908

+MS, 0.02-0.10min #(1-6)

442.1547
441.2969
443.1577
444.1604
447.3438
439.3524

C29H19N3O2H, M ,442.16

442.1550
443.1584
444.1617

Bruker Compass DataAnalysis 4.0   Acquisition Date   12.12.2019 16:08:51   Page 1 of 3

High Resolution Mass Spectrometry Report

Measured m/z vs. theoretical m/z

Meas. m/z	#	Formula	Score	m/z	err [mDa]	err [ppm]	mSigma	rdb	e⁻ Conf	z
442.1547	1	C 29 H 20 N 3 O 2	100.00	442.1550	0.3	0.7	16.5	21.5	even	1+

Mass list

#	m/z	I %	I
1	173.0780	4.0	4181
2	205.0595	4.6	4763
3	216.9225	5.4	5570
4	217.1043	18.9	19647
5	226.9510	9.1	9408
6	239.0886	4.8	5022
7	261.1300	10.9	11360
8	267.1698	15.4	15970
9	273.1672	5.4	5661
10	279.0933	5.8	6065
11	288.2526	19.8	20581
12	288.9214	3.9	4095
13	293.2081	4.0	4172
14	297.0300	4.0	4188
15	297.2398	3.9	4074
16	301.0749	25.0	25940
17	301.1404	12.7	13190
18	301.2105	7.0	7258
19	302.0778	5.5	5682
20	305.1530	4.6	4769
21	309.2029	4.4	4559
22	310.2349	100.0	103888
23	311.2382	15.5	16120
24	315.1921	7.0	7304
25	319.2241	5.6	5781
26	326.2078	5.2	5410
27	329.0696	6.1	6389
28	331.2084	4.4	4616
29	336.2142	11.5	11898
30	338.1279	4.2	4314
31	338.2299	8.1	8449
32	353.2652	6.0	6251
33	360.3228	12.9	13450
34	361.0961	3.9	4085
35	365.1053	6.4	6611
36	365.1281	8.3	8641
37	375.1428	18.2	18959
38	375.6438	10.7	11088
39	381.2968	6.8	7023
40	385.2924	4.0	4104
41	391.1556	3.9	4042
42	393.2964	5.6	5846
43	413.2657	38.4	39944
44	413.6563	4.2	4396
45	414.1580	4.1	4250
46	414.2683	9.5	9864
47	415.1546	26.1	27153
48	416.1572	8.1	8412
49	421.3283	4.7	4854
50	429.3176	4.1	4257
51	434.1415	3.9	4077
52	441.2969	30.4	31555
53	442.1547	73.3	76195
54	442.3000	10.1	10516
55	443.1577	21.5	22349
56	447.3438	14.1	14626
57	448.3468	3.9	4044
58	449.3721	6.8	7081
59	463.3752	4.9	5063
60	464.1357	6.7	7010
61	465.3694	7.4	7737
62	469.3275	6.1	6347

High Resolution Mass Spectrometry Report

#	m/z	I %	I
63	471.2173	6.4	6664
64	473.3446	4.0	4206
65	474.1803	12.8	13336
66	475.1841	4.6	4796
67	481.3642	5.3	5498
68	488.1963	5.7	5914
69	492.1821	4.3	4420
70	492.4013	12.4	12929
71	497.3576	5.6	5780
72	513.3537	4.7	4871
73	517.3700	3.8	3995
74	519.1798	11.5	11983
75	520.1839	4.6	4807
76	523.3231	5.9	6150
77	529.3481	5.1	5278
78	538.1672	48.2	50070
79	539.0447	4.1	4230
80	539.1707	15.1	15726
81	545.3427	4.0	4182
82	560.1480	7.1	7399
83	563.4625	4.1	4248
84	566.1623	4.3	4470
85	567.2294	15.3	15881
86	568.2329	5.9	6118
87	570.1924	5.3	5470
88	577.4786	4.0	4120
89	589.4787	3.9	4001
90	591.4952	5.1	5319
91	615.1934	4.8	4987
92	685.4344	16.3	16947
93	686.4371	8.0	8284
94	721.5741	5.5	5758
95	749.2765	15.4	15959
96	750.2803	7.5	7800
97	764.5716	4.2	4382
98	965.6594	6.6	6907
99	967.6730	5.8	6015
100	968.6777	3.9	4010

Acquisition Parameter

General	Fore Vacuum	2.39e+000 mBar	High Vacuum	8.47e-008 mBar	Source Type	ESI
	Scan Begin	75 m/z	Scan End	1700 m/z	Ion Polarity	Positive
Source	Set Nebulizer	0.4 Bar	Set Capillary	3600 V	Set Dry Gas	4.0 l/min
	Set Dry Heater	180 °C	Set End Plate Offset	-500 V		
Quadrupole	Set Ion Energy (MS only)	4.0 eV				
Coll. Cell	Collision Energy	8.0 eV	Set Collision Cell RF	350.0 Vpp		
Ion Cooler	Set Ion Cooler Transfer Time	75.0 µs	Set Ion Cooler Pre Pulse Storage Time	10.0 µs		

^{1}H-, ^{13}C-, HMBC-, HMQC-, TOCSY-NMR (DMSO-d$_6$, 500/126 MHz, 25 °C) and HR-ESI-MS spectra of compound 13

^{1}H NMR (500 MHz, DMSO) δ =
13.52 (s, 2H),
9.19 (d, J = 2.1 Hz, 2H),
8.74 (d, J = 8.1 Hz, 2H),
8.55 (d, J = 7.8 Hz, 2H),
8.47 (dd, J = 8.2, 2.0 Hz, 2H),
8.19 (q, J = 8.0 Hz, 1H).

A (s)
13.52

B (d)
9.19
J(2.12)

C (d)
8.74
J(8.15)

D (d)
8.55
J(7.75)

E (dd)
8.47
J(8.22, 2.05)

F (q)
8.19
J(8.00)

13
C$_{17}$H$_{11}$N$_3$O$_4$
321.29 g/mol

^{13}C NMR (126 MHz, DMSO) δ =
166.10, 158.01,
154.05, 150.21,
138.98, 138.32,
126.78, 122.26,
120.53 ppm.

13
C$_{17}$H$_{11}$N$_3$O$_4$
321.29 g/mol
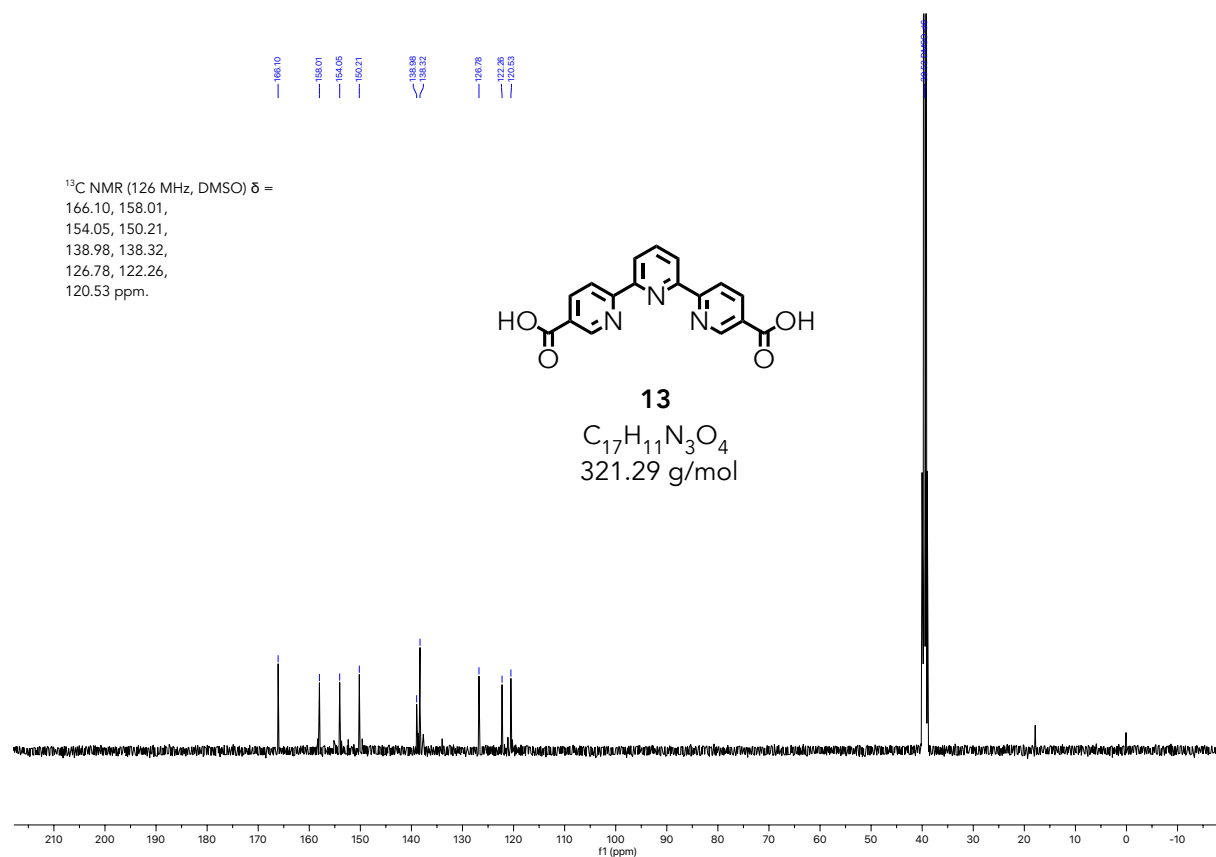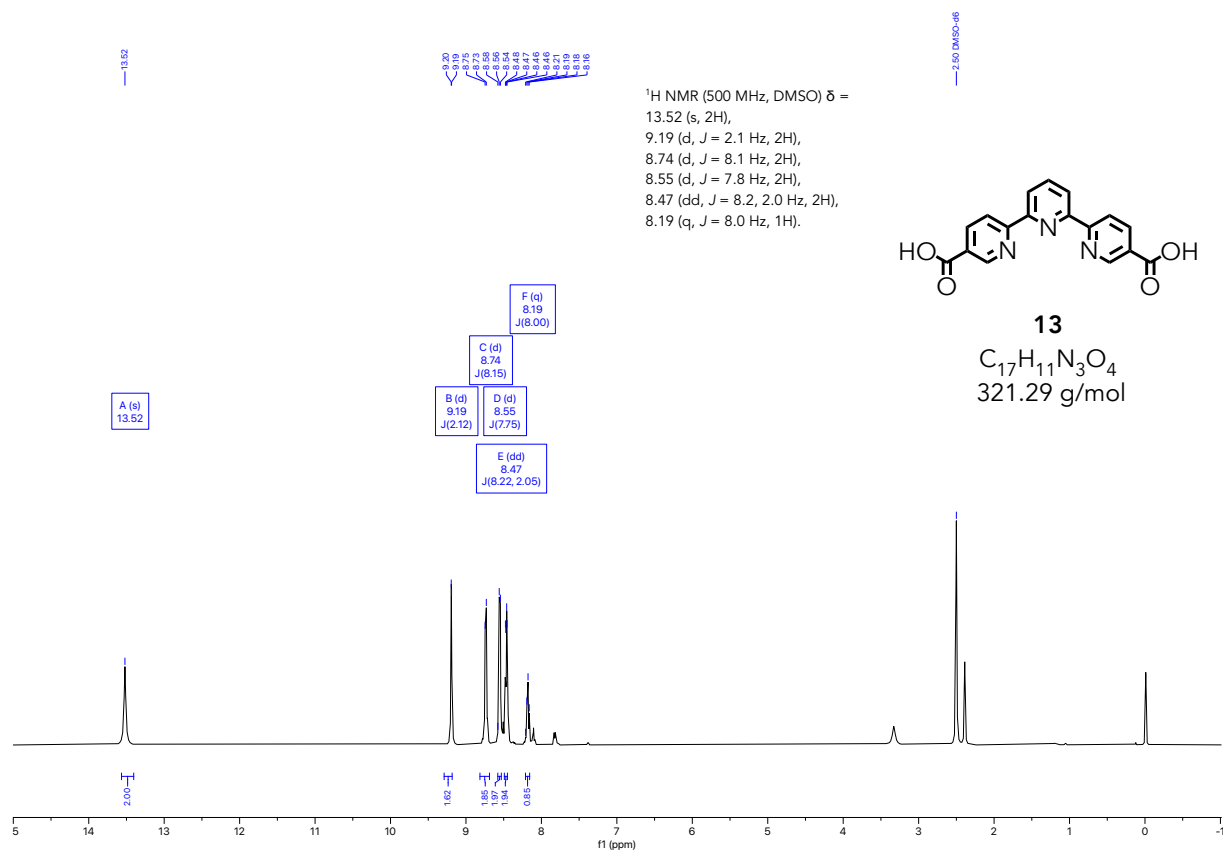
HMBC-NMR Spectrum of Compound 13
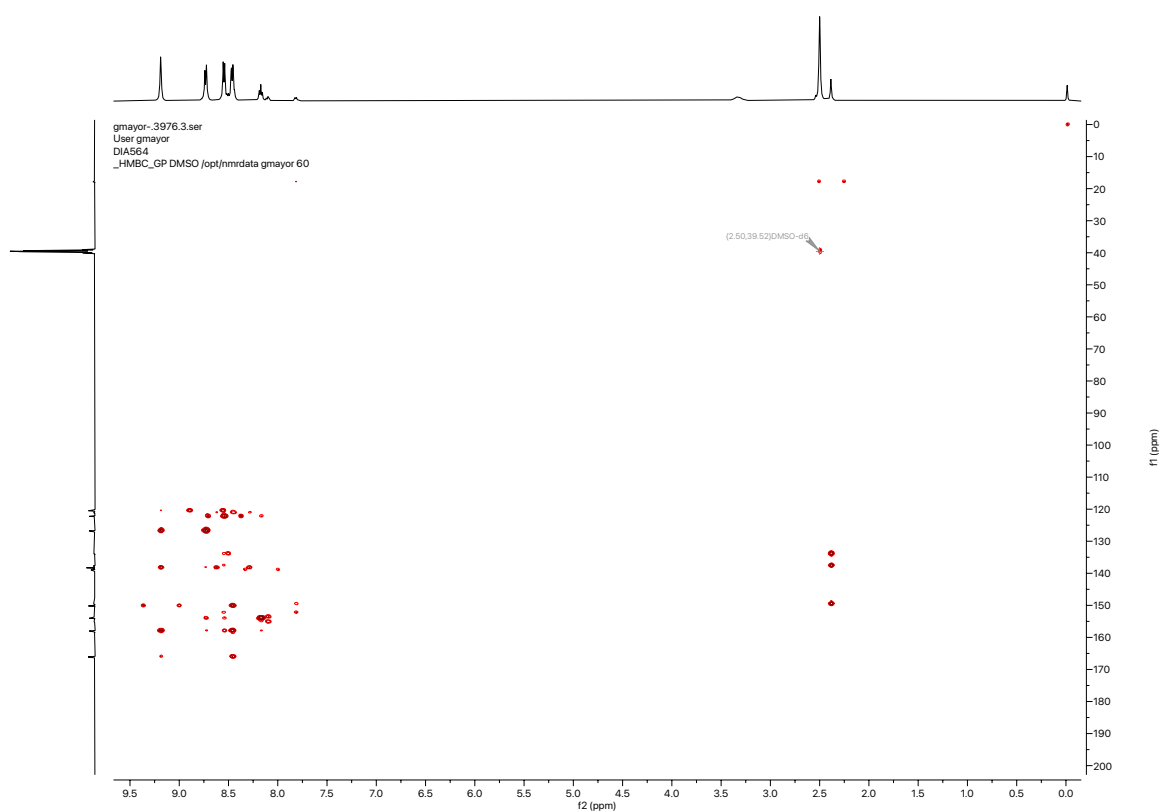
HMQC-NMR Spectrum of Compound 13

TOCSY-NMR Spectrum of Compound **13**

gmayor-.3976.4.ser
User gmayor
DIA564
_TOCSY DMSO /opt/nmrdata gmayor 60

(2.50,2.50)DMSO-d6
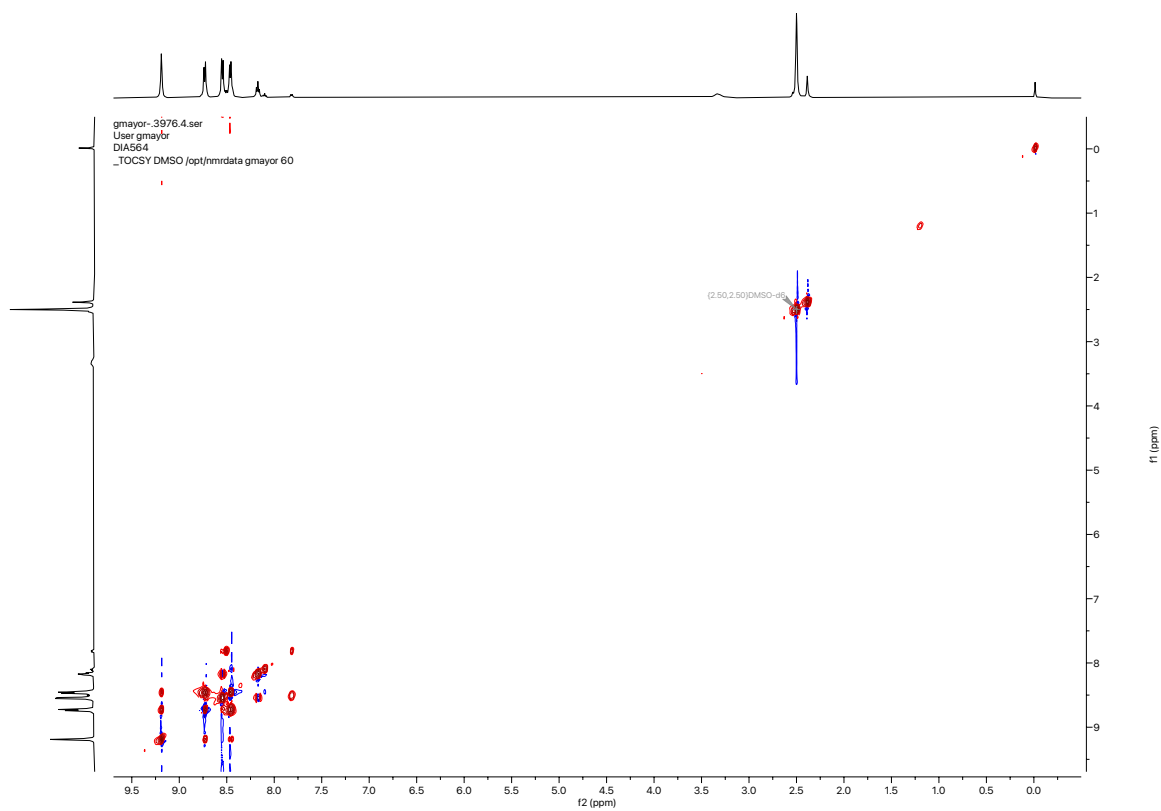
High Resolution Mass Spectrometry Report

Sample Name	**DIA564**	Instrument	maXis 4G
Comment	in MeOH analysiert	Method	22 Direct_pos_mid.m
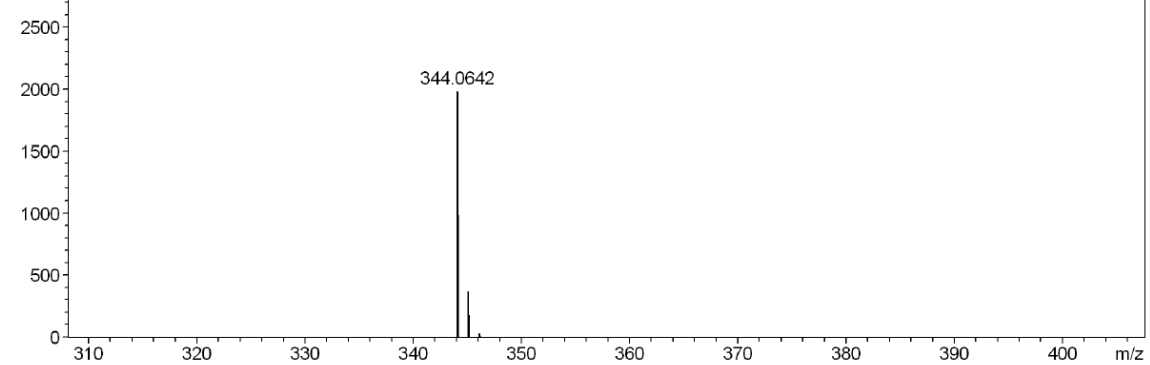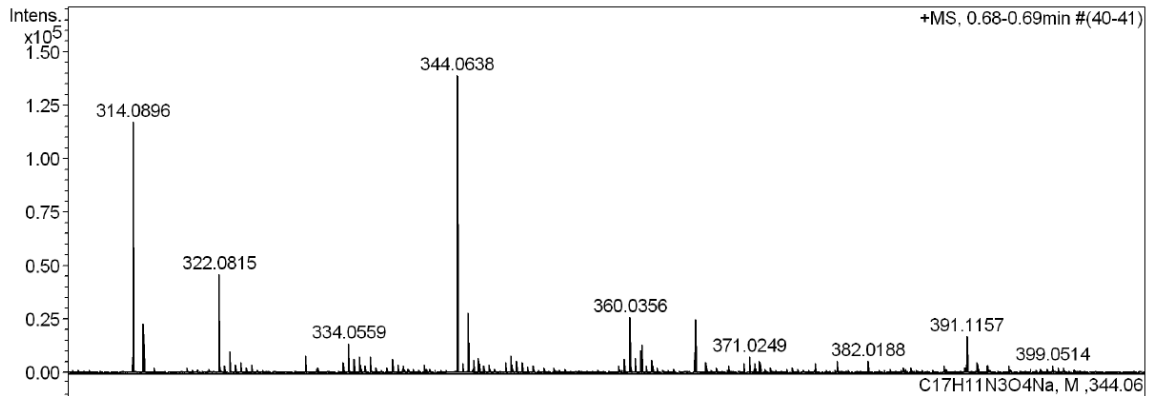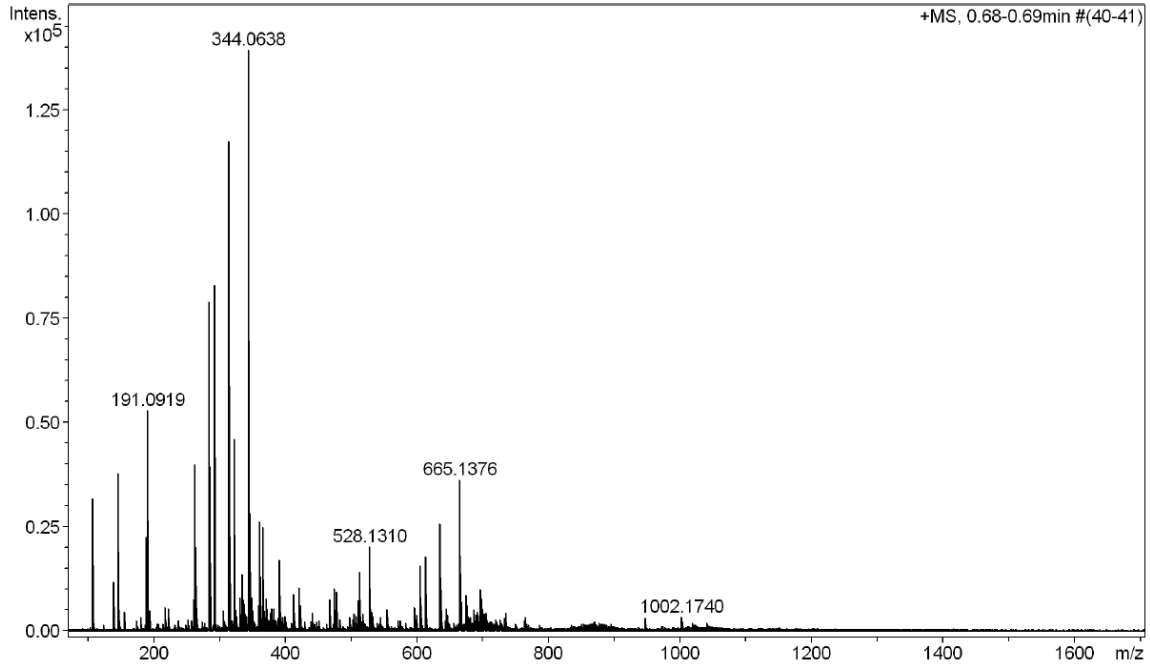
+MS, 0.68-0.69min #(40-41)

344.0638

191.0919

528.1310

665.1376

1002.1740

+MS, 0.68-0.69min #(40-41)

314.0896

322.0815

334.0559

344.0638

360.0356

371.0249

382.0188

391.1157

399.0514

C17H11N3O4Na, M ,344.06

344.0642

High Resolution Mass Spectrometry Report

Measured m/z vs. theoretical m/z

Meas. m/z	#	Formula	Score	m/z	err [mDa]	err [ppm]	mSigma	rdb	e⁻ Conf	z
344.0638	1	C 17 H 11 N 3 Na O 4	100.00	344.0642	0.4	1.2	5.3	13.5	even	1+

Mass list

#	m/z	I %	I
1	107.0412	22.8	31817
2	138.0695	8.5	11906
3	146.0581	27.3	37999
4	147.0562	3.8	5299
5	155.0634	3.4	4742
6	188.0837	16.3	22750
7	189.0818	3.1	4324
8	191.0919	37.9	52823
9	193.0878	3.6	5037
10	217.1040	4.2	5786
11	222.5438	3.9	5420
12	261.1301	5.6	7755
13	262.1332	28.8	40126
14	263.1361	5.5	7658
15	264.5694	7.9	10958
16	284.1153	56.7	79052
17	285.1184	11.8	16463
18	292.1075	59.6	83014
19	293.1105	11.4	15909
20	305.1563	3.5	4917
21	314.0896	84.3	117428
22	315.0926	16.4	22851
23	322.0815	33.1	46163
24	323.0646	7.0	9793
25	323.0842	7.2	9998
26	323.5654	3.0	4249
27	324.0638	3.7	5139
28	330.0630	5.8	8104
29	333.5561	3.7	5196
30	334.0559	9.9	13794
31	334.5562	4.9	6788
32	335.0546	5.5	7616
33	336.0546	3.6	5055
34	336.0708	5.4	7589
35	338.0519	4.7	6538
36	344.0638	100.0	139316
37	344.5467	3.3	4539
38	345.0471	8.6	12005
39	345.0664	20.4	28397
40	345.5470	4.2	5892
41	346.0456	5.0	7015
42	348.5427	3.6	5080
43	349.0430	5.9	8273
44	349.5433	3.9	5469
45	350.0419	3.7	5098
46	359.5336	4.5	6325
47	360.0356	18.9	26281
48	360.5343	5.1	7096
49	361.0338	7.7	10674
50	361.1417	9.6	13330
51	362.0323	4.5	6218
52	366.0454	17.9	24897
53	367.0486	3.7	5087
54	370.5246	3.1	4320
55	371.0249	5.6	7834
56	371.5249	3.1	4326
57	372.0237	3.9	5486
58	377.1753	3.1	4388
59	379.1931	3.9	5404
60	382.0188	4.1	5646
61	391.1157	12.3	17131
62	392.1186	3.4	4784

High Resolution Mass Spectrometry Report

#	m/z	I %	I
63	413.2652	6.4	8877
64	421.0896	7.5	10508
65	423.2189	4.6	6425
66	441.2970	3.2	4498
67	467.2454	5.5	7700
68	475.0310	7.3	10161
69	477.0307	6.8	9454
70	511.2716	5.3	7352
71	512.1538	10.2	14236
72	513.1556	3.4	4757
73	528.1310	14.5	20255
74	529.1342	3.9	5500
75	531.5612	3.4	4732
76	555.2973	3.8	5313
77	596.2050	4.1	5726
78	605.1893	11.3	15707
79	606.1921	4.5	6249
80	612.1822	12.8	17873
81	613.1851	3.7	5152
82	635.1634	18.5	25740
83	636.1663	7.2	10031
84	644.1207	3.8	5297
85	645.1229	3.7	5169
86	665.1376	26.0	36269
87	666.1399	10.0	13888
88	674.0970	6.2	8640
89	675.0974	5.9	8151
90	676.0963	4.5	6299
91	677.0983	3.6	5075
92	687.1186	3.8	5291
93	692.0970	3.4	4704
94	696.0771	5.8	8083
95	697.0783	7.2	9976
96	698.0773	5.6	7871
97	699.0763	3.9	5429
98	700.0792	3.7	5114
99	704.3652	3.2	4521
100	734.3394	3.2	4505

Acquisition Parameter

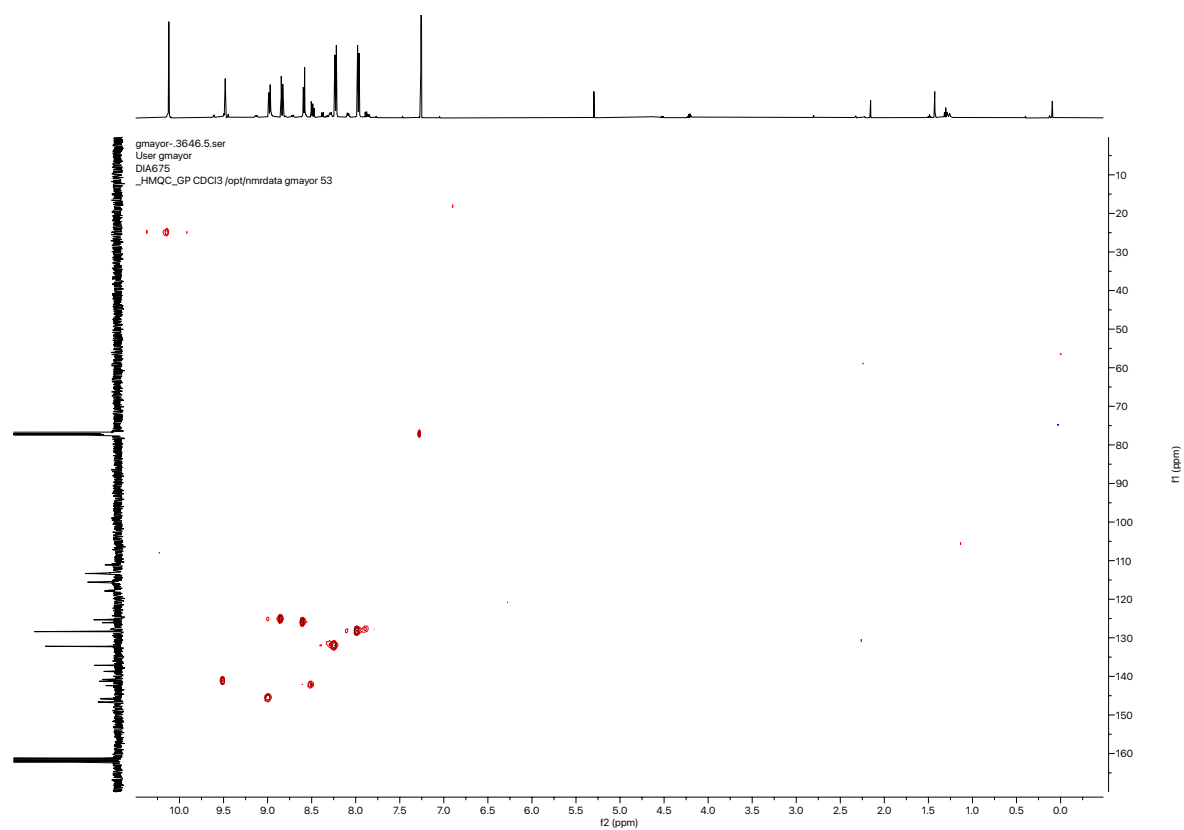| **General** | Fore Vacuum | 2.48e+000 mBar | High Vacuum | 1.33e-007 mBar | Source Type | ESI |
	Scan Begin	75 m/z	Scan End	1700 m/z	Ion Polarity	Positive
Source	Set Nebulizer	0.4 Bar	Set Capillary	3600 V	Set Dry Gas	4.0 l/min
	Set Dry Heater	180 °C	Set End Plate Offset	-500 V		
Quadrupole	Set Ion Energy (MS only)	4.0 eV				
Coll. Cell	Collision Energy	8.0 eV	Set Collision Cell RF	350.0 Vpp	100.0 Vpp	
Ion Cooler	Set Ion Cooler Transfer Time	75.0 µs	Set Ion Cooler Pre Pulse Storage Time	10.0 µs		

^{1}H-, ^{13}C-, HMQC- HMBC-, COSY-, NOESY-NMR (CDCl$_3$, 500/126 MHz, 25 °C) and HR-ESI-MS spectra of compound 22

^{1}H NMR (500 MHz, CDCl$_3$) δ
8.40 (d, J = 8.5 Hz, 2H),
8.15 (d, J = 2.8 Hz, 2H),
7.76 (s, 2H),
7.11 (dd, J = 8.5, 2.8 Hz, 2H),
4.06 (d, J = 5.4 Hz, 2H),
3.84 (s, 4H),
1.83 – 1.77 (m, 1H),

22
C$_{35}$H$_{53}$N$_5$O
559.84 g/mol

^{13}C NMR (126 MHz, CDCl$_3$) δ =
167.56, 157.07, 147.49,
142.86, 136.44, 122.14,
122.04, 105.17, 70.73,
38.08, 32.06, 32.05,
31.47, 30.17, 29.83,
29.79, 29.75, 29.49,
27.02, 22.83, 22.82, 14.26.

22
C$_{35}$H$_{53}$N$_5$O
559.84 g/mol

HMQC-NMR Spectrum of Compound **22**

gmayor-.911.2.ser
User gmayor
Group mayor
_HMQC_GP CDCl3 /opt/topspin3.5pl7 gmayor 46

(7.26,77.23)CDCl3

HMBC-NMR Spectrum of Compound **22**

gmayor-.911.3.ser
User gmayor
Group mayor
_HMBC_GPSW CDCl3 /opt/topspin3.5pl7 gmayor 46

(7.15,77.03)CDCl3

COSY-NMR Spectrum of Compound 22

gmayor-.911.6.ser
User gmayor
Group mayor
_COSY_GP CDCl3 /opt/topspin3.5pl7 gmayor 46

NOESY-NMR Spectrum of Compound 22

gmayor-.911.4.ser
User gmayor
Group mayor
_NOESY CDCl3 /opt/topspin3.5pl7 gmayor 46

High Resolution Mass Spectrometry Report

Sample Name **dia369**
Comment

Instrument   maXis 4G
Method   ms_nocolumn_300-600_pos.m
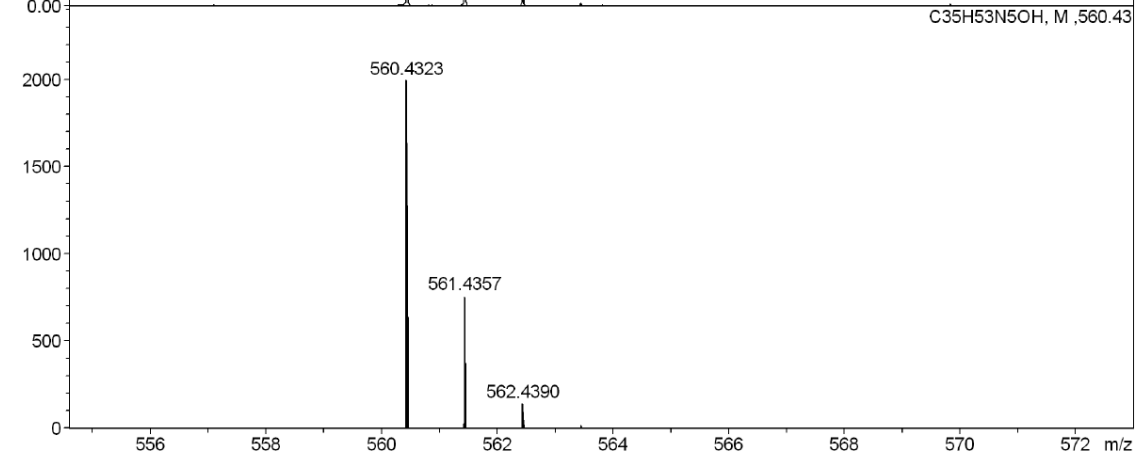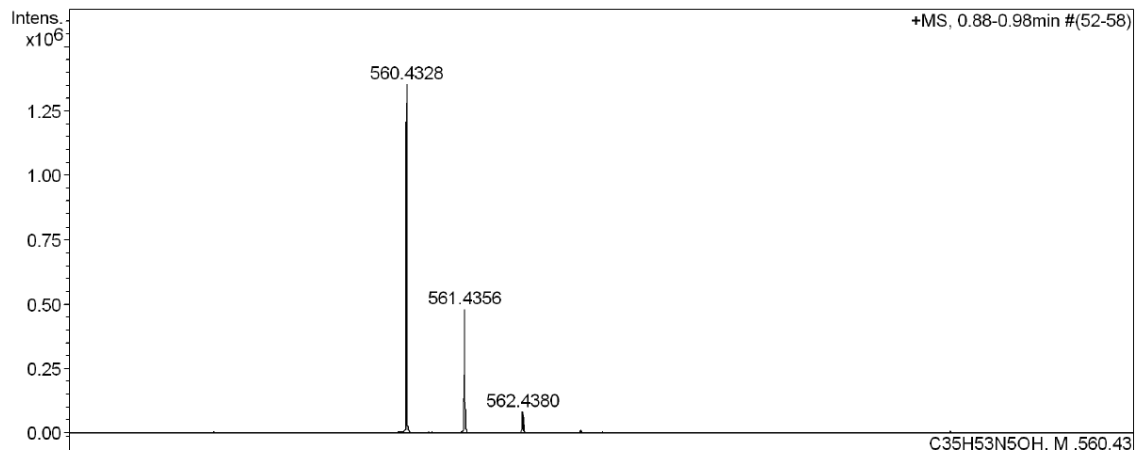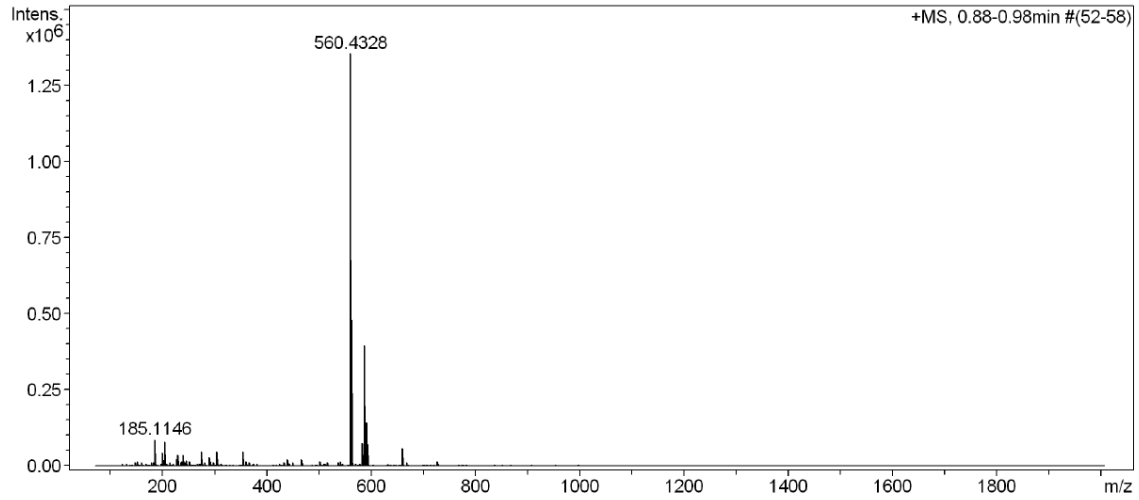
High Resolution Mass Spectrometry Report

Measured m/z vs. theoretical m/z

Meas. m/z	#	Formula	Score	m/z	err [mDa]	err [ppm]	mSigma	rdb	e⁻ Conf	z
560.4328	1	C 35 H 54 N 5 O	100.00	560.4323	-0.5	-0.9	24.9	11.5	even	1+

Mass list

#	m/z	I %	I
1	123.0918	0.6	7590
2	131.9615	0.8	10194
3	137.1074	0.5	6694
4	147.0916	0.8	11394
5	153.0337	1.3	17262
6	161.1072	0.9	11987
7	169.0111	0.7	10018
8	171.0443	0.5	6645
9	178.9952	0.9	11569
10	183.9865	0.9	11974
11	185.1146	6.5	87652
12	186.1179	0.6	7826
13	187.1222	0.6	7786
14	197.1146	0.6	8675
15	199.1301	3.3	44683
16	205.0599	6.0	80931
17	206.0640	0.5	6786
18	209.0058	0.6	7754
19	214.9172	0.8	10705
20	217.1045	0.5	6410
21	220.9341	0.6	7735
22	226.9510	1.6	21183
23	229.1406	1.7	23439
24	229.8927	2.8	38397
25	235.9097	0.9	11813
26	236.0711	0.7	9884
27	237.0844	1.1	14337
28	239.0883	2.7	36591
29	243.1348	0.8	11493
30	244.8682	1.5	20712
31	251.0527	1.2	16939
32	267.0314	0.6	8458
33	271.1874	0.6	8295
34	273.1665	0.5	6936
35	275.1612	3.6	49321
36	276.1647	0.7	8935
37	276.8942	0.6	7460
38	277.1763	0.5	6385
39	280.7195	1.0	13188
40	288.9216	2.2	30357
41	291.1559	1.2	15793
42	297.8799	0.9	11539
43	303.8971	3.6	49253
44	305.1713	0.6	8378
45	312.8555	0.6	8701
46	353.1450	3.5	47551
47	354.1483	1.0	13507
48	360.3232	1.2	16689
49	365.8675	0.9	12559
50	374.8256	0.5	7450
51	380.8428	0.7	9751
52	424.8963	0.6	8474
53	433.8548	1.0	13951
54	439.1242	0.5	7255
55	439.8717	1.8	23874
56	442.8134	0.5	6923
57	448.8304	0.9	11803
58	467.1015	1.7	23675
59	468.1018	0.8	10361
60	469.0996	0.5	7191
61	486.8663	0.5	6225
62	501.8424	1.1	15405

Bruker Compass DataAnalysis 4.0   Acquisition Date   23.04.2020 11:28:03   Page 2 of 3

High Resolution Mass Spectrometry Report

#	m/z	I %	I
63	510.8008	0.6	7468
64	513.1430	0.6	8296
65	516.8176	0.8	11393
66	536.1645	0.8	10650
67	541.1201	1.1	15009
68	542.1210	0.6	7739
69	545.4198	0.7	9700
70	560.4328	100.0	1355446
71	561.4356	35.6	483053
72	562.4380	6.2	84539
73	563.4406	0.9	12128
74	569.8292	0.6	8714
75	578.7880	0.5	7123
76	582.4137	5.7	77385
77	583.4166	2.3	31089
78	584.4198	0.5	6740
79	586.8939	29.2	396060
80	587.3954	23.2	314914
81	587.8964	9.0	122431
82	588.3971	2.5	33942
83	588.8974	0.7	8947
84	590.8891	10.5	142943
85	591.3906	9.9	134597
86	591.8900	8.7	117339
87	592.3900	5.4	73559
88	592.8908	2.3	31468
89	593.3897	1.2	16049
90	593.8900	0.6	7896
91	631.8002	0.5	6725
92	637.8167	0.5	6703
93	646.7760	0.5	6265
94	659.3595	4.3	58645
95	660.3621	1.8	24634
96	667.3509	0.8	10587
97	700.5874	0.5	6507
98	727.3464	1.3	17386
99	728.3496	0.5	7093
100	952.7991	0.5	6616

Acquisition Parameter

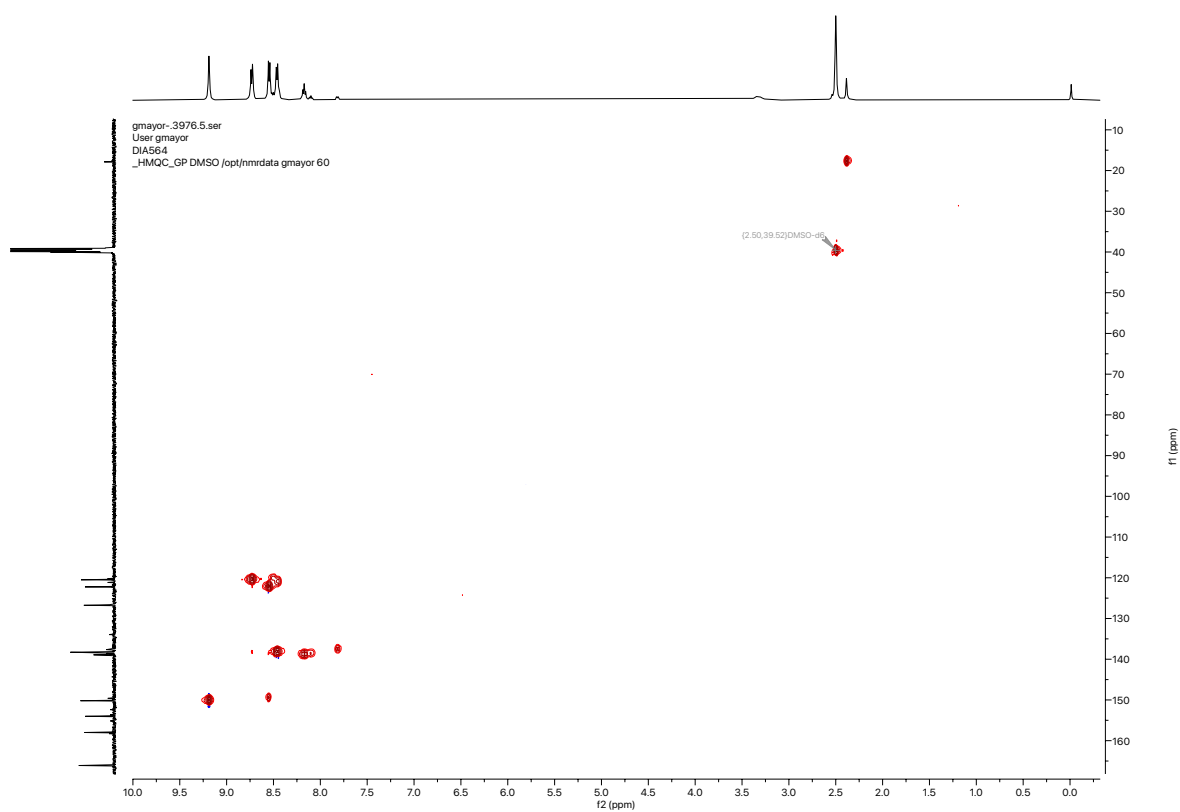| General	Fore Vacuum	2.47e+000 mBar	High Vacuum	1.03e-007 mBar	Source Type	ESI
	Scan Begin	75 m/z	Scan End	2000 m/z	Ion Polarity	Positive
Source	Set Nebulizer	2.0 Bar	Set Capillary	4500 V	Set Dry Gas	8.0 l/min
	Set Dry Heater	200 °C	Set End Plate Offset	-500 V		
Quadrupole	Set Ion Energy (MS only)	4.0 eV				
Coll. Cell	Collision Energy	8.0 eV	Set Collision Cell RF	600.0 Vpp		
Ion Cooler	Set Ion Cooler Transfer Time	75.0 µs	Set Ion Cooler Pre Pulse Storage Time	10.0 µs		

^{1}H-, ^{13}C-, HMQC-, HMBC-, DOSY-NMR (CD$_3$CN, 500/126 MHz, 25 °C) and HR-ESI-MS spectra of compound 27

^{1}H NMR (500 MHz, CD$_3$CN) δ =
9.81 (d, J = 0.5 Hz, 2H), 9.20 – 9.08 (m, 3H),
8.76 (d, J = 8.1 Hz, 2H), 8.62 (dd, J = 8.2, 1.6 Hz, 2H),
8.07 (d, J = 8.9 Hz, 2H), 8.00 (s, 2H),
7.59 (dd, J = 1.7, 0.6 Hz, 2H), 7.18 (dd, J = 8.9, 2.4 Hz, 2H),
6.32 (d, J = 2.3 Hz, 2H), 5.27 (s, 4H),
4.48 (d, J = 5.7 Hz, 2H), 2.11 – 2.06 (m, 1H),
1.53 – 1.48 (m, 4H), 1.44 – 1.22 (m, 28H), 0.94 – 0.85 (m, 6H).

27
C$_{52}$H$_{64}$CoN$_8$O$_3$P$_3$F$_{18}$
1342.3 g/mol

^{13}C NMR (126 MHz, CD$_3$CN) δ =
188.95, 173.29, 160.04, 158.39, 156.44,
154.66, 150.70, 146.72, 144.50, 142.97,
137.91, 137.12, 130.30, 128.40, 128.20,
124.25, 110.38, 75.33, 38.57, 32.69,
31.79, 30.73, 30.44, 30.41, 30.37,

27
C$_{52}$H$_{64}$CoN$_8$O$_3$P$_3$F$_{18}$
1342.3 g/mol

HMQC-NMR Spectrum of Compound **27**

HMBC-NMR Spectrum of Compound **27**
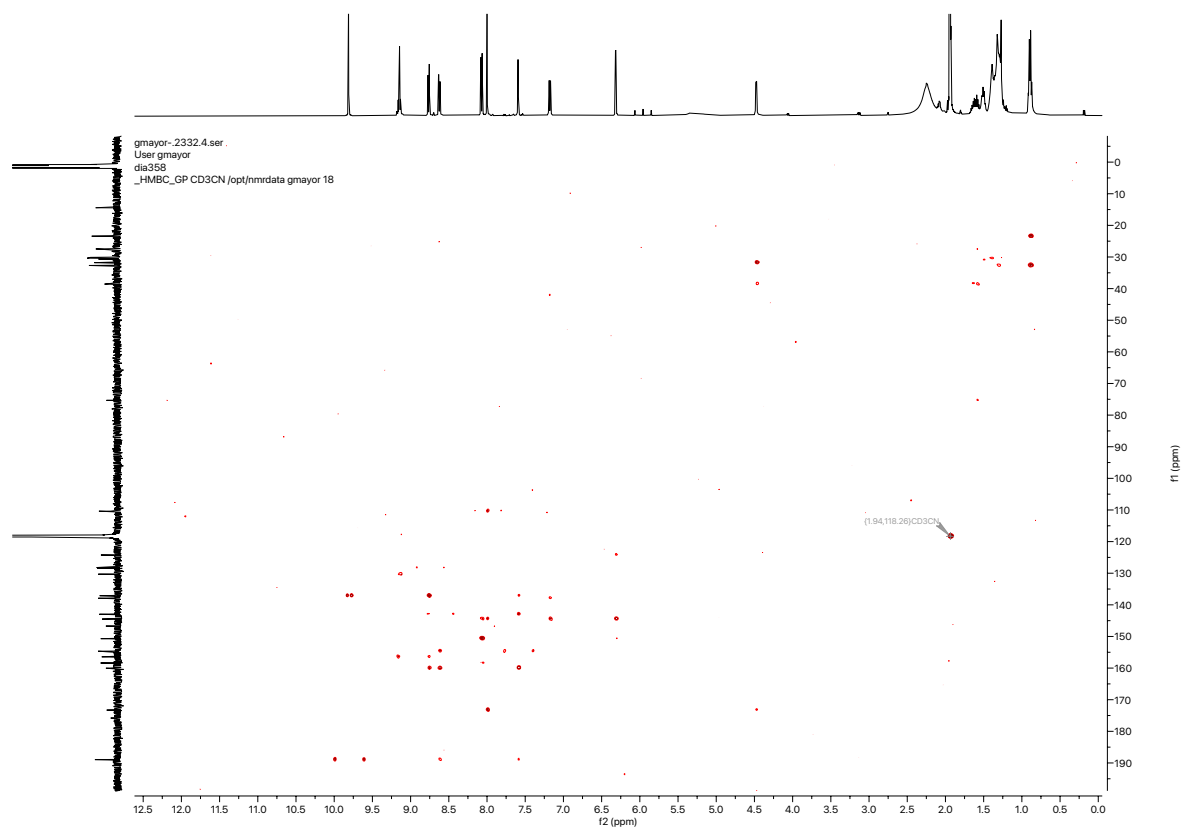
DOSY-NMR Spectrum of Compound **27**
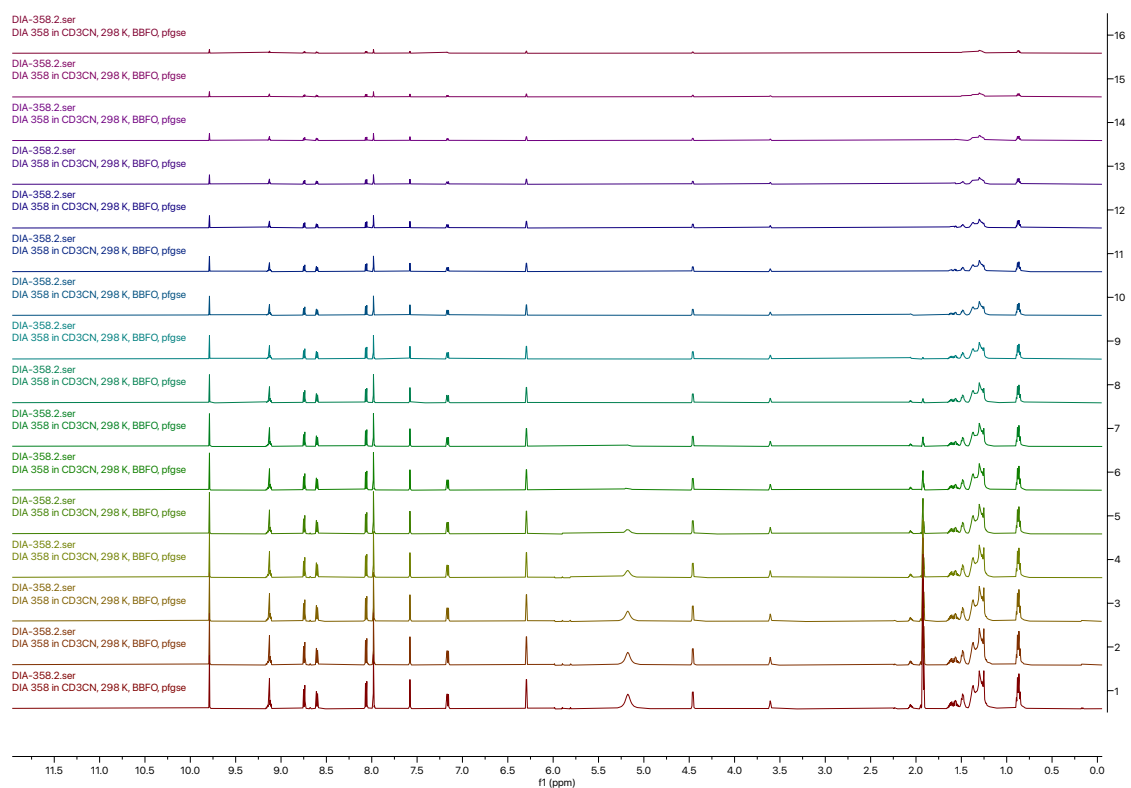
High Resolution Mass Spectrometry Report

| Sample Name | **Alfredo Di Silvestro / DIA385 HETERO** | Instrument | maXis 4G |
| Comment | 10 ug / mL in CH3CN, analyzed in MeCN | Method | 22 Direct_pos_mid.m |
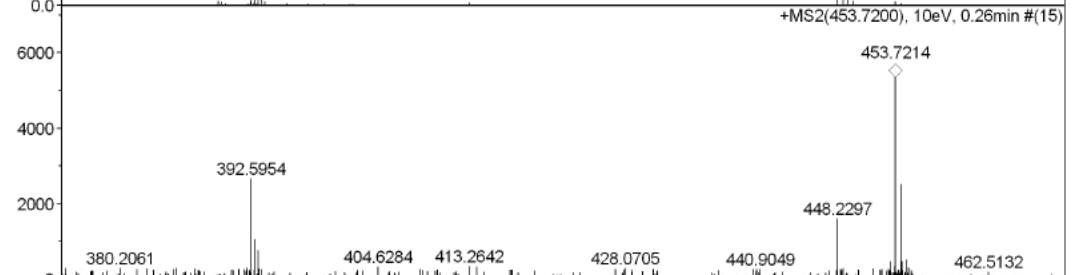
Intens.
x10^6

+MS, 0.10-0.17min #(6-10)

392.5954

290.0929

145.5500

661.3739

+MS, 0.10-0.17min #(6-10)

392.5954

448.2320

+MS2(453.7200), 10eV, 0.26min #(15)

453.7214

392.5954

448.2297

380.2061   404.6284 413.2642   428.0705   440.9049   462.5132

C52H64CoN8O3^2+, M ,907.44

453.7211

High Resolution Mass Spectrometry Report

Measured m/z vs. theoretical m/z

Meas. m/z	#	Formula	Score	m/z	err [mDa]	err [ppm]	mSigma	rdb	e⁻ Conf	z
453.7214	1	C 52 H 64 Co N 8 O 3	100.00	453.7211	-0.3	-0.7	70.9	25.0	even	2+

Mass list

#	m/z	I %	I
1	76.7969	5.2	276
2	77.4201	5.3	284
3	77.9531	5.5	296
4	78.2351	5.3	284
5	92.9610	5.2	276
6	93.7051	5.5	296
7	94.0673	7.6	408
8	102.9946	5.6	300
9	104.0211	5.0	268
10	110.1054	5.2	280
11	111.0786	5.2	276
12	111.6431	5.0	268
13	124.9067	5.3	284
14	126.9941	5.1	272
15	133.9362	5.0	268
16	136.1382	5.1	272
17	138.7087	5.6	300
18	144.1790	5.2	276
19	152.1299	5.4	288
20	159.1380	5.0	268
21	159.7751	5.2	276
22	162.4329	5.3	284
23	168.4626	5.5	292
24	168.8751	5.6	300
25	168.9087	5.5	292
26	169.8718	5.2	276
27	171.3506	5.8	308
28	171.7068	5.8	308
29	175.0161	5.1	272
30	191.3694	6.1	328
31	192.5695	5.1	272
32	194.6289	6.0	320
33	194.6840	5.2	280
34	203.9124	6.0	320
35	205.7240	5.2	276
36	206.0663	5.5	296
37	212.4697	5.5	292
38	219.7835	7.2	384
39	225.3855	5.5	292
40	230.3171	5.0	268
41	234.0288	5.0	268
42	236.3733	5.5	292
43	238.6449	5.2	276
44	250.4161	5.5	292
45	254.2954	8.5	452
46	260.0268	5.2	276
47	261.6860	5.6	300
48	262.3156	6.2	332
49	262.6435	5.3	284
50	265.9114	5.1	272
51	266.0873	5.5	296
52	268.5644	5.1	272
53	269.1350	5.1	272
54	271.6864	5.4	288
55	272.9025	8.5	452
56	274.5393	5.0	268
57	283.2971	5.2	276
58	285.2751	5.8	308
59	286.5059	5.2	276
60	288.7867	5.4	288
61	307.7618	5.4	288
62	308.0733	8.4	448

High Resolution Mass Spectrometry Report

#	m/z	I %	I
63	310.4660	5.2	280
64	312.0741	6.2	332
65	321.0040	6.0	320
66	321.0599	6.1	324
67	321.8758	5.4	288
68	326.0166	5.2	280
69	332.9843	5.3	284
70	338.5533	5.8	312
71	344.1206	5.4	288
72	346.7415	5.0	268
73	359.6639	6.6	352
74	365.9594	5.3	284
75	374.9795	5.2	280
76	380.2061	5.3	284
77	385.4449	5.2	280
78	387.2849	5.2	276
79	392.1567	5.7	304
80	392.5954	49.9	2664
81	392.9328	19.9	1060
82	393.2619	14.2	760
83	393.2775	5.8	308
84	393.3854	5.1	272
85	404.6284	6.1	324
86	413.2642	6.4	344
87	413.9866	6.2	332
88	428.0705	5.3	284
89	448.2297	30.0	1600
90	448.7348	5.2	280
91	451.6008	5.2	276
92	453.2079	5.8	312
93	453.2259	8.6	460
94	453.6700	6.3	336
95	453.7214	100.0	5336
96	454.2228	47.1	2512
97	454.2670	5.5	292
98	454.3079	8.7	464
99	454.7240	9.7	520
100	454.9823	5.7	304

Acquisition Parameter

General	Fore Vacuum	2.59e+000 mBar	High Vacuum	1.02e-007 mBar	Source Type	ESI
	Scan Begin	75 m/z	Scan End	1700 m/z	Ion Polarity	Positive
Source	Set Nebulizer	0.4 Bar	Set Capillary	3600 V	Set Dry Gas	4.0 l/min
	Set Dry Heater	180 °C	Set End Plate Offset	-500 V		

Quadrupole Set Ion Energy (MS only) 4.0 eV

Coll. Cell Collision Energy 8.0 eV Set Collision Cell RF 350.0 Vpp

Ion Cooler Set Ion Cooler Transfer Time 75.0 µs Set Ion Cooler Pre Pulse Storage Time 10.0 µs

---

Bruker Compass DataAnalysis 4.0   Acquisition Date 19.02.2020 10:15:38   Page 3 of 3

^{1}H-, ^{13}C-, HMQC-, HMBC-NMR (CD$_3$CN, 500/126 MHz, 25 °C) and HR-ESI-MS spectra of compound 30
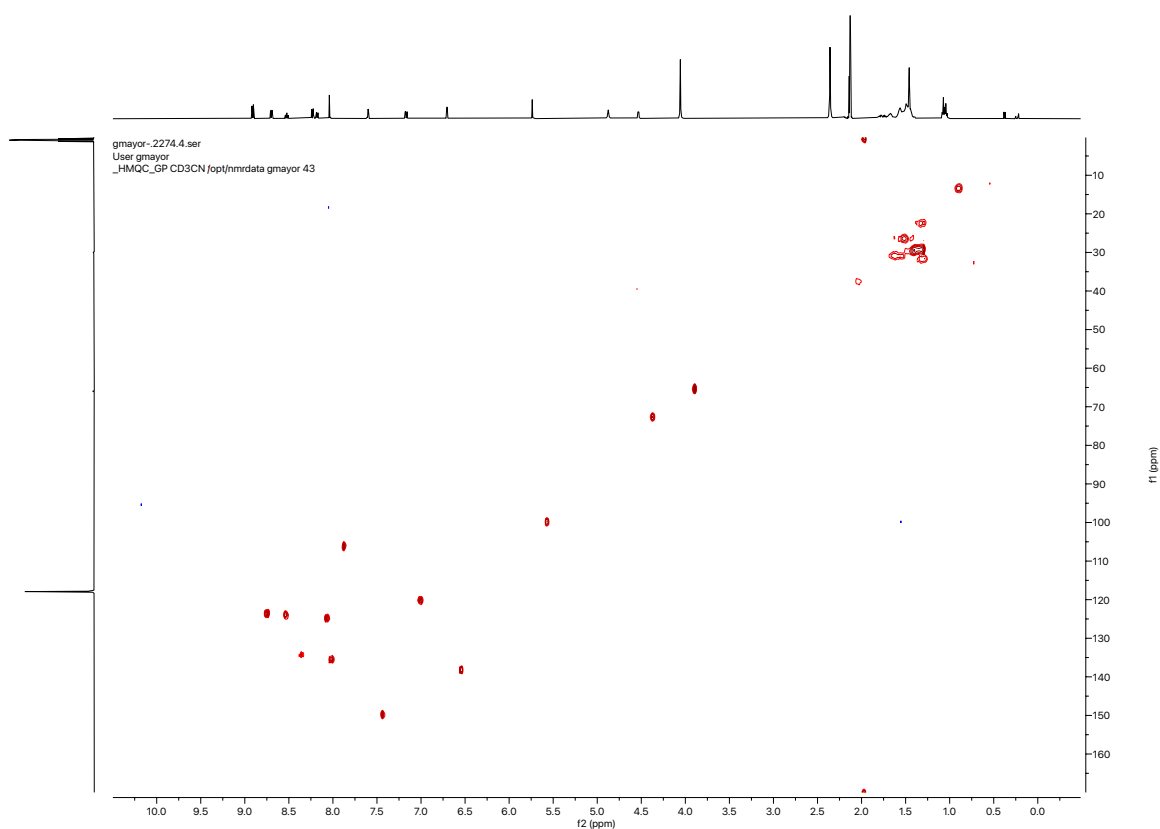
^{1}H NMR (500 MHz, CD$_3$CN) δ =
8.91 (d, J = 8.2 Hz, 1H), 8.70 (dd, J = 8.3, 0.7 Hz, 1H),
8.52 (t, J = 8.1 Hz, 0H), 8.23 (d, J = 8.9 Hz, 1H),
8.18 (ddd, J = 8.4, 1.9, 0.5 Hz, 1H), 8.04 (s, 1H),
7.60 (d, J = 1.8 Hz, 1H), 7.17 (dd, J = 8.9, 2.5 Hz, 1H),
6.70 (d, J = 2.5 Hz, 1H), 5.74 (s, 1H), 4.88 (s, 3H),

2(PF$_6$)$^-$

30
C$_{56}$H$_{72}$N$_8$O$_5$RuP$_2$F$_{12}$
1328.4 g/mol

^{13}C NMR (126 MHz, CD$_3$CN) δ =
167.26, 159.51, 156.45, 150.36, 147.86, 146.28,
139.02, 138.78, 136.09, 134.85, 125.40, 124.52,
124.17, 120.74, 106.77, 100.41, 73.22, 65.97,
38.19, 32.28, 31.54, 31.50, 30.32, 30.27, 30.01,
29.94, 29.73, 29.69, 27.05, 23.02, 22.99, 13.98.

2(PF$_6$)$^-$

30
C$_{56}$H$_{72}$N$_8$O$_5$RuP$_2$F$_{12}$
1328.4 g/mol

HMQC-NMR Spectrum of Compound **30**

HMBC-NMR Spectrum of Compound **30**
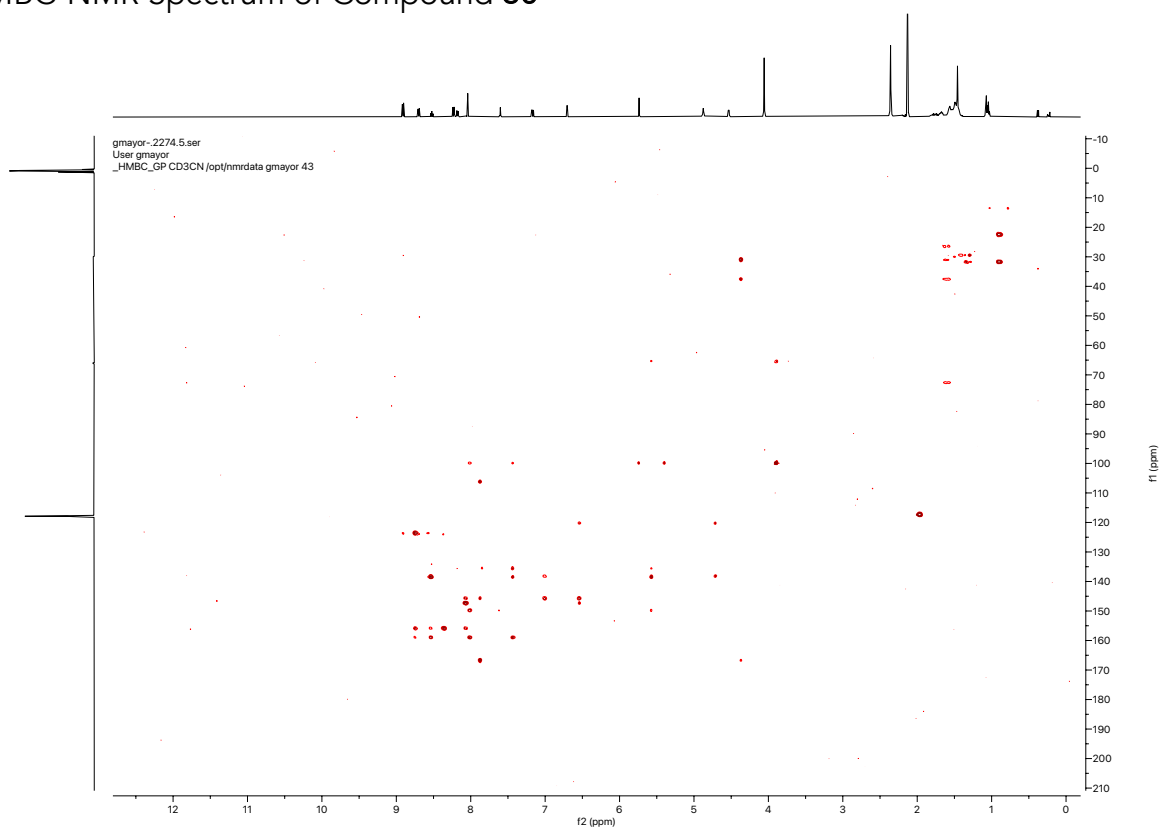
High Resolution Mass Spectrometry Report

Sample Name	**Alfredo Di Silvestro / dia503**	Instrument	maXis 4G
Comment	1 ug / mL in MeCN, analyzed in MeOH	Method	23 Direct_pos_higher.m
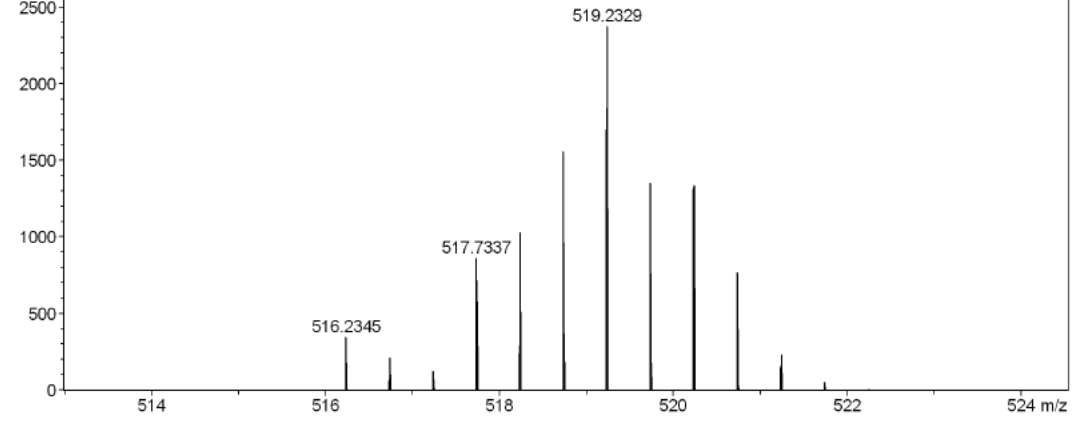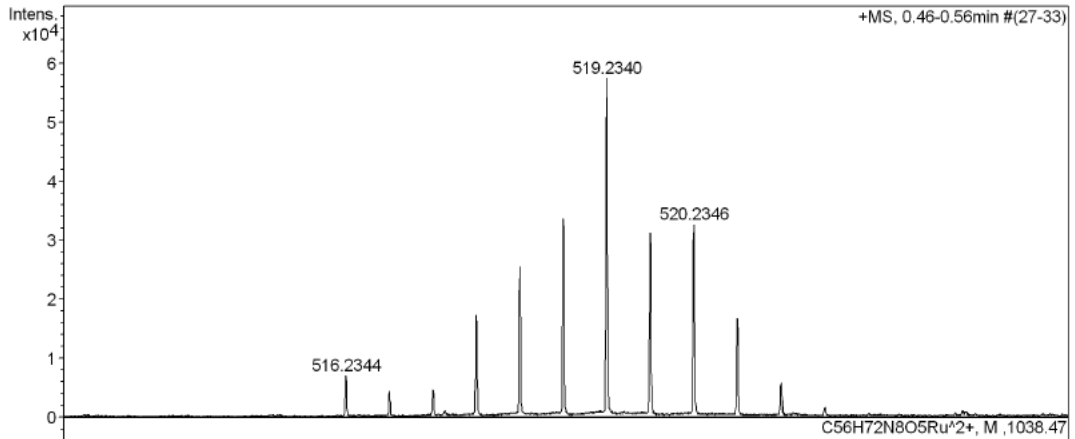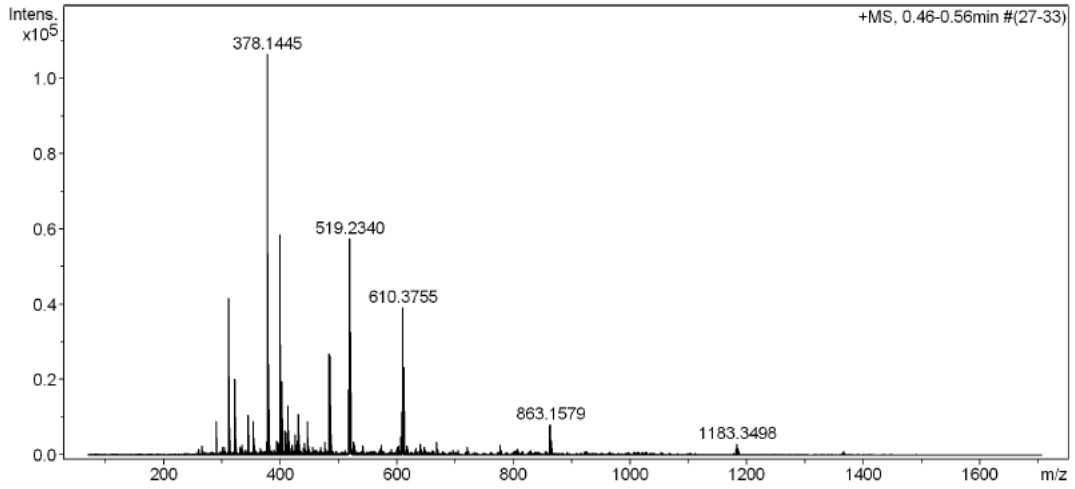
High Resolution Mass Spectrometry Report

Measured m/z vs. theoretical m/z

Meas. m/z	#	Formula	Score	m/z	err [mDa]	err [ppm]	mSigma	rdb	e⁻ Conf	z
519.2340	1	C 56 H 72 N 8 O 5 Ru	100.00	519.2337	-0.3	-0.6	11.6	25.5	odd	2+

Mass list

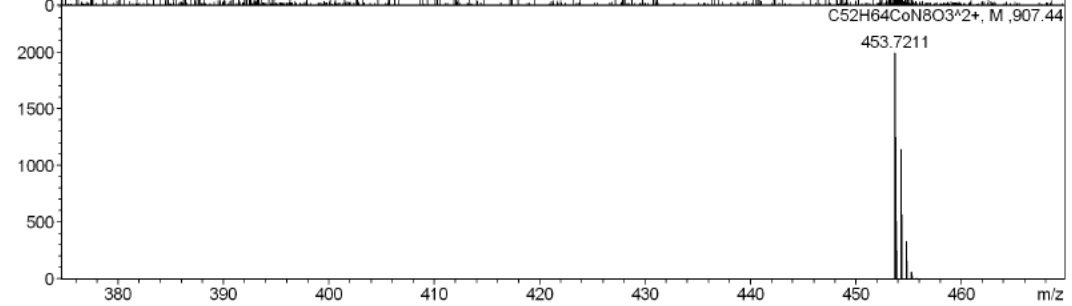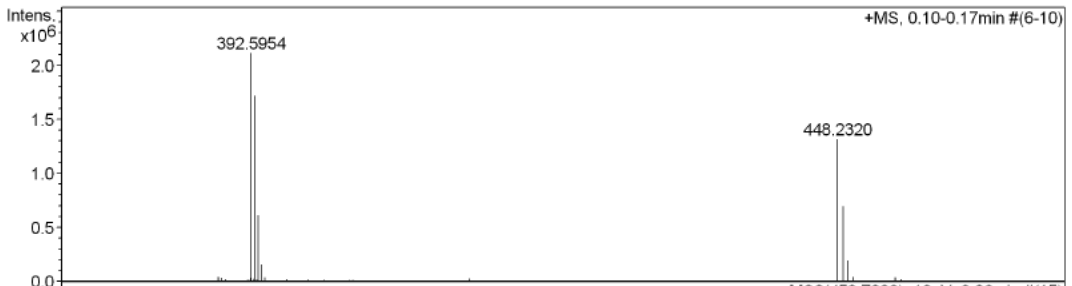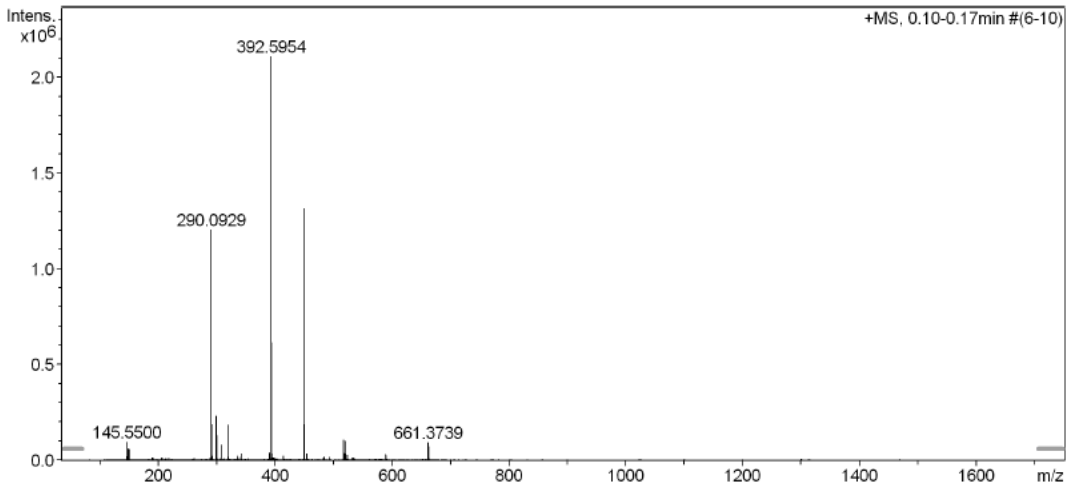| #	m/z	I %	I
1	266.2113	2.3	2478
2	290.0918	8.5	9012
3	291.0948	2.0	2177
4	301.1405	2.1	2214
5	304.2992	2.1	2246
6	312.0736	39.1	41711
7	313.0770	6.9	7389
8	322.1180	18.9	20134
9	323.1212	4.1	4326
10	334.2214	2.5	2708
11	344.0999	10.0	10624
12	345.1033	2.3	2462
13	353.2653	2.7	2883
14	354.1442	8.4	8945
15	355.1477	2.8	2942
16	376.1259	3.3	3545
17	378.1445	100.0	106560
18	379.1476	22.8	24330
19	380.1497	3.8	4000
20	381.2964	2.6	2821
21	393.2965	3.7	3979
22	395.9887	2.7	2880
23	396.6024	3.3	3518
24	397.1029	2.9	3072
25	397.6030	2.7	2826
26	397.9886	2.3	2504
27	398.1021	2.2	2314
28	400.1260	55.1	58696
29	400.3412	4.9	5172
30	401.1291	12.9	13787
31	402.1319	2.0	2162
32	402.3567	18.4	19656
33	403.3600	4.7	4978
34	408.6025	6.1	6544
35	409.1029	5.7	6087
36	409.6029	4.8	5163
37	410.1026	3.0	3218
38	413.2655	12.4	13205
39	414.2687	3.8	4016
40	421.2312	2.6	2793
41	425.2135	5.2	5550
42	428.0156	2.7	2887
43	428.3723	3.6	3869
44	430.0148	2.3	2456
45	430.3878	10.3	10978
46	431.3912	3.4	3668
47	433.1024	3.0	3150
48	441.2962	3.1	3317
49	447.3432	8.5	9091
50	448.3463	2.4	2596
51	455.1556	2.0	2165
52	469.3265	2.1	2185
53	477.1367	3.5	3741
54	484.0409	25.4	27072
55	485.0442	6.0	6404
56	485.1806	2.9	3136
57	486.0409	24.8	26422
58	487.0441	5.5	5897
59	516.2344	6.7	7158
60	516.7366	4.3	4591
61	517.2350	4.4	4734
62	517.7342	16.4	17484

Bruker Compass DataAnalysis 4.0   Acquisition Date   04.02.2020 13:10:57   Page 2 of 3

High Resolution Mass Spectrometry Report

#	m/z	I %	I
63	518.2343	24.0	25585
64	518.7344	31.6	33696
65	519.2340	54.0	57542
66	519.7352	29.5	31411
67	520.2346	30.8	32786
68	520.7356	15.9	16972
69	521.2369	5.6	5960
70	525.7417	2.1	2255
71	526.2411	3.2	3383
72	526.7425	2.1	2193
73	527.2413	2.6	2773
74	541.2445	2.3	2450
75	572.4486	2.6	2728
76	600.4786	2.0	2137
77	602.8702	2.3	2502
78	607.3761	4.7	4983
79	607.8782	3.4	3670
80	608.3774	3.3	3481
81	608.8754	10.7	11447
82	609.3756	17.3	18481
83	609.8759	21.4	22834
84	610.3755	37.0	39407
85	610.8767	22.6	24118
86	611.3763	22.1	23526
87	611.8769	13.2	14032
88	612.3785	5.0	5369
89	617.3823	2.3	2481
90	640.5802	2.8	3004
91	647.3924	2.1	2187
92	668.6099	3.3	3564
93	721.5649	2.0	2158
94	777.2517	2.7	2908
95	861.1581	7.4	7876
96	862.1622	3.5	3724
97	863.1579	7.8	8303
98	864.1607	3.6	3886
99	1182.3504	2.0	2182
100	1183.3498	2.9	3126

Acquisition Parameter

General	Fore Vacuum	2.47e+000 mBar	High Vacuum	7.73e-008 mBar	Source Type	ESI
	Scan Begin	75 m/z	Scan End	1700 m/z	Ion Polarity	Positive
Source	Set Nebulizer	0.4 Bar	Set Capillary	3600 V	Set Dry Gas	4.0 l/min
	Set Dry Heater	180 °C	Set End Plate Offset	-500 V		
Quadrupole	Set Ion Energy (MS only)	4.0 eV				
Coll. Cell	Collision Energy	8.0 eV	Set Collision Cell RF	500.0 Vpp		
Ion Cooler	Set Ion Cooler Transfer Time	100.0 µs	Set Ion Cooler Pre Pulse Storage Time	18.0 µs		

List of Abbreviations

AFM	Atomic force microscopy
aq.	aqueous
BAM	Brewster angle microscope
BINAP	2,2'-bis(diphenylphosphino)-1,1'-binaphthyl
biq	2,2'-biquinoline
(Bpin)$_2$	bis(pinacolato)diboro
bpy	2,2'-bipyridine
br	broad
Brine	saturated aqueous NaCl solution
calcd.	calculated
cat.	catalytic
CC	Column chromatography
COF	Covalent organic framework
COSY	Correlation spectroscopy
d	doublet
dba	dibenzylideneaceton
DCM	dichloromethane
DEPT	Distorsionless enhancement by polarization transfer
DIAD	diisopropyl azodicarboxylate
DME	1,2-dimethoxyethane
DMF	dimethylformamide
DMSO	dimethylsulfoxide
DNA	Deoxyribonucleic acid
DOESY	Diffusion-ordered spectroscopy
dppf	1,1'-bis(diphenylphosphino)ferrocene
EI	Electron impact

List of Abbreviations

eq.	equivalent
ESI	Electron spray ionization
Et	ethyl
Et$_2$O	diethylether
EtOAc	ethyl acetate
EtOH	ethanol
GCMS	Gas chromatography-mass spectrometry
hept	heptet
HMBC	Heteronuclear multiple bond correlation
HMQC	Heteronuclear multiple quantum correlation
HOMO	Highest occupied molecular orbital
HOPG	Highly oriented pyrolytic graphite
HPLC	High-performance liquid chromatography
HR-ESI-MS	High-resolution electron spray ionization mass spectrometry
^{i}Pr	*iso*propyl
IR	Infrared spectroscopy
LB	Langmuir-Blodgett
LC	Ligand-centred
LUMO	Lowest unoccupied molecular orbital
m	multiplet
m/z	mass per charge
MC	Metal-centered
Me	methyl
MeCN	acetonitrile
MeOH	Methanol
MeTHF	2-methyltetrahydrofuran
MLCT	Metal-to-ligand charge transfer
MO	Molecular orbital
MOF	Metal organic framework

MS	Mass spectrometry
n-BuLi	*n*-butyllithium
NMR	Nuclear magnet resonance
NOESY	Nuclear Overhauser enhancement spectroscopy
PCT	Photocleavable tag
PCI	pentacoordinate intermediate
PET	polyethylene terephthalate
Ph	phenyl
Phen	1,10-phenantroline
Ppm	parts per million
q	quartet
R.T.	room temperature
s	singlet
SAM	Self-assembled monolayer
SCO	Spin crossover
SEM	Scanning electron microscopy
STM	Scanning tunneling microcopy
t	triplet
TBAF	tetrabutylammonium fluoride
TEM	Transmission electron microscopy
TERS	Tip-enhanced Raman spectroscopy
TFA	trifluoroacetic acid
THF	tetrahydrofuran
TIPS	tris*iso*propylsilyl
TLC	Thin layer chromatography
TMS	trimethylsilyl
ToF	Time of flight
tpy	2,2':6',2''-terpyridine
UHV	Ultra-high vacuum

List of Abbreviations

UV-vis	Ultraviolet-visible spectroscopy
XPS	X-ray photoelectron spectroscopy
X-ray	X-ray spectroscopy
1D	one dimensional
2D	two dimensional
3D	three dimensional

Bibliography

(1)   Mohanty, J.; Choudhury, S. D.; Barooah, N.; Pal, H.; Bhasikuttan, A. C. 1.18 - Mechanistic Aspects of Host–Guest Binding in Cucurbiturils: Physicochemical Properties. In *Comprehensive Supramolecular Chemistry II*; Atwood, J. L., Ed.; Elsevier: Oxford, 2017; pp 435–457. https://doi.org/10.1016/B978-0-12-409547-2.11028-5.

(2)   Lehn, J.-M. Supramolecular Chemistry—Scope and Perspectives Molecules, Supermolecules, and Molecular Devices (Nobel Lecture). *Angew. Chem. Int. Ed. Engl.* **1988**, *27* (1), 89–112. https://doi.org/10.1002/anie.198800891.

(3)   Lehn, J. Supramolecular Chemistry. *Science* **1993**, *260* (5115), 1762–1763. https://doi.org/10.1126/science.8511582.

(4)   Cragg, P. J. An Introduction to Supramolecular Chemistry. In *Supramolecular Chemistry: From Biological Inspiration to Biomedical Applications*; Cragg, P. J., Ed.; Springer Netherlands: Dordrecht, 2010; pp 1–48. https://doi.org/10.1007/978-90-481-2582-1_1.

(5)   The Nobel Prize in Chemistry 1987 https://www.nobelprize.org/prizes/chemistry/1987/summary/ (accessed 2021 -10 -11).

(6)   Pedersen, C. J. The Discovery of Crown Ethers (Noble Lecture). *Angew. Chem. Int. Ed. Engl.* **1988**, *27* (8), 1021–1027. https://doi.org/10.1002/anie.198810211.

(7)   Cram, D. J. The Design of Molecular Hosts, Guests, and Their Complexes (Nobel Lecture). *Angew. Chem. Int. Ed. Engl.* **1988**, *27* (8), 1009–1020. https://doi.org/10.1002/anie.198810093.

(8)   Lancia, F.; Ryabchun, A.; Katsonis, N. Life-like Motion Driven by Artificial Molecular Machines. *Nat. Rev. Chem.* **2019**, *3* (9), 536–551. https://doi.org/10.1038/s41570-019-0122-2.

(9)   Erbas-Cakmak, S.; Leigh, D. A.; McTernan, C. T.; Nussbaumer, A. L. Artificial Molecular Machines. *Chem. Rev.* **2015**, *115* (18), 10081–10206. https://doi.org/10.1021/acs.chemrev.5b00146.

(10)   Mavroidis, C.; Dubey, A.; Yarmush, M. L. Molecular Machines. *Annu. Rev. Biomed. Eng.* **2004**, *6* (1), 363–395. https://doi.org/10.1146/annurev.bioeng.6.040803.140143.

(11)   Aprahamian, I. The Future of Molecular Machines. *ACS Cent. Sci.* **2020**, *6* (3), 347–358. https://doi.org/10.1021/acscentsci.0c00064.

(12)   Sasaki, Y.; Kubota, R.; Minami, T. Molecular Self-Assembled Chemosensors and Their Arrays. *Coord. Chem. Rev.* **2021**, *429*, 213607. https://doi.org/10.1016/j.ccr.2020.213607.

(13)   Kumar, R.; Sharma, A.; Singh, H.; Suating, P.; Kim, H. S.; Sunwoo, K.; Shim, I.; Gibb, B. C.; Kim, J. S. Revisiting Fluorescent Calixarenes: From Molecular Sensors to Smart Materials. *Chem. Rev.* **2019**, *119* (16), 9657–9721. https://doi.org/10.1021/acs.chemrev.8b00605.

(14)   Guo, C.; Sedgwick, A. C.; Hirao, T.; Sessler, J. L. Supramolecular Fluorescent Sensors: An Historical Overview and Update. *Coord. Chem. Rev.* **2021**, *427*, 213560. https://doi.org/10.1016/j.ccr.2020.213560.

(15)   Wang, Y.; Zhu, X. Nanofabrication within Unimolecular Nanoreactors. *Nanoscale* **2020**, *12* (24), 12698–12711. https://doi.org/10.1039/D0NR02674C.

(16)   Zhou, H.; Tan, J.; Zhang, X. Nanoreactors for Chemical Synthesis and Biomedical Applications. *Chem. – Asian J.* **2019**, *14* (19), 3240–3250. https://doi.org/10.1002/asia.201900967.

(17)   Vriezema, D. M.; Comellas Aragonès, M.; Elemans, J. A. A. W.; Cornelissen, J. J. L. M.; Rowan, A. E.; Nolte, R. J. M. Self-Assembled Nanoreactors. *Chem. Rev.* **2005**, *105* (4), 1445–1490. https://doi.org/10.1021/cr0300688.

(18)   Huang, F.; Anslyn, E. V. Introduction: Supramolecular Chemistry. *Chem. Rev.* **2015**, *115* (15), 6999–7000. https://doi.org/10.1021/acs.chemrev.5b00352.

(19)   Williams, G. T.; Haynes, C. J. E.; Fares, M.; Caltagirone, C.; Hiscock, J. R.; Gale, P. A. Advances in Applied Supramolecular Technologies. *Chem. Soc. Rev.* **2021**, *50* (4), 2737–2763. https://doi.org/10.1039/D0CS00948B.

(20)   Cragg, P. J. An Introduction to Supramolecular Chemistry. In *Supramolecular Chemistry: From Biological Inspiration to Biomedical Applications*; Cragg, P. J., Ed.; Springer Netherlands: Dordrecht, 2010; pp 1–48. https://doi.org/10.1007/978-90-481-2582-1_1.

(21)   Gokel, G. W.; Barbour, L. *Comprehensive Supramolecular Chemistry II*; Elsevier, 2017.

(22)   Cragg, P. J. Supramolecular Chemistry and the Life Sciences. In *Supramolecular Chemistry: From Biological Inspiration to Biomedical Applications*; Cragg, P. J., Ed.; Springer Netherlands: Dordrecht, 2010; pp 49–89. https://doi.org/10.1007/978-90-481-2582-1_2.

(23)   Oshovsky, G. V.; Reinhoudt, D. N.; Verboom, W. Supramolecular Chemistry in Water. *Angew. Chem. Int. Ed.* **2007**, *46* (14), 2366–2393. https://doi.org/10.1002/anie.200602815.

(24)   Fyfe, M. C. T.; Stoddart, J. F. Synthetic Supramolecular Chemistry. *Acc. Chem. Res.* **1997**, *30* (10), 393–401. https://doi.org/10.1021/ar950199y.

(25)   Metallo-Supramolecular Architectures Based on Terpyridine Complexes. In *Terpyridine-Based Materials*; John Wiley & Sons, Ltd; pp 129–197. https://doi.org/10.1002/9783527639625.ch4.

(26)   Schubert, U. S.; Hofmeier, H.; Newkome, G. R. *Modern Terpyridine Chemistry*; Wiley-VCH, 2006.

(27)   Lehn, J.-M. *Supramolecular Chemistry - Concepts and Perspectives*; Wiley-VCH: Weinheim, 1995.

(28)   Chakraborty, S.; Newkome, G. R. Terpyridine-Based Metallosupramolecular Constructs: Tailored Monomers to Precise 2D-Motifs and 3D-Metallocages. *Chem. Soc. Rev.* **2018**, *47* (11), 3991–4016. https://doi.org/10.1039/C8CS00030A.

(29)   Wei, C.; He, Y.; Shi, X.; Song, Z. Terpyridine-Metal Complexes: Applications in Catalysis and Supramolecular Chemistry. *Coord. Chem. Rev.* **2019**, *385*, 1–19. https://doi.org/10.1016/j.ccr.2019.01.005.

(30)   Hwang, S.-H.; Wang, P.; Moorefield, C. N.; Godínez, L. A.; Manríquez, J.; Bustos, E.; Newkome, G. R. Design, Self-Assembly, and Photophysical Properties of Pentameric Metallomacrocycles: [M5(N-Hexyl[1,2-Bis(2,2′:6′,2″-Terpyridin-4-Yl)]Carbazole)5][M = Fe(II), Ru(II), and Zn(II)]. *Chem. Commun.* **2005**, No. 37, 4672–4674. https://doi.org/10.1039/B509662F.

(31)   Newkome, G. R.; Wang, P.; Moorefield, C. N.; Cho, T. J.; Mohapatra, P. P.; Li, S.; Hwang, S.-H.; Lukoyanova, O.; Echegoyen, L.; Palagallo, J. A.; Iancu, V.; Hla, S.-W. Nanoassembly of a Fractal Polymer: A Molecular "Sierpinski Hexagonal Gasket." *Science* **2006**, *312* (5781), 1782–1785. https://doi.org/10.1126/science.1125894.

(32)   Chakraborty, S.; Sarkar, R.; Endres, K.; Xie, T.-Z.; Ghosh, M.; Moorefield, C. N.; Saunders, M. J.; Wesdemiotis, C.; Newkome, G. R. Programmed Molecular Engineering: Stepwise, Multicomponent Assembly of a Dimetallic Metallotriangulane. *Eur. J. Org. Chem.* **2016**, *2016* (30), 5091–5095. https://doi.org/10.1002/ejoc.201600883.

(33)   Sarkar, R.; Guo, K.; Moorefield, C. N.; Saunders, M. J.; Wesdemiotis, C.; Newkome, G. R. One-Step Multicomponent Self-Assembly of a First-Generation Sierpiński Triangle: From Fractal Design to Chemical Reality. *Angew. Chem. Int. Ed.* **2014**, *53* (45), 12182–12185. https://doi.org/10.1002/anie.201407285.

(34)   Jiang, Z.; Li, Y.; Wang, M.; Liu, D.; Yuan, J.; Chen, M.; Wang, J.; Newkome, G. R.; Sun, W.; Li, X.; Wang, P. Constructing High-Generation Sierpiński Triangles by Molecular Puzzling. *Angew. Chem. Int. Ed.* **2017**, *56* (38), 11450–11455. https://doi.org/10.1002/anie.201705480.

(35)   Jiang, Z.; Li, Y.; Wang, M.; Song, B.; Wang, K.; Sun, M.; Liu, D.; Li, X.; Yuan, J.; Chen, M.; Guo, Y.; Yang, X.; Zhang, T.; Moorefield, C. N.; Newkome, G. R.; Xu,

B.; Li, X.; Wang, P. Self-Assembly of a Supramolecular Hexagram and a Supramolecular Pentagram. *Nat. Commun.* **2017**, *8* (1), 15476. https://doi.org/10.1038/ncomms15476.

(36) Zhang, Z.; Wang, H.; Wang, X.; Li, Y.; Song, B.; Bolarinwa, O.; Reese, R. A.; Zhang, T.; Wang, X.-Q.; Cai, J.; Xu, B.; Wang, M.; Liu, C.; Yang, H.-B.; Li, X. Supersnowflakes: Stepwise Self-Assembly and Dynamic Exchange of Rhombus Star-Shaped Supramolecules. *J. Am. Chem. Soc.* **2017**, *139* (24), 8174–8185. https://doi.org/10.1021/jacs.7b01326.

(37) Wang, M.; Wang, C.; Hao, X.-Q.; Liu, J.; Li, X.; Xu, C.; Lopez, A.; Sun, L.; Song, M.-P.; Yang, H.-B.; Li, X. Hexagon Wreaths: Self-Assembly of Discrete Supramolecular Fractal Architectures Using Multitopic Terpyridine Ligands. *J. Am. Chem. Soc.* **2014**, *136* (18), 6664–6671. https://doi.org/10.1021/ja501417g.

(38) Wang, J.-L.; Li, X.; Lu, X.; Hsieh, I.-F.; Cao, Y.; Moorefield, C. N.; Wesdemiotis, C.; Cheng, S. Z. D.; Newkome, G. R. Stoichiometric Self-Assembly of Shape-Persistent 2D Complexes: A Facile Route to a Symmetric Supramacromolecular Spoked Wheel. *J. Am. Chem. Soc.* **2011**, *133* (30), 11450–11453. https://doi.org/10.1021/ja203645m.

(39) Lu, X.; Li, X.; Guo, K.; Wang, J.; Huang, M.; Wang, J.-L.; Xie, T.-Z.; Moorefield, C. N.; Cheng, S. Z. D.; Wesdemiotis, C.; Newkome, G. R. One Ligand in Dual Roles: Self-Assembly of a Bis-Rhomboidal-Shaped, Three-Dimensional Molecular Wheel. *Chem. – Eur. J.* **2014**, *20* (41), 13094–13098. https://doi.org/10.1002/chem.201404358.

(40) Yao, Y.; Chakraborty, S.; Zhu, S.; Endres, K. J.; Xie, T.-Z.; Hong, W.; Manandhar, E.; Moorefield, C. N.; Wesdemiotis, C.; Newkome, G. R. Stepwise, Multicomponent Assembly of a Molecular Trapezoid Possessing Three Different Metals. *Chem. Commun.* **2017**, *53* (57), 8038–8041. https://doi.org/10.1039/C7CC04080F.

(41)   Xie, T.-Z.; Guo, K.; Guo, Z.; Gao, W.-Y.; Wojtas, L.; Ning, G.-H.; Huang, M.; Lu, X.; Li, J.-Y.; Liao, S.-Y.; Chen, Y.-S.; Moorefield, C. N.; Saunders, M. J.; Cheng, S. Z. D.; Wesdemiotis, C.; Newkome, G. R. Precise Molecular Fission and Fusion: Quantitative Self-Assembly and Chemistry of a Metallo-Cuboctahedron. *Angew. Chem.* **2015**, *127* (32), 9356–9361. https://doi.org/10.1002/ange.201503609.

(42)   Morgan, G. T.; Burstall, F. H. 3. Dehydrogenation of Pyridine by Anhydrous Ferric Chloride. *J. Chem. Soc. Resumed* **1932**, No. 0, 20–30. https://doi.org/10.1039/JR9320000020.

(43)   Morgan, G.; Burstall, F. H. 347. Researches on Residual Affinity and Co-Ordination. Part XXXVII. Complex Metallic Salts Containing 2 : 6-Di-2′-Pyridylpyridine (2 : 2′ : 2″-Tripyridyl). *J. Chem. Soc. Resumed* **1937**, No. 0, 1649–1655. https://doi.org/10.1039/JR9370001649.

(44)   Constable, E. C. The Coordination Chemistry of 2,2′:6′,2″-Terpyridine and Higher Oligopyridines. In *Advances in Inorganic Chemistry*; Emeléus, H. J., Ed.; Academic Press, 1986; Vol. 30, pp 69–121. https://doi.org/10.1016/S0898-8838(08)60240-8.

(45)   Hollins, C. *The Synthesis of Nitrogen Ring Compounds Containing a Single Hetero-Atom (Nitrogen*; Van Nostrand: New York, 1924.

(46)   Tschitschibabin, A. E. Über Kondensationen Der Aldehyde Mit Ammonik Zu Pyridinbasen. *J. Für Prakt. Chem.* **1924**, *107* (1–4), 122–128. https://doi.org/10.1002/prac.19241070110.

(47)   Kröhnke, F. The Specific Synthesis of Pyridines and Oligopyridines. *Synthesis* **1976**, *1976* (1), 1–24. https://doi.org/10.1055/s-1976-23941.

(48)   Kröhnke, F. Syntheses Using Pyridinium Salts. *Angew. Chem. Int. Ed. Engl.* **1963**, *2* (5), 225–238. https://doi.org/10.1002/anie.196302251.

(49)   Owsley, D. C.; Nelke, J. M.; Bloomfield, J. J. Synthesis of 1,4 and 1,5 Diketones from N,N,N1,N1-Tetramethyl Diamides and Organolithium Reagents. *J. Org. Chem.* **1973**, *38* (5), 901–903. https://doi.org/10.1021/jo00945a011.

(50)   Constable, E. C.; Lewis, J. The Preparation and Coordination Chemistry of 2,2':6',2"-Terpyridine Macrocycles—1. *Polyhedron* **1982**, *1* (3), 303–306. https://doi.org/10.1016/S0277-5387(00)87169-7.

(51)   Newkome, G. R.; Hager, D. C.; Kiefer, G. E. Chemistry of Heterocyclic Compounds. Part 119. Synthesis of Halogenated Terpyridines and Incorporation of the Terpyridine Nucleus into a Polyetheral Macrocycle. *J. Org. Chem.* **1986**, *51* (6), 850–853. https://doi.org/10.1021/jo00356a019.

(52)   K. T. Potts; M. J. Cipullo; P. Ralli; G. Theodoridis. 2,2' : 6',2' -TERPYRIDINE. *Org. Synth.* **1986**, *64*, 189. https://doi.org/10.15227/orgsyn.064.0189.

(53)   Potts, K. T.; Usifer, D. A.; Guadalupe, A.; Abruna, H. D. 4-Vinyl-, 6-Vinyl-, and 4'-Vinyl-2,2':6',2"-Terpyridinyl Ligands: Their Synthesis and the Electrochemistry of Their Transition-Metal Coordination Complexes. *J. Am. Chem. Soc.* **1987**, *109* (13), 3961–3967. https://doi.org/10.1021/ja00247a021.

(54)   Jameson, D. L.; Guise, L. E. An Improved, Two-Step Synthesis of 2,2':6',2"-Terpyridine. *Tetrahedron Lett.* **1991**, *32* (18), 1999–2002. https://doi.org/10.1016/S0040-4039(00)78891-5.

(55)   Pabst, G. R.; Sauer, J. The New and Simple 'LEGO' System: Its Application to the Synthesis of 4-Stannyl-, 4-Bromo- and Branched Oligopyridines. *Tetrahedron* **1999**, *55* (16), 5067–5088. https://doi.org/10.1016/S0040-4020(99)00179-9.

(56)   Adrian, J. C.; Hassib, L.; De Kimpe, N.; Keppens, M. A New Approach to Symmetric 2,2':6',2"-Terpyridines. *Tetrahedron* **1998**, *54* (11), 2365–2370. https://doi.org/10.1016/S0040-4020(98)00005-2.

(57)   Sasaki, I.; Daran, J. C.; Balavoine, G. G. A. An Effective Route to Polysubstituted Symmetric Terpyridines. *Synthesis* **1999**, *1999* (05), 815–820. https://doi.org/10.1055/s-1999-3481.

(58)   Fallahpour, R.-A.; Constable, E. C. Novel Synthesis of Substituted4'-Hydroxy-2,2':6',2"-Terpyridines. *J. Chem. Soc. Perkin 1* **1997**, No. 16, 2263–2264. https://doi.org/10.1039/A704295G.

(59)   Fallahpour, R.-A.; Neuburger, M.; Zehnder, M. Ruthenium(II) Complexes of Novel 4′-Ethoxy- and 4′-Hydroxy-5,5″-Dimethyl-2,2′:6′,2″-Terpyridines: X-Ray Crystal Structures of 4′-Ethoxy-5,5″-Dimethyl-2,2″:6′,2″-Terpyridine and the Ruthenium(II) Complex of 4′-Ethoxy-5,5″-Dimethyl-2,2′:6′,2″-Terpyridine with 4′-Chloro-2,2′:6′,2″-Terpyridine. *Polyhedron* **1999**, *18* (18), 2445–2454. https://doi.org/10.1016/S0277-5387(99)00147-3.

(60)   Tohda, Y.; Eiraku, M.; Nakagawa, T.; Usami, Y.; Ariga, M.; Kawashima, T.; Tani, K.; Watanabe, H.; Mori, Y. Nucleophilic Reaction upon Electron-Deficient Pyridone Derivatives. X.One-Pot Synthesis of 3-Nitropyridines by Ring Transformation of 1-Methyl-3,5-Dinitro-2-Pyridone with Ketones or Aldehydes in the Presence of Ammonia. *Bull. Chem. Soc. Jpn.* **1990**, *63* (10), 2820–2827. https://doi.org/10.1246/bcsj.63.2820.

(61)   Uenishi, J.; Tanaka, T.; Wakabayashi, S.; Oae, S.; Tsukube, H. Ipso Substitution of 2-Alkylsulfinylpyridine by 2-Pyridyllithium; a New Preparation of Oligopyridine and Their Bromomethyl Derivatives. *Tetrahedron Lett.* **1990**, *31* (32), 4625–4628. https://doi.org/10.1016/S0040-4039(00)97692-5.

(62)   Parks, J. E.; Wagner, B. E.; Holm, R. H. Syntheses Employing Pyridyllithium Reagents: New Routes to 2,6-Disubstituted Pyridines and 6,6′-Disubstituted 2,2′-Bipyridyls. *J. Organomet. Chem.* **1973**, *56*, 53–66. https://doi.org/10.1016/S0022-328X(00)89953-2.

(63)   Astruc, D. The 2010 Chemistry Nobel Prize to R.F. Heck, E. Negishi, and A. Suzuki for Palladium-Catalyzed Cross-Coupling Reactions. *Anal. Bioanal. Chem.* **2011**, *399* (5), 1811–1814. https://doi.org/10.1007/s00216-010-4555-1.

(64)   Negishi, E. Magical Power of Transition Metals: Past, Present, and Future (Nobel Lecture). *Angew. Chem. Int. Ed.* **2011**, *50* (30), 6738–6764. https://doi.org/10.1002/anie.201101380.

(65)   Suzuki, A. Cross-Coupling Reactions Of Organoboranes: An Easy Way To Construct C⎕C Bonds (Nobel Lecture). *Angew. Chem. Int. Ed.* **2011**, *50* (30), 6722–6737. https://doi.org/10.1002/anie.201101379.

(66)   Heck, R. F. Palladium-Catalyzed Reactions of Organic Halides with Olefins. *Acc. Chem. Res.* **1979**, *12* (4), 146–151. https://doi.org/10.1021/ar50136a006.

(67)   Beletskaya, I. P.; Cheprakov, A. V. The Heck Reaction as a Sharpening Stone of Palladium Catalysis. *Chem. Rev.* **2000**, *100* (8), 3009–3066. https://doi.org/10.1021/cr9903048.

(68)   Christoffel, F.; Ward, T. R. Palladium-Catalyzed Heck Cross-Coupling Reactions in Water: A Comprehensive Review. *Catal. Lett.* **2018**, *148* (2), 489–511. https://doi.org/10.1007/s10562-017-2285-0.

(69)   Kürti, L.; Czako, B. *Strategic Applications of Named Reactions in Organic Synthesis*; Elsevier, 2005.

(70)   Hatanaka, Y.; Hiyama, T. Cross-Coupling of Organosilanes with Organic Halides Mediated by a Palladium Catalyst and Tris(Diethylamino)Sulfonium Difluorotrimethylsilicate. *J. Org. Chem.* **1988**, *53* (4), 918–920. https://doi.org/10.1021/jo00239a056.

(71)   Hatanaka, Y.; Hiyama, T. Highly Selective Cross-Coupling Reactions of Organosilicon Compounds Mediated by Fluoride Ion and a Palladium Catalyst. *Synlett* **1991**, *1991* (12), 845–853. https://doi.org/10.1055/s-1991-20899.

(72)   Tamao, K.; Sumitani, K.; Kumada, M. Selective Carbon-Carbon Bond Formation by Cross-Coupling of Grignard Reagents with Organic Halides. Catalysis by Nickel-Phosphine Complexes. *J. Am. Chem. Soc.* **1972**, *94* (12), 4374–4376. https://doi.org/10.1021/ja00767a075.

(73)   Hayashi, T.; Konishi, M.; Kobori, Y.; Kumada, M.; Higuchi, T.; Hirotsu, K. Dichloro[1,1′-Bis(Diphenylphosphino)Ferrocene]Palladium(II): An Effective Catalyst for Cross-Coupling of Secondary and Primary Alkyl Grignard and Alkylzinc Reagents with Organic Halides. *J. Am. Chem. Soc.* **1984**, *106* (1), 158–163. https://doi.org/10.1021/ja00313a032.

(74)   Zeng, F.; Negishi, E. A Novel, Selective, and Efficient Route to Carotenoids and Related Natural Products via Zr-Catalyzed Carboalumination and Pd- and Zn-

Catalyzed Cross Coupling. *Org. Lett.* **2001**, *3* (5), 719–722. https://doi.org/10.1021/ol000384y.

(75)   King, A. O.; Okukado, N.; Negishi, E. Highly General Stereo-, Regio-, and Chemo-Selective Synthesis of Terminal and Internal Conjugated Enynes by the Pd-Catalysed Reaction of Alkynylzinc Reagents with Alkenyl Halides. *J. Chem. Soc. Chem. Commun.* **1977**, No. 19, 683–684. https://doi.org/10.1039/C39770000683.

(76)   Sonogashira, K. Development of Pd–Cu Catalyzed Cross-Coupling of Terminal Acetylenes with Sp2-Carbon Halides. *J. Organomet. Chem.* **2002**, *653* (1), 46–49. https://doi.org/10.1016/S0022-328X(02)01158-0.

(77)   Miyaura, N. Synthesis of Biaryls via the Cross-Coupling Reaction of Arylboronic Acids. In *Advances in Metal-Organic Chemistry*; Liebeskind, L. S., Ed.; JAI, 1998; Vol. 6, pp 187–243. https://doi.org/10.1016/S1045-0688(98)80007-5.

(78)   Miyaura, N.; Suzuki, A. Stereoselective Synthesis of Arylated (E)-Alkenes by the Reaction of Alk-1-Enylboranes with Aryl Halides in the Presence of Palladium Catalyst. *J. Chem. Soc. Chem. Commun.* **1979**, No. 19, 866–867. https://doi.org/10.1039/C39790000866.

(79)   Miyaura, Norio.; Suzuki, Akira. Palladium-Catalyzed Cross-Coupling Reactions of Organoboron Compounds. *Chem. Rev.* **1995**, *95* (7), 2457–2483. https://doi.org/10.1021/cr00039a007.

(80)   Stille, J. K. The Palladium-Catalyzed Cross-Coupling Reactions of Organotin Reagents with Organic Electrophiles [New Synthetic Methods (58)]. *Angew. Chem. Int. Ed. Engl.* **1986**, *25* (6), 508–524. https://doi.org/10.1002/anie.198605081.

(81)   Del Valle, L.; Stille, J. K.; Hegedus, L. S. Palladium-Catalyzed Coupling of Allylic Acetates with Aryl- and Vinylstannanes. *J. Org. Chem.* **1990**, *55* (10), 3019–3023. https://doi.org/10.1021/jo00297a014.

(82)   Farina, V.; Krishnamurthy, V.; Scott, W. J. The Stille Reaction. In *Organic Reactions*; American Cancer Society, 2004; pp 1–652. https://doi.org/10.1002/0471264180.or050.01.

(83)   Cárdenas, D. J.; Sauvage, J.-P. Improved Synthesis of 2,6-Oligopyridines by Stille Cross-Coupling Reaction. *Synlett* **1996**, *1996* (9), 916–918. https://doi.org/10.1055/s-1996-5588.

(84)   Fallahpour, R.-A. Carboxylate Derivatives of Oligopyridines. *Synthesis* **2000**, *2000* (8), 1138–1142. https://doi.org/10.1055/s-2000-6331.

(85)   Fallahpour, R.-A.; Neuburger, M.; Zehnder, M. Synthesis of 4′-Azido-2,2′ : 6′,2″-Terpyridines and Their Iron(II) and Ruthenium(II) Complexes. *Synthesis* **1999**, *1999* (6), 1051–1055. https://doi.org/10.1055/s-1999-3505.

(86)   Ulrich, G.; Bedel, S.; Picard, C.; Tisnès, P. Synthesis of Bisfunctionalized-Oligopyridines Bearing an Ester Group. *Tetrahedron Lett.* **2001**, *42* (35), 6113–6115. https://doi.org/10.1016/S0040-4039(01)01195-9.

(87)   Heller, M.; Schubert, U. S. Functionalized 2,2′-Bipyridines and 2,2′:6′,2′′-Terpyridines via Stille-Type Cross-Coupling Procedures. *J. Org. Chem.* **2002**, *67* (23), 8269–8272. https://doi.org/10.1021/jo0260600.

(88)   Heller, M.; Schubert, U. S. Multi-Functionalized 2,2′:6′,2″-Terpyridines. *Synlett* **2002**, *2002* (5), 751–754. https://doi.org/10.1055/s-2002-25357.

(89)   Fallahpour, R.-A. An Efficient and Easy Route to Trimethyl Derivatives of 2,2′:6′,2. *Synthesis* **2000**, *2000* (12), 1665–1667. https://doi.org/10.1055/s-2000-8216.

(90)   Fallahpour, R.-A.; Neuburger, M. An Efficient, Easy Route for the Synthesis of 2,2′:6′,2″-Terpyridine 1′-Oxides. *Eur. J. Org. Chem.* **2001**, *2001* (10), 1853–1856. https://doi.org/10.1002/1099-0690(200105)2001:10<1853::AID-EJOC1853>3.0.CO;2-S.

(91)   Schubert, U. S.; Eschbaumer, C. New Synthetic Strategy toward Pyridine-Based Ligands for Supramolecular Chemistry Utilizing 2,6-Bis(Trimethyltin)Pyridine as

the Central Building Block. *Org. Lett.* **1999**, *1* (7), 1027–1029. https://doi.org/10.1021/ol990808s.

(92) Lehmann, U.; Henze, O.; Schlüter, A. D. 5,5″-Disubstituted 2,2′:6′,2″-Terpyridines through and for Metal-Mediated Cross-Coupling Chemistry. *Chem. – Eur. J.* **1999**, *5* (3), 854–859. https://doi.org/10.1002/(SICI)1521-3765(19990301)5:3<854::AID-CHEM854>3.0.CO;2-8.

(93) Louërat, F.; Gros, P. C. Functional Polypyridine Ligands from Copper-Mediated Room Temperature Coupling of 4-Chloro-2-Trimethylsilylpyridine. *Tetrahedron Lett.* **2010**, *51* (27), 3558–3560. https://doi.org/10.1016/j.tetlet.2010.04.133.

(94) Harzmann, G. D.; Neuburger, M.; Mayor, M. 4,4″-Disubstituted Terpyridines and Their Homoleptic FeII Complexes. *Eur. J. Inorg. Chem.* **2013**, *2013* (19), 3334–3347. https://doi.org/10.1002/ejic.201300231.

(95) Savage, S. A.; Smith, A. P.; Fraser, C. L. Efficient Synthesis of 4-, 5-, and 6-Methyl-2,2′-Bipyridine by a Negishi Cross-Coupling Strategy Followed by High-Yield Conversion to Bromo- and Chloromethyl-2,2′-Bipyridines. *J. Org. Chem.* **1998**, *63* (26), 10048–10051. https://doi.org/10.1021/jo981505z.

(96) Chavarot, M.; Pikramenou, Z. An Efficient Synthesis of Versatile Terpyridine Analogues for Cyclometallated Luminescent Cyclodextrins. *Tetrahedron Lett.* **1999**, *40* (37), 6865–6868. https://doi.org/10.1016/S0040-4039(99)01386-6.

(97) Molander, G. A.; Biolatto, B. Palladium-Catalyzed Suzuki–Miyaura Cross-Coupling Reactions of Potassium Aryl- and Heteroaryltrifluoroborates. *J. Org. Chem.* **2003**, *68* (11), 4302–4314. https://doi.org/10.1021/jo0342368.

(98) Venkataraman, D.; Du, Y.; Wilson, S. R.; Hirsch, K. A.; Zhang, P.; Moore, J. S. A Coordination Geometry Table of the D-Block Elements and Their Ions. *J. Chem. Educ.* **1997**, *74* (8), 915. https://doi.org/10.1021/ed074p915.

(99) Semenova, L. I.; Sobolev, A. N.; Skelton, B. W.; White, A. H. Structural Systematics of Rare Earth Complexes. XV Tris(2,2′:6′,2″-Terpyridine)Lanthanoid(III) Tris(Perchlorate) Complexes. *Aust. J. Chem.* **1999**, *52* (6), 519–530. https://doi.org/10.1071/ch98046.

(100) Chemistry and Properties of Terpyridine Transition Metal Ion Complexes. In *Terpyridine-Based Materials*; John Wiley & Sons, Ltd; pp 65–127. https://doi.org/10.1002/9783527639625.ch3.

(101) Mugemana, C.; Guillet, P.; Hoeppener, S.; S. Schubert, U.; Fustin, C.-A.; Gohy, J.-F. Metallo-Supramolecular Diblock Copolymers Based on Heteroleptic Cobalt(Iii) and Nickel(Ii) Bis-Terpyridine Complexes. *Chem. Commun.* **2010**, *46* (8), 1296–1298. https://doi.org/10.1039/B923270B.

(102) Sauvage, J. P.; Collin, J. P.; Chambron, J. C.; Guillerez, S.; Coudret, C.; Balzani, V.; Barigelletti, F.; De Cola, L.; Flamigni, L. Ruthenium(II) and Osmium(II) Bis(Terpyridine) Complexes in Covalently-Linked Multicomponent Systems: Synthesis, Electrochemical Behavior, Absorption Spectra, and Photochemical and Photophysical Properties. *Chem. Rev.* **1994**, *94* (4), 993–1019. https://doi.org/10.1021/cr00028a006.

(103) Frink, M. E.; Sprouse, S. D.; Goodwin, H. A.; Watts, R. J.; Ford, P. C. Synthesis and Excited-State Properties of Rhodium(III) Terpyridine Complexes. *Inorg. Chem.* **1988**, *27* (7), 1283–1286. https://doi.org/10.1021/ic00280a039.

(104) Paul, J.; Spey, S.; Adams, H.; Thomas, J. A. Synthesis and Structure of Rhodium Complexes Containing Extended Terpyridyl Ligands. *Inorganica Chim. Acta* **2004**, *357* (10), 2827–2832. https://doi.org/10.1016/j.ica.2003.12.023.

(105) Tessore, F.; Roberto, D.; Ugo, R.; Pizzotti, M.; Quici, S.; Cavazzini, M.; Bruni, S.; De Angelis, F. Terpyridine Zn(II), Ru(III), and Ir(III) Complexes: The Relevant Role of the Nature of the Metal Ion and of the Ancillary Ligands on the Second-Order Nonlinear Response of Terpyridines Carrying Electron Donor or Electron Acceptor Groups. *Inorg. Chem.* **2005**, *44* (24), 8967–8978. https://doi.org/10.1021/ic050975q.

(106) Williams, J. A. G.; Wilkinson, A. J.; Whittle, V. L. Light-Emitting Iridium Complexes with Tridentate Ligands. *Dalton Trans.* **2008**, No. 16, 2081–2099. https://doi.org/10.1039/B716743A.

(107) Novoselov, K. S.; Geim, A. K.; Morozov, S. V.; Jiang, D.; Zhang, Y.; Dubonos, S. V.; Grigorieva, I. V.; Firsov, A. A. Electric Field Effect in Atomically Thin Carbon Films. *Science* **2004**, *306* (5696), 666–669. https://doi.org/10.1126/science.1102896.

(108) August, D. P.; Dryfe, R. A. W.; Haigh, S. J.; Kent, P. R. C.; Leigh, D. A.; Lemonnier, J.-F.; Li, Z.; Muryn, C. A.; Palmer, L. I.; Song, Y.; Whitehead, G. F. S.; Young, R. J. Self-Assembly of a Layered Two-Dimensional Molecularly Woven Fabric. *Nature* **2020**, *588* (7838), 429–435. https://doi.org/10.1038/s41586-020-3019-9.

(109) Nierengarten, J. F.; Dietrich-Buchecker, C. O.; Sauvage, J. P. Synthesis of a Doubly Interlocked [2]-Catenane. *J. Am. Chem. Soc.* **1994**, *116* (1), 375–376. https://doi.org/10.1021/ja00080a045.

(110) Zoppellaro, G.; Ivanova, A.; Enkelmann, V.; Geies, A.; Baumgarten, M. Synthesis, Magnetic Properties and Theoretical Calculations of Novel Nitronyl Nitroxide and Imino Nitroxide Diradicals Grafted on Terpyridine Moiety. *Polyhedron* **2003**, *22* (14), 2099–2110. https://doi.org/10.1016/S0277-5387(03)00258-4.

(111) Gaviña, P.; Tatay, S. Synthesis of a Novel Ditopic Ligand Incorporating Directly Bonded 1,10-Phenanthroline and 2,2′:6′,2″-Terpyridine Units. *Tetrahedron Lett.* **2006**, *47* (20), 3471–3473. https://doi.org/10.1016/j.tetlet.2006.03.025.

(112) Sasaki, I.; Daran, J. C.; Balavoine, G. G. A. An Effective Route to Polysubstituted Symmetric Terpyridines. *Synthesis* **1999**, *1999* (05), 815–820. https://doi.org/10.1055/s-1999-3481.

(113) 5,5″-Disubstituted 2,2′:6′,2″-Terpyridines through and for Metal-Mediated Cross-Coupling Chemistry - Lehmann - 1999 - Chemistry – A European Journal - Wiley Online Library https://chemistry-europe.onlinelibrary.wiley.com/doi/abs/10.1002/(SICI)1521-3765(19990301)5:3%3C854::AID-CHEM854%3E3.0.CO;2-8 (accessed 2021 - 05 -14).

(114) Colasson, B. X.; Dietrich-Buchecker, C.; Sauvage, J.-P. Improved Synthesis of 5,5″-Dibromo-2,2′:6′,2″-Terpyridine. *Synlett* **2002**, *2002* (02), 0271–0272. https://doi.org/10.1055/s-2002-19767.

(115) Copper-Catalyzed Trifluoromethylation of Aryl Iodides with Potassium (Trifluoromethyl)trimethoxyborate - Knauber - 2011 - Chemistry – A European Journal - Wiley Online Library https://chemistry-europe.onlinelibrary.wiley.com/doi/full/10.1002/chem.201002749 (accessed 2021 -05 -14).

(116) Köytepe, S.; Erdoğan, S.; Seçkin, T. Synthesis of Polyimide from 5,5″-Bis(Bromomethyl)-2,2′:6′,2″-Terpyridine and Investigation of the Polymer Sorption Behavior towards Some Metal Ions. *J. Hazard. Mater.* **2009**, *162* (2), 695–702. https://doi.org/10.1016/j.jhazmat.2008.05.126.

(117) Cao, L.; Lin, Z.; Peng, F.; Wang, W.; Huang, R.; Wang, C.; Yan, J.; Liang, J.; Zhang, Z.; Zhang, T.; Long, L.; Sun, J.; Lin, W. Self-Supporting Metal–Organic Layers as Single-Site Solid Catalysts. *Angew. Chem. Int. Ed.* **2016**, *55* (16), 4962–4966. https://doi.org/10.1002/anie.201512054.

(118) Constable, E. C.; Ward, M. D. Synthesis and Co-Ordination Behaviour of 6′,6″-Bis(2-Pyridyl)-2,2′ : 4,4″ : 2″,2‴-Quaterpyridine; 'Back-to-Back' 2,2′ : 6′,2″-Terpyridine. *J. Chem. Soc. Dalton Trans.* **1990**, No. 4, 1405–1409. https://doi.org/10.1039/DT9900001405.

(119) Lin, C.-P.; Florio, P.; Campi, E. M.; Zhang, C.; Fredericks, D. P.; Saito, K.; Jackson, W. R.; Hearn, M. T. W. Synthesis of Substituted Terpyridine Ligands for Use in Protein Purification. *Tetrahedron* **2014**, *70* (45), 8520–8531. https://doi.org/10.1016/j.tet.2014.09.074.

(120) Newkome, G. R.; He, E. Nanometric Dendritic Macromolecules: Stepwise Assembly Bydouble(2,2′:6′,2″-Terpyridine)Ruthenium(I)Connectivity. *J. Mater. Chem.* **1997**, *7* (7), 1237–1244. https://doi.org/10.1039/A700127D.

(121) Armspach, D.; Constable, E. C.; Housecroft, C. E.; Neuburger, M.; Zehnder, M. Carbaborane-Functionalised 2,2′:6′,2″-Terpyridine Ligands for

Metallosupramolecular Chemistry: Syntheses, Complex Formation, and the Crystal and Molecular Structures of 4′-(Ortho-Carboranyl)-2,2′:6′,2″-Terpyridine and 4′-(Ortho-Carboranylpropoxy)-2,2′:6′,2″-Terpyridine1This Paper Is Dedicated to Professor Ken Wade on the Occasion of His 65th Birthday.1. *J. Organomet. Chem.* **1998**, *550* (1), 193–206. https://doi.org/10.1016/S0022-328X(97)00238-6.

(122) Hovinen, J. Synthesis of 4′-Substituted 2,2′:6′,2″-Terpyridines via a Mitsunobu Reaction. *Tetrahedron Lett.* **2004**, *45* (29), 5707–5709. https://doi.org/10.1016/j.tetlet.2004.05.105.

(123) Wolfe, J. P.; Åhman, J.; Sadighi, J. P.; Singer, R. A.; Buchwald, S. L. An Ammonia Equivalent for the Palladium-Catalyzed Amination of Aryl Halides and Triflates. *Tetrahedron Lett.* **1997**, *38* (36), 6367–6370. https://doi.org/10.1016/S0040-4039(97)01465-2.

(124) Hogg, R.; Wilkins, R. G. 57. Exchange Studies of Certain Chelate Compounds of the Transitional Metals. Part VIII. 2,2′,2″-Terpyridine Complexes. *J. Chem. Soc. Resumed* **1962**, No. 0, 341–350. https://doi.org/10.1039/JR9620000341.

(125) Holyer, R. H.; Hubbard, C. D.; Kettle, S. F. A.; Wilkins, R. G. The Kinetics of Replacement Reactions of Complexes of the Transition Metals with 2,2′,2″-Terpyridine. *Inorg. Chem.* **1966**, *5* (4), 622–625. https://doi.org/10.1021/ic50038a027.

(126) Henderson, I. M.; Hayward, R. C. Substituent Effects on the Stabilities of Polymeric and Small Molecule Bis-Terpyridine Complexes. *Polym. Chem.* **2012**, *3* (5), 1221–1230. https://doi.org/10.1039/C2PY20042B.

(127) Sauvage, J. P.; Collin, J. P.; Chambron, J. C.; Guillerez, S.; Coudret, C.; Balzani, V.; Barigelletti, F.; De Cola, L.; Flamigni, L. Ruthenium(II) and Osmium(II) Bis(Terpyridine) Complexes in Covalently-Linked Multicomponent Systems: Synthesis, Electrochemical Behavior, Absorption Spectra, and Photochemical and Photophysical Properties. *Chem. Rev.* **1994**, *94* (4), 993–1019. https://doi.org/10.1021/cr00028a006.

(128) Campagna, S.; Puntoriero, F.; Nastasi, F.; Bergamini, G.; Balzani, V. Photochemistry and Photophysics of Coordination Compounds: Ruthenium. In *Photochemistry and Photophysics of Coordination Compounds I*; Balzani, V., Campagna, S., Eds.; Topics in Current Chemistry; Springer: Berlin, Heidelberg, 2007; pp 117–214. https://doi.org/10.1007/128_2007_133.

(129) Tatikonda, R.; Cametti, M.; Kalenius, E.; Famulari, A.; Rissanen, K.; Haukka, M. Mononuclear Ru(II) PolyPyridyl Water Oxidation Catalysts Decorated with Perfluoroalkyl C8H17-Tag Bearing Chains. *Eur. J. Inorg. Chem.* **2019**, *2019* (41), 4463–4470. https://doi.org/10.1002/ejic.201900579.

(130) Rupp, M.; Auvray, T.; Rousset, E.; Mercier, G. M.; Marvaud, V.; Kurth, D. G.; Hanan, G. S. Photocatalytic Hydrogen Evolution Driven by a Heteroleptic Ruthenium(II) Bis(Terpyridine) Complex. *Inorg. Chem.* **2019**, *58* (14), 9127–9134. https://doi.org/10.1021/acs.inorgchem.9b00698.

(131) Baráth, E. Hydrogen Transfer Reactions of Carbonyls, Alkynes, and Alkenes with Noble Metals in the Presence of Alcohols/Ethers and Amines as Hydrogen Donors. *Catalysts* **2018**, *8* (12), 671. https://doi.org/10.3390/catal8120671.

(132) Fujii, A.; Hashiguchi, S.; Uematsu, N.; Ikariya, T.; Noyori, R. Ruthenium(II)-Catalyzed Asymmetric Transfer Hydrogenation of Ketones Using a Formic Acid−Triethylamine Mixture. *J. Am. Chem. Soc.* **1996**, *118* (10), 2521–2522. https://doi.org/10.1021/ja954126l.

(133) Ghosh, R.; Jana, N. Ch.; Panda, S.; Bagh, B. Transfer Hydrogenation of Aldehydes and Ketones in Air with Methanol and Ethanol by an Air-Stable Ruthenium−Triazole Complex. *ACS Sustain. Chem. Eng.* **2021**, *9* (13), 4903–4914. https://doi.org/10.1021/acssuschemeng.1c00633.

(134) Catherine E., H.; Alan G., S. *Inorganic Chemistry | 4th Edition | Pearson*, 4th ed.; Pearson.

(135) Ulrich S., S.; Harald, H.; George R., N. *Modern Terpyridine Chemistry | Wiley*; Wiley-VCH.

(136) Braterman, P. S.; Song, J. I.; Peacock, R. D. Electronic Absorption Spectra of the Iron(II) Complexes of 2,2'-Bipyridine, 2,2'-Bipyrimidine, 1,10-Phenanthroline, and 2,2':6',2''-Terpyridine and Their Reduction Products. *Inorg. Chem.* **1992**, *31* (4), 555–559. https://doi.org/10.1021/ic00030a006.

(137) Steube, J.; Burkhardt, L.; Päpcke, A.; Moll, J.; Zimmer, P.; Schoch, R.; Wölper, C.; Heinze, K.; Lochbrunner, S.; Bauer, M. Excited-State Kinetics of an Air-Stable Cyclometalated Iron(II) Complex. *Chem. – Eur. J.* **2019**, *25* (51), 11826–11830. https://doi.org/10.1002/chem.201902488.

(138) Baillargeon, J.; Xie, Y.; Raithel, A. L.; Ghaffari, B.; Staples, R. J.; Hamann, T. W. Spin-Doctoring Cobalt Redox Shuttles for Dye-Sensitized Solar Cells. *Inorg. Chem.* **2018**, *57* (18), 11633–11645. https://doi.org/10.1021/acs.inorgchem.8b01772.

(139) Aroua, S.; Todorova, T. K.; Hommes, P.; Chamoreau, L.-M.; Reissig, H.-U.; Mougel, V.; Fontecave, M. Synthesis, Characterization, and DFT Analysis of Bis-Terpyridyl-Based Molecular Cobalt Complexes. *Inorg. Chem.* **2017**, *56* (10), 5930–5940. https://doi.org/10.1021/acs.inorgchem.7b00595.

(140) Nie, H.-J.; Yao, C.-J.; Sun, M.-J.; Zhong, Y.-W.; Yao, J. Ruthenium-Bis-Terpyridine Complex with Two Redox-Asymmetric Amine Substituents: Potential-Controlled Reversal of the Direction of Charge-Transfer. *Organometallics* **2014**, *33* (21), 6223–6231. https://doi.org/10.1021/om500904k.

(141) Maestri, M.; Armaroli, N.; Balzani, V.; Constable, E. C.; Thompson, A. M. W. C. Complexes of the Ruthenium(II)-2,2':6',2''-Terpyridine Family. Effect of Electron-Accepting and -Donating Substituents on the Photophysical and Electrochemical Properties. *Inorg. Chem.* **1995**, *34* (10), 2759–2767. https://doi.org/10.1021/ic00114a039.

(142) Dobrawa, R.; Ballester, P.; Saha-Möller, C. R.; Würthner, F. Thermodynamics of 2,2':6',2''-Terpyridine-Metal Ion Complexation. In *Metal-Containing and Metallosupramolecular Polymers and Materials*; ACS Symposium Series;

American Chemical Society, 2006; Vol. 928, pp 43–62. https://doi.org/10.1021/bk-2006-0928.ch004.

(143) Harzmann, G. D.; Frisenda, R.; Zant, H. S. J. van der; Mayor, M. Single-Molecule Spin Switch Based on Voltage-Triggered Distortion of the Coordination Sphere. *Angew. Chem. Int. Ed.* **2015**, *54* (45), 13425–13430. https://doi.org/10.1002/anie.201505447.

(144) Brandl, T.; Abbassi, M. E.; Stefani, D.; Frisenda, R.; Harzmann, G. D.; Zant, H. S. J. van der; Mayor, M. Enhanced Separation Concept (ESC): Removing the Functional Subunit from the Electrode by Molecular Design. *Eur. J. Org. Chem.* **2019**, *2019* (31–32), 5334–5343. https://doi.org/10.1002/ejoc.201900432.

(145) Henderson, I. M.; Hayward, R. C. Kinetic Stabilities of Bis-Terpyridine Complexes with Iron(II) and Cobalt(II) in Organic Solvent Environments. *J. Mater. Chem.* **2012**, *22* (40), 21366–21369. https://doi.org/10.1039/C2JM33870J.

(146) Chiper, M.; Meier, M. A. R.; Kranenburg, J. M.; Schubert, U. S. New Insights into Nickel(II), Iron(II), and Cobalt(II) Bis-Complex-Based Metallo-Supramolecular Polymers. *Macromol. Chem. Phys.* **2007**, *208* (7), 679–689. https://doi.org/10.1002/macp.200600605.

(147) Lohmeijer, B. G. G.; Schubert, U. S. Playing LEGO with Macromolecules: Design, Synthesis, and Self-Organization with Metal Complexes. *J. Polym. Sci. Part Polym. Chem.* **2003**, *41* (10), 1413–1427. https://doi.org/10.1002/pola.10685.

(148) Meier, M. A. R.; Lohmeijer, B. G. G.; Schubert, U. S. Characterization of Defined Metal-Containing Supramolecular Block Copolymers. *Macromol. Rapid Commun.* **2003**, *24* (14), 852–857. https://doi.org/10.1002/marc.200350031.

(149) Moss, G. P.; Smith, P. a. S.; Tavernier, D. Glossary of class names of organic compounds and reactivity intermediates based on structure (IUPAC Recommendations 1995). *Pure Appl. Chem.* **1995**, *67* (8–9), 1307–1375. https://doi.org/10.1351/pac199567081307.

(150) Qin, W.; Long, S.; Panunzio, M.; Biondi, S. Schiff Bases: A Short Survey on an Evergreen Chemistry Tool. *Molecules* **2013**, *18* (10), 12264–12289. https://doi.org/10.3390/molecules181012264.

(151) Xu, S.-Q.; Liang, R.-R.; Zhan, T.-G.; Qi, Q.-Y.; Zhao, X. Construction of 2D Covalent Organic Frameworks by Taking Advantage of the Variable Orientation of Imine Bonds. *Chem. Commun.* **2017**, *53* (16), 2431–2434. https://doi.org/10.1039/C6CC09906H.

(152) Ciaccia, M.; Stefano, S. D. Mechanisms of Imine Exchange Reactions in Organic Solvents. *Org. Biomol. Chem.* **2014**, *13* (3), 646–654. https://doi.org/10.1039/C4OB02110J.

(153) Osowska, K.; Miljanić, O. Š. Oxidative Kinetic Self-Sorting of a Dynamic Imine Library. *J. Am. Chem. Soc.* **2011**, *133* (4), 724–727. https://doi.org/10.1021/ja109754t.

(154) Osowska, K.; Miljanić, O. Š. Self-Sorting of Dynamic Imine Libraries during Distillation. *Angew. Chem. Int. Ed.* **2011**, *50* (36), 8345–8349. https://doi.org/10.1002/anie.201102813.

(155) Givelet, C.; Sun, J.; Xu, D.; J. Emge, T.; Dhokte, A.; Warmuth, R. Templated Dynamic Cryptophane Formation in Water. *Chem. Commun.* **2011**, *47* (15), 4511–4513. https://doi.org/10.1039/C1CC10510H.

(156) Rao, V. K.; Reddy, S. S.; Krishna, B. S.; Naidu, K. R. M.; Raju, C. N.; Ghosh, S. K. Synthesis of Schiff's Bases in Aqueous Medium: A Green Alternative Approach with Effective Mass Yield and High Reaction Rates. *Green Chem. Lett. Rev.* **2010**, *3* (3), 217–223. https://doi.org/10.1080/17518251003716550.

(157) Di Giovannantonio, M.; Kosmala, T.; Bonanni, B.; Serrano, G.; Zema, N.; Turchini, S.; Catone, D.; Wandelt, K.; Pasini, D.; Contini, G.; Goletti, C. Surface−Enhanced Polymerization via Schiff-Base Coupling at the Solid–Water Interface under PH Control. *J. Phys. Chem. C* **2015**, *119* (33), 19228–19235. https://doi.org/10.1021/acs.jpcc.5b05547.

(158) Godoy-Alcántar, C.; Yatsimirsky, A. K.; Lehn, J.-M. Structure-Stability Correlations for Imine Formation in Aqueous Solution. *J. Phys. Org. Chem.* **2005**, *18* (10), 979–985. https://doi.org/10.1002/poc.941.

(159) Saggiomo, V.; Lüning, U. On the Formation of Imines in Water—a Comparison. *Tetrahedron Lett.* **2009**, *50* (32), 4663–4665. https://doi.org/10.1016/j.tetlet.2009.05.117.

(160) Rathelot, P.; Vanelle, P.; Gasquet, M.; Delmas, F.; Crozet, M.; Timon-David, P.; Maldonado, J. Synthesis of Novel Functionalized 5-Nitroisoquinolines and Evaluation of in Vitro Antimalarial Activity. *Eur. J. Med. Chem.* **1995**, *30* (6), 503–508. https://doi.org/10.1016/0223-5234(96)88261-4.

(161) Shi, L.; Ge, H.-M.; Tan, S.-H.; Li, H.-Q.; Song, Y.-C.; Zhu, H.-L.; Tan, R.-X. Synthesis and Antimicrobial Activities of Schiff Bases Derived from 5-Chloro-Salicylaldehyde. *Eur. J. Med. Chem.* **2007**, *42* (4), 558–564. https://doi.org/10.1016/j.ejmech.2006.11.010.

(162) Guo, Z.; Xing, R.; Liu, S.; Zhong, Z.; Ji, X.; Wang, L.; Li, P. Antifungal Properties of Schiff Bases of Chitosan, N-Substituted Chitosan and Quaternized Chitosan. *Carbohydr. Res.* **2007**, *342* (10), 1329–1332. https://doi.org/10.1016/j.carres.2007.04.006.

(163) Sriram, D.; Yogeeswari, P.; Myneedu, N. S.; Saraswat, V. Abacavir Prodrugs: Microwave-Assisted Synthesis and Their Evaluation of Anti-HIV Activities. *Bioorg. Med. Chem. Lett.* **2006**, *16* (8), 2127–2129. https://doi.org/10.1016/j.bmcl.2006.01.050.

(164) Hu, J.; Gupta, S. K.; Ozdemir, J.; Beyzavi, M. H. Applications of Dynamic Covalent Chemistry Concept toward Tailored Covalent Organic Framework Nanomaterials: A Review. *ACS Appl. Nano Mater.* **2020**, *3* (7), 6239–6269. https://doi.org/10.1021/acsanm.0c01327.

(165) Balch, H. B.; Evans, A. M.; Dasari, R. R.; Li, H.; Li, R.; Thomas, S.; Wang, D.; Bisbey, R. P.; Slicker, K.; Castano, I.; Xun, S.; Jiang, L.; Zhu, C.; Gianneschi, N.; Ralph, D. C.; Brédas, J.-L.; Marder, S. R.; Dichtel, W. R.; Wang, F. Electronically

Coupled 2D Polymer/MoS2 Heterostructures. *J. Am. Chem. Soc.* **2020**, *142* (50), 21131–21139. https://doi.org/10.1021/jacs.0c10151.

(166) Kandambeth, S.; Shinde, D. B.; Panda, M. K.; Lukose, B.; Heine, T.; Banerjee, R. Enhancement of Chemical Stability and Crystallinity in Porphyrin-Containing Covalent Organic Frameworks by Intramolecular Hydrogen Bonds. *Angew. Chem. Int. Ed.* **2013**, *52* (49), 13052–13056. https://doi.org/10.1002/anie.201306775.

(167) Cai, S.-L.; Zhang, Y.-B.; Pun, A. B.; He, B.; Yang, J.; Toma, F. M.; Sharp, I. D.; Yaghi, O. M.; Fan, J.; Zheng, S.-R.; Zhang, W.-G.; Liu, Y. Tunable Electrical Conductivity in Oriented Thin Films of Tetrathiafulvalene-Based Covalent Organic Framework. *Chem. Sci.* **2014**, *5* (12), 4693–4700. https://doi.org/10.1039/C4SC02593H.

(168) Liu, Y.; Ma, Y.; Zhao, Y.; Sun, X.; Gándara, F.; Furukawa, H.; Liu, Z.; Zhu, H.; Zhu, C.; Suenaga, K.; Oleynikov, P.; Alshammari, A. S.; Zhang, X.; Terasaki, O.; Yaghi, O. M. Weaving of Organic Threads into a Crystalline Covalent Organic Framework. *Science* **2016**, *351* (6271), 365–369. https://doi.org/10.1126/science.aad4011.

(169) Zhong, J.; Zhang, L.; August, D. P.; Whitehead, G. F. S.; Leigh, D. A. Self-Sorting Assembly of Molecular Trefoil Knots of Single Handedness. *J. Am. Chem. Soc.* **2019**, *141* (36), 14249–14256. https://doi.org/10.1021/jacs.9b06127.

(170) Beves, J. E.; Campbell, C. J.; Leigh, D. A.; Pritchard, R. G. Tetrameric Cyclic Double Helicates as a Scaffold for a Molecular Solomon Link. *Angew. Chem. Int. Ed.* **2013**, *52* (25), 6464–6467. https://doi.org/10.1002/anie.201302634.

(171) Ayme, J.-F.; Beves, J. E.; Leigh, D. A.; McBurney, R. T.; Rissanen, K.; Schultz, D. Pentameric Circular Iron(II) Double Helicates and a Molecular Pentafoil Knot. *J. Am. Chem. Soc.* **2012**, *134* (22), 9488–9497. https://doi.org/10.1021/ja303355v.

(172) Sanders, J. K. M. Adventures in molecular recognition. The ins and outs of templating. *Pure Appl. Chem.* **2000**, *72* (12), 2265–2274. https://doi.org/10.1351/pac200072122265.

(173) Black, S. P.; Sanders, J. K. M.; Stefankiewicz, A. R. Disulfide Exchange: Exposing Supramolecular Reactivity through Dynamic Covalent Chemistry. *Chem. Soc. Rev.* **2014**, *43* (6), 1861–1872. https://doi.org/10.1039/C3CS60326A.

(174) Lehn, J.-M. Dynamic Combinatorial Chemistry and Virtual Combinatorial Libraries. *Chem. – Eur. J.* **1999**, *5* (9), 2455–2463. https://doi.org/10.1002/(SICI)1521-3765(19990903)5:9<2455::AID-CHEM2455>3.0.CO;2-H.

(175) Lehn, J.-M. From Supramolecular Chemistry towards Constitutional Dynamic Chemistry and Adaptive Chemistry. *Chem. Soc. Rev.* **2007**, *36* (2), 151–160. https://doi.org/10.1039/B616752G.

(176) Furlan, R. L. E.; Otto, S.; Sanders, J. K. M. Supramolecular Templating in Thermodynamically Controlled Synthesis. *Proc. Natl. Acad. Sci.* **2002**, *99* (8), 4801–4804. https://doi.org/10.1073/pnas.022643699.

(177) Matson, B. D.; Carver, C. T.; Ruden, A. V.; Yang, J. Y.; Raugei, S.; Mayer, J. M. Distant Protonated Pyridine Groups in Water-Soluble Iron Porphyrin Electrocatalysts Promote Selective Oxygen Reduction to Water. *Chem. Commun.* **2012**, *48* (90), 11100–11102. https://doi.org/10.1039/C2CC35576K.

(178) Montalvo-González, R.; Ariza-Castolo, A. Molecular Structure of Di-Aryl-Aldimines by Multinuclear Magnetic Resonance and X-Ray Diffraction. *J. Mol. Struct.* **2003**, *655* (3), 375–389. https://doi.org/10.1016/S0022-2860(03)00279-5.

(179) Lombardo, D.; Kiselev, M. A.; Magazù, S.; Calandra, P. Amphiphiles Self-Assembly: Basic Concepts and Future Perspectives of Supramolecular Approaches. *Adv. Condens. Matter Phys.* **2015**, *2015*, e151683. https://doi.org/10.1155/2015/151683.

(180) Deamer, D. W. Role of Amphiphilic Compounds in the Evolution of Membrane Structure on the Early Earth. *Orig. Life Evol. Biosph.* **1986**, *17* (1), 3–25. https://doi.org/10.1007/BF01809809.

(181) Przestalski, S.; Sarapuk, J.; Kleszczyńska, H.; Gabrielska, J.; Hladyszowski, J.; Trela, Z.; Kuczera, J. Influence of Amphiphilic Compounds on Membranes. *Acta Biochim. Pol.* **2000**, *47* (3), 627–638. https://doi.org/10.18388/abp.2000_3984.

(182) Kashapov, R.; Gaynanova, G.; Gabdrakhmanov, D.; Kuznetsov, D.; Pavlov, R.; Petrov, K.; Zakharova, L.; Sinyashin, O. Self-Assembly of Amphiphilic Compounds as a Versatile Tool for Construction of Nanoscale Drug Carriers. *Int. J. Mol. Sci.* **2020**, *21* (18), 6961. https://doi.org/10.3390/ijms21186961.

(183) Akiyama, T. Development of Fullerene Thin-Film Assemblies and Fullerene-Diamine Adducts towards Practical Nanocarbon-Based Electronic Materials. *Bull. Chem. Soc. Jpn.* **2019**, *92* (7), 1181–1199. https://doi.org/10.1246/bcsj.20190079.

(184) Kise, R.; Fukumi, A.; Shioya, N.; Shimoaka, T.; Sonoyama, M.; Amii, H.; Takagi, T.; Kanamori, T.; Eda, K.; Hasegawa, T. Fluorous Property of a Short Perfluoroalkyl-Containing Compound Realized by Self-Assembled Monolayer Technique on a Silicon Substrate. *Bull. Chem. Soc. Jpn.* **2019**, *92* (4), 785–789. https://doi.org/10.1246/bcsj.20180356.

(185) Hasan, A.; Saxena, V.; Pandey, L. M. Surface Functionalization of Ti6Al4V via Self-Assembled Monolayers for Improved Protein Adsorption and Fibroblast Adhesion. *Langmuir* **2018**, *34* (11), 3494–3506. https://doi.org/10.1021/acs.langmuir.7b03152.

(186) Kwok, D. Y.; Vollhardt, D.; Miller, R.; Li, D.; Neumann, A. W. Axisymmetric Drop Shape Analysis as a Film Balance. *Colloids Surf. Physicochem. Eng. Asp.* **1994**, *88* (1), 51–58. https://doi.org/10.1016/0927-7757(94)80085-5.

(187) Langmuir-Blodgett Films | Condensed matter physics, nanoscience and mesoscopic physics https://www.cambridge.org/ch/academic/subjects/physics/condensed-matter-

physics-nanoscience-and-mesoscopic-physics/langmuir-blodgett-films-introduction, https://www.cambridge.org/ch/academic/subjects/physics/condensed-matter-physics-nanoscience-and-mesoscopic-physics (accessed 2021 -06 -16).

(188) Crane, J. M.; Putz, G.; Hall, S. B. Persistence of Phase Coexistence in Disaturated Phosphatidylcholine Monolayers at High Surface Pressures. *Biophys. J.* **1999**, *77* (6), 3134–3143. https://doi.org/10.1016/S0006-3495(99)77143-2.

(189) Film Deposition. In *Langmuir-Blodgett Films: An Introduction*; Petty, M. C., Ed.; Cambridge University Press: Cambridge, 1996; pp 39–64. https://doi.org/10.1017/CBO9780511622519.005.

(190) Honig, E. P. Molecular Constitution of X- and Y-Type Langmuir-Blodgett Films. *J. Colloid Interface Sci.* **1973**, *43* (1), 66–72. https://doi.org/10.1016/0021-9797(73)90347-0.

(191) Feltham, R. D.; Brant, P. XPS Studies of Core Binding Energies in Transition Metal Complexes. 2. Ligand Group Shifts. *J. Am. Chem. Soc.* **1982**, *104* (3), 641–645. https://doi.org/10.1021/ja00367a001.

(192) Ivanova, T.; Naumkin, A.; Sidorov, A.; Eremenko, I.; Kiskin, M. X-Ray Photoelectron Spectra and Electron Structure of Polynuclear Cobalt Complexes. *J. Electron Spectrosc. Relat. Phenom.* **2007**, *156–158*, 200–203. https://doi.org/10.1016/j.elspec.2006.12.005.

(193) Moulder, J. F.; Chastain, J. *Handbook of X-Ray Photoelectron Spectroscopy : A Reference Book of Standard Spectra for Identification and Interpretation of XPS Data*; Perkin-Elmer Corporation, 1992.

(194) Haraguchi, H.; Fujiwara, K.; Fuwa, K. A Study of Cobalt Complexes by X-Ray Photoelectron Spectroscopy. *Chem. Lett.* **1975**, *4* (5), 409–414. https://doi.org/10.1246/cl.1975.409.

(195) Dash, K. C.; Folkesson, B.; Larsson, R.; Mohapatra, M. An XPS Investigation on a Series of Schiff Base Dioxime Ligands and Cobalt Complexes. *J. Electron*

Spectrosc. Relat. Phenom. **1989**, *49* (3), 343–357. https://doi.org/10.1016/0368-2048(89)85022-4.

(196) August, D. P.; Dryfe, R. A. W.; Haigh, S. J.; Kent, P. R. C.; Leigh, D. A.; Lemonnier, J.-F.; Li, Z.; Muryn, C. A.; Palmer, L. I.; Song, Y.; Whitehead, G. F. S.; Young, R. J. Self-Assembly of a Layered Two-Dimensional Molecularly Woven Fabric. *Nature* **2020**, *588* (7838), 429–435. https://doi.org/10.1038/s41586-020-3019-9.

(197) Fenn, J. B.; Mann, M.; Meng, C. K.; Wong, S. F.; Whitehouse, C. M. Electrospray Ionization for Mass Spectrometry of Large Biomolecules. *Science* **1989**, *246* (4926), 64–71. https://doi.org/10.1126/science.2675315.

(198) Karas, Michael.; Hillenkamp, Franz. Laser Desorption Ionization of Proteins with Molecular Masses Exceeding 10,000 Daltons. *Anal. Chem.* **1988**, *60* (20), 2299–2301. https://doi.org/10.1021/ac00171a028.

(199) Tanaka, K.; Waki, H.; Ido, Y.; Akita, S.; Yoshida, Y.; Yoshida, T.; Matsuo, T. Protein and Polymer Analyses up to m/z 100 000 by Laser Ionization Time-of-Flight Mass Spectrometry. *Rapid Commun. Mass Spectrom.* **1988**, *2* (8), 151–153. https://doi.org/10.1002/rcm.1290020802.

(200) Jarrold, M. F. Peptides and Proteins in the Vapor Phase. *Annu. Rev. Phys. Chem.* **2000**, *51* (1), 179–207. https://doi.org/10.1146/annurev.physchem.51.1.179.

(201) Wilm, M. Principles of Electrospray Ionization. *Mol. Cell. Proteomics* **2011**, *10* (7). https://doi.org/10.1074/mcp.M111.009407.

(202) Coon, J. J.; Syka, J. E. P.; Shabanowitz, J.; Hunt, D. F. Tandem Mass Spectrometry for Peptide and Protein Sequence Analysis. *BioTechniques* **2005**, *38* (4), 519–523. https://doi.org/10.2144/05384TE01.

(203) Mapping Extracellular Matrix Proteins in Formalin-Fixed, Paraffin-Embedded Tissues by MALDI Imaging Mass Spectrometry | Journal of Proteome Research https://pubs.acs.org/doi/abs/10.1021/acs.jproteome.7b00713 (accessed 2021 -10 -15).

(204) Mairhofer, L.; Eibenberger, S.; Cotter, J. P.; Romirer, M.; Shayeghi, A.; Arndt, M. Quantum-Assisted Metrology of Neutral Vitamins in the Gas Phase. *Angew. Chem. Int. Ed.* **2017**, *56* (36), 10947–10951. https://doi.org/10.1002/anie.201704916.

(205) Eibenberger, S.; Gerlich, S.; Arndt, M.; Tüxen, J.; Mayor, M. Electric Moments in Molecule Interferometry. *New J. Phys.* **2011**, *13* (4), 043033. https://doi.org/10.1088/1367-2630/13/4/043033.

(206) Tüxen, J.; Gerlich, S.; Eibenberger, S.; Arndt, M.; Mayor, M. Quantum Interference Distinguishes between Constitutional Isomers. *Chem. Commun.* **2010**, *46* (23), 4145–4147. https://doi.org/10.1039/C0CC00125B.

(207) Rodewald, J.; Haslinger, P.; Dörre, N.; Stickler, B. A.; Shayeghi, A.; Hornberger, K.; Arndt, M. New Avenues for Matter-Wave-Enhanced Spectroscopy. *Appl. Phys. B* **2016**, *123* (1), 3. https://doi.org/10.1007/s00340-016-6573-y.

(208) Schätti, J.; Kriegleder, M.; Debiossac, M.; Kerschbaum, M.; Geyer, P.; Mayor, M.; Arndt, M.; Köhler, V. Neutralization of Insulin by Photocleavage under High Vacuum. *Chem. Commun.* **2019**, *55* (83), 12507–12510. https://doi.org/10.1039/C9CC05712A.

(209) Li, A.; Turro, C.; Kodanko, J. J. Ru(II) Polypyridyl Complexes as Photocages for Bioactive Compounds Containing Nitriles and Aromatic Heterocycles. *Chem. Commun.* **2018**, *54* (11), 1280–1290. https://doi.org/10.1039/C7CC09000E.

(210) Adams, S. R.; Tsien, R. Y. Controlling Cell Chemistry with Caged Compounds. *Annu. Rev. Physiol.* **1993**, *55* (1), 755–784. https://doi.org/10.1146/annurev.ph.55.030193.003543.

(211) Debiossac, M.; Schätti, J.; Kriegleder, M.; Geyer, P.; Shayeghi, A.; Mayor, M.; Arndt, M.; Köhler, V. Tailored Photocleavable Peptides: Fragmentation and Neutralization Pathways in High Vacuum. *Phys. Chem. Chem. Phys.* **2018**, *20* (16), 11412–11417. https://doi.org/10.1039/C8CP01058G.

(212) Schätti, J.; Kriegleder, M.; Debiossac, M.; Kerschbaum, M.; Geyer, P.; Mayor, M.; Arndt, M.; Köhler, V. Neutralization of Insulin by Photocleavage under High

Vacuum. *Chem. Commun.* **2019**, *55* (83), 12507–12510. https://doi.org/10.1039/C9CC05712A.

(213) Prasad, S.; Mandal, I.; Singh, S.; Paul, A.; Mandal, B.; Venkatramani, R.; Swaminathan, R. Near UV-Visible Electronic Absorption Originating from Charged Amino Acids in a Monomeric Protein. *Chem. Sci.* **2017**, *8* (8), 5416–5433. https://doi.org/10.1039/C7SC00880E.

(214) Burstall, F. H. 34. Optical Activity Dependent on Co-Ordinated Bivalent Ruthenium. *J. Chem. Soc. Resumed* **1936**, No. 0, 173–175. https://doi.org/10.1039/JR9360000173.

(215) Paris, J. P.; Brandt, W. W. CHARGE TRANSFER LUMINESCENCE OF A RUTHENIUM(II) CHELATE. *J. Am. Chem. Soc.* **1959**, *81* (18), 5001–5002. https://doi.org/10.1021/ja01527a064.

(216) Arias-Rotondo, D. M.; McCusker, J. K. An Overview of the Physical and Photophysical Properties of [Ru(Bpy)3]2+. In *Visible Light Photocatalysis in Organic Chemistry*; John Wiley & Sons, Ltd, 2018; pp 1–24. https://doi.org/10.1002/9783527674145.ch1.

(217) Borg, O. A.; Godinho, S. S. M. C.; Lundqvist, M. J.; Lunell, S.; Persson, P. Computational Study of the Lowest Triplet State of Ruthenium Polypyridyl Complexes Used in Artificial Photosynthesis. *J. Phys. Chem. A* **2008**, *112* (19), 4470–4476. https://doi.org/10.1021/jp8000702.

(218) Lewis, N. S.; Nocera, D. G. Powering the Planet: Chemical Challenges in Solar Energy Utilization. *Proc. Natl. Acad. Sci.* **2006**, *103* (43), 15729–15735. https://doi.org/10.1073/pnas.0603395103.

(219) Campagna, S.; Puntoriero, F.; Nastasi, F.; Bergamini, G.; Balzani, V. Photochemistry and Photophysics of Coordination Compounds: Ruthenium. In *Photochemistry and Photophysics of Coordination Compounds I*; Balzani, V., Campagna, S., Eds.; Topics in Current Chemistry; Springer: Berlin, Heidelberg, 2007; pp 117–214. https://doi.org/10.1007/128_2007_133.

(220) Balzani, V.; Bergamini, G.; Marchioni, F.; Ceroni, P. Ru(II)-Bipyridine Complexes in Supramolecular Systems, Devices and Machines. *Coord. Chem. Rev.* **2006**, *250* (11), 1254–1266. https://doi.org/10.1016/j.ccr.2005.11.013.

(221) Lytle, F. E.; Hercules, D. M. Luminescence of Tris(2,2′-Bipyridine)Ruthenium(II) Dichloride. *J. Am. Chem. Soc.* **1969**, *91* (2), 253–257. https://doi.org/10.1021/ja01030a006.

(222) Gleria, M.; Minto, F.; Beggiato, G.; Bortolus, P. Photochemistry of Tris(2,2′-Bipyridine)Ruthenium(II) in Chlorinated Solvents. *J. Chem. Soc. Chem. Commun.* **1978**, No. 7, 285a–285a. https://doi.org/10.1039/C3978000285A.

(223) Durham, B.; Walsh, J. L.; Carter, C. L.; Meyer, T. J. Synthetic Applications of Photosubstitution Reactions of Poly(Pyridyl) Complexes of Ruthenium(II). *Inorg. Chem.* **1980**, *19* (4), 860–865. https://doi.org/10.1021/ic50206a014.

(224) Durham, B.; Caspar, J. V.; Nagle, J. K.; Meyer, T. J. Photochemistry of Tris(2,2′-Bipyridine)Ruthenium(2+) Ion. *J. Am. Chem. Soc.* **1982**, *104* (18), 4803–4810. https://doi.org/10.1021/ja00382a012.

(225) Salassa, L.; Garino, C.; Salassa, G.; Gobetto, R.; Nervi, C. Mechanism of Ligand Photodissociation in Photoactivable [Ru(Bpy)2L2]2+ Complexes: A Density Functional Theory Study. *J. Am. Chem. Soc.* **2008**, *130* (29), 9590–9597. https://doi.org/10.1021/ja8025906.

(226) White, J. K.; Schmehl, R. H.; Turro, C. An Overview of Photosubstitution Reactions of Ru(II) Imine Complexes and Their Application in Photobiology and Photodynamic Therapy. *Inorganica Chim. Acta* **2017**, *454*, 7–20. https://doi.org/10.1016/j.ica.2016.06.007.

(227) Cannizzo, A.; Mourik, F. van; Gawelda, W.; Zgrablic, G.; Bressler, C.; Chergui, M. Broadband Femtosecond Fluorescence Spectroscopy of [Ru(Bpy)3]2+. *Angew. Chem. Int. Ed.* **2006**, *45* (19), 3174–3176. https://doi.org/10.1002/anie.200600125.

(228) Bhasikuttan, A. C.; Suzuki, M.; Nakashima, S.; Okada, T. Ultrafast Fluorescence Detection in Tris(2,2′-Bipyridine)Ruthenium(II) Complex in Solution: Relaxation

Dynamics Involving Higher Excited States. *J. Am. Chem. Soc.* **2002**, *124* (28), 8398–8405. https://doi.org/10.1021/ja026135h.

(229) Durham, B.; Caspar, J. V.; Nagle, J. K.; Meyer, T. J. Photochemistry of Tris(2,2'-Bipyridine)Ruthenium(2+) Ion. *J. Am. Chem. Soc.* **1982**, *104* (18), 4803–4810. https://doi.org/10.1021/ja00382a012.

(230) Greenough, S. E.; Horbury, M. D.; Smith, N. A.; Sadler, P. J.; Paterson, M. J.; Stavros, V. G. Excited-State Dynamics of a Two-Photon-Activatable Ruthenium Prodrug. *ChemPhysChem* **2016**, *17* (2), 221–224. https://doi.org/10.1002/cphc.201501075.

(231) Wachter, E.; Heidary, D. K.; Howerton, B. S.; Parkin, S.; Glazer, E. C. Light-Activated Ruthenium Complexes Photobind DNA and Are Cytotoxic in the Photodynamic Therapy Window. *Chem. Commun.* **2012**, *48* (77), 9649–9651. https://doi.org/10.1039/C2CC33359G.

(232) Knoll, J. D.; Albani, B. A.; Durr, C. B.; Turro, C. Unusually Efficient Pyridine Photodissociation from Ru(II) Complexes with Sterically Bulky Bidentate Ancillary Ligands. *J. Phys. Chem. A* **2014**, *118* (45), 10603–10610. https://doi.org/10.1021/jp5057732.

(233) Blau, F. Die Destillation Pyridinmonocarbonsaurer Salze. *Berichte Dtsch. Chem. Ges.* **1888**, *21* (1), 1077–1078. https://doi.org/10.1002/cber.188802101201.

(234) Blau, F. Über die trockene Destillation von pyridincarbonsauren Salzen. *Monatshefte Für Chem. Verwandte Teile Anderer Wiss.* **1889**, *10* (1), 375–388. https://doi.org/10.1007/BF01516447.

(235) Elsevier, C. J.; Reedijk, J.; Walton, P. H.; Ward, M. D. Ligand Design in Coordination Chemistry: Approaches to New Catalysts, New Materials, and a More Sustainable Environment. *Dalton Trans.* **2003**, No. 10, 1869–1880. https://doi.org/10.1039/B303975G.

(236) Bozec, H. L.; Renouard, T. Dipolar and Non-Dipolar Pyridine and Bipyridine Metal Complexes for Nonlinear Optics. *Eur. J. Inorg. Chem.* **2000**, *2000* (2),

229–239. https://doi.org/10.1002/(SICI)1099-0682(200002)2000:2<229::AID-EJIC229>3.0.CO;2-A.

(237) Schubert, U. S.; Eschbaumer, C. Macromolecules Containing Bipyridine and Terpyridine Metal Complexes: Towards Metallosupramolecular Polymers. *Angew. Chem. Int. Ed.* **2002**, *41* (16), 2892–2926. https://doi.org/10.1002/1521-3773(20020816)41:16<2892::AID-ANIE2892>3.0.CO;2-6.

(238) Kaes, C.; Katz, A.; Hosseini, M. W. Bipyridine: The Most Widely Used Ligand. A Review of Molecules Comprising at Least Two 2,2′-Bipyridine Units. *Chem. Rev.* **2000**, *100* (10), 3553–3590. https://doi.org/10.1021/cr990376z.

(239) Chen, D.; Zhao, Q.; Liu, W. Discovery of Caerulomycin/Collismycin-Type 2,2′-Bipyridine Natural Products in the Genomic Era. *J. Ind. Microbiol. Biotechnol.* **2019**, *46* (3–4), 459–468. https://doi.org/10.1007/s10295-018-2092-7.

(240) Bönnemann, H.; Brinkmann, R. Eine kobalt-katalysierte Einstufen-Synthese von Dipyridinen. *Synthesis* **1975**, *1975* (09), 600–602. https://doi.org/10.1055/s-1975-23850.

(241) Summers, L. A. The Bipyridines. In *Advances in Heterocyclic Chemistry*; Katritzky, A. R., Ed.; Academic Press, 1984; Vol. 35, pp 281–374. https://doi.org/10.1016/S0065-2725(08)60151-8.

(242) Badger, G. M.; Sasse, W. H. F. 123. Synthetic Applications of Activated Metal Catalysts. Part II. The Formation of Heterocyclic Diaryls. *J. Chem. Soc. Resumed* **1956**, No. 0, 616–620. https://doi.org/10.1039/JR9560000616.

(243) Sasse, W. H. F.; Whittle, C. P. 259. Synthetical Applications of Activated Metal Catalysts. Part XII. The Preparation of Symmetrically Substituted 2,2′-Bipyridyls. *J. Chem. Soc. Resumed* **1961**, No. 0, 1347–1350. https://doi.org/10.1039/JR9610001347.

(244) Sasse, W. H. F. 610. Synthetical Applications of Activated Metal Catalysts. Part VII. The Formation of 2,2′-Bipyridyl and 2-2′-Pyrrolylpyridine from Pyridine

under the Influence of Degassed Raney Nickel. *J. Chem. Soc. Resumed* **1959**, No. 0, 3046–3049. https://doi.org/10.1039/JR9590003046.

(245) Fanta, P. E. The Ullmann Synthesis of Biaryls. *Synthesis* **1974**, *1974* (01), 9–21. https://doi.org/10.1055/s-1974-23219.

(246) Nakamaru, K. Synthesis, Luminescence Quantum Yields, and Lifetimes of Trischelated Ruthenium(II) Mixed-Ligand Complexes Including 3,3′-Dimethyl-2,2′-Bipyridyl. *Bull. Chem. Soc. Jpn.* **1982**, *55* (9), 2697–2705. https://doi.org/10.1246/bcsj.55.2697.

(247) Eisenbach, C. D.; Göldel, A.; Terskan-Reinold, M.; Schubert, U. S. Block Copolymers with Bipyridine Containing Segments: Synthesis and Self-Organization by Cu(I) Complexation. *Macromol. Chem. Phys.* **1995**, *196* (4), 1077–1091. https://doi.org/10.1002/macp.1995.021960410.

(248) Wang, Z.; Reibenspies, J.; Motekaitis, R. J.; Martell, A. E. Unusual Stabilities of 6,6′-Bis(Aminomethyl)-2,2′-Bipyridyl Chelates of Transition-Metal Ions and Crystal Structures of the Ligand and Its Copper(II) and Nickel(II) Complexes. *J. Chem. Soc. Dalton Trans.* **1995**, No. 9, 1511–1518. https://doi.org/10.1039/DT9950001511.

(249) Iyoda, M.; Otsuka, H.; Sato, K.; Nisato, N.; Oda, M. Homocoupling of Aryl Halides Using Nickel(II) Complex and Zinc in the Presence of Et4NI. An Efficient Method for the Synthesis of Biaryls and Bipyridines. *Bull. Chem. Soc. Jpn.* **1990**, *63* (1), 80–87. https://doi.org/10.1246/bcsj.63.80.

(250) Tamao, K.; Kodama, S.; Nakajima, I.; Kumada, M.; Minato, A.; Suzuki, K. Nickel-Phosphine Complex-Catalyzed Grignard Coupling—II: Grignard Coupling of Heterocyclic Compounds. *Tetrahedron* **1982**, *38* (22), 3347–3354. https://doi.org/10.1016/0040-4020(82)80117-8.

(251) Parks, J. E.; Wagner, B. E.; Holm, R. H. Syntheses Employing Pyridyllithium Reagents: New Routes to 2,6-Disubstituted Pyridines and 6,6′-Disubstituted 2,2′-Bipyridyls. *J. Organomet. Chem.* **1973**, *56*, 53–66. https://doi.org/10.1016/S0022-328X(00)89953-2.

(252) Yamamoto, Y.; Azuma, Y.; Mitoh, H. General Method for Synthesis of Bipyridines: Palladium Catalyzed Cross-Coupling Reaction of Trimethylstannyl-Pyridines with Bromopyridines. *Synthesis* **1986**, *1986* (07), 564–565. https://doi.org/10.1055/s-1986-31705.

(253) Matondo, H.; Souirti, S.; Baboulène, M. Improved Synthesis of Azaheteroarylboronic Acids Using Tris- Trimethylsilylborate Under Mild Conditions. *Synth. Commun.* **2003**, *33* (5), 795–800. https://doi.org/10.1081/SCC-120016325.

(254) Cook, X. A. F.; Gombert, A. de; McKnight, J.; Pantaine, L. R. E.; Willis, M. C. The 2-Pyridyl Problem: Challenging Nucleophiles in Cross-Coupling Arylations. *Angew. Chem. Int. Ed.* **2021**, *60* (20), 11068–11091. https://doi.org/10.1002/anie.202010631.

(255) Newkome, G. R.; Patri, A. K.; Holder, E.; Schubert, U. S. Synthesis of 2,2′-Bipyridines: Versatile Building Blocks for Sexy Architectures and Functional Nanomaterials. *Eur. J. Org. Chem.* **2004**, *2004* (2), 235–254. https://doi.org/10.1002/ejoc.200300399.

(256) Hapke, M.; Brandt, L.; Lützen, A. Versatile Tools in the Construction of Substituted 2,2′-Bipyridines—Cross-Coupling Reactions with Tin, Zinc and Boron Compounds. *Chem. Soc. Rev.* **2008**, *37* (12), 2782–2797. https://doi.org/10.1039/B810973G.

(257) Debiossac, M.; Schätti, J.; Kriegleder, M.; Geyer, P.; Shayeghi, A.; Mayor, M.; Arndt, M.; Köhler, V. Tailored Photocleavable Peptides: Fragmentation and Neutralization Pathways in High Vacuum. *Phys. Chem. Chem. Phys.* **2018**, *20* (16), 11412–11417. https://doi.org/10.1039/C8CP01058G.

(258) Schätti, J.; Kriegleder, M.; Debiossac, M.; Kerschbaum, M.; Geyer, P.; Mayor, M.; Arndt, M.; Köhler, V. Neutralization of Insulin by Photocleavage under High Vacuum. *Chem. Commun.* **2019**, *55* (83), 12507–12510. https://doi.org/10.1039/C9CC05712A.

(259) Li, A.; Turro, C.; Kodanko, J. J. Ru(II) Polypyridyl Complexes as Photocages for Bioactive Compounds Containing Nitriles and Aromatic Heterocycles. *Chem. Commun.* **2018**, *54* (11), 1280–1290. https://doi.org/10.1039/C7CC09000E.

(260) Zeng, L.; Gupta, P.; Chen, Y.; Wang, E.; Ji, L.; Chao, H.; Chen, Z.-S. The Development of Anticancer Ruthenium(II) Complexes: From Single Molecule Compounds to Nanomaterials. *Chem. Soc. Rev.* **2017**, *46* (19), 5771–5804. https://doi.org/10.1039/c7cs00195a.

(261) Laemmel, A.-C.; Collin, J.-P.; Sauvage, J.-P. Efficient and Selective Photochemical Labilization of a Given Bidentate Ligand in Mixed Ruthenium(II) Complexes of the Ru(Phen)2L2+ and Ru(Bipy)2L2+ Family (L = Sterically Hindering Chelate). *Eur. J. Inorg. Chem.* **1999**, *1999* (3), 383–386. https://doi.org/10.1002/(SICI)1099-0682(199903)1999:3<383::AID-EJIC383>3.0.CO;2-9.

(262) Baranoff, E.; Collin, J.-P.; Furusho, J.; Furusho, Y.; Laemmel, A.-C.; Sauvage, J.-P. Photochemical or Thermal Chelate Exchange in the Ruthenium Coordination Sphere of Complexes of the Ru(Phen)2L Family (L = Diimine or Dinitrile Ligands). *Inorg. Chem.* **2002**, *41* (5), 1215–1222. https://doi.org/10.1021/ic011014o.

(263) Durham, B.; Caspar, J. V.; Nagle, J. K.; Meyer, T. J. Photochemistry of Tris(2,2′-Bipyridine)Ruthenium(2+) Ion. *J. Am. Chem. Soc.* **1982**, *104* (18), 4803–4810. https://doi.org/10.1021/ja00382a012.

(264) Van Houten, J.; Watts, R. J. Temperature Dependence of the Photophysical and Photochemical Properties of the Tris(2,2′-Bipyridyl)Ruthenium(II) Ion in Aqueous Solution. *J. Am. Chem. Soc.* **1976**, *98* (16), 4853–4858. https://doi.org/10.1021/ja00432a028.

(265) Ford, P. C. The Ligand Field Photosubstitution Reactions of D6 Hexacoordinate Metal Complexes. *Coord. Chem. Rev.* **1982**, *44* (1), 61–82. https://doi.org/10.1016/S0010-8545(00)80517-2.

(266) Havrylyuk, D.; Stevens, K.; Parkin, S.; Glazer, E. C. Toward Optimal Ru(II) Photocages: Balancing Photochemistry, Stability, and Biocompatibility Through Fine Tuning of Steric, Electronic, and Physiochemical Features. *Inorg. Chem.* **2020**, *59* (2), 1006–1013. https://doi.org/10.1021/acs.inorgchem.9b02065.

(267) Juris, A.; Barigelletti, F.; Balzani, V.; Belser, P.; Zelewsky, A. V. New Photosensitizers of the Ruthenium-Polypyridine Family for the Water Splitting Reaction. *Isr. J. Chem.* **1982**, *22* (2), 87–90. https://doi.org/10.1002/ijch.198200018.

(268) Yang, R.; Dai, L. X. Synthesis and Electronic Spectra of Ruthenium(II)-1,1'-Biisoquinoline Complexes. *Chin. Chem. Lett.* **1993**, *4* (11), 1021–1024.

(269) Zhu, Z.-Y.; Mao, C.; Yang, R.-Y.; Dai, L.-X.; Nie, C.-S. Surface-Enhanced Raman Scattering of Ru(II) Homo- and Heterolytic Complexes with 2,2'-Bipyridine and 1,1'-Biisoquinoline in Aqueous Silver Sol. *J. Raman Spectrosc.* **1993**, *24* (4), 221–226. https://doi.org/10.1002/jrs.1250240407.

(270) Godt, A.; Ünsal, Ö.; Roos, M. Synthesis of 3,5-Disubstituted 4-Hydroxybenzoates by Aryl–Aryl and Alkynyl–Aryl Coupling. *J. Org. Chem.* **2000**, *65* (9), 2837–2842. https://doi.org/10.1021/jo991907m.

(271) Aggarwal, A. V.; Jester, S.-S.; Taheri, S. M.; Förster, S.; Höger, S. Molecular Spoked Wheels: Synthesis and Self-Assembly Studies on Rigid Nanoscale 2D Objects. *Chem. – Eur. J.* **2013**, *19* (14), 4480–4495. https://doi.org/10.1002/chem.201203444.

(272) Lei, S.; Ver Heyen, A.; De Feyter, S.; Surin, M.; Lazzaroni, R.; Rosenfeldt, S.; Ballauff, M.; Lindner, P.; Mössinger, D.; Höger, S. Two-Dimensional Oligo(Phenylene-Ethynylene-Butadiynylene)s: All-Covalent Nanoscale Spoked Wheels. *Chem. – Eur. J.* **2009**, *15* (11), 2518–2535. https://doi.org/10.1002/chem.200801939.

(273) Vains, J. B. R. D.; Papet, A. L.; Marsura, A. New Symmetric and Unsymmetric Polyfunctionalized 2,2'-Bipyridines. *J. Heterocycl. Chem.* **1994**, *31* (4), 1069–1077. https://doi.org/10.1002/jhet.5570310463.

(274) Howerton, B. S.; Heidary, D. K.; Glazer, E. C. Strained Ruthenium Complexes Are Potent Light-Activated Anticancer Agents. *J. Am. Chem. Soc.* **2012**, *134* (20), 8324–8327. https://doi.org/10.1021/ja3009677.

(275) Xie, W.-W.; Liu, Y.; Yuan, R.; Zhao, D.; Yu, T.-Z.; Zhang, J.; Da, C.-S. Transition Metal-Free Homocoupling of Unactivated Electron-Deficient Azaarenes. *Adv. Synth. Catal.* **2016**, *358* (6), 994–1002. https://doi.org/10.1002/adsc.201500445.

(276) Ashby, M. T.; Govindan, G. N.; Grafton, A. K. Metal-Assisted Racemization of the Atropisomers of a 1,1'-Binaphthyl Skeleton via a Syn Transition State. *J. Am. Chem. Soc.* **1994**, *116* (11), 4801–4809. https://doi.org/10.1021/ja00090a028.

(277) Sullivan, B. P.; Salmon, D. J.; Meyer, T. J. Mixed Phosphine 2,2'-Bipyridine Complexes of Ruthenium. *Inorg. Chem.* **1978**, *17* (12), 3334–3341. https://doi.org/10.1021/ic50190a006.

(278) Klassen, D. M. Excited States of Mixed Ligand Complexes of Ruthenium (II) with 2-(2-Pyridyl) Quinoline and 2,2-Biquinoline. *Chem. Phys. Lett.* **1982**, *93* (4), 383–386. https://doi.org/10.1016/0009-2614(82)83714-7.

(279) Bertuzzi, G.; Pecorari, D.; Bernardi, L.; Fochi, M. An Organocatalytic Enantioselective Direct **α**-Heteroarylation of Aldehydes with Isoquinoline N-Oxides. *Chem. Commun.* **2018**, *54* (32), 3977–3980. https://doi.org/10.1039/C8CC01735B.

(280) Stephens, D. E.; Lakey-Beitia, J.; Burch, J. E.; Arman, H. D.; Larionov, O. V. Mechanistic Insights into the Potassium Tert-Butoxide-Mediated Synthesis of N-Heterobiaryls. *Chem. Commun.* **2016**, *52* (64), 9945–9948. https://doi.org/10.1039/C6CC04816A.

(281) Dongare, P.; Myron, B. D. B.; Wang, L.; Thompson, D. W.; Meyer, T. J. [Ru(Bpy)3]2+∗ Revisited. Is It Localized or Delocalized? How Does It Decay? *Coord. Chem. Rev.* **2017**, *345*, 86–107. https://doi.org/10.1016/j.ccr.2017.03.009.

(282) Schmid, L.; Kerzig, C.; Prescimone, A.; Wenger, O. S. Photostable Ruthenium(II) Isocyanoborato Luminophores and Their Use in Energy Transfer and Photoredox Catalysis. *JACS Au* **2021**, *1* (6), 819–832. https://doi.org/10.1021/jacsau.1c00137.

(283) Li, A.; Turro, C.; Kodanko, J. J. Ru(II) Polypyridyl Complexes as Photocages for Bioactive Compounds Containing Nitriles and Aromatic Heterocycles. *Chem. Commun.* **2018**, *54* (11), 1280–1290. https://doi.org/10.1039/C7CC09000E.

(284) Rapp, T. L.; Wang, Y.; Delessio, M. A.; Gau, M. R.; Dmochowski, I. J. Designing Photolabile Ruthenium Polypyridyl Crosslinkers for Hydrogel Formation and Multiplexed, Visible-Light Degradation. *RSC Adv.* **2019**, *9* (9), 4942–4947. https://doi.org/10.1039/C8RA09764J.

(285) Loftus, L. M.; Al-Afyouni, K. F.; Turro, C. New RuII Scaffold for Photoinduced Ligand Release with Red Light in the Photodynamic Therapy (PDT) Window. *Chem. – Eur. J.* **2018**, *24* (45), 11550–11553. https://doi.org/10.1002/chem.201802405.

(286) Doniach, S.; Sunjic, M. Many-Electron Singularity in X-Ray Photoemission and X-Ray Line Spectra from Metals. *J. Phys. C Solid State Phys.* **1970**, *3* (2), 285–291. https://doi.org/10.1088/0022-3719/3/2/010.

(287) Shirley, D. A. High-Resolution X-Ray Photoemission Spectrum of the Valence Bands of Gold. *Phys. Rev. B* **1972**, *5* (12), 4709–4714. https://doi.org/10.1103/PhysRevB.5.4709.

(288) Hesse, R.; Chassé, T.; Szargan, R. Peak Shape Analysis of Core Level Photoelectron Spectra Using UNIFIT for WINDOWS. *Fresenius J. Anal. Chem.* **1999**, *365* (1), 48–54. https://doi.org/10.1007/s002160051443.

(289) Scofield, J. H. Hartree-Slater Subshell Photoionization Cross-Sections at 1254 and 1487 EV. *J. Electron Spectrosc. Relat. Phenom.* **1976**, *8* (2), 129–137. https://doi.org/10.1016/0368-2048(76)80015-1.

(290) Frydman, E.; Cohen, H.; Maoz, R.; Sagiv, J. Monolayer Damage in XPS Measurements As Evaluated by Independent Methods. *Langmuir* **1997**, *13* (19), 5089–5106. https://doi.org/10.1021/la962058q.

(291) Montalvo-González, R.; Ariza-Castolo, A. Molecular Structure of Di-Aryl-Aldimines by Multinuclear Magnetic Resonance and X-Ray Diffraction. *J. Mol. Struct.* **2003**, *655* (3), 375–389. https://doi.org/10.1016/S0022-2860(03)00279-5.

Curriculum Vitae

Personal Information

Name: Alfredo Di Silvestro

DoB: 20.08.1991

Citizenship: Italian

E-Mail: alfredo.disilvestro@unibas.ch

Education

03/2017-11/2021 **Doctor of Philosophy (PhD) in Chemistry**, Department of Chemistry, University of Basel.

Supervisor: Prof. Dr. Marcel Mayor, University of Basel

Co-referee: Prof. Dr. Oliver Wenger, University of Basel

Externe-referee: Prof. Dr. A. Dieter Schlüter , ETH Zürich

08/2015-02/2017 **Master of Science in Chemistry (M.Sc.)**, Department of Chemistry, University of Basel.

Master thesis: Tailor-Made Phthalocyanine with Photocleavable Tags for Interferometry Experiments.

Supervisor: Prof. Dr. Marcel Mayor, University of Basel

08/2011-08/2015 **Bachelor of Science in Chemistry (B.Sc.),** Department of Chemistry, University of Basel.

Teaching Activities

03/2017-11/2021 Laboratory teacher of bachelor students and master students in organic chemistry (550 + hrs), Department of Chemistry, University of Basel.

Institutional Responsibilities

03/2017-11/2021   Direct-Injection-Electrospray Mass Spectrometer, maintenance and trainer, Department of Chemistry, University of Basel.

03/2017-11/2021   Circular Dichroism Spectrophotometer, maintenance and trainer, Department of Chemistry, University of Basel.

Personal Skills

Languages   German (Native)

Italian (Native)

English (Full Professional Proficiency)

French (Limited Working Proficiency)

Spanish (Good knowledge in speaking)

List of Publications

Kinetically Inert Amphiphilic Heteroleptic Co(III) Terpyridine Complex Suitable for 2D Polymerisation at an Air/Water Interface. A. Di Silvestro, M. Mayor, *European Journal of Organic Chemistry*, **2022**. Manuscript close to submission.

From the Loom to the Laboratory: Molecular Textiles, A. Di Silvestro, M. Mayor, *CHIMIA* **2019**, *73*, 455-461

Optimized reconstitution of membrane proteins into synthetic membranes, R. Goers, J. Thomma, N. Ritzmann, A. Di Silvestro, C. Alter, G. Gunkel-Grabole, D. Fotiadis, D. J. Müller, W. Meier, *Commun Chem*, **2018**, *35*, 1-10.